ORNL/TM-2012/571

Propulsion Materials

VEHICLE TECHNOLOGIES OFFICE

2012

annual progress report

U.S. DEPARTMENT OF ENERGY | Energy Efficiency & Renewable Energy

U.S. Department of Energy
Office of Vehicle Technologies
1000 Independence Avenue S.W.
Washington, DC 20585-0121

FY 2012

Progress Report for Propulsion Materials

Energy Efficiency and Renewable Energy
Office of Vehicle Technologies
Advanced Materials Technologies

Patrick B. Davis	**Program Manager, OVT**
Carol L. Schutte	**Team Leader, Advanced Materials Technologies**
Jerry L. Gibbs	**Technology Manager**

January 2013

CONTENTS

INTRODUCTION
Propulsion Materials R&D: Enabling Materials Technologies to Meet Vehicle Technologies Program Goals

The Department of Energy's (DOE's) Office of Vehicle Technologies (OVT) is pleased to introduce the *FY 2012 Annual Progress Report for the Propulsion Materials Research and Development Program.* Together with DOE national laboratories, and in partnership with universities and private industry across the United States, the Propulsion Materials program continues to invest in research and development (R&D) that provides enabling materials technologies for fuel-efficient and environmentally friendly commercial and passenger vehicles.

This introduction summarizes the objectives, progress and highlights of the program in FY 2012. The Propulsion Materials program actively supports the energy security and reduction of greenhouse emissions goals of the OVT Program by investigating and identifying the materials properties that are most essential for continued development of cost-effective, highly efficient, and environmentally friendly next-generation heavy and light duty powertrains. The technical approaches available to enhance propulsion systems focus on improvements in both vehicle efficiency and fuel substitution, both of which must overcome performance limitations of materials currently in use. The Propulsion Materials activities work with National Laboratories, industry experts, and OVT Program teams to develop strategies that overcome materials limitations in powertrain performance. The technical maturity of the portfolio of funded projects ranges from basic science to subsystem prototype validation.

The Propulsion Materials activity is structured to serve as an enabling partner and supporter of the following OVT research and development (R&D) activities:

(a) Hybrid and Vehicle Systems
(b) Energy Storage
(c) Power Electronics and Electrical Machines
(d) Advanced Combustion Engines
(e) Fuels and Lubricants

Projects within the Propulsion Materials activity address materials concerns that directly impact critical technology barriers within each of the above programs – barriers that include fuel efficiency, thermal management, emissions reduction, improved reliability, waste-heat recovery and reduced manufacturing costs. The program engages only the barriers that involve fundamental, high-risk materials issues.

Enabling Advanced Technologies

The Propulsion Materials activity focuses on key technical deficiencies in materials performance that limit expanded capabilities of advanced combustion engines, electric-drive systems, and fuels and lubricants. It provides materials R&D expertise and advanced materials testing and development that support the goals of combustion, hybrid and power electronics development. The program provides enabling materials support for combustion, hybrid and power electronics development, including the following:

- Materials for high-efficiency combustion technologies, for example, homogenous-charge compression ignition (HCCI)
- Materials for 55% thermal efficiency for heavy-duty diesel engines
- Materials for waste-heat recovery via thermoelectric modules, with potential for 10% increase in fuel efficiency
- Materials technologies for effective reduction of tailpipe emissions, including diesel particulate filters, catalyst development, characterization and testing, as well as exhaust gas recirculation (EGR) coolers
- Materials technologies for electric and hybrid-electric vehicles, including advanced power electronics materials and electric motors
- Materials for alternate-fuels, including materials compatibility and corrosion in bio-fuels
- Alternatives to rare and costly materials, for example, rare-earth elements, and technologies to improve overall materials availability, for example, recycling

The program supports these core technology areas by providing materials expertise, testing capabilities, and technical solutions for materials problems. The component development, materials processing, and characterization that the program provides are enablers of the successful development of efficient, durable and emissions-compliant engines.

Program Organization

The Propulsion Materials Program consists of four R&D projects (shown below) that support the OVT Program propulsion technologies. Each project consists of several R&D agreements.

(1) Materials for Electric and Hybrid Drive Systems
-Develop materials appropriate for automotive power electronics, electric motors, and other electric and hybrid system applications.
(2) Materials for High Efficiency Engines
-Develop materials for next generation high efficiency engines, address anticipated issues with engine cylinder block, head, crankshafts, pistons, valves and valve train, fuel injectors, turbochargers, and exhaust gas recirculation (EGR) systems.
(3) Materials for Control of Exhaust Gases and Energy Recovery Systems
-Develop materials for exhaust aftertreatment and waste heat recovery applications
(4) Materials by Design (Application Specific Materials Simulation, Characterization & Synthesis)
-Adopt computational materials design – atomic-scale characterization protocol to develop advanced materials for NOx catalysts, thermoelectric generators, and electric motors; provide a pathway to transition Basic Energy Science research to practical applications.

Research and development projects and agreements are evaluated annually using strategic objectives. Agreements are evaluated on relevance to OVT Program objectives and supported team's priorities, strength of industrial support for the activity, and perceived value of the R&D activity to the OVT Program. In order to keep the program fresh and up-to-date, at least 10% of the agreements are retired annually. New projects are selected by competitive solicitation in accordance with identified OVT needs.

Selected Highlights

(1) Materials for Electric and Hybrid Drive Systems

The goal of the Automotive Power Electronics and Electric Machines (APEEEM) Program is to reduce the size, weight and volume of power electronics without increasing the cost or reducing the reliability. Many, if not most technical barriers are directly linked to the contemporary materials limitations of subcomponents found within devices that comprise inverters, converters and motors. The materials limitations include:

- Insufficient power density in permanent magnets
- Insufficient bandgap
- Excessive thermal insulation
- Excessive electrical insulation
- Insufficient temperature capability
- Availability of key strategic materials

The role of the Propulsion Materials program is to provide materials support for the components and systems under development by the APEEM sub-program. Research activities will develop improved materials and processes for development of improved thermal management systems, capacitors, motors and power electronics.

In one project, researchers at Oak Ridge National Laboratory (ORNL) are exploring rare earth-free compounds for candidate permanent magnet materials, taking advantage of ORNLs extensive capabilities in computational science, materials synthesis, processing, and characterization. The EV Everywhere Grand Challenge identifies non-rare earth motor architectures as a key long term strategy for reducing and stabilizing motor costs, and recognizes that basic research discoveries in permanent magnet materials are required to meet the program's goals. Strong permanent magnets are critical components of the drive systems used in electric vehicles. State of the art magnets, such as $(Nd,Dy)_2(Fe,Co)_{14}B$, contain rare-earth elements, which have rising costs, limited domestic supply, and a projected critical supply risk. Replacement materials must achieve elevated temperature operation to minimize motor cooling needs, while also retaining competitive magnetic energy density.

The ORNL effort targets both new materials and understudied compounds from the literature. Combining light transition metals like Fe and Co, which tend to be strongly magnetic, with heavy transition metals like Hf and W, which tend to induce the magnetic anisotropy needed to oppose demagnetization, has been identified as one of the most promising routes to development of new hard ferromagnets without rare-earths. These efforts have led to the identification and study of the Hf-Co system, and the discovery of promising permanent magnet properties in alloys of composition $Hf_2Co_{11}B$.

These Hf-Co-B alloys are being produced by melt-spinning, a relatively common and scalable industrial manufacturing technique (Figure 1a). The material has complex micro- and nano- structures, which likely contribute to the desired performance characteristics. The TEM image shown in Figure 1b shows crystallites as small as 5 nm and as large as 50 nm. This nano-structure, which has not yet been optimized, is expected to be responsible for the good magnetic performance highlighted by the hysteresis loop shown

Figure 1c. This hysteresis loop, collected at room temperature, shows good “squareness” and a high coercive field. These properties are required to achieve a large energy product, which is a measure of the energy that can be stored in the material’s magnetic field. The room-temperature energy product of $Hf_2Co_{11}B$ is compared with common non-rare earth permanent magnets in Figure 1d. The new alloy, though not yet fully optimized, has properties that are competitive with other non-rare-earth magnetic materials which have been studied for decades, such as AlNiCo. In fact, these non-optimized $Hf_2Co_{11}B$ ribbons achieve energy products approaching half that of melt-spun flakes of state of the art $Nd_2Fe_{14}B$. In addition, the Curie temperature of $Hf_2Co_{11}B$ is about 150°C higher than $Nd_2Fe_{14}B$, which is critical for enabling stable use at higher operating temperatures, like those expected in future high-performance electric motors. Propulsion Materials researchers are continuing to study this material to better understand its behavior and to define routes toward optimizing its permanent magnet properties through compositional and microstructural tuning.

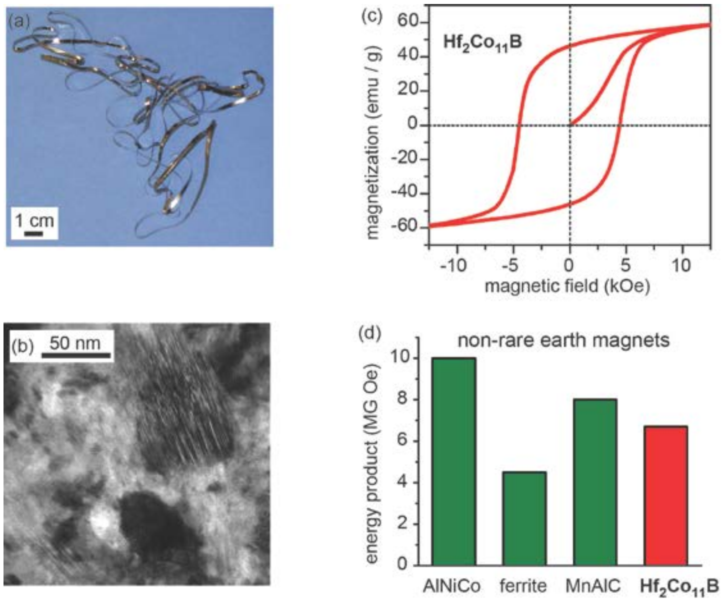

Figure 1. (a) A sample of $Hf_2Co_{11}B$ produced by melt-spinning. (b) TEM image of the complex nano-structure of the material showing a wide range of crystallite sizes, some as small as 5 nm. (c) Magnetic hysteresis loop of melt-spun $Hf_2Co_{11}B$ showing high coercivity (~4.5 kOe) and good “squareness”. (d) comparison of magnetic energy products for non-rare earth magnets.

This initial study of $Hf_2Co_{11}B$ has already produced competitive properties, and further optimization is expected to be possible. While optimization of the cost and performance of well-known magnets, including rare-earth magnets, continues, discoveries like the one highlighted here are most likely to produce disruptive, breakthrough developments to enable future generations of widely-available permanent magnet motors. The availability of new high-performance magnets without rare earth elements could result in lower cost motors and a more stable supply chain. Since magnets make up about 30% of the total cost of electric motors for automotive applications, the potential technical and economic impacts are significant.

(2) Materials for High Efficiency Engines

In support of OVT Program goals, the materials for high efficiency engines project develops materials, materials treatments, coatings and surface treatments necessary to overcome materials-related hurdles. This project focuses on key material-related technical issues identified by the Advanced Combustion Engine (ACE) group and industrial partners.

A project at ORNL was tasked with defining the critical exposure conditions that lead to aluminum corrosion in various fuel blends containing ethanol, and made the discovery that aluminum and *dry* ethanol are fundamentally incompatible at elevated temperatures. This research activity demonstrated that a wide range of aluminum alloys are vulnerable to extensive corrosive attack in ethanol-containing environments having very low water concentrations, at elevated temperature, and after exposure times on the order of hours.

The corrosion reaction sequence observed for Al in ethanol-containing blends can be described as follows: on exposure to dry ethanol, the passive film on aluminum is susceptible to dehydration and/or penetration by the alcohol. Film breakdown exhibits a finite incubation period which is sensitive to ppm levels of water in the alcohol, temperature, and possibly stress state. Once the passive oxide layer is penetrated, the base metal is exposed to ethanol and active corrosion is initiated. It was shown that Al corrosion typically initiates at isolated points associated with initial film penetration/breakdown within hours, and with time these spots grow in number and size until they overlap and eventually cover the entire exposed surface. An example of the corrosion reaction progression is presented in Figure 2. Depending on other environmental factors, it may be possible to saturate the fuel environment with corrosion products such that subsequent precipitation from solution quenches the corrosion reaction. Experiments involving the galvanic coupling of aluminum with other metals such as carbon steel, copper, and brass clearly demonstrated that galvanic corrosion is not a significant factor in the proposed aluminum/ethanol corrosion mechanism.

Once the aluminum corrosion reaction is initiated, the reactivity rate is strongly dependent on the concentration of water in the ethanol fuel, as well as the concentration of ethanol in the fuel. Figure 3 gives a representative example of the effect of ethanol concentration on the corrosion rate. At reduced water concentrations, aluminum is particularly susceptible to rapid rates of corrosion in ethanol fuel blends at temperatures above 80°C. Elevated levels of water suppress aluminum reactivity with ethanol by encouraging the passive aluminum oxide or hydrated aluminum oxide layer to remain protective or to reform if penetrated. It appears that commercial ethanol-containing fuels are not highly corrosive to aluminum due to the hygroscopic nature of ethanol – it is not uncommon for “real-world” ethanol fuel blends to contain water levels approaching 1%, which is sufficient to eliminate aluminum corrosion in most environments. Observations of aluminum/ethanol corrosion in engines appear to be isolated to areas where un-combusted dry fuel is allowed to pool and stagnate at an elevated temperature.

Viable routes for investigation to mitigate this reactivity/corrosion problem include: (a) the development of an aluminum alloy composition that allows for a more tenacious, less defective, passive oxide layer and/or a more rapid reforming of a protective layer, especially at lower water levels; and (b) development

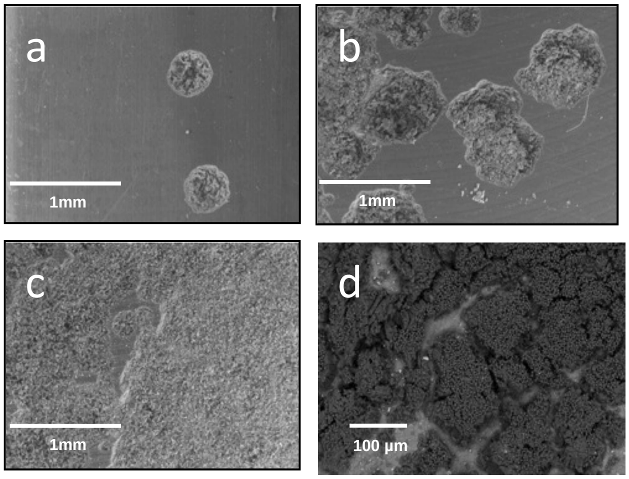

Figure 2. *SEM images of an aluminum alloy exposed to anhydrous E100 at 78°C for time periods a) 3 hours b) 4 hours c) 12 hours and d) 24 hours.*

Figure 3. *Corrosion of aluminum in increasing concentrations of dry ethanol synthetic fuel blend C at 120°C for a 24 hour time period.*

of a fuel additive package that is compatible with engine performance and fuel economy that decreases aluminum reactivity in the presence of ethanol. Further, the present study was carried out under tightly controlled laboratory conditions, using reagent grade simulated fuels. Therefore, the effect of impurities in commercial grade fuel blends is relatively unknown and needs future study, particularly for future designs where engine temperatures and ethanol contents of fuel may increase.

(3) Materials for Control of Exhaust Gases and Energy Recovery Systems

Roughly 30% of the chemical energy stored in the fuel consumed by an internal combustion engine is contained within the flow of engine exhaust gases. This project focuses on development of materials necessary to efficiently control the flow of thee exhaust gases while extracting the maximum amount of usable energy from them with minimal negative impact on overall efficiency. The evolving combustion regimes and fuels that high efficiency engines will need to utilize in the future complicate the objective of this project. Materials developed under this project will be used for high performance components including: thermo-electrics, high temperature exhaust manifolds, exhaust gas recirculation (EGR) coolers, advanced turbochargers, direct energy conversion devices, exhaust gas sensors, and exhaust aftertreatment devices and catalysts.

The combined approach of first principles modeling and experimental studies in a project at ORNL have resulted in two significant advances in the understanding and design of automotive emissions catalyst materials, one of which provides a potential pathway toward developing NO_x treatment strategies that are effective at exhaust temperatures as low as 150^{o}C. The automotive industry is facing an unprecedented challenge over the next decade to achieve new fuel economy standards while simultaneously meeting new emission regulations for light-duty vehicles. New corporate average fuel economy standards (CAFE) have led to extensive work on engine technologies that offer higher fuel efficiency, including diesel engines and lean-burn gasoline engines. The emissions from these engines generally contain high concentrations of NO_x and very low or no hydrocarbons (HC) and CO. Commercial catalysts have been developed that effectively treat NO_x under oxidizing conditions and are adequate for treating emissions from contemporary engines. However, further advances in engine technologies are resulting in reduced combustion temperatures and are thus leading to lower temperature exhaust conditions that necessitate the need for lower temperature catalysts. The US DRIVE Advanced Combustion and Emission Control (ACEC) team has identified the need for emission control catalysts that can effectively treat engine emissions at 150°C to meet ACEC2020 and beyond vehicle emission targets. This goal necessitates new materials or designs, since current NOx treatment systems are effective only at temperatures of 200^{o}C and higher.

This research effort focuses on the search for durable emission treatment catalysts (Lean NOx traps, three-way catalysts, oxidation catalysts, and selective catalytic reduction catalysts) from a protocol based on an integrated approach between computational modeling/design and experimental testing of new catalyst materials to rapidly identify the key physiochemical parameters necessary for improving catalytic efficiency. Two areas of recent success are highlighted: (1) understanding and improving the durability and stability of supported platinum within catalysts, and (2) discovery of a new low temperature NO_x treatment catalyst material which resulted from structural insights gained through theoretical studies of these systems under the Propulsion Materials program.

First principles studies and experimental work on Pt/alumina systems [Figure 4] led to the suggestion that θ-alumina is a better surrogate for modeling γ-alumina than α-alumina (Narula, C.K. et a. *J. Phys. Chem. C*, **2012**, *116*, 5628). Results also show that platinum particles of three atoms or more are energetically favored over single atoms and that palladium incorporation (as low as 10 at%) leads to Pt-Pd nanoparticles with Pd on the shell. The Pt-Pd particles are hydrothermally more stable than Pt particles alone at elevated temperatures. Interestingly, the sintering of Pt-Pd particles occurs via a combining of individual particles in a mode that results in Pd remaining on the surface.

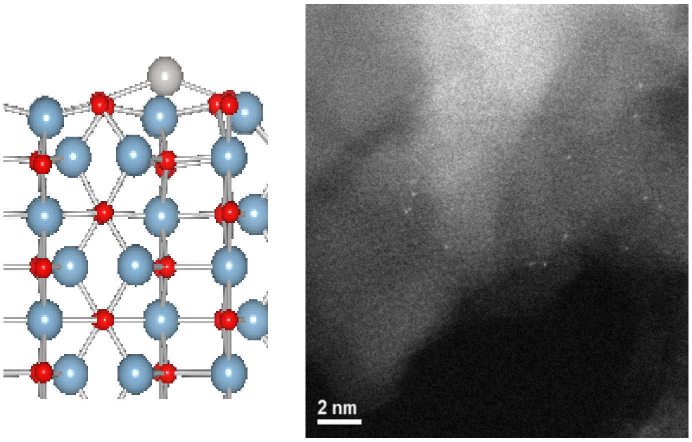

Figure 4: Single Pt atoms on alumina – theoretical model (left) and TEM of synthesized catalyst (right)

First principles studies of zeolites Cu-ZSM-5 and Cu-SSZ-13 [Figure 5] with support from the Propulsion Materials Program provided insights into the design of heterobimetallic zeolites that allow effective treatment of NO_x

at temperatures as low as 150^{o}C. Our analysis suggested that a second trivalent cation can be introduced inside the channels of these zeolites in the vicinity of the Cu cation.

Experimentally, a series of heterobimetallic zeolites were synthesized by incorporating secondary metal cations M (Sc3+, Fe^{3+}, In^{3+}, and La^{3+}) in Cu-exchanged ZSM-5, zeolite-beta, and SSZ-13 under carefully controlled experimental conditions. Characterization by modern techniques does not reveal a definite structure but suggests that the secondary cation is hosted in the zeolite structure in the vicinity of Cu. Our experimental results show that the CuFe-SSZ-13 catalyst exhibits high NO$_x$ conversion efficiency at 150°C under fast-SCR conditions at 50,000h^{-1} space velocity while retaining performance in 250-650°C comparable to commercial Cu-SSZ-13 under fast SCR conditions. After aging, the loss in performance is ~10%, with all tests conducted on powder samples. Two patent applications have been filed on this process.

Here, fast-SCR refers to the reaction where NO and NO$_2$ in emission react with NH$_3$ (or other reductants) to produce N$_2$. This is different from standard SCR where NO and oxygen react with ammonia to produce N$_2$. Thus standard SCR dominates NO$_x$ treatment when NO$_x$ emissions from engines contain no NO$_2$, such as during a cold start where fast SCR occurs once engine warms up and produces some NO$_2$. Test results also show that the new ORNL catalyst is effective even at low NO$_2$ concentrations. With NO$_2$/NO$_x$ ratio of 0.1, 0.25, and 0.4, the NO$_x$ conversion at 150^{o}C was 55, 66, and 68% respectively. Under standard SCR, the new catalyst performed as well as a production catalyst. The detailed study is available in published literature (Narula, C.K. et al. *J. Phys. Chem. C*, **2012**, *116*, 23322). By comparison, current production type NO$_x$ catalysts exhibits only 40% NOx conversion at 150°C under standard or fast SCR conditions.

The next step toward development of this new catalyst is engine testing. Effort is also underway to define a catalyst material that can effectively reduce at least 90% NO$_x$ even under standard SCR conditions.

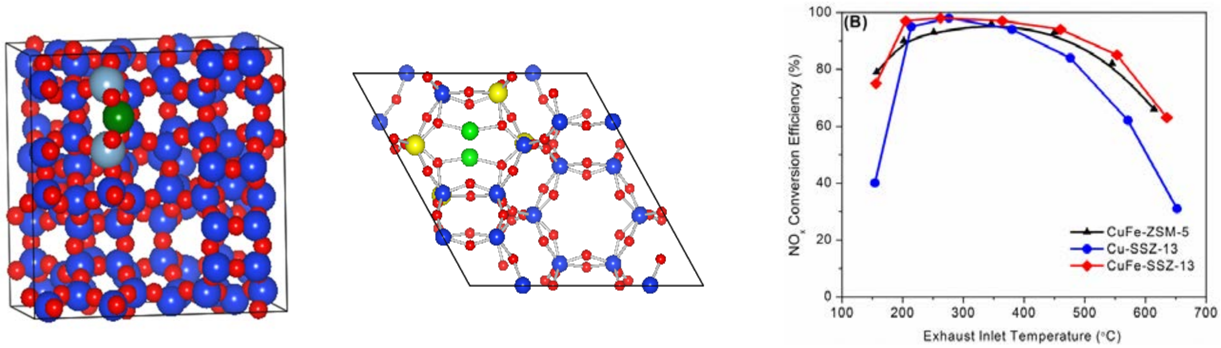

Fig. 5. Theoretical models of Cu-ZSM-5 (left), Cu-SSZ-13 (middle), and experimentally observed NOx reduction under fast SCR conditions by heterobimetallic CuFe-ZSM-5 and CuFe-SSZ-13 (right).

Materials by Design (Application Specific Materials Simulation, Characterization and Synthesis)

Application specific materials simulation, characterization, and synthesis is a materials discovery and development approach consisting of computational modeling and materials characterization, often at the nanoscale (i.e., length scales down to and including the sub-atomic) to elucidate and enable the prediction of structure-function relationships of materials to be developed for specific applications. Propulsion materials research uses “materials by design” to ensure the success of emerging technologies such as new power electronics, advanced internal combustion engines, hybrid systems, and emission reduction technologies. This approach, along with advanced materials characterization instrumentation and synthesis techniques, will be used to postulate new materials, compositions, and structures to greatly enhance the materials properties necessary for advanced high performance propulsion systems. Highlights from these efforts are described below.

The thermoelectric materials research within the Propulsion Materials program is of particular value to electric vehicles (EV) and the DOE EV Everywhere Program. Thermoelectric devices provide direct solid state conversion between heat and electricity. These devices have the potential to provide significant fuel economy benefits, such as for EV zonal climate control, as well as for exhaust waste heat recovery to provide additional electrical power for vehicles with internal combustion engines. A key challenge is to identify new or improved high performance thermoelectric materials that are suitable for these applications. Materials with high performance near room temperature are needed for climate control, while different materials optimized for exhaust temperatures are required for waste heat recovery. In both cases materials must have well characterized and reliable performance.

Propulsion Materials Program researchers at ORNL are using theoretical modeling tools to identify and guide optimization of advanced thermoelectric materials for use in waste heat recovery, in line with the DOE goal of attaining a 10 percent increase in fuel economy from this technology. ORNL staff have conducted extensive investigations of the electronic structure and thermoelectric capabilities of a candidate material, lead selenide (PbSe), using an in house-developed Boltzmann transport code in combination with commercially available density functional theory codes. It was found (see Figure 6) that performance (measured as the “figure-of-merit”, usually referred to as ZT) more than double that of previously found values for this material could be attained using p-type doped material. The doping level needed to achieve this performance level was identified from the calculations. This is important because the efficiency of a thermoelectric device is directly related to the average ZT of the device. These ORNL predictions of high performance in doped PbSe have now been experimentally confirmed, so that PbSe is now known to be a high performance

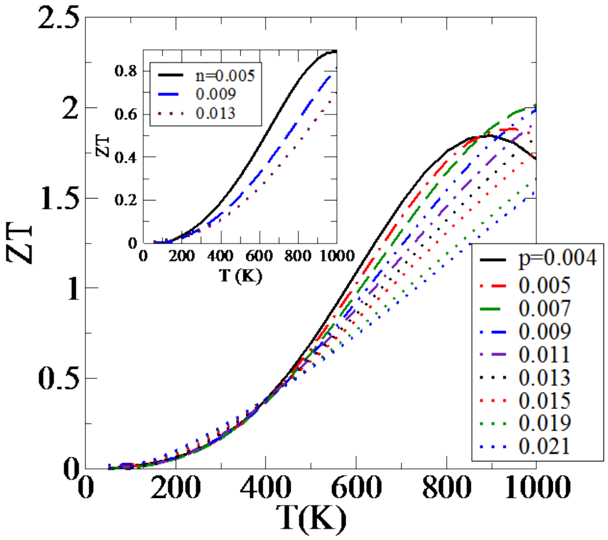

Figure 6: Predicted thermoelectric figure-of-merit ZT of hole-doped PbSe. Doping levels given in carriers per unit cell. Inset: predictions for n-type PbSe.

thermoelectric. Researchers used these predictive capabilities to conduct studies of several materials, including bismuth selenide (Bi_2Se_3) and copper bismuth sulfide ($CuBiS_2$) potentially of use in room-temperature thermoelectric modules for climate control in EVs. Such modules, if sufficiently efficient, offer the promise of reducing the vehicle range penalty currently associated with EV climate control. ORNL researchers found that one of these materials, p-type Bi_2Se_3, could yield thermoelectric performance approaching that of bismuth telluride (Bi_2Te_3), the material currently used for room temperature heating and cooling applications. This discovery was an important step toward enabling larger scale implementation of these systems because it demonstrated that materials free of the scarce and expensive element tellurium can have equal performance.

As mentioned, the reliable characterization of the transport properties that comprise ZT is essential for the development and deployment of thermoelectric energy recovery and climate control systems. For this reason, researchers in the ORNL High Temperature Materials Laboratory (HTML) initiated and led, under the auspices of the International Energy Agency (IEA), two test program round-robins between 2009 and 2012. This was an international collaboration involving Canada, China and Germany with 10 participating laboratories. The focus was on bulk bismuth telluride and lab-to-lab variability of all the transport properties needed to extract ZT including Seebeck coefficient, electrical conductivity, thermal diffusivity, specific heat, and thermal conductivity. Detailed analysis was conducted in 2012 and test procedures for all the transport properties were developed and published in two journal papers. An example of a recommended test method for the Seebeck coefficient is presented in Figure 7.

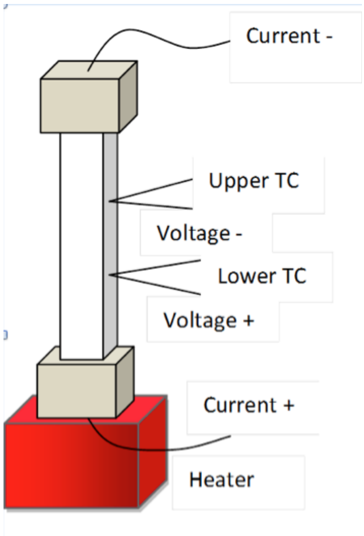

Figure 7: A schematic diagram of the “four point” method used to measure the Seebeck coefficient at the ORNL HTML and other laboratories.

A major success of the ORNL-IEA program is highlighted in Figure 8, which depicts the overall uncertainties in the second round robin of the ZT calculated from the measured transport quantities such as resistivity, thermal conductivity, and Seebeck coefficient. The uncertainty in ZT at 300 K is 11.7 percent and about 20 percent at 475 K (mainly due to variability in the thermal conductivity measurements). Specific heat measurement remains the most challenging test for transport properties. It is expected that future efforts following the test procedures recommended from these round robin results will reduce the variability to the 10 percent level.

Results from the theoretical studies described earlier, as well as the round robins, will help develop and validate high-performance thermoelectric materials for vehicular applications.

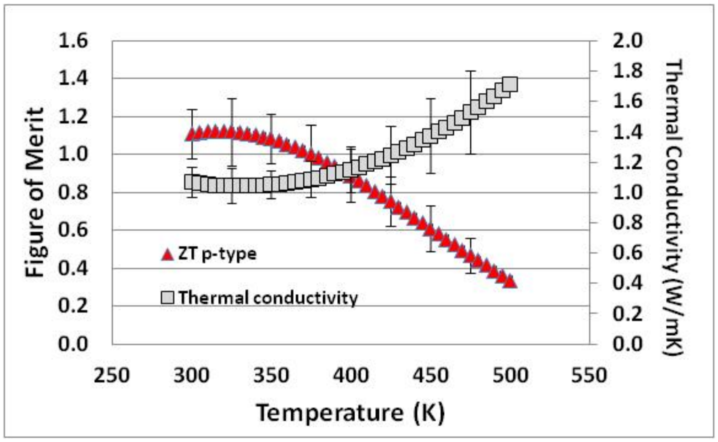

Figure 8: Calculated thermal conductivity and figure of merit, ZT, with associated uncertainties, for p-type Bi_2Te_3.

These materials are expected to ultimately aid in the deployment and consumer acceptance of new generations of vehicles, such as in the EV Everywhere program, and to enable substantial fuel savings in conventional internal combustion engine powered vehicles.

Carol L. Schutte
Team Leader, Advanced Materials Technologies
Office of Vehicle Technologies
Energy Efficiency and Renewable Energy

Jerry L. Gibbs
Technology Manager
Office of Vehicle Technologies
Energy Efficiency and Renewable Energy

Project 18516 – Materials for Hybrid and Electric Drive Systems

Agreement 19201 – Non-Rare Earth Magnetic Materials

M. A. McGuire, N. J. Ghimire, D.J. Singh*
Materials Science and Technology Division
Oak Ridge National Laboratory
P.O. Box 2008, MS 6056, Bldg. 3150
Oak Ridge, TN 37831-6056
(865) 574-5496; fax: (865) 574-4814; e-mail: mcguirema@ornl.gov
** University of Tennessee, Knoxville, TN*

DOE Technology Manager: Jerry L. Gibbs
(202) 586-1182; fax: (202) 586-1600; e-mail: jerry.gibbs@ee.doe.gov
ORNL Technical Advisor: J. Allen Haynes
(865) 576-2894; fax: (865) 574-4913; e-mail: haynesa@ornl.gov

Contractor: Oak Ridge National Laboratory, Oak Ridge, Tennessee
Prime Contract No.: DE-AC05-00OR22725

Objectives

- Discover new, strong, permanent magnet materials which do not contain rare earth elements.
- Develop an understanding of the magnetic properties of discovered materials using properties measurements and first-principles calculations to direct work towards improved permanent magnet properties.

Approach

- Investigate understudied known materials and search for new materials in rare earth-free systems which hold promise for the discovery of new high-temperature ferromagnets with the large magnetic moments and strong anisotropies required for technologically useful permanent magnet materials.
- Target materials which contain a high concentration of magnetic 3*d* elements (e.g. Cr, Mn, Fe, Co) along with heavier 4*d* or 5*d* transition metals (e.g. Zr, Hf, Nb, Ta, Mo, W) which have strong spin-orbit coupling.
- Focus on anisotropic crystal structures to allow strong magnetocrystalline anisotropy.

Accomplishments

- Increased energy product of $Hf_2Co_{11}B$ alloy ribbons to values approaching half that of optimized rare-earth magnet ribbons, and identified the microstructure of $Hf_2Co_{11}B$ alloys which supports the observed promising permanent magnet properties.
- Produced amorphous $Hf_2Co_{11}B$ alloys by melt spinning, and demonstrated effects of annealing to enhance permanent magnet properties.
- Published technical reports on discovery of ferromagnetism in $ZrFe_{12-x}Al_x$ and $HfFe_{12-x}Al_x$, and our detailed study of the magnetic properties of ferromagnetic $Cr_{11}Ge_{19}$.

Future Direction

- Optimize $Hf_2Co_{11}B$ and closely related materials by fine tuning melt-spinning conditions, chemical compositions, and post-processing, including crystallization of amorphous ribbons in high magnetic fields.
- Examine high magnetic field processing as a means of stabilizing anisotropic ferromagnetic phases.

- Continue exploratory searches for new ternary and quaternary ferromagnets in candidate chemical systems combining Cr/Mn/Fe/Co, heavy transition metals, and light p-block elements using metal-flux crystal growth techniques.

Introduction

The strategic importance of rare earth elements (REEs) and the associated potential problems are receiving increased attention due to their use in permanent magnets (PMs) for electric motors. There are currently no alternative PM materials competitive with $Nd_2Fe_{14}B$ which do not contain REEs. The development of such materials would allow progress toward lowering the cost of electrical propulsion systems toward the performance goals of \$12 /kW by 2015 and \$8 /kW by 2020 for the Hybrid and Electric Propulsion subprogram set forth by the FreedomCAR and Vehicles Technologies Program. The Propulsion Materials Technology activity has identified limited domestic supply of materials required for advanced vehicle technology, among them REEs, as a key barrier to enabling expanded capabilities of electric drive systems.

One of the most important figures-of-merit for permanent magnet materials is called the maximum energy product, given the symbol BH_{max}. This represents the amount of magnetic energy available to do work. It is defined as the maximum magnitude of the product of the magnetic induction B and the applied field H that is realized in the material's demagnetization curve. Typical values of BH_{max} at room temperature for the best rare-earth magnets are 40-50 MGOe for sintered magnets and about 10 MGOe for bonded magnets. Note that MGOe (mega-Gauss-Oersted) is a unit of energy density, and 1 MGOe = 7.96 kJ/m^3.

The technical barrier that must be overcome in this research area is related to the role that the REE plays in current state-of-the-art PMs. Realizing good PM behavior (large remanent magnetization and high coercivity) requires strong magnetic anisotropy. This anisotropy gives preference to a particular orientation of the magnetic moment, and presents an energetic barrier to the reorientation of the net moment required to demagnetize the material. There are two sources of magnetic anisotropy: shape anisotropy (an extrinsic property) and magnetocrystalline anisotropy (an intrinsic property). Shape anisotropy results from the difference in demagnetization factors along different directions in non-spherical magnetic particles. Magnetocrystalline anisotropy arises from the interactions between the magnetic moments and the crystal lattice, giving a preferred direction for the magnetization. Spin-orbit interactions couple the magnetic moment (spin) to the atomic orbitals of the magnetic atoms. Strong covalent bonding can fix the orientation of these atomic orbitals with respect to the crystal structure. The combination of these two phenomena, covalent bonding and spin-orbit coupling, results in a preferred direction for the alignment of the magnetic moments, which is manifested as magnetocrystalline anisotropy. This is expected to be strongest in materials with anisotropic (non-cubic) crystallographic structures.

In REE magnets, the strong spin-orbit coupling and large magnetic moment of the REE is crucial to providing strong magnetic anisotropy. The primary technical barrier to the development of better non-rare earth PMs is achieving strong magneto-crystalline anisotropy in the absence of REEs. Strong spin-orbit coupling is not unique to REEs. Its strength is proportional to the atomic number, and is thus high in all heavy elements. PtCo has strong magnetocrystalline anisotropy due to the large spin-orbit coupling of Pt and its interaction with the 3*d* Co moments. Despite the high cost of Pt, this material has seen commercial use in magnetic recording applications. This example demonstrates the potential of using heavy *d*-block transition metals to play the role of REEs.

We believe that the most promising chemical systems for discovery and development of new PM materials are those that include the 3*d* transition metals Cr, Mn, Fe, and Co with heavy 4*d* or 5*d* metals like Zr, Hf, Nb, Ta, Mo, W. Identifying and analyzing known compounds containing these elements is one path toward new hard ferromagnets. However, the discovery of entirely new materials is likely to have the largest long-term impact on technology. This requires examining ternary (or higher) systems, as binary compositional phase diagrams are generally well characterized. We note that moving beyond binary compounds was important in the development of RE magnets as well. Better PM properties are realized in ternary $Nd_2Fe_{14}B$-based materials than the in the best binary compounds based on $SmCo_5$.

This project's objective is to use the ideas outlined above to target new and known materials with the aim of identifying rare earth-free chemical systems which contain permanent magnets with potential for use in electric motors. Replacing $Nd_2Fe_{14}B$ is a serious and important materials challenge which likely will require long term research efforts, and which must begin with advancements in performance and understanding of non-RE magnets, and perhaps most importantly, the discovery and development of new materials.

Results

We review here several accomplishments from our research in FY2012. These include: (1) magnetic and microstructural characterization of $Hf_2Co_{11}B$ alloy ribbons with energy products that approach half that of optimized $Nd_2Fe_{14}B$ melt-spun ribbons, (2) production of amorphous $Hf_2Co_{11}B$ alloys by melt spinning and the demonstration of post-annealing to enhance permanent magnetic properties, turning magnetically soft amorphous material into magnetically hard crystalline material, and (3) detailed studies of complex ferromagnetism in anisotropic, rare earth-free $ZrFe_{12-x}Al_x$, $HfFe_{12-x}Al_x$, and $Cr_{11}Ge_{19}$.

High energy product in crystalline $Hf_2Co_{11}B$ ribbons

These materials were identified as promising candidates for non-rare earth permanent magnets based on the following criteria: (1) they contain a high concentration of Co, (2) they contain the heavy transition metal Hf, (3) they adopt an anisotropic crystal structure, and (4) the Zr analogue has been reported to be a high temperature ferromagnet. Our study of these materials is ongoing. In FY2012, we demonstrated the highest energy products ever reported for this family of alloys, as reported below.

Alloys of composition $Hf_2Co_{11}B$ were made by arc-melting and melt-spinning. By melt-spinning at a relatively low wheel speed of 16 m/s (relatively slow quenching rate) we were able to produce ribbons that were mostly crystalline, and that displayed promising permanent magnet properties. Figure 1 shows the magnetic behavior of this material at room temperature. High coercivity is observed, with intrinsic coercive fields near 4.5 kOe. The hysteresis loop also shows good "squareness," which is important in attaining high energy products. The energy product is shown in the lower panel of Figure 1. A maximum energy product BH_{max} = 6.7 MGOe is reached at fields of about 2 kOe. This value is comparable to most grades of AlNiCo (4-10 MGOe), and is about half the value obtained for melt-spun ribbons of $Nd_2Fe_{14}B$ (14-16 MGOe). The Curie temperature of $Hf_2Co_{11}B$ is near 760 K, about 150 K higher than that of $Nd_2Fe_{14}B$. We expect that further optimization of these materials is possible, through fine tuning of melt-spinning conditions and chemical composition. The melt-spun flakes may prove useful for bonded magnet applications.

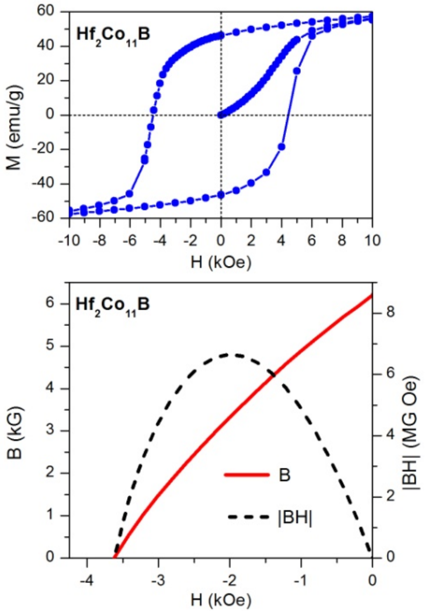

Figure 1. (top) Magnetization loop for magnetically hard $Hf_2Co_{11}B$ melt-spun ribbon showing magnetization M vs. applied field H.(bottom) The corresponding demagnetization curve showing magnetic induction B and energy product |BH| vs. H.

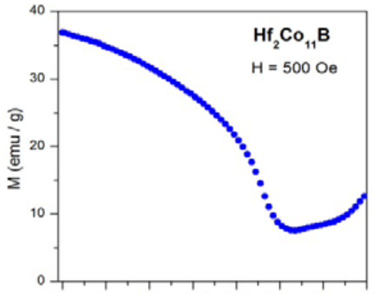

Figure 2. Magnetization vs. temperature for a magnetically hard $Hf_2Co_{11}B$ ribbon measured on warming to 1000 K in an applied field of 500 Oe. The Curie temperature of the main phase is identified as T_C = 760 K.

Inspection of the temperature dependence of the magnetization shown in Figure 2 reveals unusual behavior above the Curie temperature. A relatively large magnetic moment is observed up to 1000K. This suggests that some free cobalt metal is present in the as-spun material. The measurements also suggested that some irreversible transformations occur above the Curie temperature. These observations suggested a complex microstructure may be expected. Figure 3 shows SEM and TEM images of magnetically hard $Hf_2Co_{11}B$. Indeed a multi-phase microstructure is observed. Small crystallites (~ 5 – 150 nm) with complex crystal structures are observed, with a small amount of amorphous material between the grains. The coexistence of crystalline and amorphous material suggests an exchange-spring mechanism may be partially responsible for the good permanent magnet behavior.

The sample melt spun at 16 m/s contained some specimens with softer magnetic behavior than that shown in Figure 1. These specimens also had different microstructures, with a larger amorphous component, suggesting they were cooled at a higher than optimal rate. The large range of grain sizes observed in the best material, and the presence of both hard and soft samples in the melt spun ribbons, indicates further optimization will likely improve magnetic properties.

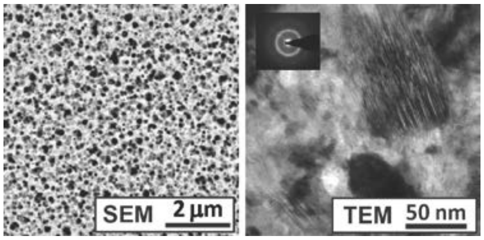

Figure 3. Backscattered scanning electron microscopy (SEM) and bright field transmission electron microscopy (TEM) images of a cross section of a magnetically hard $Hf_2Co_{11}B$ ribbon. The images show a fine-grained, multi-phase microstructure.

<u>*Production and crystallization of amorphous $Hf_2Co_{11}B$ ribbons*</u>

We successfully produced amorphous $Hf_2Co_{11}B$ ribbons by conducting melt-spinning experiments at significantly higher wheel speeds (24 m/s). As expected, the amorphous material is a very soft ferromagnet (see Figure 4). However, the availability of an amorphous precursor allows a systematic study of microstructural development to be pursued. We have already demonstrated that annealing this material for relatively short times results in significant hardening of the magnetic properties. This is shown for one annealing temperature in Figure 5. These measurements, coupled with microstructural studies, may provide a good route to improving the magnetic properties in this family of alloys.

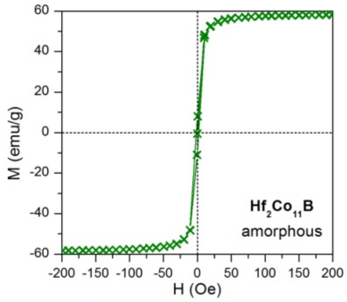

Figure 4. Room temperature magnetization loop from an amorphous $Hf_2Co_{11}B$ ribbon, showing very soft ferromagnetism.

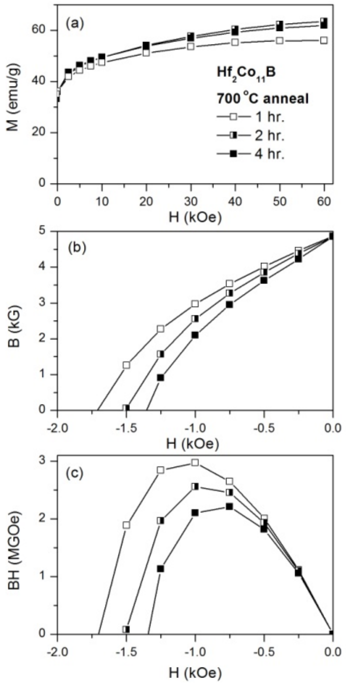

Figure 5. Magnetic properties resulting from annealing amorphous $Hf_2Co_{11}B$ ribbons at 700^oC for varying times.

To achieve the best permanent magnet properties, it is desirable to have anisotropic microstructures and crystallographic alignment of magnetic crystallites. The best $Hf_2Co_{11}B$ alloys we have made by melt spinning have isotropic microstructures, so enhanced performance is expected if anisotropy could be induced in the ribbons. We have begun exploring thermo-magnetic processing as a means to achieve this. Preliminary experiments have demonstrated a strong influence of an applied magnetic field on the crystallization of amorphous $Hf_2Co_{11}B$ ribbons at high temperatures. An example is shown in Figure 6. The magnetic field induces growth of highly anisotropic grains, which are not present in the sample annealed without at zero field. The effects are promising, and the systematic exploration of the application of these techniques to these alloys and other materials is continuing.

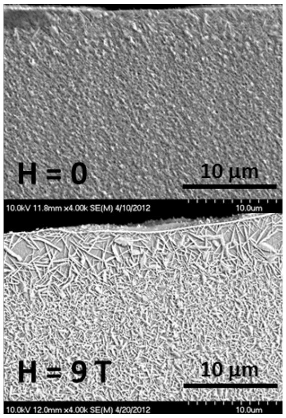

Figure 6. Backscatter SEM images of $Hf_2Co_{11}B$ showing the effects of annealing amorphous ribbons in a magnetic field (9 Tesla, lower panel) versus annealing without a magnetic field (upper panel). The field induces growth of highly anisotropic grains.

<u>Complex magnetism in (Zr/Hf)$Fe_{12-x}Al_x$ and $Cr_{11}Ge_{19}$</u>

During FY2012, we completed our investigation of the $ThMn_{12}$-type aluminides $ZrFe_{12-x}Al_x$ and $HfFe_{12-x}Al_x$. A technical report summarizing our findings has been published in the scientific literature. The magnetic properties of these materials are summarized in Table I. One of the more surprising observations is a decrease in Curie temperature and magnetic moment with increasing Fe content. Density functional theory calculations were performed to help understand this behavior. The calculations indicated effective antiferromagnetic interactions among Fe atoms when they reside on one of the crystallographic positions available for Fe. Crystallographic studies showed that increasing the Fe content results in a higher concentration of Fe on this particular site, which explains the lower Curie temperatures in the more Fe rich materials. Our calculations also indicated the presence of magnetic moments on Hf and Zr in these materials, which is important if these heavy transition metals are to enhance magnetic anisotropy through spin-orbit coupling. Further details can be found in: M.A. McGuire, N. Ghimire, D.J. Singh, "*Ferromagnetism in $ZrFe_{12-x}Al_x$ and $HfFe_{12-x}Al_x$ (x = 6.0, 6.5, 7.0)*," Journal of Applied Physics 111 (2012) 093918.

Table I. Curie temperature (T_C) of $ZrFe_{12-x}Al_x$ and $HfFe_{12-x}Al_x$.and the saturation moment (M_S) and remanent moment (M_r) measured at T = 2 K.

composition	T_C (K)	M_S (μ_B / Fe)	M_r (μ_B / Fe)
$ZrFe_5Al_7$	271	1.46	0.15
$ZrFe_{5.5}Al_{6.5}$	233	1.37	0.6
$ZrFe_6Al_6$	170-190	0.96	0.3
$HfFe_5Al_7$	263	1.39	0.13
$HfFe_{5.5}Al_{6.5}$	230	1.32	0.39
$HfFe_6Al_6$	180-195	0.96	0.44

We also examined the Cr based ferromagnet $Cr_{11}Ge_{19}$. This material has a very anisotropic crystal structure. It is tetragonal with a c/a ratio of ~9 (a = 5.8 Å, c = 52.3 Å). The Curie temperature is low (88 K) and the remanent magnetization is small; however, study of this material produced good science and highlights some interesting physics associated with low-symmetry ferromagnetism. In addition to being strongly uniaxial, the crystal structure of $Cr_{11}Ge_{19}$ also is non-centrosymmetric (lacks an inversion center). Often this results in what is known as helimagnetism. The magnetic moments are not collinear in the ordered state, but instead their directions follow a helix that propagates along a specific crystallographic direction. Complex behaviors which appear to arise due to interactions between helices and applied magnetic fields were observed in $Cr_{11}Ge_{19}$. Unusual AC magnetic susceptibility data from $Cr_{11}Ge_{19}$ are shown in Figure 7. In addition, we reported evidence of strong magneto-elastic effects, causing an unusual response of the crystal lattice and its vibrations to the onset of magnetic ordering. A technical report summarizing our results was published in the scientific literature: N.J Ghimire, M.A. McGuire, D.S. Parker, et al., "*Complex itinerant ferromagnetism in noncentrosymmetric* $Cr_{11}Ge_{19}$," PHYSICAL REVIEW B 85 (2012) 224405.

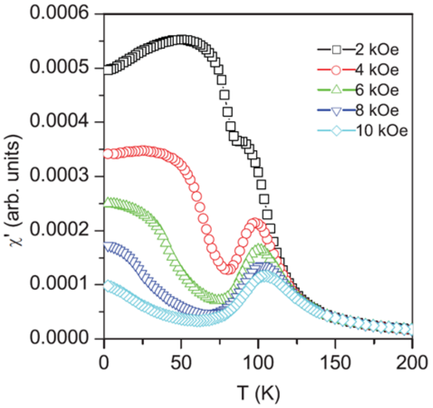

Figure 7. The measured AC magnetic susceptibility of $Cr_{11}Ge_{19}$*. The unusual behavior below the Curie temperature (88 K) reveals similarities to known helimagnetic materials, and indicates complex, unusual magnetism in this material.*

Conclusions

Several important achievements were made in FY2012. The most exciting, interesting, and impactful is the discovery of high energy products and high Curie temperatures in $Hf_2Co_{11}B$ alloys. Evidence suggests further improvements should be possible, and multiple paths toward higher performance are being pursued. The production of amorphous, magnetically-soft $Hf_2Co_{11}B$ alloys by melt-spinning is an important step in achieving control over microstructures and associated magnetic behavior, and thermo-magnetic processing provides an intriguing new approach to microstructure refinement. Our studies of complex ferromagnetism in $ZrFe_{12-x}Al_x$, $HfFe_{12-x}Al_x$, and $Cr_{11}Ge_{19}$ did not lead to candidate permanent magnet materials; however, this work did elucidate some important basic physics of these materials, and furthers our understanding of complex, anisotropic, rare earth-free ferromagnets. Building on the base we have established in the first years of this work, we are confident that our ongoing research on optimizing materials of current interest and targeting new ferromagnetic compounds will continue to push back the frontiers of non-rare earth permanent magnet materials.

Agreement 23278 – Low-Cost Direct Bonded Aluminum (DBA) Substrates

H.-T. Lin, M. K. Ferber, A. A. Wereszczak, and S. B. Waters
Ceramic Science and Technology Group
Oak Ridge National Laboratory
P.O. Box 2008, MS 6068, Bldg. 4515
Oak Ridge, TN 37831-6068
(865) 576-8857; fax: (865) 574-6098; e-mail: linh@ornl.gov

DOE Technology Manager: Jerry L. Gibbs
(202) 586-1182; fax: (202) 586-1600; e-mail: jerry.gibbs@ee.doe.gov
ORNL Technical Advisor: J. Allen Haynes
(865) 576-2894; fax: (865) 574-6098; e-mail: haynesa@ornl.gov

---

Contractor: Oak Ridge National Laboratory, Oak Ridge, Tennessee
Prime Contract No.: DE-AC05-00OR22725

Objectives

- Develop low-cost and thermomechanically robust direct-bonded aluminum (DBA) substrates that are least 25% lighter than conventional direct-bonded copper (DBC) substrates.
- Benchmark the architecture, microstructure, interfacial properties, and fatigue resistance of contemporary DBAs and DBCs for comparison to any new DBAs developed in this project.

Approach

- Identify and develop innovative processing methods to fabricate low-cost DBAs.
- Identify and develop innovative ways to fabricate their ceramic constituent (e.g., low-cost AlN substrate)
- Benchmark existing commercial available DBA and direct-bonded copper (DBC) substrates through metallographical and non-destructive examinations and mechanical and thermal characterizations.

Accomplishments

- Completed benchmarking of physical and mechanical properties of commercial DBA and DBC substrates.
- Completed non-destructive evaluation (NDE) of commercial DBA and DBC substrates using scanning acoustic microscopy (SAM).
- Completed initial characterization and trial of copper-clad Al ribbon for DBA substrate bonding applications.

Future Direction

- Complete optimization of processing routes for DBA manufacturing via brazing or a bridging metallurgical coating bonding process with strong and coherent bonding.
- Benchmark thermal cycle fatigue resistance of commercial DBA and DBC substrates.
- Assess the candidacy of strong and thermally-conductive silicon nitride substrates for use in future DBC and DBA substrates for particular use with GaN and SiC wide band-gap semiconductors.

Introduction

Application of low-cost direct-bonded aluminum (DBA) substrates will enable cost reduction of inverter insulated gate bipolar transistor (IGBT) power modules while concomitantly sustaining or improving thermal management and improving thermomechanical reliability performance. Compared to copper and direct-bonded copper (DBC) substrates, aluminum has a lower elastic modulus so it imparts a lower residual stress on the ceramic substrate it sandwiches in these components, contributing to improved mechanical reliability of the entire substrate during application. Also, wire and ribbon used for bonding in power electronic modules tend to be aluminum, so the coefficient of thermal expansion of DBAs is compatible with them (unlike DBCs). The use of a DBA substrate will also lessen the weight by up to 50% as compared to presently used DBC substrates, contributing to tangible weight reduction of the inverter and converter in automotive power electronics.

In addition to weight reduction, reducing cost, improving volumetric power, extending reliability, and improving thermal management all contribute to the goals of the Vehicle Technology's APEEM program. If lower cost DBAs could be fabricated, then their application would inherently address these goals too. DBA substrates are presently difficult to fabricate due to bonding difficulty between aluminum and aluminum oxide. DBAs are now only available from a limited numbers of suppliers and are thus expensive. Despite Toyota presently using DBA substrates in their 2010 Prius, domestic automotive OEMs would more seriously consider using DBA substrates in their own inverters if they were more readily available and less expensive.

The objective of this subtask is to develop low-cost, high quality, and thermomechanically robust DBA substrates, which have both electric and mechanical properties equivalent to (common) commercially available DBA substrates. The ultimately goal is to facilitate the achievement of 2015 APEEM goal of $12/kW for electric traction system, and inexpensive DBAs would help realize that goal.

Results

DBA Processing

Efforts to develop the low-cost DBA substrates were continued in FY2012. A commercial Al-12Si brazing compound paste (designated as DayBraze 729) inquired from Johnson Manufacturing Company, Iowa was employed for bonding the Al and Al_2O_3 ceramic. Note the eutectic temperature of Al-Si is 610°C. Thus, the hot pressing conditions at temperature between 580 and 600°C in Ar or N were applied for the bonding experiments. In addition, HNO_3 acid was used to remove the Al_2O_3 thin film formed due to the oxidation Al plates in ambient air prior to the hot processing. Many attempts were carried out by various combinations of temperature and environment under the same applied load of 5 MPa. Visual examinations of all hot-pressed Al-Al_2O_3 and Al-AlN substrates revealed sound joining. However, all of the hot-pressed Al-Al_2O_3 and Al-AlN substrates could be easily peeled off manually, indicative of very poor interfacial bonding strength. Efforts to identify alternative processing approaches such as different brazing compound or metallurgical coating of Al-Si to form a adherent and strong bonding between Al and Al_2O_3 and AlN ceramic will be continued in FY2013.

Hybrid cladding for Potential DBA Substrate

A developmental Cu-cladding Al ribbon was acquired from Materion, Ohio. The advantages of Cu-cladded Al ribbon for DBA substrates are that the Cu-cladded Al material exhibits 45% higher thermal conductivity and also carries 30% higher current density than Al cladding alone. Microstructure of the Cu-cladding Al ribbon was analyzed via scanning electron microscopy (SEM) equipped with an EDAX system. The analysis showed that the Al material used in this Cu-cladding ribbon is a Si-rich Al alloy (Fig. 1) making it potentially and directly bondable to ceramic substrates without the use of Al-Si brazing compound. Therefore, the application of Cu-cladding Al ribbon might potentially contribute to the cost reduction of DBA substrate plus with the enhancement of both electrical and thermal properties. Initial attempts were made to bond the Cu-cladded Al ribbon to AlN and Al_2O_3

ceramic substrate at temperature ranging between 580-600°C for 30 minutes under an applied load of 5 MPa in argon (Ar). Visual observations after hot pressing showed there was no bonding between the ribbon and ceramic substrates despite the fact that employed temperatures reached the eutectic temperature of the Si-rich Al alloy.

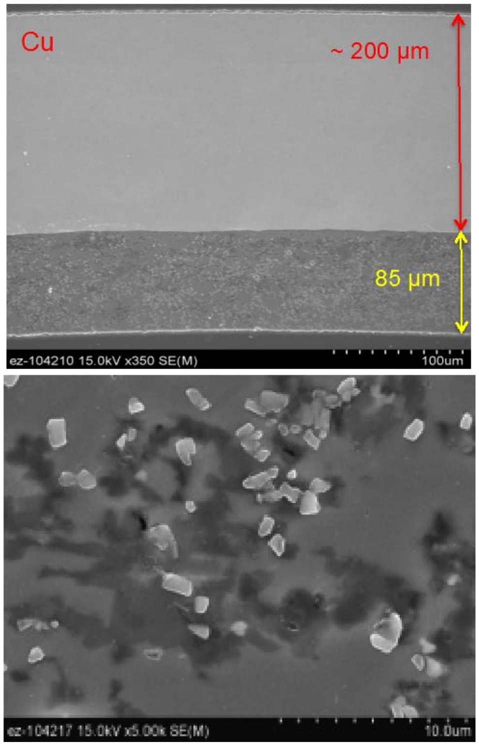

Figure 1. SEM micrograph of an as-received developmental Cu-cladded Al ribbon from Materion, OH.

The explanation for the absence of bonding was sought. The microstructure of Si-rich Al layer after the hot pressuring at 610°C in Ar is shown in Fig. 2. The composition analysis via energy dispersive X-ray spectroscopy (EDAX) showed that the eutectic phase formed in the region where the alloy contained Cu and Al, but not Al and Si. The Cu and Al alloy exhibited a eutectic at 548°C, which is lower than the Al-Si eutectic at 577°C. The formation of Al-Cu eutectic phases thus forms earlier than the Al-Si eutectic phase during the processing at 610°C, resulting in no reaction (i.e., no bonding) between the Si-rich Al layer and Al_2O_3 ceramic substrates. Thus, an alternative bonding approach needs to be developed to ensure a strong bonding between Cu-cladded Al ribbon and Al_2O_3 and AlN ceramic substrates without Al-Cu eutectic formation preempting its formation.

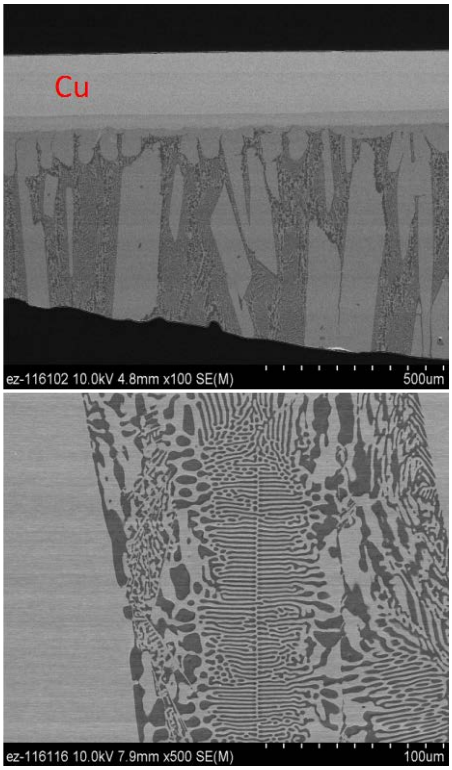

Figure 2. SEM micrographs of a developmental Cu-cladded Al ribbon after the attempted bonding process at 600°C for 30 minutes. Note that the formation eutectic morphology of Al-Cu alloy was observed (bottom photo).

Benchmarking of commercial DBA and DBC substrates

Physical properties, i.e., coefficient of thermal expansion (CTE) and thermal diffusivity, of commercially available DBA and DBC substrates were measured and completed. The data serves as a benchmark and also an input for residual stress and reliability modeling of these substrates in service. Note the measured CTE and thermal diffusivity values would be a composite value of combined contributions from each constituent (metals and ceramics) and also the interface.

Thermal expansion:

Elongation versus temperature curves of DBC substrates containing aluminum oxide (Al_2O_3) or aluminum nitride (AlN) ceramic substrates is shown in Fig. 3. The (internal) ceramics in these tri-layer substrates serve as an electrical insulator. Each plot consists of two curves; namely, a first run on a fresh specimen and repeated run on that same specimen.

A large hysteresis loop was observed for both DBC substrates during the first run. However, the extent of hysteresis decreased during the second run of the same sample. The AlN-DBC exhibited a larger hysteresis loop than that for the Al_2O_3-DBC, probably due to the larger CTE mismatch existing in the copper (Cu) (16.5 x 10^{-6}/°C) - AlN (4.5 x 10^{-6}/°C) system as compared to the Cu (16.5 x 10^{-6}/°C) - Al_2O_3 (8.2 x 10^{-6}/°C) system. The apparent decrease in the hysteresis loop in the second run most likely resulted from an annealing effect during the first run that relieved some of the original residual thermal stress stemming from the substrate's high temperature manufacturing process. Thus, the CTE values of these DBC substrates were calculated by curve fitting the second run data between room temperature and 400°C. The thermal expansion curves of DBCs and DBAs, both with AlN substrates, are compared in Fig. 3 and 4. It is interesting to note that there is no apparent difference between these two substrates. Aluminum (Al) has a lower Young’s modulus (and also yield strength) than Cu, which might have an impact to the extent of hysteresis loop, although the Al-AlN system has a larger CTE mismatch than the Cu-AlN system. On the other hand, the AlN-DBA substrates from two different suppliers exhibited different composite CTE values. This might result from the differences in microstructure and chemical compositions in the AlN ceramic and Al alloy used in the two DBAs, as well as the interfacial characteristics (such as microstructure, flaws and chemistry) between AlN and Al substrate.

To verify the contribution of CTE mismatch and thus residual stress on the observed hysteresis strain-temperature curves, finite element analysis was used for model simulation. It was assumed that the CTE of the constituents and yield strength of aluminum metal remain constant during the thermal cycle. Figure 5 shows the modeled strain vs. temperature curve, and similar trends as that obtained by the experiment. Note that the plastic (permanent) deformation in aluminum metal during processing could contribute to the residual stress and strain. In addition, externally applied loading during processing could further augment the level of residual stress and strain, thus resulting in the much larger hysteresis loop.

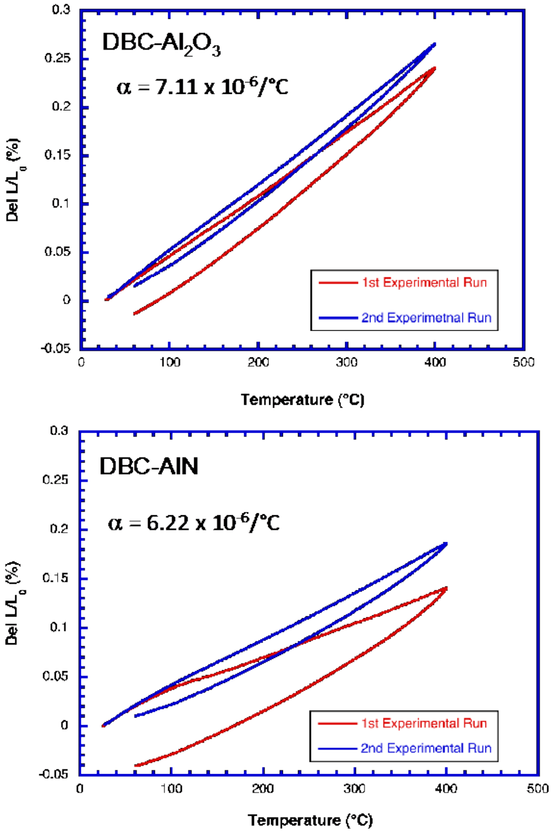

Figure 3. Elongation versus temperature curves of DBC commercial DBC substrates with Al_2O_3 (top) and AlN (bottom) ceramic.

Thermal diffusivity:

The thermal diffusivity of commercially available DBC and DBA substrates are compared in Fig. 6, with AlN, Al_2O_3 or Si_3N_4 ceramic substrates. Thermal diffusivity (λ) is related to thermal conductivity (κ), density (ρ), and heat capacity (Cp) according to $\lambda = \kappa/\rho \bullet Cp$. The thermal property of these electronic substrates plays a key role in the dissipation of heat generated by the power electronic component during operation. The capability of heat dissipation will influence the long-term reliability and lifetime of the system. It was anticipated that the AlN-DBC substrate would exhibit the highest thermal diffusivity among the three samples (Fig.

6a) because AlN has such a high thermal conductivity. Results showed the Si_3N_4-DBC exhibited a 2-times higher thermal diffusivity than the Al_2O_3-DBC. It is worth noting that Si_3N_4 has much better mechanical performance (high fracture strength and toughness) and thus better mechanical reliability than both AlN and Al_2O_3 under the same service conditions. Thus, there is an increased interest in the use of Si_3N_4 substrates by the automotive industry in high power and high temperature devices such as wide-band-gap (WBG) IGBT with GaN and SiC.

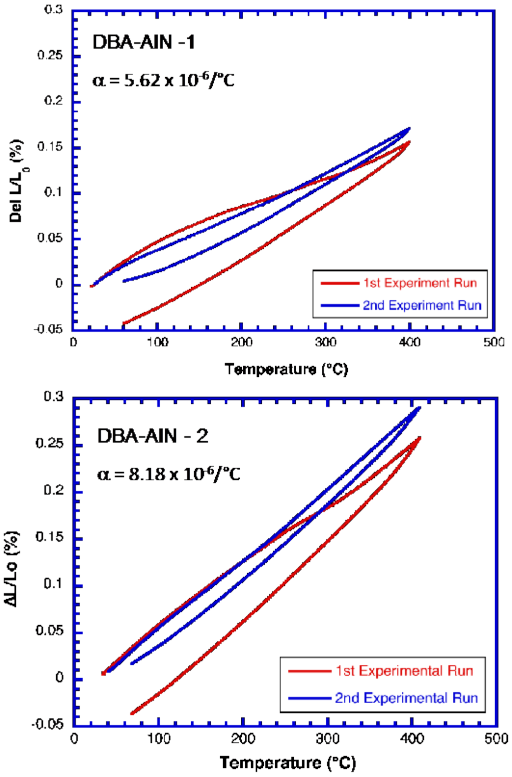

Figure 4. Elongation versus temperature curves of commercial DBA substrates with AlN ceramic.

The thermal diffusivities of different DBCs and DBAs are compared in Fig. 6b. The thermal diffusivity of C-DBC with AlN is comparable to the D-DBA with AlN (Fig. 6b) and minor differences were measured in two DBA substrates acquired from two different sources (Fig. 6c). The slight differences in thermal response could result from the variations in AlN purity (especially oxygen content) and interfacial microstructure and chemistry or within the scatter of material properties - all of which affect thermal conductivity.

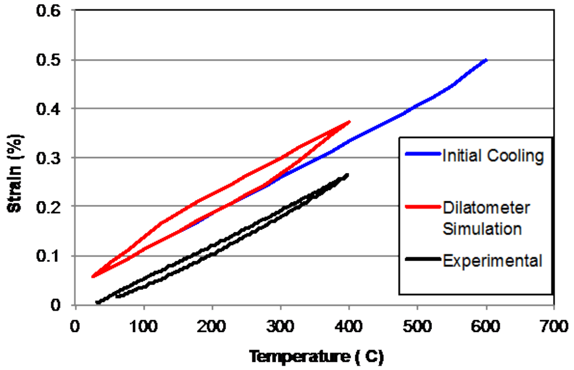

Figure 5. Simulation of strain versus temperature curves of commercial DBA substrates with AlN ceramic using finite element analysis.

Nondestructive characterization

Scanning acoustic microscopy (SAM), shown in Fig. 7, was employed as a nondestructive tool to detect the presence of defects (e.g., voids, cracks, or delamination) in the as-received and thermally cycled DBA and DBC substrates. The SAM system has the ability to create images by generating a pulse of ultrasound, which is focused to a pinpoint spot. The pulse is sent into a sample, which is immersed in the water, and reflected off of interfaces. The frequency of the pulse and design of the lens are chosen to optimize spot size resolution and depth penetration for each application. In the reflection mode of operation the same transducer, which scans over a 2D surface of samples, is used to send and receive the ultrasonic pulse. Return echoes arrive at different times based upon the depth of the reflecting feature and the velocity of sound in the materials. The operator positions an electronic gate to capture the depth of interest. The amount of ultrasound reflected at the interface is based on the differences (i.e., impedance mismatch) in the materials at the interface. The greater the impedance mismatch the more the ultrasound signal is reflected. The time gating is then used to select specific region to examine. A schematic of the probe and substrate is illustrated in Fig. 8.

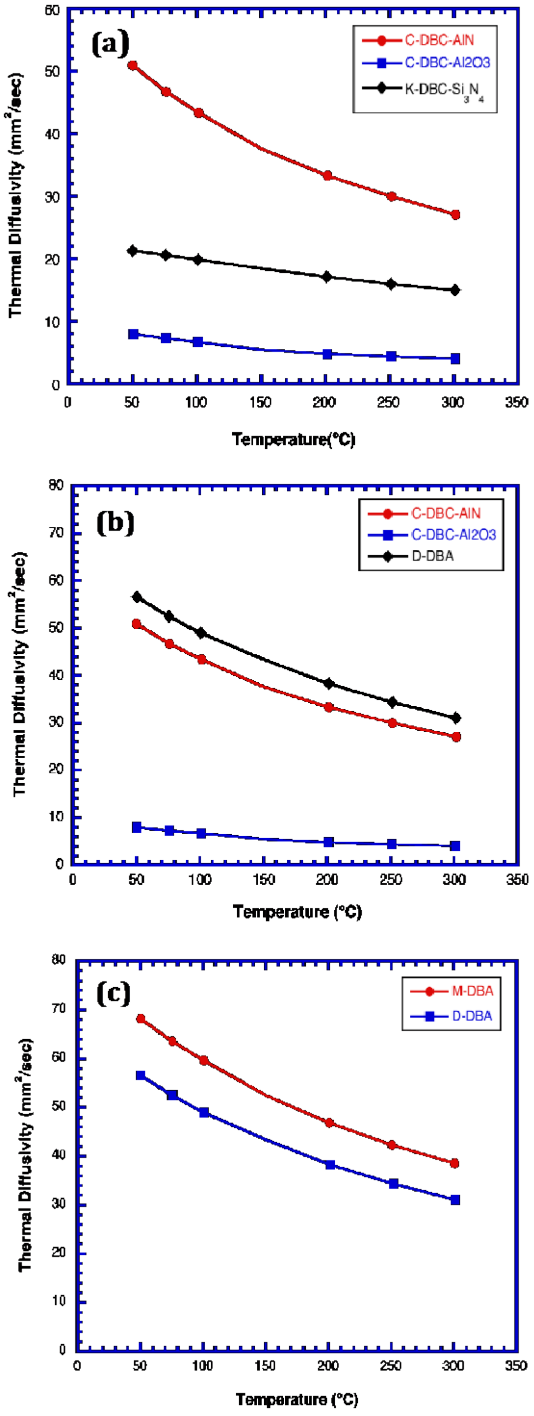

Figure 6. Thermal diffusivity data as a function of temperature for commercial DBC and DBA substrates with AlN, Al_2O_3, and Si_3N_4 ceramic.

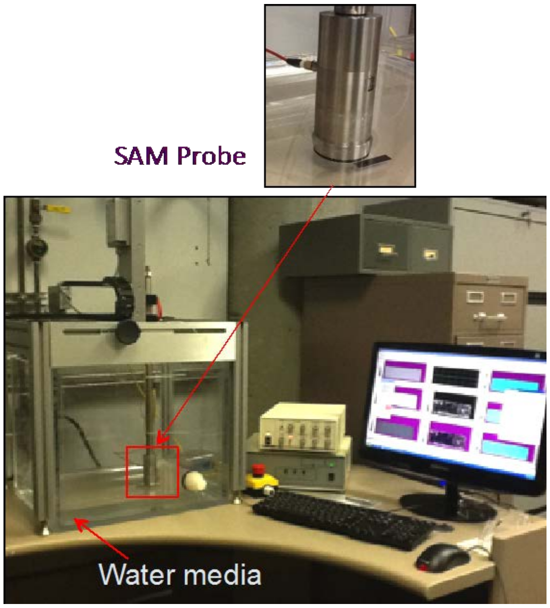

Figure 7. Photo of scanning acoustic microscopy system. The arrow indicates the probe with the enlarged photo inserted.

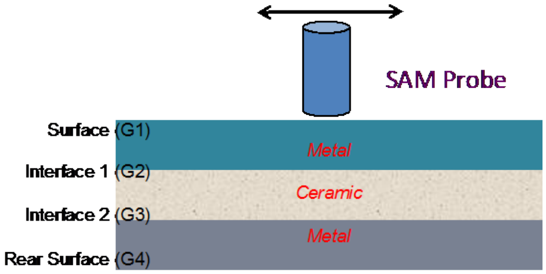

Figure 8. Schematic of SAM probe with gate designations for a DBA or DBC type substrate.

The echoes from each scan position are typically displayed as a brightness (echo amplitude) line. Time-Of-Flight (TOF) information, which is also collected, can be used to estimate speed of sound within the material. If density of materials is known, the elastic modulus can also be calculated as well in the analysis.

Figure 9 shows the SAM images of two commercial DBA substrates (designated as M-DBA and D-DBA) both having AlN. The scratch line visible in Gate 4 in Fig. 9 (rear surface) was intentionally introduced for identification and confirmation purposes. In general, the as-received commercial M-DBA exhibited no apparent defects within the resolution of this SAM system, while the commercial D-DBA showed white strips present at Gate 2, which likely indicates the presence of a defect or secondary phase along the aluminum - AlN interface after processing. The previously reported SEM analysis of a metallographic polished cross section of the as-received D-DBA indicated there was a thin layer of Al-Si secondary phase present at the interface, which could correspond to the observed image (as shown in Fig. 9, bottom).

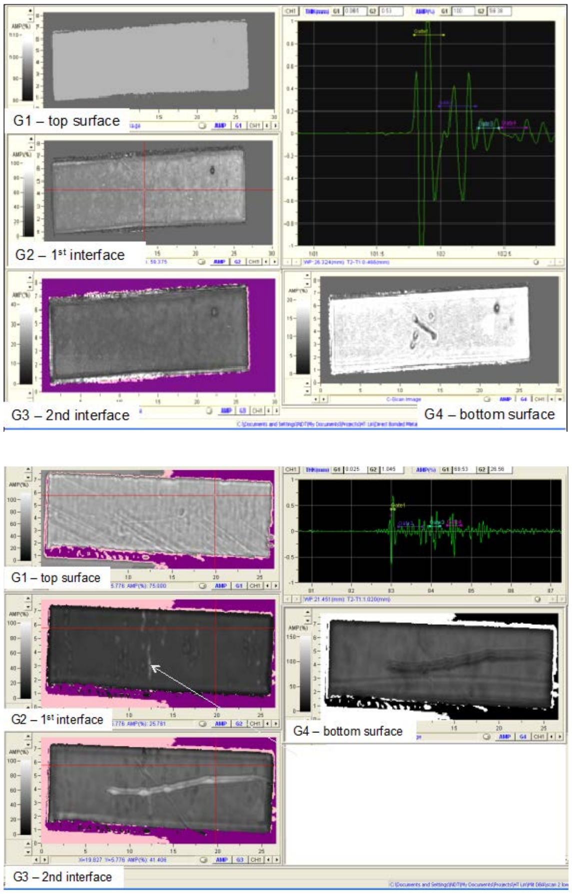

Figure 9. SAM images of commercial M-DBA (top) and D-DBA (bottom).

In addition, the SAM images of DBC substrates with AlN and Al_2O_3 are shown in Fig. 10 (top) and Fig 10 (bottom), respectively. Results also showed that no identifiable defects were detected at these interfacial layers suggesting these two DBC substrates exhibited good coherent interfacial bonding and quality. The SAM results of these DBC substrates are consistent with the SEM observations of polished cross section samples showing no flaws or secondary phases. These comparisons suggest that the SAM technique is a useful tool to detect the possible defects present before and/or after thermal cycle tests of DBAs and DBCs.

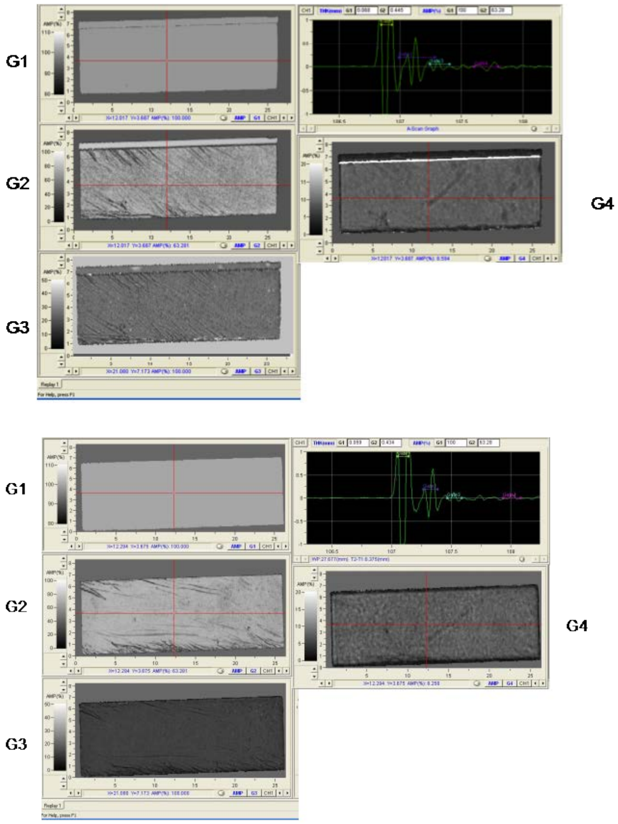

Figure 10. SAM images of commercial DBC with AlN (top) and DBC with Al_2O_3 ceramic (bottom).

Silicon nitride substrates for DBAs

Silicon nitride ceramics are known to exhibit much better mechanical properties such as fracture strength (800 – 900 MPa) and toughness (7-9 MPa•$m^{1/2}$) than that of AlN ceramic (450 MPa and 4 MPa•$m^{1/2}$, typically). Thus, silicon nitride, even with lower thermal conductivity (70 – 90 W/m•K), can provide similar thermal resistance as compared with AlN ceramic under the same application conditions. Also, because the silicon nitride ceramics have the twice the fracture strength and toughness of AlN ceramic that enables the use of silicon nitride substrate, which is half thickness of the AlN substrate. In addition, the cost of silicon nitride ceramic could be substantially reduced by using the low cost Si powders as the starting material. Note the cost of Si powder is at least 2-order of magnitude lower than the silicon nitride powders, which could offer an effectively alternative route for producing low-cost DBA and DBC substrates.

The development of DBC substrates with Si_3N_4 ceramic has been mostly conducted in foreign countries, mainly in Japan through companies such as Kyocera and Toshiba. Thus, these high performance substrates with Si_3N_4 ceramics have to be imported from Japan.

A study to characterize the thermal conductivity of silicon nitride ceramic materials developed at ORNL with both high fracture toughness (up to 12 MPa•$m^{1/2}$) and strength (up to 1200 MPa) was initiated. The patent application of ORNL silicon nitride ceramics was officially granted in June 2011. The thermal conductivity of Si_3N_4 discs with 12.7 mm in diameter and 2 mm in thickness was measured using the laser flash technique. The preliminary results showed the silicon nitride sintered with 8% Gd_2O_3 and 2% SiO_2 exhibited a thermal conductivity of 42.8 W/m•K, and the one sintered with 8% Lu_2O_3 and 2% MgO exhibited a thermal conductivity of 77.6 W/m•K. Note the thermal conductivity of commercial AlN ranges between 150 and 250 W/m•K depending on the material suppliers. Both the microstructure and composition of these ORNL Si_3N_4 ceramics developed were originally tailored for the purpose of high performance structural component applications at elevated temperatures, as shown in Fig. 11. It is reasonable to anticipate that the thermal conductivity of these ORNL Si_3N_4 ceramics could be significantly improved via careful engineering of microstructure and compositions. It has been reported the presence of oxygen has a detrimental impact to the thermal conductivity of Si_3N_4. Therefore, control of sintering cycle and environment plus additional post thermal heat treatment could be implemented to remove the oxygen off the beta silicon nitride grains and secondary phases(s), thus resulting in significant improvement of thermal conductivity.

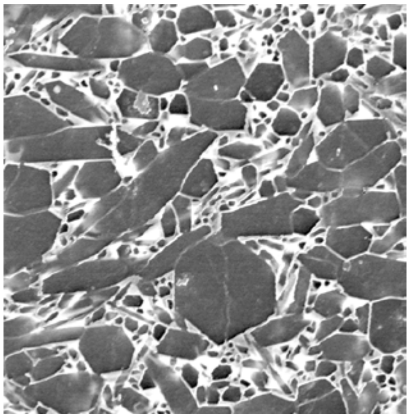

8%Lu_2O_3-2MgO

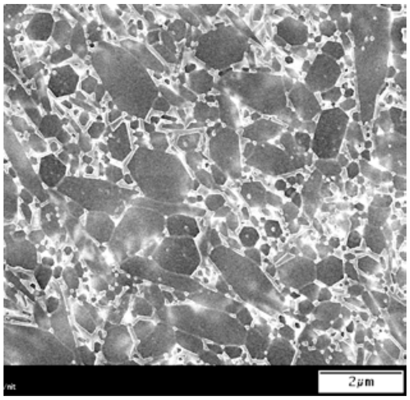

8%Gd_2O_3-2SiO_2

Figure 11. SEM micrographs of an ORNL-fabricated, thermally conductive silicon nitride with 8% Lu_2O_3 and 2% MgO and 8% Gd_2O_3 and 2% SiO_2 sintering additives.

Summary

Results of DBA substrates made with commercial Al-Si brazing compounds showed weak bonding. Thus, alternative materials, such as Cu-clad Al ribbon might have potential for substrate application and where characterized. Furthermore, identification of alternative processing methods (e.g., brazing or bridging metallurgical coatings) to fabricate DBA substrates that has potential for low-cost manufacturing will be continued in FY2013.

Benchmarking of the physical properties (including CTE and thermal conductivity) of commercially available DBC and DBA substrates was completed. These generated properties serve as a reference for the DBA substrates developed under this subtask and also used as input for their thermal stress and reliability modeling in power electronic components. Hysteresis loops in the CTE curves were observed for all of the DBA and DBC substrates, which could be attributed to the difference in CTE values and also processing condition (temperature and applied stress) of substrates. Substrates manufactured with AlN exhibited the highest thermal diffusivity among all of the materials evaluated, which included substrates containing Al_2O_3 and Si_3N_4.

Substrates with Si_3N_4 ceramics exhibited a higher thermal conductivity than substrates containing Al_2O_3. This is the first primary step in accelerating availability of low-cost DBA substrates. The Si_3N_4 ceramics exhibit great potential to be used as a substrate in next generation WBG IGBT with GaN and SiC devices. Preliminary evaluation of thermal conductivity of Si_3N_4 ceramics developed at ORNL showed that the thermal property strongly depends upon the sintering additives and resultant microstructure. The thermal conductivity and also mechanical properties (strength and toughness) will be evaluated in FY2013. Composition as well as processed will be engineered to optimize the mechanical performance and thermal conductivity.

References

1. H. Yoshida, Y. Kuromitsu, M. Toriumi, M. Yuzawa, Ceramic substrate used for fabricating electric or electronic circuit, US Patent No. 5130498, 1992.
2. Y. Nagatomo, R. Muranaka, H. Hayashi, Y. Kuromitsu, N. Kuwano, Fracture Process of Aluminum/Aluminum Nitride Interfaces during Thermal Cycling, *Materials Science Forum*, 638-642, 3895, 2010.
3. S. Gerhard, Method for manufacturing a power semiconductor device and direct bonded substrate thereof, US Patent No. 6670216, 2003.
4. J.Y. Kim, J.S. Hardy, and K.S. Weil, Aluminum Air Brazing for Joining Ceramics, in Advances in Ceramic Coatings and Ceramic-Metal Systems: *Ceramic Engineering and Science Proceedings*, 26, 3, 2008.
5. X.S. Ning, C. Nagata, M. Sakuraba, T. Tanaka: Process for preparing a ceramic electronic circuit board and process for preparing aluminum or aluminum alloy bonded ceramic material, US patent No. 5965193, 1999.
6. M. Nobuyuki, K. Hajime, S. Yasuyuki, Method for directly bonding ceramic and metal members and laminated body of the same, US Patent No. 4849292, 1989.
7. Y. Kuromitsu, Y. Nagatomo, H. Tonomura, K. Akiyama, C.M. Montesa, N. Shibata, T. Tohei, and Y. Ikuhara, Direct Bonded Aluminum (DBA) on Aluminum Nitride (AlN) substrates through Transient Liquid Phase and its Application, *6th International Conference on Integrated Power Electronic Systems (CIPS) Proceedings*, 2010.
8. H. Knoll, W. Weidenauer, P. Ingram, S. Bennemann, S. Brand, M. Petzold, , Ceramic substrates with aluminum metallization for power application, *Electronic System-Integration Technology Conference (ESTC), 2010 3rd* ,1-5, 13-16, 2010.
9. A. Lindemann, Properties of Direct Aluminum Bonded Substrates for Power Semiconductor Components, *IEEE Transactions on Power Electronics*, 22 (2), 2007.
10. C. R. Eddy, Jr. and D. K. Gaskill, “Silicon Carbide as a Platform for Power Electronics,” Science, 324 [5933] 1398-1400 (2009).
11. K. Hirao, Y. Zhou, H. Hyuga, T. Ohji, and D. Kusano, “High Thermal Conductivity Silicon Nitride Ceramics,” *J. Korean Ceramic Society*, Vol. 49, No. 4, pp. 380-384, 2012.
12. Y. Zhou, H. Hyuga, D. Kusano, Y. Yoshizawa, and K. Hirao, “A Tough Silicon Nitride Ceramic with High Thermal Conductivity,” *Adv. Mater.*, 23 (39), 4563-67, 2011.

Publications/Presentations

1. Poster on this project was presented at DOE Advanced Power Electronics and Electric Motors R&D FY12 Kickoff Meeting, Nov. 3, 2011
2. Oral presentation on this project was presented at DOE Annual Merit Review, Arlington, VA, May 14-17, 2012.

Agreement 23279 - Improved Organics for Power Electronics and Electric Motors

A. A. Wereszczak, T. G. Morrissey, H. -T. Lin, and H. Wang
Oak Ridge National Laboratory
P.O. Box 2008, MS 6068, Bldg. 4515
Oak Ridge, TN 37831-6068
(865) 576-1169; fax: (865) 574-6098; e-mail: wereszczakaa@ornl.gov

DOE Technology Manager: Jerry L. Gibbs
(202) 586-1182; fax: (202) 586-1600; e-mail: jerry.gibbs@ee.doe.gov
ORNL Technical Advisor: J. Allen Haynes
(865) 576-2894; fax: (865) 574-4913; e-mail: haynesa@ornl.gov

Contractor: Oak Ridge National Laboratory, Oak Ridge, Tennessee
Prime Contract No.: DE-AC05-00OR22725

Objectives

- Develop thermally conductive and low-cost epoxy molding compounds (EMCs) with sustained electrical insulation, magnetic insusceptibility, thermal expansion control, and mechanical resilience for power electronic and electric motor application.
- Enable new or improved thermal management strategies in power electronics and electric motors that decrease the maximum temperature of their operation.

Approach

- Use alternative fillers that are characteristically low-cost, electrically insulative, and thermally conductive.
- Collaborate with EMC manufacturer(s) to optimize particle size distribution so as to fully exploit filler properties.
- Collaborate with power module and electric motor designers, manufacturers, and end-users to integrate and exploit thermally conductive EMCs.

Accomplishments

- Developed magnesium oxide (MgO)-filled EMCs.
- Achieved a thermal conductivity of 3 W/mK which is approximately a 3x improvement over currently used silica-containing EMCs.
- Filed an invention disclosure on the development of hybrid-filled EMCs.

Future Direction

- Process hybrid-filled EMCs to achieve a thermal conductivity of least 5 W/mK without compromise of processing control, electrical insulation, magnetic insusceptibility, thermal expansion response, and mechanical resilience.
- Continue to collaborate with EMC manufacturers and power module and electric motor designers, manufacturers, and end-users to integrate thermally-conductive EMCs into power electronic, motor, and future wireless charging applications.

Introduction

The Vehicle Technology Program's Advanced Power Electronics and Electric Motors (APEEM) program has emphasized cost-reducing research targets, challenges, and areas. These include high-temperature components, packaging, and reliability for long-term transformation technologies, and thermal management technologies to reduce volume and enhance thermal reliability. The technical goals of this project directly address that emphasis.

The goals of this project are to develop, characterize, and test candidate organic or epoxy molding compounds (EMCs) that are thermally conductive and that have the potential to be low-cost, volume-reducing, and better-performing alternatives to presently used compounds for at least the following applications:

- dielectrics in power electronic devices,
- potting compounds used with capacitors,
- potting compounds used in motors, and
- potting compounds for future wireless charging stations.

For all these application, any candidate EMC must, first and foremost, possess electrical insulative behavior. But it needs to be not susceptible to magnetic fields so autogenous heating does not occur. The EMC also needs to provide a barrier to moisture penetration to the constituents it mechanically protects. Lastly, the thermal expansion response of the EMC must sufficiently match that of the constituents it protects.

An example of an EMC microstructure is shown in Fig. 1. In this example, a wide particle size distribution of silicon-dioxide-filler is used. But silicon dioxide has a low thermal conductivity (see Table I) as does the continuous epoxy phase, so this EMC will consequently also have an overall low thermal conductivity.

Our approach is to use different fillers that are thermally conductive with optimized particle size distribution and volume fraction to produce a more thermally conductive EMC. Unfortunately, the more thermally conductive fillers listed in Table I have other limitations that lessen their attractiveness for use. Boron nitride, silicon carbide, aluminum nitride, and beryllium oxide all have high thermal conductivities, but either are expensive or have issues of toxicity, and are not under serious consideration as lone fillers. Both aluminum oxide and magnesium oxide (MgO) were considered initially; however, the latter was selected for exploration in FY12 because MgO is less abrasive, and its use in future EMCs would therefore impart less wear on the molds and components it comes into contact with as it is injected in its uncured state.

Thermal finite element analysis results and discussions with APEEM Principal Investigators revealed that an EMC thermal conductivity of 5 W/mK would enable attractive new thermal management options so this project seeks to develop an EMC that achieves at least that value.

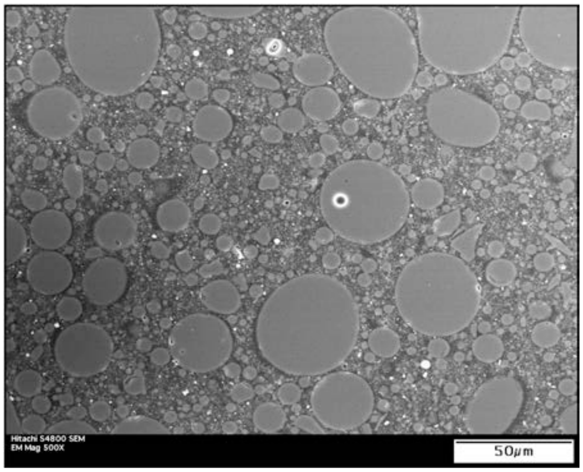

Figure 1. Example of a SiO_2-based filled EMC from a power module from a hybrid vehicle's power inverter.

Table I. Examples of candidate fillers for EMCs.

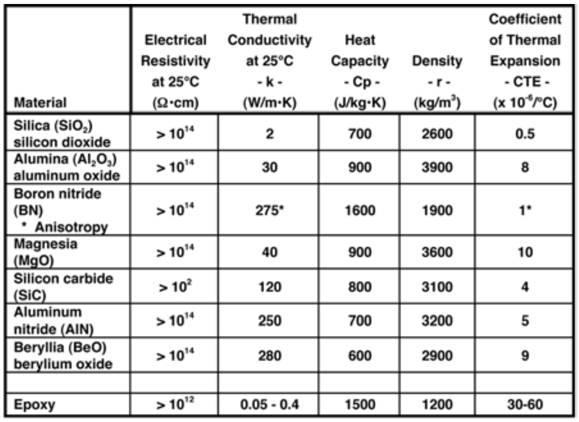

Material	Electrical Resistivity at 25°C (Ω·cm)	Thermal Conductivity at 25°C - k - (W/m·K)	Heat Capacity - Cp - (J/kg·K)	Density - r - (kg/m³)	Coefficient of Thermal Expansion - CTE - (x 10^{-6}/°C)
Silica (SiO_2) silicon dioxide	> 10^{14}	2	700	2600	0.5
Alumina (Al_2O_3) aluminum oxide	> 10^{14}	30	900	3900	8
Boron nitride (BN) * Anisotropy	> 10^{14}	275*	1600	1900	1*
Magnesia (MgO)	> 10^{14}	40	900	3600	10
Silicon carbide (SiC)	> 10^{2}	120	800	3100	4
Aluminum nitride (AlN)	> 10^{14}	250	700	3200	5
Beryllia (BeO) berylium oxide	> 10^{14}	280	600	2900	9
Epoxy	> 10^{12}	0.05 - 0.4	1500	1200	30-60

Results

FY12 studies focused on the consideration of MgO-filled EMCs. MgO is a common dielectric ceramic material that is often used by itself, for example, as filler between co-axial heaters that require the outer shell to be electrically isolated from the internal core. It is an inexpensive filler and is a "soft" ceramic making its consideration as a filler in EMCs attractive because surfaces that come into contact with it during its rheological processing may not experience wear.

A bimodal powder size distribution was targeted since that was suggested by our subcontractor, SolEpoxy Inc. (Olean, NY). MgO powder was supplied by Ube, and a blend of two MgO powders, whose measured particle size distributions are shown in Fig. 2, was used.

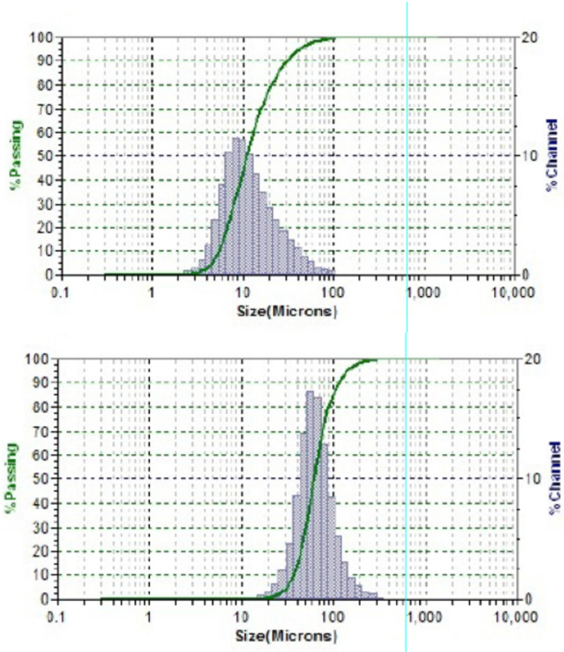

Figure 2. Particle size distributions of the two MgO powders (upper, 10C, and lower, 50C) used as filler.

SolEpoxy was tasked to fabricate MgO-EMCs by varying the blend of the two powders and to try to maximize the volume fraction without compromise to rheological flow and processibility. A nominal weight percentage of 75% of 10C powder, 50C powder, or a blend of the two was chosen. A powder blend of the two at a weight percentage of 80% was studied as well. SolEpoxy concluded that a weight percentage greater than 80% caused processing difficulties, so a higher MgO powder content was not pursued. This is an important identified threshold, because its (maximum) 80 wt % produced a thermal conductivity (maximum) of 3 W/mK.

SolEpoxy fabricated 50-mm diameter disks of five different MgO-filled compositions, and they are shown in Fig. 3. SolEpoxy measured electrical properties, and ORNL measured all other properties.

Figure 3. 50-mm diameter disks of processed MgO-EMCs with different particle size distributions and volume fractions of MgO filler.

Numerous relevant properties were measured for the various MgO-EMC blends and the results are summarized in Table II. Elastic modulus and Poisson's ratio were measured using resonance ultrasound spectroscopy. Room temperature thermal conductivity was measured at ORNL using a hot disk thermal constants analyzer. Coefficient of thermal expansion was measured at ORNL using a dual rod dilatometer. All other values in Table II were measured by SolEpoxy.

Of the five composition sets, three had equivalent amounts of MgO but with different particle size distributions. This enabled a preliminary exam on their effect on thermal conductivity. Within experimental uncertainty of thermal conductivity measurement of ± 5%, the MgO particle size distribution did not appear to have an observable effect.

Table II. Measured responses.

Property	**Unfilled Epoxy**	**MgO 75 10C**	**MgO 75 10C+50C**	**MgO 75 50C**	**MgO 80 10C+50C**
wt % MgO	0	74	74	76	79
vol % MgO	0	48	49	52	56
Density (g/cc)	1.19 ± 2%	2.35 ± 2%	2.36 ± 2%	2.42 ± 2%	2.52 ± 2%
Elastic Modulus (GPa)	3.0 ± 5%	19 ± 5%	18 ± 5%	20 ± 5%	24 ± 5%
Poisson's Ratio	0.32 ± 5%	0.28 ± 5%	0.27 ± 5%	0.25 ± 5%	0.25 ± 5%
Therm. Cond., 25°C, (W/mK)	0.24 ± 5%	2.4 ± 5%	2.0 ± 5%	2.2 ± 5%	2.9 ± 5%
Therm. Cond., 110°C, (W/mK)	0.23	1.9	1.9	1.8	2.5
Ave CTE (ppm/°C)	64 ± 5%	30 ± 5%	32 ± 5%	30 ± 5%	30 ± 5%
Dielectric Strength, 900 µm film, (kV/mm)	54	37	40	32	32
Surface Resistivity, 500V, (Ω)	4.8E+15	4.9E+15	5.0E+15	5.1E+15	4.2E+15
Volume Resistivity, 500V, (Ω•cm)	7.2E+15	4.9E+15	6.0E+15	5.9E+15	5.4E+14
Dielectric Constant, at 10 kHz	5.51	5.66	5.13	3.54	6.2
Dissipation Factor, at 10 kHz	0.0048	0.0063	0.003	0.0089	0.0065

Two of the sets had the same 50/50 MgO powder blend but different volume fractions; 49% and 56%. Here the effect of the higher volume fraction conclusive increased the thermal conductivity; namely, a 15% increase in MgO volume fraction increased thermal conductivity by approximately 20%.

A room temperature thermal conductivity of 2.9 W/mK was achieved with a 50/50 blend of the 10C and 50C powders for a total volume fraction of 56%. SolEpoxy concluded that a volume fraction larger than that compromises processibility and recommended against its increase. Customers who would therefore potentially use MgO-filled EMC would not be able to readily process MgO-EMC components with a volume fraction greater than 56%. Being that MgO is an inexpensive filler, it therefore may be further concluded that in order to achieve a thermal conductivity greater than 3 W/mK, a more expensive filler (having higher thermal conductivity such as AlN shown in Table I) would need to be used.

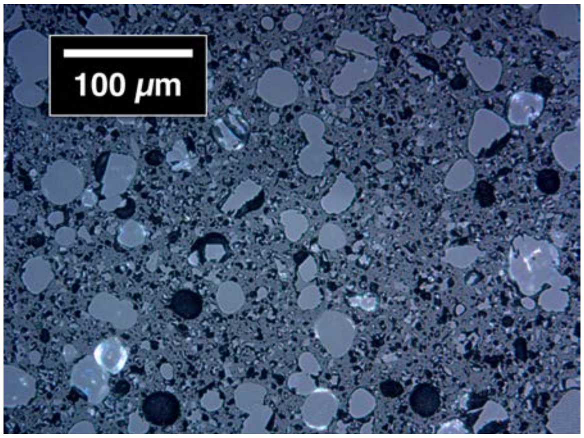

Figure 4. Polished microstructure of the 56 volume percent MgO-EMC.

The measured electrical properties of all the evaluated MgO compositions show they are indeed desirably electrically insulative.

Conclusions

Magnesium oxide (MgO) is an attractive, low-cost filler for epoxy molding compounds. Its use sustains electrically insulative behavior.

A thermal conductivity of 3 W/mK can be achieved with a MgO-filled EMC for a volume content of 56% MgO.

The different 100/0, 50/50, and 0/100 particle-size distribution blends produced equivalent thermal conductivities.

Thermal conductivity was sensitive to volume fraction of filler between 49 and 56%. An increase of ~15% in filler content increased thermal conductivity by ~20%.

A filler content greater than 56% compromises processibility of EMCs that would be formed via molding processes such as injection molding.

If a thermal conductivity of 5 W/mK or more is needed, then it will likely require the use of a (more expensive) filler material with higher thermal conductivity.

Agreement 23726 - Novel Manufacturing Technologies for High-Power Induction and Permanent Magnet Electric Motors − (GM CRADA)

Principal Investigator: Glenn J. Grant
Energy Materials
Pacific Northwest National Laboratory
902 Battelle Blvd., K2-03
Richland, Washington 99356
(509) 375-6890; fax: (509) 375-4448; e-mail: glenn.grant@pnnl.gov

Blair E. Carlson
Manager, Lightweight Materials Processing
General Motors R&D
30500 Mound Rd.
Warren, Michigan 48090
E-mail: blair.carlson@gm.com

DOE Technology Manager: Jerry L. Gibbs
(202) 586-1182; fax: (202) 586-1600; e-mail: jerry.gibbs@ee.doe.gov

Field Technical Manager: Dean Paxton
(509) 375-2620; fax (509) 375-2186; e-mail: dean.paxton@pnnl.gov

---

Contractor: *Pacific Northwest National Laboratory*
Contract No.: *DE-AC05-76RL01830*

Objective

- Develop and deploy high-power induction and permanent magnet rotors and stators that are lighter weight, have better cooling, and have a lower manufacturing cost through the application of novel solid-state joining and fabrication technologies.
- Apply solid-state processing techniques to improve performance of a low-cost soft magnetic material used in the rotors of high-power induction motors.

Approach

- Develop solid-state joining techniques and manufacturing processes that increase the efficiency of electric motors through lightweighting; improvements in electric and magnetic properties; and improvements in assembly space efficiency, packaging, and cost.
- Develop friction stir welding (FSW) process parameters and evaluate proper tool materials and techniques to produce defect-free friction stir welds in copper (Cu) alloys specified by project partners.
- Develop a fundamental knowledge of solid-state joints between copper materials and between dissimilar copper-aluminum (Al) materials. This should lead to strategies and techniques that will be used to produce a joining process with low thermal input and low distortion of adjacent parts and joints with a high degree of structural integrity and high thermal and electrical continuity.
- Use fundamental knowledge to develop techniques to manufacture copper and aluminum rotor and stator assemblies for high-power induction and permanent magnet motor systems. Demonstrate efficiency benefits and commercial applications of joined or processed components (industry collaborators).
- Transfer performance data and manufacturing technology to industry through a Cooperative Research and Development Agreement (CRADA) with General Motors (GM), ensuring a clear path to commercialization.

Milestones, Metrics, and Accomplishments

- **Milestone**: Characterize the microstructure and mechanical properties of Cu/Cu joints. Joints will be evaluated based on metrics established by the team including strength, toughness, and fatigue performance. Gate is established on minimum mechanical performance threshold established by the project team.
- **Milestone**: Develop, fabricate, and test actively cooled welding fixture to allow for FSW of copper and aluminum rotor parts.
- **Milestone**: Demonstrate a robust weld process on Cu/Al dissimilar material welds and verify that mechanical properties pass the metrics established by the team.

Introduction

The purpose of this project is to develop and deploy high-power induction and permanent magnet rotors and stators that are lighter weight, have better cooling, and have a lower manufacturing cost through the application of novel solid-state joining and fabrication technologies. Barriers to achieving these objectives have been identified that focus on the manufacturability of novel rotor designs. The project team will apply FSW to join copper subassemblies and copper/aluminum joints to eventually produce prototype lightweight, high-efficiency rotor assemblies. Fundamental work tasks will first focus on Cu/Cu FSW and dissimilar Cu/Al FSW joints. Later tasks will involve full rotor assembly and testing by GM. In addition, the project will apply solid-state processing techniques to improve the performance of a low-cost soft magnetic material used in the rotors of high-power induction motors. While GM provides the motor design, Pacific Northwest National Laboratory (PNNL) will employ a novel method to fabricate the ferrous-based laminates specific to the GM motor. The PNNL-developed method is based on nanoscale powder synthesis and friction extrusion/consolidation. This new fabrication process may allow for fewer energy-intensive processing steps to reach the microstructure and laminate thicknesses required for a high-performance soft magnetic material at a lower manufacturing cost. The project is a cost-shared CRADA between PNNL and GM.

Background

New manufacturing techniques can cause step changes in the overall cost of manufactured assemblies if the new technique can create a fundamental shift in the way a subsystem is constructed. For example, an electric motor has numerous components that are sensitive to high temperature. Fusion welding, which requires very high temperature to melt the materials being joined, cannot be accomplished directly adjacent to heat sensitive parts like sensitive electronics, wiring and insulation, or where coated laminates or substrates are located nearby. This restriction might require the part to be assembled through a much more complicated multistep process. If another joining technology were available that did not heat the part, the costly multistep assembly could be avoided.

One example of a joining technology that could satisfy the need for lower adjacent part temperatures is FSW. Previous work by PNNL and others has shown that friction stir welds can be made in copper alloys that have excellent mechanical, electrical, and thermo-mechanical performance. FSW has a particular advantage in welding copper due to the wide range of weld-specific energy levels that can be applied by the process. Conventional fusion welding must deliver a high level of energy to melt the copper on each side of the joint line. In many applications, the high part temperatures during fusion welding can lead to distortion or overheated adjacent parts. Often, copper joining is required in assemblies where heat sensitive electronics, wiring, or coated laminates, or substrates are located nearby. FSW may provide a lower heat input joining technique in these special applications where adjacent parts in the assembly can be damaged.

In addition, the next generation of rotor designs may be Cu/Al hybrids or have aluminum components to reduce the rotating mass. Joints are anticipated to be needed between copper and aluminum. The development of solid-state joining techniques (e.g., FSW) is logical for specialized dissimilar joints, like these, that cannot be fusion welded due to the radically different melt temperatures of the components.

Approach

The project will develop the FSW process parameters and evaluate proper tool materials and techniques to produce defect-free friction stir welds in copper alloys specified by project partners. In addition, the project team will develop statistical confidence around the manufacturing process used to fabricate high-power induction motor rotor assemblies by applying a set of mechanical test methods and procedures to evaluate process robustness. Further, the project team will investigate the application of FSW to other joining issues around electric drive systems (e.g., dissimilar joining between Al/Cu and potentially Al/Al joints) in specific configurations.

Finally, to address the overarching goal of improving energy efficiency in the induction motor design, the project team will apply solid-state processing techniques to fabricate a low-cost soft magnetic material with unique properties that has the potential to display high magnetic flux density (B) and low iron loss (W). Amorphous iron-based metal and alloys offer excellent soft magnetic properties. Literature reports the material may reduce the core losses of motors by more than 70 percent and the efficiency of an induction motor with amorphous iron core can easily reach 80 percent. However, the production cost of an amorphous iron core is high. Specifically, the thickness of amorphous iron sheet cannot exceed 25 μm due to the requirement of ultra-fast quenching. This task will focus on developing a cost-effective method to produce a soft iron alloy sheet with magnetic properties comparable to those of the amorphous iron alloy and with thickness greater than 100 um. This method is based on a modified friction consolidation and extrusion method, where the material is subjected to high strain under a hydrostatic state of stress. This solid-state process has shown the ability to produce ultra-fine grain size in bulk solids.

This project will be divided into three primary task areas: Task 1 will focus on solid-state joining of Cu materials used in the rotor assemblies of high-power induction motors. Task 2 will focus on dissimilar material joining, primarily Cu to Al with an emphasis on components and assembly performance improvement. Task 3 will develop a unique solid-state process to create appropriate microstructures and magnetic performance in bulk soft magnetic materials that may be able to improve on the efficiency of stack laminates in the rotor assembly.

Results

Work completed during FY 2012 has focused primarily on FSW trials on Cu bar materials and Cu rotor end caps (Task 1). The induction motor rotor represents an excellent example of a multi-material assembly that may be manufactured more efficiently and at a lower cost if new manufacturing techniques could be developed. This project is investigating using solid-state welding (i.e., FSW) to assemble this component.

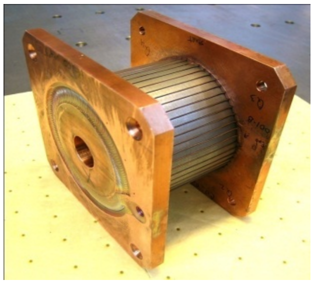

Figure 1. Rotor concepts fabricated with FSW

During FY 2012, the project team investigated a wide range of tool materials, tool designs, and process parameters to aid in establishing a robust process. Figure 2 shows a process window established for C101 copper using a FerroTic® tool with a 0.25-in. deep penetration. The circular dots indicate conditions in which either the tool failed or the weld had significant defects. Square symbols are successful welds (based on surface condition only). Welds with optimum mechanical properties exist within the region of the square symbols. The process of parameter development narrows the weld conditions to those with the appropriate defect-free quality and appropriate mechanical performance.

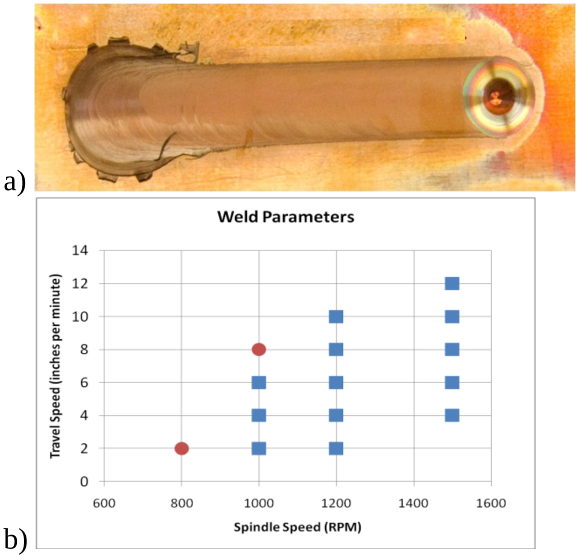

Figure 2. a) Typical FSW weld in C101 copper, b) copper FSW weld parameter map using a FerroTic stepped spiral tool. Circle symbols indicate failed welds, and square symbols indicate conditions where the visual observation of the weld surface passed a set of criteria.

The weld process parameter development also focused on several tool designs. Figure 3 shows two of the primary tool concepts being tested—the Stepped Spiral tool and the Triflat tool. These designs and variations of these tools are well known in commercial applications of FSW, especially in Al welding, but their performance in copper welding is yet to be determined.

FSW weld trials have been completed on both linear welds on Cu plate and on two-dimensional circular configurations. Welds have been developed for both monolithic materials and for plates that have cutouts for Cu bars running the length of the rotors. Short bar segments are inserted into the larger plates and welded in one assembly as shown in Figure 4.

Figure 3. Two tool designs that will be investigated in this project include the stepped spiral tool (on the left) and the three flat tool (on the right). (Pictures are for illustration only; actual designs will vary.)

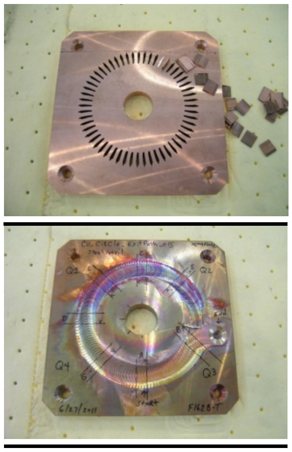

Figure 4. Cu plates with small Cu bar segments welded to simulate rotor endcap configuration

Several challenges have emerged involving control of the process and weld quality. A circular weld involves returning to the beginning of the weld start area; and in some cases, over-running a previously welded area. This creates an ever-changing set of boundary conditions including a temperature field that changes throughout the weld.

Figure 5 show a plot of tool temperature vs. time taken during the course of a circular weld. This plot shows the continuously increasing temperature during welding. The lack of tool (and thus weld) temperature stability can create a wide range of defects, including excess flash and loss of material (see Figure 6).

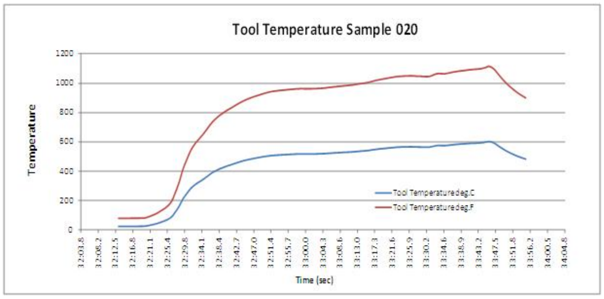

Figure 5. Tool temperature vs. time during a circular weld

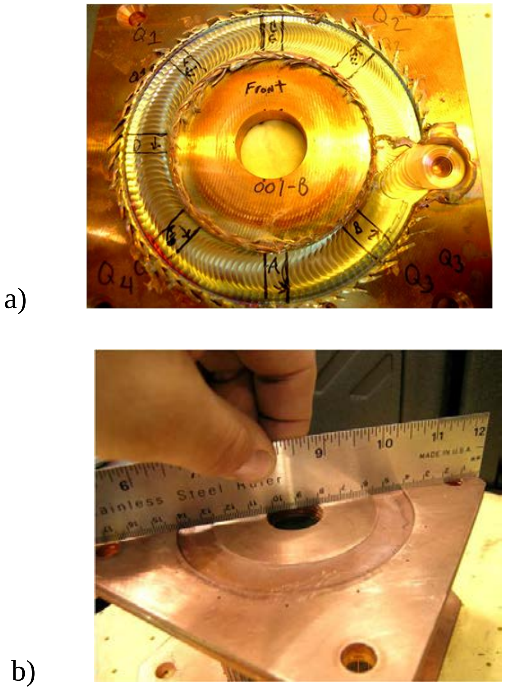

Figure 6. Circular weld run too hot showing a) excessive flash and loss of material. b) excessive distortion

Loss of weld material leads to internal defects and loss of electrical continuity in the joint, a particularly important property that must be maintained in an end cap weld. To compensate for a weld that is too hot, the process parameters can be set to generate less heat in the process. If the parameters are set too low, however, this can lead to defects usually manifested by voids developed in the weld direction (Figure 7).

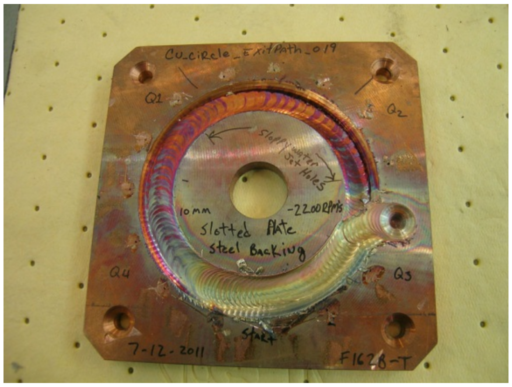

Figure 7. Surface breaching void defect due to weld parameters that did not deliver enough weld energy for a consolidated joint

One of the solutions to changing boundary conditions being used in this project is weld process control by adaptive programming. To adapt to changing temperature conditions the weld parameters are allowed to change through a torque and power-based feedback system. This system controls power and tool temperature through a feedback nested loop controller and can make high speed adjustments to power to keep tool temperatures within a set range. The system, once fully developed, is expected to solve several current challenges to maintaining welds of consistent quality.

Conclusions

Motor designs, like all complex assemblies, are a compromise between performance and cost (both cost of materials and cost of manufacturing). New manufacturing processes can be critical in this balance because they can both be enabling of lower cost materials and can introduce a lower cost manufacturing process. In many cases, the new manufacturing process may even directly increase the efficiency of the part by producing an assembly that displays better thermal, mechanical, or electric/magnetic properties. This project will use new solid-state joining and processing technologies to achieve both increased performance and a lower manufacturing cost. Figure 8 is an illustration of how this project maps to the goals of the DOE's program on Advanced Power Electronics and Electrical Motors.

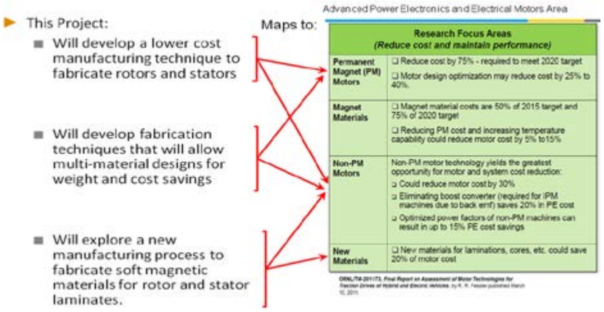

This Project:
- Will develop a lower cost manufacturing technique to fabricate rotors and stators
- Will develop fabrication techniques that will allow multi-material designs for weight and cost savings
- Will explore a new manufacturing process to fabricate soft magnetic materials for rotor and stator laminates.

Maps to:

Advanced Power Electronics and Electrical Motors Area

Research Focus Areas *(Reduce cost and maintain performance)*	
Permanent Magnet (PM) Motors	❑ Reduce cost by 75% - required to meet 2020 target ❑ Motor design optimization may reduce cost by 25% to 40%.
Magnet Materials	❑ Magnet material costs are 50% of 2015 target and 75% of 2020 target ❑ Reducing PM cost and increasing temperature capability could reduce motor cost by 5% to15%
Non-PM Motors	Non-PM motor technology yields the greatest opportunity for motor and system cost reduction: ❑ Could reduce motor cost by 30% ❑ Eliminating boost converter (required for IPM machines due to back emf) saves 20% in PE cost ❑ Optimized power factors of non-PM machines can result in up to 15% PE cost savings
New Materials	❑ New materials for laminations, cores, etc. could save 20% of motor cost

Figure 8. Project objectives and how they map to the DOE goals and targets for the Advanced Power Electronics and Electrical Motors Area

Specifically, the project will develop the fundamental understanding of solid-state joints between Cu materials and between Cu and Al dissimilar joints so that they can be achieved with low thermal input, low distortion of adjacent parts, a high degree of structural integrity, and a high degree of thermal and electrical continuity. This fundamental information will be used to develop techniques to manufacture Cu and Al rotor and stator assemblies for high-power induction and permanent magnet motor systems. Joined or processed components will be evaluated and tested by industry collaborators to demonstrate efficiency benefits and commercial applications.

Project 19026: Permanent Magnet Development for Automotive Traction Motors (co-funded by Agreement 13295 – Propulsion Materials)

Principal Investigator: Iver E. Anderson
Division of Materials Sciences and Engineering
Ames Laboratory (USDOE), Iowa State University
Ames, IA 50011
Voice: 515- 294-9791; Fax: (515) 294-8727; E-mail: andersoni@ameslab.gov

DOE Technology Development Manager: Susan A. Rogers
Voice: 202-586-8997; Fax: 202-586-1600; E-mail: Susan.Rogers@ee.doe.gov
DOE Technology Manager (Propulsion Materials): Jerry L. Gibbs
(202) 586-1182; fax: (202) 586-1600; e-mail: jerry.gibbs@ee.doe.gov

Lab Program Manager: Thomas A. Lograsso
Voice: 515- 294-4446; Fax: (515) 294-8727; E-mail: lograsso@ameslab.gov

---

Objectives

- Develop the materials and processes needed to fabricate high performance permanent magnets (PM) that can be used for advanced traction drive motors with an internal PM rotor design to meet APEEM goals for enhanced performance at elevated temperature (180-200˚C) and reduced cost.
- Anisotropic magnets should be developed to satisfy the need for magnets with maximum magnetic energy density and minimum content of valuable materials. If possible, improved magnet forming processes and mechanical properties also should be developed to further reduce motor manufacturing costs and extend lifetime in service.
- While magnet materials meeting the technical specifications are currently achieved using rare earth (RE) permanent magnets, the market factors of rising RE demand, uncertain RE cost, and near total foreign control of RE supplies dictate that alternative non-RE magnets must be developed.

Approach

This program consisted in FY2012 of two major thrust areas.

- **Thrust Area 1:** Continued investigation of ***RE anisotropic*** permanent magnets, driven by industry needs, placing effort on generating anisotropic particulate for bonded magnets and on novel processing of sintered RE permanent magnets, exploiting the improved high temperature tolerance of the Ames mixed rare earth (MRE)-Fe-B alloys to minimize or eliminate the use of Dy.
- Developed aligned microstructures in MRE-Fe-B magnet alloy particulate with little or no Dy content, preferring controlled rapid solidification as a low cost route to make large gains in net-shape bonded magnet strength and reduced magnet cost and waste for simplified motor manufacturing.
- Refined processing of anisotropic sintered permanent magnets of MRE-Fe-B alloys with little or no Dy content by single stage hot deformation (SSHD) to enable the maximum energy product to be realized in bulk magnets starting from Zn-coated amorphous flake particulate, using pressure-driven liquid phase densification/crystallization/sintering, and producing aligned nano-grained magnets.
- **Thrust Area 2:** New high strength ***non-RE anisotropic*** permanent magnets will be developed that meet the requirements for advanced interior PM electric traction motors. The investigation will involve theory and modeling efforts, as well as experimental synthesis of magnet compounds and prototype magnet fabrication and characterization.

- Near-term development of non-RE anisotropic permanent magnets is focused on attempts to improve the best of the non-RE systems, alnico, by using modern high-resolution characterization techniques to gain enhanced knowledge of coercivity mechanisms in existing alnico magnet types and, then, by developing innovative alloying and processing to improve coercivity and magnetic energy product using greater control of nano-structure and microstructure.
- Long-term development of new non-RE anisotropic permanent magnets also is pursued with significant input from theory and modeling, seeking to discover novel phases based on Fe-Co-X with beneficial intrinsic properties, i.e., high Curie temperature, magnetization and magnetic anisotropy.
- If the new non-RE permanent magnet phases have insufficient magnetic properties as single-phase magnets, increased properties will be sought by further extrinsic manipulation, including use of a soft magnetic second phase to produce enhanced exchange coupling.
    - It should be noted that this task area is extremely high risk, but if successful it will revolutionize the cost structure of permanent magnet motors and reduce the reliance on foreign controlled commodities for hybrid and electric vehicle production.

Major Accomplishments

- Developed new single stage hot deformation (SSHD) method to fabricate fully dense anisotropic magnets from Zn-coated glassy $MRE_2(Fe,Co)_{14}B$ flake with reduced Dy content. Key parts of this development included design and implementation of a high purity method for Zn evaporative coating of magnet alloy flake particulate, innovative pressure and temperature cycle design, and TEM characterization that revealed Zn penetration of aligned nano-crystalline grain boundaries.
- Completed detailed microstructural and semi-quantitative chemical analysis, including 3-D atom probe studies, of non-RE commercial anisotropic alnico types 5-7, 8, and 9, in the finished magnet condition.
- Quantified differences in nano-scale morphology and structure between transverse (normal to direction of applied field during magnetic annealing) sections of alnico 5-7 with the classical (magnetic) bcc Fe-Co “bricks” and (non-magnetic) B2 AlNi “mortar” pattern in a ratio of about 2:1, (bcc):(B2), compared to the unusual alnico 8 & 9 pattern of “mosaic tile” with bcc Fe-Co faceted “tiles” and $L2_1$ $(Ni,Co,Fe)_2AlTi$ matrix phase in a ratio of about 1:1, (bcc):($L2_1$). The (magnetic) bcc:matrix ratio difference can be significant in the higher remanence/saturation of alnico 5-7.
- Discovered further nano-scale details of complex matrix phase in alnico 8 & 9, including discovery of pure Cu nano-rod phase at “points” of Fe-Co tiles and Fe-Co precipitates in the $L2_1$ matrix, as well as an unexpectedly high Co and Fe content in the matrix phase of both alnico 5-7 and 8 & 9, which seems to represent a “wasted” alloy addition, especially of valuable Co.
- Quantified more differences in nano-scale morphology between alnico 5-7 and 8 & 9, most importantly between the shape anisotropy for the bcc Fe-Co phase in longitudinal (parallel to direction of applied field during magnetic annealing) sections, where 5-7 has about 1:3 (width:length), compared to about 1:10 for 8 & 9. This shape difference can be significant in the much higher coercivity of alnico 8 & 9.
- Used magneto-optic Kerr effect (MOKE) observations to correlate length scale of apparent domain wall pinning sites to micron-scale features in cast alnico 5-7 and 9 magnets.
- Analyzed grain boundaries and product phases on micron-scale (with SEM) in commercial sintered (powder processed) alnico 8 finished magnets and identified composition of “contaminant” grain boundary phases.
- Performed theoretical analysis of possible impact from high Co and Fe content in matrix phase of alnico 5-7 and 8 & 9, using 3-D atom probe measurements, and determined that matrix phase in both alnico types may be ferromagnetic, which can negatively impact nano-scale interface effect on coercivity and points to possible benefits of alloy modifications or processing (annealing) changes to enhance coercivity.

- Used theoretical tools based on genetic algorithm (GA) on existing computer clusters and initial time on supercomputers (NERSC and Jaguar) to expand investigation of potential new Fe-Co-X phases, with special emphasis on alloying into Co_7Hf and Co_5Zr with Fe and other 4d and 5d elements and established some initial correlations with findings of exploratory experimental findings.
- Exploratory combinatorial synthesis work on Fe-Co-X systems, where X=5d and 4d (e.g., W, Ta, Mo, Hf) demonstrated (for X=Mo) formation of an aligned columnar structure with nano-metric spacing that demonstrated single permanent magnet phase behavior with a coercivity of about 2 kOe over a significant composition range, somewhat reminiscent of alnico.
- In experimental synthesis investigations, a capability for dual beam cluster deposition in an applied field was developed and demonstrated for producing aligned nano-metric exchange coupled magnet samples from separate sources of Fe-Co and Co_7Hf nano-particulate. In a similar pursuit, a chemical synthesis approach was developed for producing a nano-composite magnet sample of Fe-Co-W in a Fe-Co matrix.

Future Directions

- Continue focused work on improved processing of ***RE anisotropic*** permanent magnets, stepping up studies on innovative processing of sintered (fully dense) anisotropic RE permanent magnets, exploiting the improved high temperature tolerance of the Ames mixed rare earth (MRE)-Fe-B alloys, pushing for little or no Dy content.
    - Further develop SSHD method to fabricate fully dense anisotropic magnets from Zn-coated glassy $MRE_2(Fe,Co)_{14}B$ flake with lower Dy content and verify high temperature stability and perform preliminary experiments on comminution of finished magnets to generate anisotropic magnetic powder for experiments on producing high performance net shaped bonded magnets.
- In the effort to develop new high strength ***non-RE anisotropic*** permanent magnets that meet the requirements for advanced interior PM electric traction motors, accelerate the near-term prospects for enhanced alnico by continued efforts to understand coercivity mechanisms and the linkage to microstructure that can be controlled in bulk alnico magnets. Enhance progress on long-term magnet prospects by applying the increased speed of supercomputer calculations (using 45M node hours just granted on a FY2013 INCITE award to B. Harmon and K-M. Ho) to more focused composition regions of the selected Fe-Co-X systems, following the down-selection of promising magnet alloy compositions from early FY2012. In general, it is critical that the investigation maintains the close collaboration of theory and modeling efforts, of experimental magnet material synthesis work, and of detailed characterization studies on the new materials.
    - Provide detailed characterization results, including 3-D atom probe, TEM, and SEM, on heat treated commercial alnico samples and on experimental chill cast modified alnico alloy samples to allow improved selection of alnico compositions and development of better bulk magnet processing approaches, including advanced powder processing.
    - Expand use of MOKE, magnetic force microscopy (MFM), and hysteresisgraph measurements to observe domain wall pinning and hysteresis values for correlation with microstructural analysis results at all relevant magnifications to gain more complete and useful knowledge of alnico coercivity mechanisms.
    - Produce fully pre-alloyed alnico powder, initially centered on a preferred alnico 8 composition, and consolidate to full density with subsequent magnetic annealing and heat treatments designed on the basis of improved understanding of magnetic property optimization.
    - Extend exploration with theoretical tools to investigate possible alnico interface/phase configurations and potential new Fe-Co-X phases on existing clusters and supercomputers (access from new INCITE award).

- Based on theoretical guidance, pursue promising regions of ternary Fe-Co-X systems for further investigation by full suite of experimental synthesis methods.
- Maintain WebEx contact and bi-annual workshops with team.

Technical Discussion: [Research Highlight Examples]

New Understanding of Alnico Magnets Helps Design Improvements

to Boost Properties for Drive Motors (Kramer, McCallum, Constantinides, Anderson)

Atomic-scale characterization and theoretical analysis provide clues about how rare earth-free alnico magnets can be improved for drive motor use with changes in processing and alloy design: Alnico magnets have been selected as the best near-term candidate to replace rare earth (RE) magnets in permanent magnet (PM) motors for HEV and PHEV drive systems. While these aluminum-nickel-cobalt-iron (Al-Ni-Co-Fe) PM alloys have been used widely since 1940s, their development was “on hold” for about 40 years; displaced by superior RE magnets, especially neodymium-iron-boron (Nd-Fe-B) which have a 5 times energy product (MGOe) advantage at room temperature. However, for traction motors, wind power generation and other elevated temperature uses (above 180˚C), Nd-Fe-B has only a 20 MGOe vs. 10 MGOe margin over the best [1] alnico (type 9), which also has many advantages over Nd-Fe-B, including superior corrosion resistance and broadly available alloy constituents, although Co costs are relatively high.

Alnico magnets that can match Nd-Fe-B at motor operating temperatures basically will require increased resistance to field reversals, yet there is scant understanding of these “coercivity” mechanisms for alnico magnets, beyond a preference for high content of magnetic Fe-Co (bcc) “bricks” that are highly elongated for “shape anisotropy” in a non-magnetic “mortar” (matrix). Our new study uses modern atomic-scale characterization on 3 types of commercial anisotropic (strongest) alnico magnets.

Significant differences (see copper nano-rods) were found in the nano-scale morphologies and, especially, in the structural/chemical make-up of matrix phases for different alnico magnet types. One shocking observation was that the best alnico, which contains 1.5X the Co content of the classical alloy, appears to “waste” nearly half of this Co by trapping it in the matrix phase that is supposed to be non-magnetic. Recent theory results suggest that this useless Co may even degrade the magnetic strength. These findings direct us to substitute lower cost elements, e.g., Ni, Cu, Mn, for the Co, if possible, saving up to 20% of the alloy cost and perhaps improving the magnets. Linked microstructure and magnetic domain observations showed that promise for raising alnico strength also lies at the 10-100 micron scale, prime for our powder metallurgy methods. These pathways to improved alnico should allow us to double the energy product and reduce the cost by at least 10%, in contrast to the predicted upward cost trajectory for Nd-Fe-B magnets, especially with significant added Dy for high temperature tolerance.

Development of Single-Stage Hot Deformation for Anisotropic Magnets from Zn-coated MRE-Fe-B Flake Powder (McCallum, Anderson, Kramer)

Simplification of the process for conversion of amorphous melt spun flake particulate to anisotropic nano-crystalline magnets can also benefit from high temperature tolerance of MRE-Fe-B alloy to reduce Dy use:

Commercial anisotropic magnets (termed MQ-III) used over-quenched flake particulate to avoid casting segregation/annealing, but needed very expensive two-stage hot deformation process (hot pressing and die-upset forging) to produce fully dense magnets from Nd-Fe-B alloys. Eventually the pressure of the marketplace force MQ-III out of the commercial arena, i.e., it is no longer a commercial product. In our studies, a new single stage hot deformation (SSHD) method (see Fig. 2) is being developed to fabricate fully dense

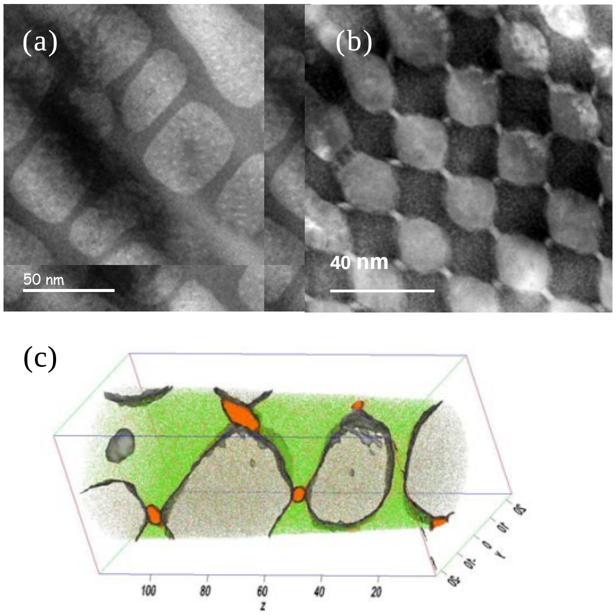

Figure 1. Collection of micrographs showing (a) STEM image of the 5-7 alloy showing the ‘brick-and-mortar’ morphology, and (b) shows a ‘mosaic-tile’ morphology in alnico 8. Atom probe tomography (c) shows the isolated copper (orange) at the ‘tile’ points in 8. The Fe-Co phase is light gray regions. APT was obtained with collaboration of M. Miller at the ORNL ShaRE User Facility, sponsored by BES.

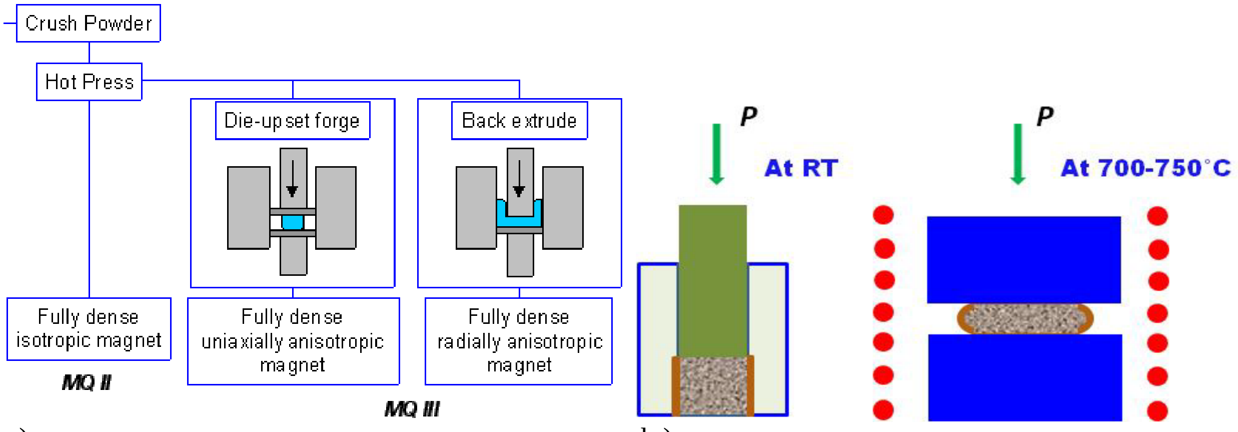

a.) b.)

Figure 2. Schematic comparison of: a) two stage hot deformation in the MQ III process and, b) the pre-compaction step at room temperature (RT) and single hot deformation stage of the new SSHD process.

The idea of using a very small addition (ideally a very thin surface layer) of low melting Zn is for “lubrication” of the flake particulate during initial hot pressing just above the Zn melting point to promote re-arrangement and densification of the flake particulate to full density (Fig. 3). A continued temperature rise at full pressure is intended to promote full crystallization of the flake under a uni-axial stress that promotes aligned growth of nano-crystals to ~30-60nm by ~150-300nm (Fig. 3).

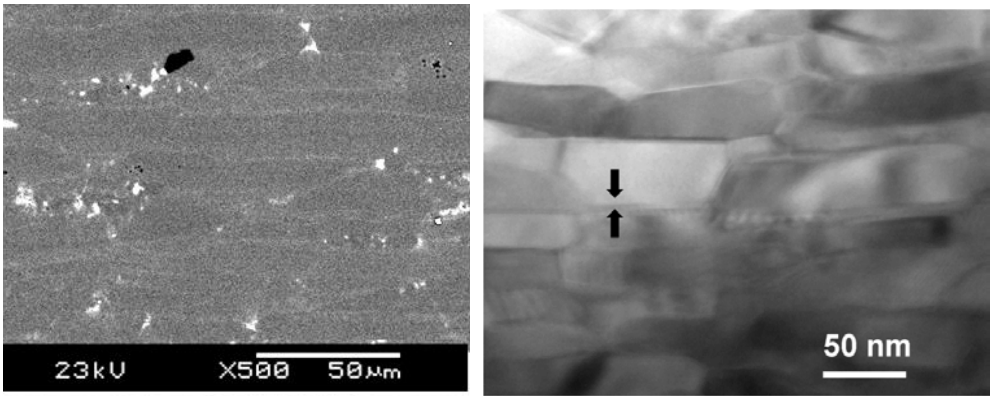

a) b)

Figure 3. Micrographs showing, a) full densification for flake particulate 1% Zn addition (light contrast) as a surface plating and, b) TEM micrograph of aligned nano-crystalline grains within a transformed flake particle after pressing above the crystallization temperature.

SQUID magnetometer measurements indicate coercivity of 10.8 kOe and 21.3 MGOe for only 1% Zn content (sample in Fig. 3a), showing ability for full consolidation. Further TEM studies are needed to probe interfacial reaction products at nano-grain interfaces. High temperature magnetometer measurements are needed to determine temperature coefficients of coercivity and remanence and to establish the lower limit of Dy needed to permit magnet operation above 180˚C.

Computational Prediction and Discovery of Magnet Materials (Wang, Ho, Harmon)

This computational project is in close collaboration with experimental synthesis and processing groups lead by Ames Laboratory that are striving to meet the goal of the development of PM materials to meet performance and cost goals for advanced electric drive motors: Promising material structures have been explored in Fe-Co-X systems in a range of stoichiometries around target compositions which were identified as candidate new non-RE magnet alloys. Crystal and interface structures were predicted at the atomic level using a genetic algorithm (GA) with first-principles density functional calculations for the energy and properties evaluations.

This research has been focused on computational prediction of crystal structures of $HfCo_7$, Hf_2Co_{11}, Zr_2Co_{11} and related alloys. The choice of systems was motivated by experimental observations that Hf-Co and Zr-Co alloys could be promising materials for high performance permanent magnet without rare-earth due to their high magnetic anisotropy [3,4]. The magneto-crystalline anisotropy K_1 of $HfCo_7$ alloy is 1.3 MJ/m^3 along with an appreciable saturation magnetic polarization J_s of 8.9 kG [3]. Hf_2Co_{11} alloy also exhibits similar magnetic anisotropy to that of $HfCo_7$ phase. It was also reported that Zr_2Co_{11} has high uni-axial anisotropy (1.1 MJ/m^3) and the Curie temperature is around 500 ºC [5-7]. Moreover, doping Fe into $HfCo_7$ alloy and B into Hf_2Co_{11} alloys was shown experimentally [12] to further improve the anisotropy and saturation magnetic polarization. However, the crystal structure of these alloys remains elusive. Different experiments [3, 7-12] suggested different crystal structures and the number of atoms in the unit cell proposed by experiment is also controversial and ranges from 16 to about 120 atoms. The uncertainty in the crystal structures greatly hinders further investigation and optimization of the structures and properties of the materials for high quality permanent magnets.

Using the computer time allocation on NERSC through the NISE program, a systematic search was performed to determine the low-energy atomistic structures for $HfCo_7$, Hf_2Co_{11-x} (Fig. 4) and Zr_2Co_{11-x} alloys (with x=0.0, 0.5, 0.6, 0.8 respectively) with the number of atoms in the unit cell ranging from 16 to 117. The computational algorithm and code used in this global structure search is the first-principles adaptive genetic algorithm (GA) code developed recently by our group at Ames Laboratory under the support of DOE-BES [13-15]. Through this global search, we predicted the lowest-energy structures for $HfCo_7$ up to 64 atoms per unit cell and those for Hf_2CO_{11-x} (see Fig. 5), as well as those for Zr_2Co_{11-x} up to 117 atoms per unit cell. Preliminary comparison of the calculated X-ray diffraction spectra from our structure models with available experimental data [12] is very encouraging, e.g., for $HfCo_{5.25}$ (Fig. 6).

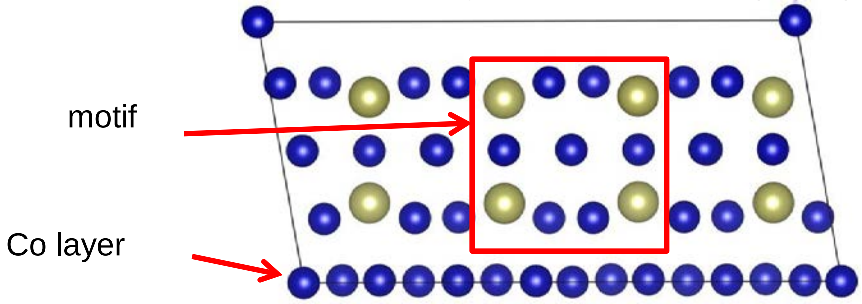

Figure 4. Example of atomic plane portion showing repeating motif from Hf_2Co_{11-x} studies with GA code.

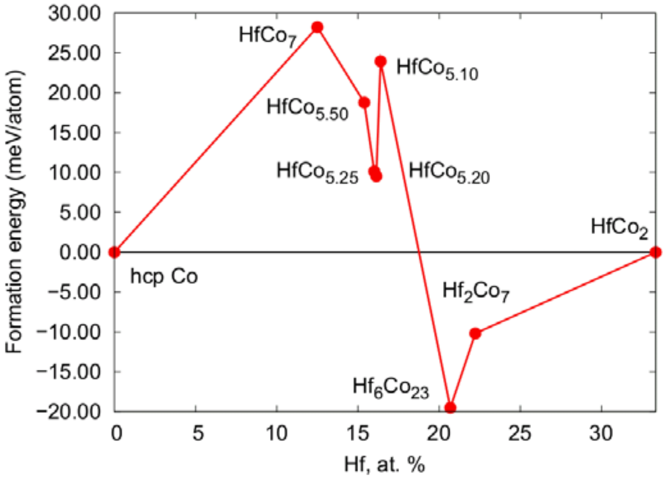

Figure 5. Summary of free energy of formation relative to hcp Co for calculated phases in Co-Hf.

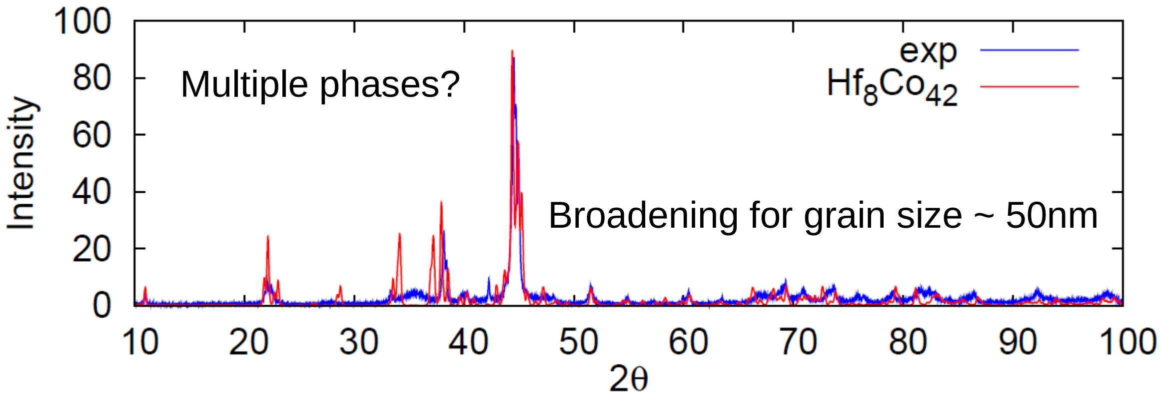

Figure 6. Comparison of calculated and experimental [3] X-ray diffraction patterns for apparent $HfCo_{5.25}$ phase.

As mentioned above in Fig. 6, because of possible mixed phases in the experimental samples, careful analysis of experimental X-ray data in comparison with the X-ray spectra from the theoretically predicted structure models is underway. We are working closely with Prof. D. Sellmyer's group at University of Nebraska at Lincoln (UNL) and the experimental groups at Ames Laboratory (M. J. Kramer, W. McCallum, and I. Anderson) on these analyses in order to finally resolve the structures of these phases. At the same time, we also collaborate with Dr. V. Antropov's group at Ames Laboratory to study the magnetic properties of the structures obtained from our search. The preliminary results indicate that these structures exhibit reasonably high magnetic anisotropy and are promising for permanent magnetic applications.

Conclusions

In experimental research on RE magnets, the development of a new single stage hot deformation (SSHD) method to fabricate fully dense anisotropic magnets from Zn-coated glassy $MRE_2(Fe,Co)_{14}B$ flake is promising as a manufacturing process for near-net shape fully dense sintered magnets with reduced Dy content. Alternatively, this relatively simple approach to generate aligned nano-metric grains may also be useful for crushing into micron sized equi-axed particulate that can be blended with a high temperature polymer and molded in-place into a rotor under an alignment field for further manufacturing advantage. Both of these directions for the process need further development to add assurance that industrial adoption can succeed and both depend on reduction or stabilization of the market for RE supplies in the future.

If the RE market rises or continues in uncertainty, we believe that the best near-term non-RE permanent magnet option is a modified version of today's alnico, based on the Al-Ni-Co-Fe system. Since coercivity is the primary deficiency for alnico, the detailed microstructural and semi-quantitative chemical analysis of commercial anisotropic alnico types 5-7, 8, and 9 in the finished magnet condition has been critical for analysis of the nano-metric and micron-scale features that contribute to long standing differences in coercivity and remanence between 5-7 and 8 & 9. Although our observations can lead one to nano-scale reasons for increased coercivity in 8 & 9 due to a far greater shape anisotropy for the Fe-Co phase, compared to 5-7, other analysis methods (MOKE and SEM-EDS) of both cast and powder processed versions of 8 & 9 are starting to show that micron-scale domain wall pinning may be more important. This observation also agrees with the theory work of our ORNL team member that suggests that the Al-Ni based matrix phase in 8 & 9 may also be ferromagnetic, not the intended non-magnetic phase. Both of these findings have guided us to specific plans for new powder processing work in FY2013, since by this route it is possible to gain control and increase the probable micron-scale pinning sites in an approach that is very adaptable to large-scale manufacturing of magnets. On the other hand, the apparent nano-scale reason for increased remanence of 5-7 is supported by our observation of a significantly greater ratio of Fe-Co phase to matrix phase (2:1), compared to the surprisingly low ratio, only 1:1, for the 8 & 9 and is very likely to be the dominant explanation. The significance here is that a coercivity increase of about 1.5-2.0X that is coupled with a remanence that maintains that of 5-7 would be likely to raise the energy product of alnico to the minimum level needed for some advanced drive motor designs.

For the long-term pursuit of alternative non-RE permanent magnet materials, we believe that the expanded and targeted efforts and initial results of our Theory Group show the value of this portion of our team for this discovery process. A prime example of the growing value is revealed by the strong interaction of the experimental synthesis studies (at Nebraska) and the structural characterization efforts (at Ames and Nebraska) with the theoretical investigations using both genetic algorithm (GA) and DFT tools (at Ames) to approach specification of a promising metastable magnetic phase, $HfCo_{5.25}$, that can be further alloyed with Fe, B, and other elements. These further complex alloying studies will be facilitated greatly by the expanded supercomputer access afforded by our very recent INCITE award and by new experimental work that works in concert with the new theory findings. Certainly, our exploratory combinatorial synthesis work on such Fe-Co-X systems, where X=5d and 4d (e.g., W, Ta, Mo, Hf, Zr) and other dopants (e.g., B, Si, N, C) has also demonstrated its worth in providing a rapid survey tool that is useful for both theory and experiment and the recent upgrade of high rate structural and magnetic analysis capabilities have made this even more valuable. The alloy specific experimental synthesis capabilities of cluster deposition and low temperature chemical synthesis have provided new results that show potential for producing aligned nano-metric exchange coupled magnet samples, where it is likely that the cluster deposition method can reach further into the metastable phase region for these new PM compounds. However, both methods can be useful for enhancement of the magnetization of new PM phases by enhanced exchange coupling.

Publications

Manh Cuong Nguyen, Xin Zhao, Min Ji, Cai-Zhuang Wang, Bruce Harmon and Kai-Ming Ho, "Atomic Structure and Magnetic Properties of Fe1-x Cox Alloys", J. Appl. Phys. 111 (2012), 07e338.

Wang, D. P., N. Poudyal, C. B. Rong, Y. Zhang, M. J. Kramer, and J. P. Liu, Exchange-coupled nanoscale SmCo/NdFeB hybrid magnets, J Magn Magn Mater 324 (2012), pp. 2836, DOI 10.1016/j.jmmm.2012.04.018.

Tang, W., K. W. Dennis, M. J. Kramer, I. E. Anderson, and R. W. McCallum, Studies of sintered MRE-Fe-B magnets by DyF3 addition or diffusion treatment (MRE = Nd+Y+Dy), J Appl Phys 111

Tang, W., K. W. Dennis, M. J. Kramer, I. E. Anderson, and R. W. McCallum, Studies of sintered MRE-Fe-B magnets by DyF3 addition or diffusion treatment (MRE = Nd+Y+Dy), J Appl Phys 111 (2012)Artn 07a736, DOI 10.1063/1.3679465.

Rong, C. B., Y. Q. Wu, D. P. Wang, Y. Zhang, N. Poudyal, M. J. Kramer and J. P. Liu, Effect of pressure loading rate on the crystallographic texture of NdFeB nanocrystalline magnets, J Appl Phys 111 (2012)Artn 07a717, DOI 10.1063/1.3675173.

Poudyal, N., C. B. Rong, Y. Zhang, D. P. Wang, M. J. Kramer, R. J. Hebert, and J. P. Liu, Self-nanoscaling in FeCo alloys prepared via severe plastic deformation, J Alloy Compd 521 (2012), pp. 55, DOI 10.1016/j.jallcom.2012.01.026.

Oster, N. T., D. T. Cavanaugh, K. W. Dennis, M. J. Kramer, R. W. McCallum, and I. E. Anderson, Effects of Ag additions on melt-spun RE2Fe14B microstructure and texture, J Appl Phys 111 (2012)Artn 07a723, DOI 10.1063/1.3677680

Golkar, F., M. J. Kramer, Y. Zhang, R. W. McCallum, R. Skomski, D. J. Sellmyer, and J. E. Shield, Structure and magnetic properties of Co-W clusters produced by inert gas condensation, J Appl Phys 111 (2012)Artn 07b524, DOI 10.1063/1.3676425.

R. Skomski, B. Balamurugan, T. A. George, M. Chipara, X.-H. Wei, J. E. Shield, and D. J. Sellmyer, "Hysteresis and Relaxation in Granular Permanent Magnets," J. Appl. Phys. **111**, 07B507-1-3 (2012).

R. Skomski, J. E. Shield, and D. J. Sellmyer, "An Elemental Question," Magnetics Technology International 2011, UKIP Media & Events, p. 26-29.

A. Kashyap, R. Skomski, P. Manchanda, J. E. Shield, and D. J. Sellmyer, "Layered transition-metal permanent-magnet structures," J. Appl. Phys. **109**, 07A714-1-3 (2011).

V. Sharma, P. Manchanda, R. Skomski, D. J. Sellmyer, and A. Kashyap, "Anisotropy of heavy transition metal dopants in Co," J. Appl. Phys. **109**, 07A727-1-3 (2011).

W.Y. Zhang, S. Valloppilly, X.Z. Li, R. Skomski, J.E. Shield, and D.J. Sellmyer, "Coercivity enhancement in Zr_2Co_{11}-based nanocrystalline materials due to Mo addition," IEEE Trans. Mag. **48**, 3603-3605 (2012).

B. Balamurugan, B. Das, R. Skomski, D.J. Sellmyer et al., "Assembly of uniaxially aligned rare-earth-free nanomagnets," Appl. Phys. Lett. **101**, 122407 (2012).

D.J. Sellmyer and B. Balamurugan, "Assembly of nano-objects for permanent-magnet materials," Magnetics Technology International 2012, UKIP Media & Events, p. 40-44.

B. Balamurugan, R. Skomski, B. Das, D.J. Sellmyer et al., “Magnetism of dilute Co(Pt) and Co(Hf) nanoclusters,” J. Appl. Phys. Lett. **111** 07B532 (2012)

B. Balamurugan, D.J. Sellmyer, G.C. Hadjipanayis, and R. Skomski, “Prospects for nanoparticle-based permanent magnets,” Scripta Materialia **67**, 542 (2012).

R. Skomski, A. Kashyap, and D.J. Sellmyer, “A Quantum-Mechanical Relaxation Model,” J. Appl. Phys. **111**, 07D507 (3 pages) (2012); doi: 10.1063/1.3679605.

R. Skomski, P.K. Sahota, B. Balamurugan, J.E. Shield, A. Kashyap, and D.J. Sellmyer, “Geometrical Aspects of Hard-Soft Exchange Coupling,” Proc. REPM’12, Nagasaki 2012, p. 155-158.

B. Das, B. Balamurugan, W. Y. Zhang, R. Skomski, E. S. Krage, S. R. Valloppilly, J. E. Shield, and D. J. Sellmyer, “Magnetism of Less Common Cobalt-Rich Alloys,” Proc. REPM’12, Nagasaki 2012, p. 427-430.

References

1. S. Constantinides (Arnold Magnetic Technologies), 2011, private communication.
2. W. Tang et al, “Anisotropic Hot-Deformed MRE-Fe-B Magnets With Zn Powder addition”, IEEE Trans. Magn. Vol. 48, 2012 (in press).
3. D. Sellmyer (University of Nebraska), private communication.
4. M. A. McGuire, N. J. Ghimire, and D. J. Singh, Oak Ridge National Laboratory Propulsion Materials 2011 Annual Report, page 11, http://www.ornl.gov/sci/propulsionmaterials/pdfs/Annual_Report_2011.pdf
5. T. Ishikawa and K. Ohmori, “Hard Magnetic Phase in Rapidly Quenched Zr-Co-B alloys”, IEEE Trans. Magn. 26 (5), 1370-1372 (1990).
6. S. Constantinides (Arnold Magnetic Technologies), 2011, private communication.
7. W. Tang et al, “Anisotropic Hot-Deformed MRE-Fe-B Magnets With Zn Powder addition”, IEEE Trans. Magn. Vol. 48, 2012 (in press).
8. D. Sellmyer (University of Nebraska), private communication.
9. M. A. McGuire, N. J. Ghimire, and D. J. Singh, Oak Ridge National Laboratory Propulsion Materials 2011 Annual Report, page 11, http://www.ornl.gov/sci/propulsionmaterials/pdfs/Annual_Report_2011.pdf
10. T. Ishikawa and K. Ohmori, “Hard Magnetic Phase in Rapidly Quenched Zr-Co-B alloys”, IEEE Trans. Magn. 26 (5), 1370-1372 (1990).
11. E. Burzo, R. Grossinger, P. Hundegger, et al., “Magnetic Properties of $ZrCo_{5.1-x}Fe_x$ Alloys”, J. Appl. Phys. 70 (10, Part I), 6550-6552 (1991).
12. A. M. Gabay, Y. Zhang, and G. C. Hadjipanayis, “Cobalt-Rich Magnetic Phases in Zr-Co Alloys”, J. Magn. Magn. Mater. 236 (1-2), 37-41 (2001).
13. K. H. J. Buschow, J. H. Wernick and G. Y. Chin, “Note on the Hf-Co Phase Diagram”, *J. Less-Common. Met.* **59**, 61(1978).
14. K. H. J. Buschow, “Differences in magnetic properties between amorphous and crystalline alloys”, *J. Appl. Phys.* **53**, 7713 (1982).
15. B. G. Demczyk and S. F. Cheng, “Structures of Zr_2Co_{11} and $HfCo_7$ intermetallic Compounds”, J. Appl. Cryst. 24, 1023-1026 (1991).
16. G. V. Ivanova, N.N. Shchegoleva, A.M. Gabay, “Crystal structure of Zr2Co11 hard magnetic compound”, J. Alloys Compd. 432, 135-141 (2007).
17. W.Y. Zhang, et al. “Coercivity Enhancement in Zr_2Co_{11}-Based Nanocrystalline Materials Due to Mo Addition”, IEEE Trans. Magn. 48, No. 11, (2012) (accepted).
18. S. Q. Wu, M. Ji, C. Z. Wang, M. C. Nguyen, K. Umemoto, R. M. Wentzcovitch, K. M. Ho,“Adaptive Genetic Algorithm Method for Crystal Structure Prediction*Phys. Rev. Lett.* submitted.

19. Manh Cuong Nguyen, Xin Zhao, Min Ji, Cai-Zhuang Wang, Bruce Harmon, and Kai-Ming Ho, J. *Appl. Phys*., **111**, 07E338 (2012).
20. Min Ji, K. Umemoto, C. Z. Wang, K. M. Ho and R. M. Wentzcovitch,, Phys. Rev. B (Rapid Communications) **84**, 220105(R) (2011).

Patents

1. R. W. McCallum, Y-W. Xu, I. E. Anderson, K. W. Dennis, and M. J. Kramer, U.S. Patent Application (PCT) filed November 18, 2002, “Permanent Magnet Alloy with Improved High Temperature Performance,” under examination.

Awards

Ames Lab proposal (Harmon, Ho, Wang) selected by the DOE (20 October 2012) to receive a 2013 Innovative and Novel Computational Impact on Theory and Experiment (INCITE) award.

Project 18518 – Materials for High Efficiency Engines

Agreement 8697 - NO_x Sensor Development

Leta Y. Woo and Robert S. Glass
Lawrence Livermore National Laboratory
P.O. Box 808, L-103
Livermore, CA 94551-9900
(925) 423-7140; fax: (925) (422-5844); e-mail: glass3@llnl.gov

DOE Technology Manager: Jerry L. Gibbs
(202) 586-1182; fax: (202) 586-1600; e-mail: jerry.gibbs@ee.doe.gov

---

Contractor: Lawrence Livermore National Laboratory, Livermore, California
Prime Contract No.: W-7405-Eng-48; LLNL-TR-510234

Objectives

- Develop an inexpensive, rapid-response, high-sensitivity and selective electrochemical sensor for oxides of nitrogen (NO_x) for compression-ignition, direct-injection (CIDI) OBD II systems
- Explore and characterize novel, effective sensing methodologies based on impedance measurements and designs and manufacturing methods that are compatible with mass fabrication
- Transfer the technology to industry for commercialization

Approach

- Use an ionic (O^{2-}) conducting ceramic as a solid electrolyte and metal or metal-oxide electrodes
- Correlate NO_x concentration with changes in cell impedance
- Evaluate sensing mechanisms and aging effects on long-term performance using electrochemical techniques
- Collaborate with Ford Research Center and EmiSense Technologies, LLC to optimize sensor performance and perform dynamometer and on-vehicle testing

Accomplishments

- Developed a Cooperative Research and Development Agreement (CRADA) with EmiSense Technologies, LLC, a Salt Lake City, UT company which has licensed the LLNL NO_x sensor technology
- Completed advanced engine dynamometer testing at Ford Motor Company of FY12 prototypes demonstrating robust performance under aggressive driving conditions
- Publications/Presentations:
    - W. L. Du Frane, L.Y. Woo, R.S. Glass, R.F. Novak, and J.H. Visser, “Substrate Effects on Electrochemical NO_x Sensor Based on Porous Y_2O_3-Stabilized ZrO_2 (YSZ) and Sr-doped $LaMnO_3$ (LSM), presented at the 221st Meeting of the Electrochemical Society, Seattle, Washington, May 6-10, 2012.
    - W. L. Du Frane, L.Y. Woo, R.S. Glass, R.F. Novak, and J.H. Visser, “Substrate Effects on Electrochemical NO_x Sensor Based on Porous Y_2O_3-Stabilized ZrO_2 (YSZ) and Sr-doped $LaMnO_3$ (LSM). *ECS Transactions*, submitted 2012.
    - L.Y. Woo and R. S. Glass, “NO_x Sensor Development,” project ID #PM005, Annual Merit Review and Peer Evaluation. Washington, D.C., May 15, 2012

Future Directions

- Finish the development of more advanced prototypes suitable for cost-effective, mass manufacturing and for optimizing performance, including long-term stability and cross-sensitivity, in laboratory, dynamometer, and on-vehicle tests
- Working through the CRADA with EmiSense Technologies, LLC, and in collaboration with Ford Motor Company, bring the NO_x sensor technology to commercialization

---

Introduction

NO_x compounds, specifically NO and NO_2, are pollutants and potent greenhouse gases. Compact and inexpensive NO_x sensors are necessary in the next generation of diesel (CIDI) automobiles to meet government emission requirements and enable the more rapid introduction of more efficient, higher fuel economy CIDI vehicles.[1-3]

Because the need for a NO_x sensor is recent and the performance requirements are extremely challenging, most are still in the development phase.[4-6] Currently, there is only one type of NO_x sensor that is sold commercially, and it seems unlikely to be able to meet more stringent future emission requirements.

Automotive exhaust sensor development has focused on solid-state electrochemical technology, which has proven to be robust for in-situ operation in harsh, high-temperature environments (e.g., the oxygen stoichiometric sensor). Solid-state sensors typically rely on yttria-stabilized zirconia (YSZ) as the oxygen-ion conducting electrolyte, which has been extensively explored, and then target different types of metal or metal-oxide electrodes to optimize the response.[2-6]

Electrochemical sensors can be operated in different modes, including amperometric (current based) and potentiometric (potential based), both of which are direct current (dc) measurements. Amperometric operation is costly due to the electronics necessary to measure the small sensor signal (nanoampere current at ppm NO_x levels), and cannot be easily improved to meet the future technical performance requirements. Potentiometric operation has not demonstrated enough promise in meeting long-term stability requirements, where the voltage signal drift is thought to be due to aging effects associated with electrically driven changes, both morphological and compositional, in the sensor.[7]

Our approach involves impedancemetric operation, which uses alternating current (ac) measurements at a specified frequency. The approach is described in detail in previous reports and several publications.[8-12] Impedancemetric operation has shown the potential to overcome the drawbacks of other approaches, including higher sensitivity towards NO_x, better long-term stability, potential for subtracting out background interferences, total NO_x measurement, and lower cost materials and operation.[8-11]

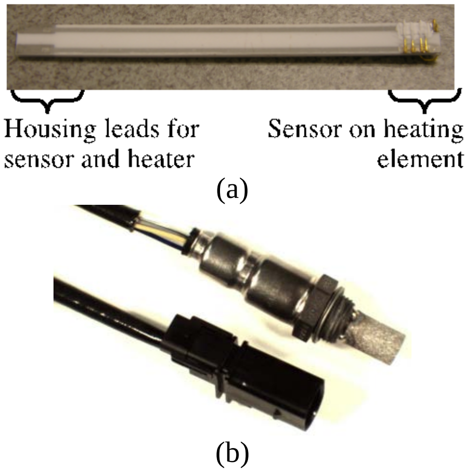

Figure 1. Picture of (a) alumina substrate with imbedded heater, provided by Ford Motor Company, suitable for packaging into (b) protective sensor housing.

Past LLNL research and development efforts have focused on characterizing different sensor materials and understanding complex sensing mechanisms.[8-12] Continued effort has led to improved prototypes with better performance, including increased sensitivity (to less than 5 ppm) and long-term stability, with more appropriate designs for mass fabrication, including incorporation of an alumina substrate with an imbedded heater and a protective sensor housing (see Fig. 1). Using multiple frequency measurements, an algorithm has been developed to subtract out that portion of the response due to interfering species.

Efforts in FY 2012 have continued building on previous work to modify prototypes to improve performance, including drift and sample-to-sample reproducibility. Other progress this year includes dynamometer testing using advanced emission test protocols to confirm robustness and durability in FY12 prototypes. As noted above, the LLNL NO_x sensor technology has been licensed to EmiSense Technologies, located in Salt Lake City, and another accomplishment this past year was the development of a CRADA for joint development activities. This will greatly accelerate the commercialization efforts for this technology.

Background

For a two-electrode electrochemical cell, impedancemetric sensing requires that at least one of the electrodes act as the "sensing" electrode with selective response to NO_x over other gas phase components. This contrasts to the case in potentiometric sensing, which relies on differential measurements between the two electrodes. The impedancemetric sensor design is quite flexible and can either contain one sensing electrode and one counter (i.e., non-sensing) electrode, or two sensing electrodes. It opens up the opportunity to use a wide variety of materials, both metal and metal oxides.

Both electrode composition and microstructure influence sensitivity, which relies on limiting the oxygen reaction on the electrode so that the NO_x reaction can be resolved.[9-11] In general, for the "sensing" electrode a dense microstructure is required with appropriate composition to limit the catalytic activity towards oxygen.[10-11]

Measured sensor impedance is a complex quantity with both magnitude and phase angle information. The phase angle has been found to provide a more stable response at higher operating frequencies and we prefer it for the sensor signal.[8-12]

In previous work, impedancemetric sensing using either gold or strontium-doped lanthanum manganite (LSM) electrodes, the latter being an electronically conducting metal oxide, was investigated in laboratory and engine testing. Preliminary results indicated that gold electrodes have good stability and the potential for low water cross-sensitivity, but also have a higher thermal expansion coefficient and lower melting temperature than the YSZ electrolyte, which limit processing flexibility. LSM electrodes have high melting temperatures and better thermal expansion match with YSZ, but have shown higher water cross-sensitivity than gold.

Experimental

Two different sensing materials, Au and LSM, were investigated. Figure 2a shows a schematic of a prototype using Au wire as the sensing electrode and alumina with an imbedded Pt resistive heater as the substrate (70 mm × 4 mm × 1 mm, see Fig. 1a). The substrate has a total of four leads, two leads for the Pt resistive heater located on one side, and two leads for the sensor located on the opposite side.

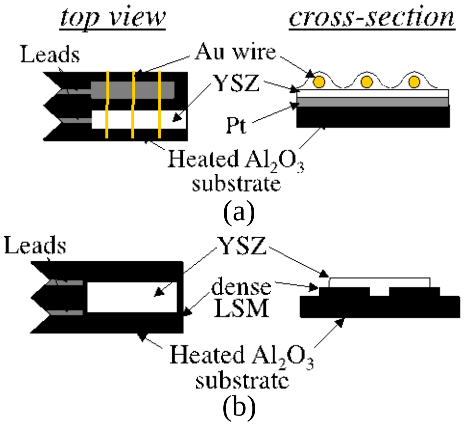

Figure 2. Schematic of NO_x prototype sensors using either (a) Au wire or (b) dense LSM as the sensing electrode.

One of the substrate leads contacted the Pt counter electrode. Yttria-stabilized zirconia (YSZ, 8 mol % yttria doping) slurry was then applied on top of the Pt. Au wires were then added and additional YSZ slurry was applied on top of the wires with the entire assembly fired at 1000°C to produce the porous YSZ electrolyte. The second substrate lead for the sensor housing contacted the Au wire.

Figure 2b shows a schematic of the prototype using LSM as the sensing electrode. A dense pellet was prepared with commercial $(La_{0.85}Sr_{0.15})_{0.98}Mn$ oxide powder (Praxair) by pressing in a uniaxial die and sintering at 1250°C. Two pieces of LSM (6 mm × 2 mm × 1 mm) were machined and attached to the top of the substrate using Pt paste and fired to 1200°C. YSZ slurry was applied on top of the dense LSM pieces and the assembly fired at 1000°C.

A laboratory study of both the Au wire and LSM prototypes was also performed using 0.5 mm thick alumina substrates without imbedded heaters to evaluate aging and reproducibility. The alternative substrate was more suitable for longer-term continuous controlled temperature testing in a laboratory tube furnace. The sensor geometries were similar to that shown in Fig. 2.

LSM prototypes were found to have more variability in aging and reproducibility, so a subset of laboratory experiments focused on evaluating only LSM prototypes using modified substrate compositions. The modified substrate compositions were used to investigate the role of thermal expansion mismatch between the sensor components and the underlying substrate. Modified substrate compositions included YSZ substrates with thermal expansion behavior to match the prototype sensor YSZ electrolyte. YSZ substrates coated with a thin alumina layer were also used to identify the role of electrical insulation between sensor components and the underlying substrate while still maintaining better thermal expansion match.

YSZ substrates were prepared with commercial powders pressed into dense pellets using a uniaxial die before firing at 1500°C. Alumina-coated YSZ substrates were prepared with a thin alumina layer applied using a slurry painted onto the unfired dense pellet before co-firing at 1500°C.

Laboratory experiments were performed in a quartz tube (21.4 mm I.D.) placed inside a tube furnace with both electrodes exposed to the same environment. The gas composition was controlled by mixing air, N_2, and a 1000 ppm NO/NO_2 feed using a standard gas handling system equipped with thermal mass flow controllers. The total gas flow rate was fixed at 1000 ml/min. Measurements were made at 650°C.

For the subset of experiments focused on evaluating LSM prototypes using modified substrate compositions, prior to testing, sensors were 'burned-in' for a period of 68 ± 5 hours at 650°C in 10.5% O_2. During this time, impedance and phase angle were measured using a constant frequency 5 Hz, 100 mV signal. Testing began immediately following this burn-in procedure. To test sensors, impedance measurements were performed at 550, 600, and 650°C in 10.5% O_2 with varying levels of added NO. Impedance phase angle (θ_{5Hz}) was used to measure sensor response to step changes in NO content. The step changes followed the protocol 0, 100, 80, 60, 50, 40, 30, 20, 15, 10, 5, and back to 0 ppm with 2 minutes between the steps. For analysis of the sensor response to different NO concentrations, signals were averaged over one minute of data collection, approximately 30 seconds prior to and 30 seconds after each step change.

Dynamometer engine testing of real diesel exhaust was performed at Ford Research Center using an engine test cell fitted with engine gas recirculation (EGR) and a urea-based selective catalytic reduction (SCR) system for reducing NO_x emissions. The exhaust gas composition was evaluated with a chemiluminescent NO_x analyzer and a paramagnetic oxygen analyzer. Prototype sensors were packaged with a housing (see Fig. 1b) and directly mounted into the exhaust tailpipe manifold alongside a commercially available NO_x sensor.

For laboratory testing, impedance measurements were performed using a Solartron 1260 Impedance Analyzer in combination with a Solartron 1287 Electrochemical Interface. Dynamometer engine testing at Ford used a stand-alone Solartron 1260 Impedance Analyzer. Computer-controlled data acquisition used the commercially available ZPlot software (Scribner Associates, Inc.).

Results and Discussion

Laboratory testing: Longer-term aging studies of Au and LSM

A laboratory study of both the Au wire and LSM prototypes was performed using 0.5 mm thick alumina substrates without imbedded heaters to evaluate aging and reproducibility. Previous testing had indicated stable response for older generation prototypes (prior to FY 2012) using either Au or LSM at aging times of up to 500 hrs. Continued testing of more recent FY12 prototypes with newer YSZ slurry formulations confirmed the stability of Au-based prototype sensors, but indicated some variation among samples in LSM performance, including some with signal drift.

Figures 3 and 4 show results for the two prototype sensors (Au and LSM) tested side-by-side for measurements at 5 Hz and 100 mV excitation, where the left y-axis corresponds to the phase angle signal of the Au prototype sensor while the right y-axis corresponds to the LSM prototype sensor signal. In Fig. 3, the dynamic prototype sensor response is shown in 10.5% O_2 when 100 ppm of NO is introduced, with time on the x-axis in minutes. The Au prototype sensor showed identical dynamic response when testing at 24 h, at ~500 h, and again at nearly 1000 h. The LSM prototype sensor, however, showed baseline drift at those same aging times, although maintaining overall sensitivity to 100 ppm NO.

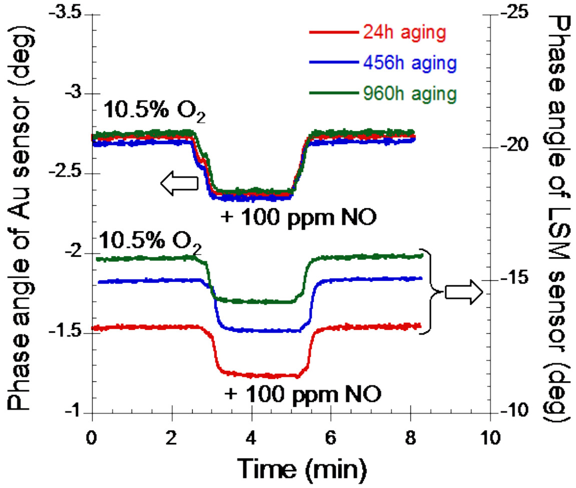

Figure 3. Phase angle response of Au prototype (left y-axis) and LSM prototype (right y-axis) in 10.5% O_2 with 2 min addition of 100 ppm NO at different aging times.

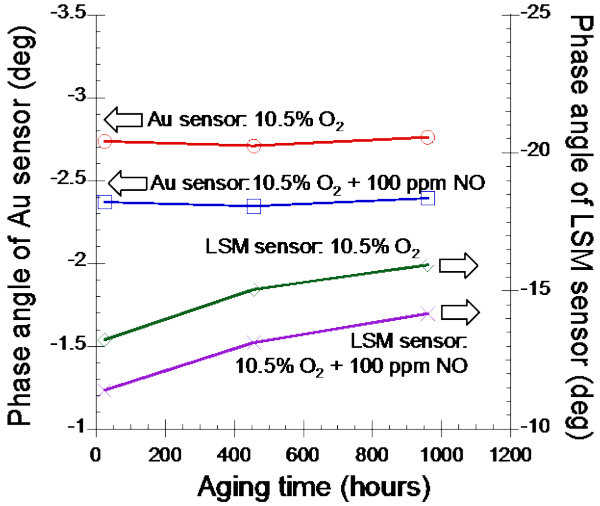

Figure 4. Plot of phase angle response of Au prototype (left y-axis) and LSM prototype (right y-axis) vs. aging time that corresponds to data in Fig. 3 for 10.5% O_2 with and without addition of 100 ppm NO.

In Fig. 4, the prototype sensor signal (i.e., phase angle) is shown for different aging times for Au (left y-axis) and LSM (right y-axis), with aging time in hours on the x-axis. The poor sample-to-sample reproducibility of LSM prototype sensors and variability in performance was attributed to the formation and growth of random microcracks due to thermal expansion mismatch between the sensor components (YSZ and LSM) and the substrate (alumina). The microcracks were observed on some sensors after processing at 1000°C. Figure 5 shows a micrograph of a typical microcrack that was visible within the lower strength porous YSZ electrolyte after processing. Cracks up to ~30 µm thick have been observed, while some sensors showed no visible cracking. However, alumina is an ideal substrate material because of its high electrical resistivity, inertness, and proven compatibility with embedded heaters. In addition, while microcracking was sporadically observed in the sensors evaluated here, it is believed that this issue will be resolved with design modification and improved mass manufacturing processes.

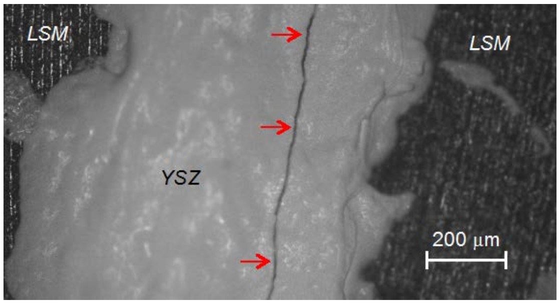

Figure 5. Example of visible micro-cracking occurring on the top surface of the porous YSZ electrolyte.

Laboratory testing: Modifying substrate composition to improve LSM prototypes

To provide guidance in mitigating microcracking in the LSM prototype sensors, a subset of laboratory experiments examined the effect of different substrate compositions with different thermal expansions. Table 1 shows the thermal mismatch between the materials used in the LSM prototype sensor discussed above (see Fig. 2b).

Table 1. Coefficients of thermal expansion for materials used in LSM prototype sensors.

Material	Coefficient of thermal expansion (10^{-6}/°C)
Al_2O_3	8
YSZ	10.5
LSM	10

Dense YSZ substrates were used because they have identical thermal expansion match to the porous YSZ electrolyte. YSZ substrates with thin Al_2O_3 coating layers were also fabricated to increase electrical resistance of substrates without significantly altering their thermal expansion mismatch with the porous YSZ electrolyte. For sensors using both of these substrate types, there was no visible microcracking in the top surfaces of the YSZ electrolyte layers. It has not yet been confirmed that cracks do not exist subsurface of the YSZ electrolyte, although this is not thought to be likely.

The effects of microcracking on impedancemetric sensor performance were evaluated using the phase angle response at 5 Hz, labeled as θ_{5Hz}. Higher θ_{5Hz} magnitude is generally desirable to improve signal resolution. The baseline (0 ppm NO_x) θ_{5Hz} magnitude signal was determined by averaging steady-state data points taken every 20 seconds for two hours during the burn-in procedure between 60 and 62 hrs. Figure 6 shows results comparing the baseline values for the three different substrates, as well as sensor-to-sensor reproducibility.

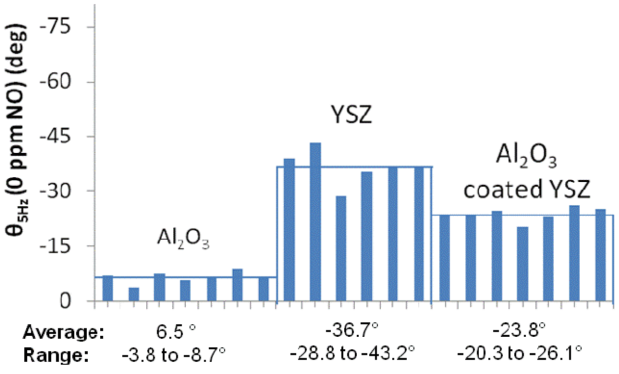

Figure 6. Baseline (0 ppm NO) values for 5 Hz phase angles at 650°C in a 10.5% O_2 for replicate sensors built on Al_2O_3, YSZ, or Al_2O_3 coated YSZ substrates; average of each substrate group is also shown.

Baseline values were consistently highest for sensors on YSZ substrates, followed by sensors on Al_2O_3 coated YSZ substrates, and then sensors on Al_2O_3 substrates. Al_2O_3 coated YSZ substrates gave the best sensor-to-sensor reproducibility of baseline values. Sensor response to varying concentrations of NO is shown in Figure 7. All sensors in this study had rapid responses, with response times (10-90%) of approximately 5 seconds.

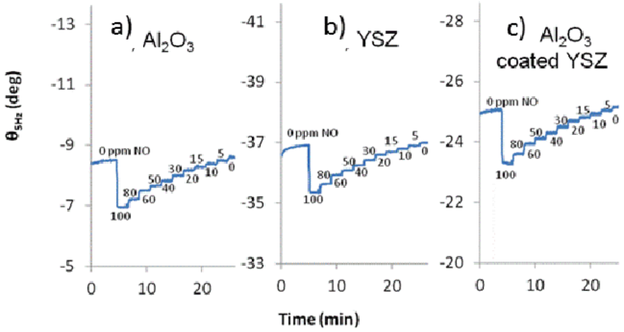

Figure 7. Sensor response as measured using the phase angle at 5 Hz phase (θ_{5Hz}) for sensors built on (a) Al_2O_3, (b) YSZ, and (c) Al_2O_3 coated YSZ at 650°C in a 10.5% O_2.

Irrespective of substrate, all sensors showed high sensitivity to NO. In addition, a linear dependence on NO concentration in the range of 0-20 ppm was observed for sensors built on all three substrates, as shown in Figure 8. Sensitivity declined at higher NO concentrations, which is in line with our previous results.[11]

Linear fits to the data in the 0-20 ppm NO range determined that the sensitivity to NO_x was relatively independent of substrate and temperature at the three temperatures employed (550, 600, and 650°C). The average NO sensitivity for the six replicate sensors was 0.019, 0.017, and 0.016 deg/ppm for sensors on YSZ, Al_2O_3 coated YSZ, Al_2O_3 substrates, respectively. This indicates that microcracking, apparent on the Al_2O_3 substrates in particular, had minimal influence on sensitivity to NO. If microcracking should cease after a given time period, the sensors may remain functional. However, degradation in sensor performance, and ultimate failure would be anticipated if the cracking continued to longer time scales.

Future designs using Al_2O_3 substrates will need to address the thermal mismatch between Al_2O_3 and YSZ to avoid microcracking in the YSZ electrolyte. One approach could be to use alternative designs with the electrode-electrolyte interfaces in the same plane as the substrate. Another approach could be to reduce the occurrence rate of microcracking by altering the high temperature processing procedure. Such alterations may include reducing the heating/cooling rates, dwelling at intermediate temperatures, or reducing the final processing temperature.

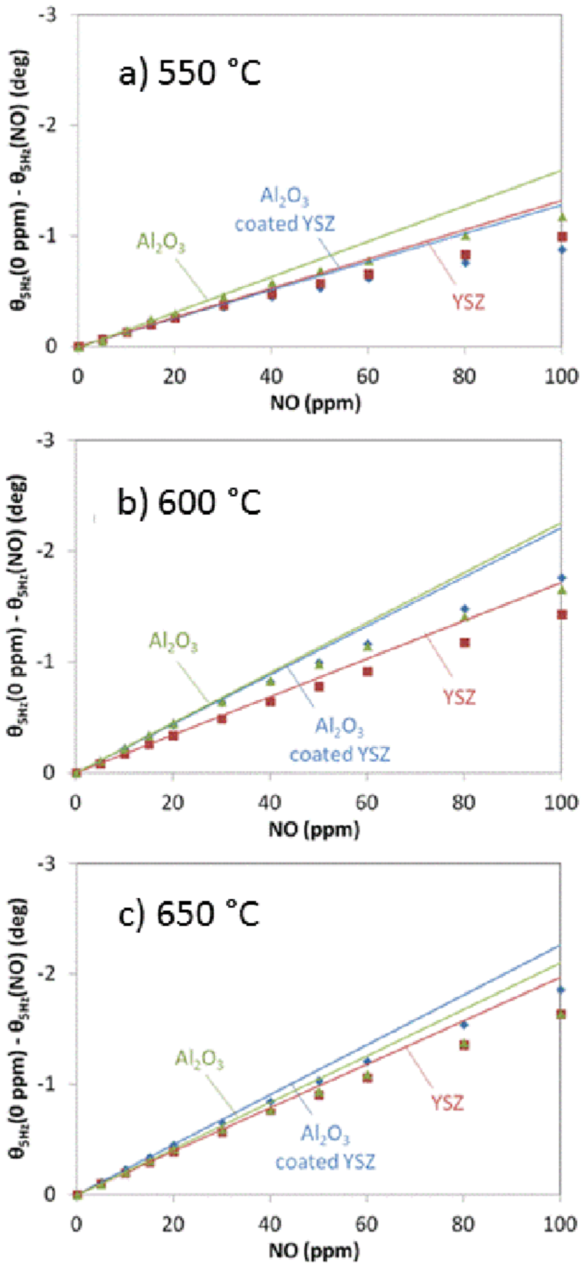

Figure 8. Average sensor response as measured by θ_{5Hz} for sensors built on Al_2O_3 (green triangles), YSZ (red squares), or Al_2O_3 coated YSZ (blue diamonds) substrates at (a) 550, (b) 600, and (c) 650°C. Linear fits to data for 0-20 ppm NO are also shown.

Dynamometer engine testing of FY 2012 prototypes

Dynamic dynamometer engine testing of FY12 prototypes was conducted at Ford Research Center. Prototype sensors were packaged by a U.S. supplier into appropriate housings (see Fig. 1b) and then placed directly in the exhaust manifold at the tailpipe for exposure to real-world diesel exhaust. Figure 9 shows dynamic data from a portion of EPA US06 or Supplemental Federal Test Procedure (SFTP), which is a high acceleration aggressive dynamometer driving schedule; time, in seconds, is on the x-axis.

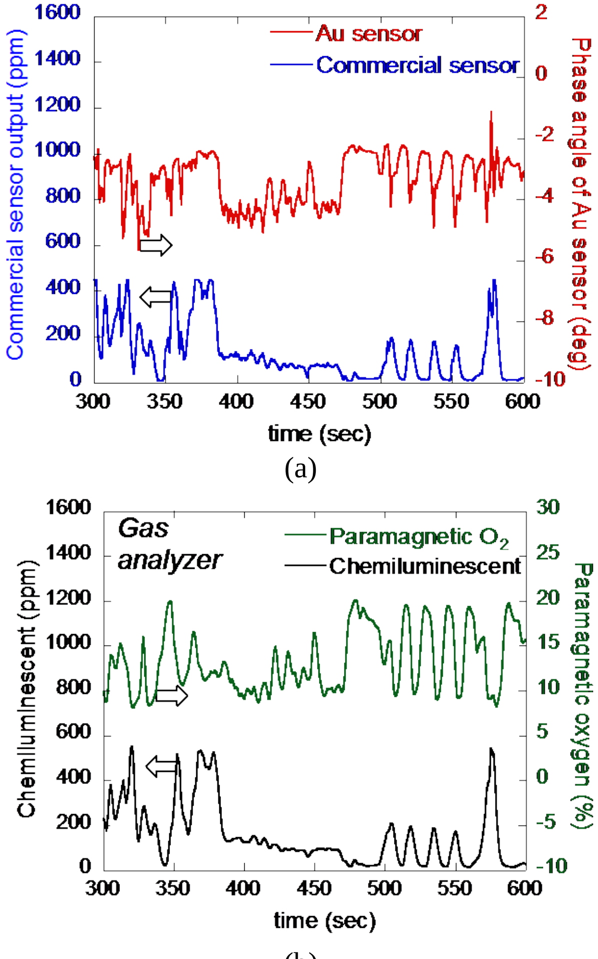

(a)

(b)

Figure 9. Dynamometer test: (a) Phase angle response of Au prototype sensor (red, right y-axis) compared with a commercial NO_x sensor (blue, left y-axis) and (b) data from paramagnetic oxygen analyzer (green, right y-axis) and chemiluminescent NO_x analyzer (black, left y-axis).

In Fig. 9a, the left y-axis corresponds to the commercial sensor output (blue curve) and the right y-axis corresponds to the raw phase angle output from the Au prototype sensor (red curve), showing reasonable agreement. In Fig. 9b, data taken simultaneously using bench analyzers are shown, where the left y-axis corresponds to the chemiluminescent analyzer (black curve) and the right y-axis corresponds to the paramagnetic oxygen analyzer (green curve). As expected, the oxygen response from about 425 to 450 sec. is seen in both the Au prototype sensor (Fig. 9a, red curve, right y-axis) and in the paramagnetic oxygen analyzer (Fig. 9b, green curve, right y-axis).

Commercial sensors include data processing and electronics whereas the measurement with the Au prototype sensor only included the raw phase angle signal without any additional processing. During actual advanced operation of the prototype sensor, additional signal processing will be necessary to remove oxygen interference. Previously, we have demonstrated algorithms suitable for compensating for interferences.[12] Future work includes working with our CRADA partners (EmiSense) to design appropriate electronics and refine strategies for reducing interferences when the NO_x sensors are used in OBD II systems.

Additional FY 2012 testing at Ford Research Center included evaluation on an advanced high-flow (40 Liters/min) test stand with controlled mass flow controllers to alter a range of gas concentrations (O_2, CO_2, H_2O, and NO_x). The test stand also included output from a commercial sensor located near the prototype sensor under evaluation. These data are now being used to further refine strategies for reducing interferences.

Other research highlights in FY 2012

To further understand impedancemetric sensing mechanisms and to guide improvement of materials and geometries for mass manufacturing and commercialization, alternative configurations of the LSM prototype sensor were investigated. An asymmetric (LSM/YSZ/Pt) through-plane geometry, shown in Fig. 10, was evaluated that differs from the previously discussed symmetric (LSM/YSZ/LSM) in-plane configuration (see Fig. 2b). As previously discussed, the electrode-electrolyte interfaces in the same plane as the substrate could reduce microcracking.

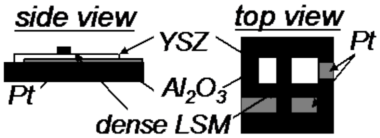

Figure 10. Schematic of alternative asymmetric NO_x prototype sensor using dense LSM as the sensing electrode.

Preliminary results indicated that the alternative through-plane geometry seemed to inhibit crack growth within the YSZ electrolyte leading to more reproducible behavior. Also, the through-plane geometry with a thin YSZ electrolyte layer (~100-250 μm) should lead to improved ionic conductivity and reduced bulk ionic resistance, which may also improve performance. The alternative asymmetric LSM prototype sensor geometry also provides a platform for elucidating the contributions from the Pt and LSM electrodes as well as the YSZ electrolyte resistance to the overall sensing performance. Electrochemical evaluation and sensor performance testing is ongoing and continues into FY 2013. A more complete analysis of data obtained using the three different sensor prototypes will be provided in an upcoming publication.

Conclusions

Work in FY 2012 continued to build on previous efforts to modify prototypes to improve performance. Although previous aging studies indicated good long-term performance of both Au and LSM prototype sensors, more recent laboratory testing indicated variability (sample-to-sample reproducibility) in drift behavior for the LSM prototype sensors. Altering substrate composition to reduce thermally induced strain and the subsequent formation of microcracks improved sensor performance, and would be a viable option for resolving the issue during mass manufacturing.

Engine dynamometer testing of FY12 prototype sensors at Ford Research Center confirmed robustness and durability seen in previous testing. The prototype sensor showed reasonable agreement with a commercially available sensor. Additional electronics and strategies are being developed with our CRADA partners to reduce interferences.

Other progress in FY 2012 included alternative geometries for the LSM prototype sensor to improve performance. An asymmetric through-plane geometry was investigated with preliminary results indicating improved sample-to-sample reproducibility. The alternative geometry also serves as a platform for elucidating the contributions from the Pt and LSM electrodes as well as the YSZ electrolyte resistance to the overall sensing performance. Electrochemical evaluation and sensor performance testing is ongoing and continues into FY 2013.

A major milestone for this past year was the development of a CRADA with EmiSense Technologies, who have licensed the LLNL NO_x sensor technology. EmiSense has extensive experience and resources for the development of emission control sensors, and the partnership with EmiSense will accelerate efforts to bring the LLNL NO_x sensor technology to commercialization. We continue our long-standing collaboration with Ford Motor Company in this effort.

References

1. N. Yamazoe, *Sens. Actuators, B*, **108**, 2 (2005).
2. R. Moos, *Int. J. Appl. Ceram. Technol.*, **2**, 401 (2005).
3. S. Akbar, P. Dutta, and C. Lee, *Int. J. Appl. Ceram. Technol.*, **3**, 302 (2006).
4. F. Menil, V. Coillard, and C. Lucat, *Sensors and Actuators B*, **67**, 1 (2000).
5. S. Zhuiykov and N. Miura, *Sens. Actuators, B*, **121**, 639 (2007).
6. J. W. Fergus, *Sens. Actuators, B*, **121**, 652 (2007).
7. S. -W. Song, L. P. Martin, R. S. Glass, E. P. Murray, J. H. Visser, R. E. Soltis, R. F. Novak, and D. J. Kubinski, *J. Electrochem. Soc.*, **153**, H171 (2006).
8. L. P. Martin, L. Y. Woo, and R. S. Glass, *J. Electrochem. Soc.*, **154**, J97 (2007).
9. L. Y. Woo, L. P. Martin, R. S. Glass, and R. J. Gorte *J. Electrochem. Soc.*, **154**, J129 (2007).
10. L. Y. Woo, L. P. Martin, R. S. Glass, W. Wang, S. Jung, R. J. Gorte, E. P. Murray, R. F. Novak, and J. H. Visser. *J. Electrochem. Soc.*, **155**, J32 (2008).
11. L.Y. Woo, R.S. Glass, R.F. Novak, and J.H. Visser. *J. Electrochem. Soc.*, **157**, J81 (2010).
12. L.Y. Woo, R.S. Glass, R.F. Novak, and J.H. Visser. *Sensor Actuat. B-Chem.*, **157**, 115 (2011).

Publications/Presentations

W. L. Du Frane, L.Y. Woo, R.S. Glass, R.F. Novak, and J.H. Visser, "Substrate Effects on Electrochemical NO_x Sensor Based on Porous Y_2O_3-Stabilized ZrO_2 (YSZ) and Sr-doped $LaMnO_3$ (LSM)," presented at the 221st Meeting of the Electrochemical Society, in Seattle, Washington May 6-10, 2012.

W. L. Du Frane, L.Y. Woo, R.S. Glass, R.F. Novak, and J.H. Visser, "Substrate Effects on Electrochemical NO_x Sensor Based on Porous Y_2O_3-Stabilized ZrO_2 (YSZ) and Sr-doped $LaMnO_3$ (LSM)," *ECS Transactions*, submitted 2012.

L.Y. Woo and R. S. Glass, "NO_x Sensor Development," project ID #PM005, Annual Merit Review and Peer Evaluation. Washington, D.C., May 15, 2012.

Agreement 11752 – Materials for HCCI Engines

G. (Murali) Muralidharan
Oak Ridge National Laboratory
(865)574-4281: fax: (865) 574-4357; e-mail: muralidhargn@ornl.gov

DOE Technology Manager: Jerry L. Gibbs
(202) 586-1182; fax: (202) 586-1600; e-mail: jerry.gibbs@ee.doe.gov
ORNL Technical Advisor: J. Allen Haynes
(865) 576-2894; fax: (865) 574-4913; e-mail: haynesa@ornl.gov

---

Contractor: Oak Ridge National Laboratory, Oak Ridge, Tennessee
Prime Contract No.: DE-AC05-00OR22725

Objectives

- Identify and catalog the materials operating conditions in homogeneous charge compression-ignition (HCCI) engines and use computational design concepts to develop advanced materials for such applications.
- Interact with designers of HCCI engines and manufacturers of components in order to identify the components that will be affected by the harsh operating conditions resulting from the HCCI design.

Approach

- Identify engine components, currently used materials, and current operating conditions and compare them with the expected component operating conditions for HCCI engines.
- Demonstrate the feasibility of the "materials-by-design" approach for the highest-priority item. Improve material performance for HCCI applications through computational modeling and experimental validation.

Accomplishments

- Valves were previously identified as the priority components for development of new alloys with lower Ni contents (enabling lower cost) and improved high temperature properties.
- A series new Ni-containing alloys with the potential to exceed 100 million cycles at a stress greater than 25ksi at 870^{o}C have been designed and have been identified based upon small heats and high temperature in-situ tensile tests.
- After several initially unsuccessful initial attempts at rolling heats of various candidate new alloys, plates of these materials have been successfully rolled and fatigue specimens are currently being machined.

Future Direction

- Fatigue tests on new lower-Ni valve alloys will be completed at stresses of 25-35ksi at 870^{o}C and target properties will be compared with properties achieved.
- Continue to communicate with automotive companies, valve manufacturers, and other teams on the progress made through computational design.

Introduction

There has been an increasing interest in HCCI combustion in recent years because of its potential to increase engine combustion efficiency and reduce emissions. However, the use of HCCI combustion will subject the engine components to significantly higher temperatures and pressures. The temperatures for diesel engines will reach over 1600°F (870^{o}C), and pressure may reach > 2000 psi (138 bar), which is approximately four times that of the normal combustion engine. Such severe engine operating conditions will require a significant improvement in materials performance in order to take advantage of the HCCI engine concept. This project address the identification of materials requirements for HCCI engines for automotive and truck applications and the development of advanced, yet cost-effective, materials through computational design.

"Materials-by-design" is an Oak Ridge National Laboratory (ORNL) concept that encompasses a collection of materials-related techniques including modeling, correlation, and materials modification. The premise behind materials-by-design is that mechanical properties are correlated to microstructure and phase chemistry. The phase composition and microstructure can be achieved through thermodynamic equilibrium or through non-equilibrium techniques such as quenching, rapid casting solidification, or mechanical working. These characteristics can then be correlated to desired mechanical properties through equilibrium thermodynamics or through a variety of correlation techniques. The correlations allow untested compositions or treatments to be modeled so that desired trends can be rapidly established. Small heats of targeted materials can then be processed to confirm the modeled properties and to broaden the correlation data base.

Finally, there are several techniques, such as magnetic processing or low-temperature carburizing, that can be applied to allow further modification and optimization of desired properties. Materials-by-design is ideally suited to cast materials and heavily thermally processed materials (e.g., stainless steels, Ni alloys, cast irons, alloy steels, and brazed wrought aluminum alloys), and the concept has been successfully applied in such diverse areas as high-temperature furnace components, exhaust valves, exhaust manifolds, and tube fittings. Figure 1 and Table 1 provide an outline of the materials-by-design approach and a summary of the techniques that can be applied.

In our approach, we examined critical heavy-duty diesel engine materials and identified means to reduce their cost for acceptance in HCCI applications. This is being accomplished through the following tasks:

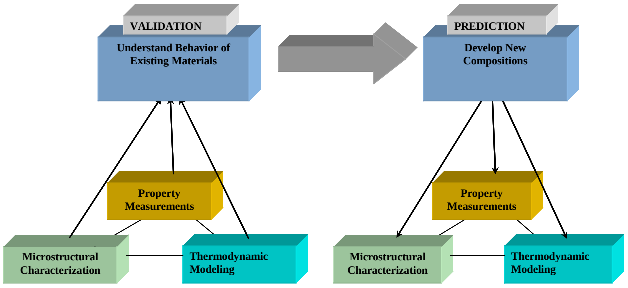

Figure 1. *Overall approach for materials-by-design.*

Task 1. Identify critical material requirements for HCCI engines based on their operating conditions. This task was accomplished through interactions with advanced engine and component designers. The interactions included personal visits to six companies: Caterpillar, Cummins Engine, Deer, International Truck, Eaton Corp., and General Motors. Visits were supplemented by a literature search, a review of advanced engine design studies, and follow-up discussions afterward. The key outcomes from this task included: (1) identification of operating conditions for advanced engine concepts, with a focus on the HCCI concept; (2) identification of components most affected by these operating conditions; (3) identification of currently used materials, new requirements, and performance targets; and (4) ranking of the highest-priority items for study by the materials by design approach.

Task 2. Demonstrate the feasibility of materials-by-design approach for the highest-priority item. In this task, the details of the currently used material in the highest-priority component was identified. Specifically, material compositions, processing methods, mechanical properties, corrosion properties, and cost were examined.

Based on the available mechanical properties data, microstructural analysis, and thermodynamic phase stability calculations, the underlying mechanism that delivers the current properties was identified.

Table 1. ORNL materials-by-design toolbox

Modeling	Experimentation	Characterization
Thermodynamic modeling of material properties vs alloy composition	Ultra-high-gauss magnetic stabilization of alloy steels	Advanced microscopy techniques
Neural-network modeling of diverse, nonlinear materials properties and process variations	Low-temperature gas carburization of finished components	X- ray and neutron scattering
Detailed microstructure based empirical modeling	Ability to produce small quantities of materials and fabricate them into test bars for property measurements and production of prototype components by a variety of methods, including sand and die casting, extrusion, forging and rolling	Surface and bulk property measuring techniques
Non-equilibrium modeling of solidified structures		
Extrapolation of properties from simple alloy systems to complex systems using interaction parameters		

Task 3. Improve materials performance for HCCI application through computational modeling and experimental validation. In this task, computational modeling (key basis for the material-by-design concept) was used to identify compositions that will deliver the desired phases for two purposes: (1) improving property performance and (2) finding alternatives to reduce cost for both current and improved performance. The outcome of the analysis was e validated through experimentation. The validation was carried out in the following steps:

1. Prepare compositions identified based on computational design in 1-lb heats for microstructural analysis and very limited property determination; compare the results with output based on computational analysis for validation.
2. Scale up the validated composition into 20-lb to 100-lb heats and cast them into ingots for processing trials.
3. Subject cast ingots to processing steps that are currently used by industry. Develop optimum processing and heat-treatment conditions to obtain the desired microstructure.
4. Carry out microstructural analysis and mechanical properties analysis on the material processed and heat-treated with optimum conditions.
5. Prepare prototype components for HCCI engine tests.

Interaction with industrial partners, primarily in the form of telephone conversations and site visits occurred during all three tasks as outlined earlier. In particular, telephone conversations have occurred this year with Eaton corporation in potential transfer of the valve materials to industrial practice. This collaboration is expected to result in the rapid transfer of materials improvement from this project to industry for use in HCCI and other advanced engine concepts.

Results

Materials Development through Computational Design

The first component that was identified as critical was exhaust valves. Ni-based alloys have been identified as potential candidates for improved valve materials. There is particular interest in increasing the operating temperature of exhaust valves to ~1600°F (870°C) from 1400°F (760°C). High temperature fatigue strength has been identified as a critical factor in determining the performance of these alloys in the valve application. An understanding of the strengthening mechanisms in existing materials was required to use the computational modeling approach to developing materials with improved properties and lower cost.

An evaluation of the microstructure of various Ni-based alloys and correlation with limited information on the fatigue properties that are available show that the volume fraction of the γ' phase is likely to be a dominant factor in determining the performance of these alloys at high temperatures. Since the size of the strengthening precipitates is also critical, it is anticipated that the kinetics of coarsening this phase would also be influential in the long-term performance of the alloys in this application. Based upon discussions with various users and suppliers, a range of Ni-based alloys with potentially varying weight fractions (or volume fractions) of γ' have been identified in efforts to correlate the fatigue properties with the microstructure of the alloys. The selection of nine commercial Ni-based alloys included Alloy 751, Waspaloy, Udimet 520, and Udimet 720 with Ni+Co contents ranging from 66 wt.% to 76 wt. %. To obtain initial information on the microstructures of these alloys at equilibrium, thermodynamic calculations have been carried out using JMatPro V4.1. Comparison of the results of the calculations showed that all alloys have a matrix of γ with the major strengthening phase as γ'. One or more carbide phases such as $M_{23}C_6$, MC, and M_7C_3 may also be present in different alloys. The primary difference between the microstructures of the various alloys is in the weight percent of the γ' phase at a given temperature and the highest temperature at which the γ' phase is stable in the different alloys.

Development of Improved Alloys through Computational Modeling: Using the microstructures of these alloys as a guide, computational thermodynamics was used to design new alloys with microstructure similar to the commercial alloys in an effort to obtain materials with desirable properties. In contrast to the commercially available alloys with Ni+Co contents greater than 66 wt%, the Ni+Co content in these newly identified candidate alloys is less than 50 wt. % (Ni being replaced with other elements such as Fe) with the potential to achieve comparable properties. The lower Ni content implies that the alloys will be of lower cost with the potential to achieve targeted fatigue life.

Based upon the results of this computational alloy design process, small batches of the new lower-Ni candidate alloys were cast. The alloys were then homogenized, and rolled at high temperatures. Small tensile specimens were machined from these alloys and tensile tests were conducted *in-situ* at 870°C. Based upon the results of the tensile tests, several of the candidate alloys from the newly developed suite of potential compositions with Ni+Co contents of 50% or less were down-selected for the preparation of larger sized heats. These were cast under inert gas cover and then mechanically processed into plates for further machining.

Fatigue Property Measurement

Rotating beam fatigue tests were conducted on the new alloys *in-situ* at a temperature of 870°C and stresses of 25 Ksi(172.4 MPa), 35 Ksi (241.3MPa) and 45 Ksi(310.2MPa). Results show that one of the alloys exceeded the targeted lifetime of 100 million cycles at 25 Ksi. It was ascertained that further improvement in properties were needed to achieve lifetimes of 100 million cycles at stresses greater than 25Ksi.

Design and Fabrication of Improved Alloys

To achieve better high temperature, high cycle fatigue lives, several new small batches of alloys were designed and cast in the shape of small ingots (~1"x1"x3"-4" in size) in vacuum, annealed, processed to small plates, and were heat-treated. These alloys were designed to have higher volume fraction of strengthening phases along with elements that would beneficially affect the coarsening behavior of the intermetallic precipitates. Tensile specimens were prepared from these plates and tests were performed *in-situ* at 870°C. Figure 2 shows the improvements that were obtained in the high temperature yield strengths of the alloys achieved when compared to the results reported last year. It should be noted that over 70% improvements have been achieved in the high temperature yield strengths of the new lower-Ni alloys when compared to the 751 baseline alloy. Previous results show that this increase in yield strength is the mini-

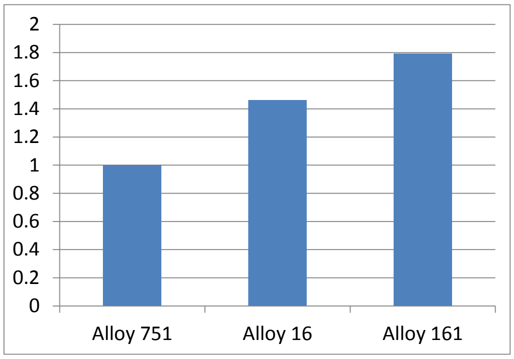

Figure 2*. Ratio of yield strength measured at 870°C for a typical new generation of alloy (Alloy 161) normalized to that of the baseline alloy 751. Also shown for comparison are the results from Alloy 16 highlighted last year.*

mum requirement to achieve improved high cycle fatigue life at these temperatures. The improvement achieved in the high temperature yield strengths of these alloys is promising.

Since a larger heat was required for preparation of fatigue specimens, two of the new lower-Ni candidate alloys were initially down-selected for the preparation of larger sized heats in inert gas cover.
In subsequent experiments, larger ingots of the two down-selected alloys were cast using inert gas cover as shown in Figure 3 and were annealed in preparation for rolling. However, significant difficulties were encountered during rolling following the annealing treatment resulting in poor quality plates. Although one of the plates seem to have been successfully rolled (see Figure 4), useful fatigue specimens could not be obtained from the plates due to defects such as pores and cracking and hence these heats were abandoned. Since the plates had been successfully processed earlier following vacuum arc casting, the cause for this difficulty was not clear. A second set of ingots were prepared using vacuum arc casting but this time the rolling parameters were modified in an attempt to avoid the issues faced previously. This resulted in successful processing of the alloys. Fatigue specimens are currently being machined from these alloys.

Figure 3. *Inert gas cover melts prepared from two improved alloys Alloy 41M3 and Alloy 200.*

Figure 4. *One of the alloys from Figure 3 was rolled into a long plate but was found to contain internal defects and hence was not useful.*

Figure 5. *New alloys were successfully rolled to a length of over 8"required for fatigue tests (from an initial length of about 3.5") using modified rolling parameters. This figure shows a successfully processed Alloy 200.*

Conclusions

- Computational thermodynamics models have been used to identify several promising lower-Ni alloy compositions for valves with the potential to have desirable fatigue performance at higher temperatures. Small heats have been cast and tensile properties were measured at 870^{o}C.
- Rotating beam fatigue tests performed on the new lower-Ni alloys showed a life of over 100 million cycles at 25 Ksi at 870^{o}C but further work was required to improve fatigue lifetime at higher stresses.
- New batch of alloys with potential for improved fatigue performance at higher temperatures have been designed and tensile tests have been completed, indicating 70% higher yield strength at 870^{o}C than the baseline 751 alloy.
- A larger batch of alloys of down-selected compositions were prepared in inert gas cover but rolling resulted in material with unexpected poor quality. This barrier was overcome by modifying rolling parameters.

- Subsequently, vacuum arc casting of alloys has been completed and new lower-Ni candidate alloys have been processed in the form of plate. Fatigue specimens are currently being machined.

Agreement 13329—Design Optimization of Piezoceramic Multilayer Actuators for Heavy-Duty Diesel Engine Fuel Injectors

Hua-Tay Lin, Hong Wang, and Andrew A. Wereszczak
Ceramic Science and Technology Group
Oak Ridge National Laboratory
P.O. Box 2008, MS 6068
Oak Ridge, TN 37831-6068
(865) 576-1169; fax: (865) 574-6098; e-mail: linh@ornl.gov

DOE Technology Manager: Jerry L. Gibbs
(202) 586-1182; fax: (202) 586-1600; e-mail: Jerry.gibbs@ee.doe.gov
ORNL Technical Advisor: J. Allen Haynes
(865) 576-2894; fax: (865) 574-4913; e-mail: haynesa@ornl.gov

Contractor: Oak Ridge National Laboratory, Oak Ridge, Tennessee
Contract No.: DE-AC05-00OR22725

Objectives

1. Apply established structural ceramic probabilistic design and reliability analysis to piezoelectric multilayer actuators (PMLAs).
2. Generate required micromechanical property data on lead zirconate titanate (PZT) piezoceramics and macromechanical property data on PMLAs for input into the design and reliability analysis of the latter.
3. Identify minimum mechanical performance requirements for fuel injector PMLAs.
4. Adapt these strategies to improve reliability of PMLAs that are candidates for use in diesel engine fuel injectors.

Approach

1. Evaluate PMLA reliability under representative service conditions.
2. Link constituent piezoceramic micromechanical and PMLA macromechanical responses.

Accomplishments

1. Completed the humidity study for testing the mechanical strength of poled PZT under various electrical conditions. Modified the ball-on-ring setup for a large PZT plate specimen and conducted a temperature effect study on the mechanical strength of the PZT plates.
2. Developed the electric cycle test method for PZT stacks at high electric field levels by using a piezodilatometer. Tested and characterized the fatigue response of a commercial PZT stack under accelerated testing conditions.
3. Investigated impedance analysis as a small signal measurement for the characterization of PZT stacks.

Future Direction

1. Complete study of the effects of humidity and temperature (80% RH, 85°C) on the mechanical properties of selected PZT ceramics.
2. Complete study of thermal response and cyclic fatigue of short PZT stacks (typically of PZT plates consisting of 10 PZT layers) upon cycling the electric field to up to two times the coercive field.
3. Complete study of cyclic fatigue of short PZT stacks in higher-temperature environment.

Introduction

The use of piezoelectric multilayer actuators (PLMAs) as diesel fuel injectors has the potential to reduce injector response time, provide greater precision and control of the fuel injection event, and reduce energy consumption. Compared with conventional solenoid operation of an injector, the alternative use of a PMLA can enable precise rate shaping of the entire injection cycle that accurately controls injection timing and fuel quantity. PMLA (or piezo-stack) fuel injectors contain a solid-state ceramic actuator that converts electric energy into linear motion, precisely controlling the needle's opening and closing. This capability results in an engine with outstanding performance, improved fuel economy, low noise, and low emissions. Though their use is very attractive for the reasons mentioned, uncertainty continues as to how reliable piezo-actuated fuel injectors will be in the challenging environment of a heavy vehicle diesel engine. Though piezoelectric function is the obvious primary function of lead zirconate titanate (PZT) ceramic PMLAs for fuel injectors, their reliability may be a performance and life limiter because the PZT ceramic within them is brittle, lacks high strength, and may exhibit fatigue susceptibility. That brittleness and relatively low strength can be overcome with a proper probabilistic component design methodology.

This project undertakes the reliability characterization of candidate PMLAs used in these fuel injectors and the piezoceramics used in the PMLAs. Testing and characterization of the piezoceramics and piezo stacks have continued based on recommendations from Cummins Inc. Environmental effect studies have been conducted on the mechanical properties of PZT at various ages, and electric cycle tests under high-field levels have been performed using a commercial PZT stack available in a short configuration that is suitable for testing in a piezodilatometer previously developed under this task.

Approaches

1. Piezoceramic Characterization

The effect of humidity on mechanical properties was studied by pretreating specimens in a controlled humidity chamber (Fig. 1a). A potassium bromide (KBr) solution was prepared (70.8 g of KBr dissolved in 110 g of water) and kept in a tray within the humidity chamber. The relative humidity (RH) of the cabinet was maintained at 85% at room temperature. PSI-5A4E (Piezo System, Inc., 10 × 10 × 0.267 mm, electroded and poled/polarized) specimens were used as the PZT material because this material has been extensively studied in this project, as reported previously. A ball-on-ring setup (BoR, Fig. 1b) was used in testing and evaluating the mechanical properties of the pretreated PZT specimens under various electric conditions: open circuit (OC) and ± Ec (cohesive electric field of the PZT).

Transverse failure of the PZT stacks has been a continuous concern in this application. The failure mode is related to the delamination and the controllability of the fracture path in this multilayer structure. Such concerns can be addressed by testing the flexural strength of bar specimens using 4-point bending. The specimens in this study had a nominal size of 2.5 × 3.5 × 30 mm. The 4-point bending setup had a loading span of 6.35 mm and a supporting span of 19.05 mm. The test was performed in an ORNL instrumented indentation system with a crosshead rate of 0.001 mm/s.

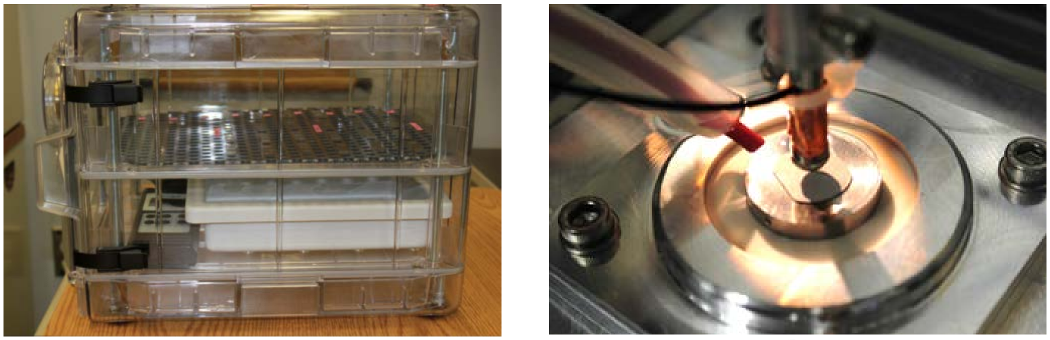

(a) (b)

Fig. 1. (a) Humidity chamber used for pretreating PZT specimens, and (b) ball-on-ring setup showing PZT specimen, loading ball and supporting ring that sits on an alumina disk.

2. PMLA Characterization

2.1 Mechanical properties

The short PZT stacks were EPCOS stacks or 10-layer PZT plates (12 × 12 × 0.74 mm). They were extracted from prototype EPCOS stacks and supplied by Cummins on September 21, 2011, and February 14, 2012. Testing of the first batch of specimens was performed on the BoR setup that was built into the ORNL instrumented indentation system. The test setup included a ϕ 6.35 mm steel ball and ϕ 9.95 mm steel ring. The tests were performed at room temperature with a crosshead speed of 0.01 mm/s. The second batch of test specimens were tested using a self-aligning BoR with triple alumina-tube support of ϕ 9.5 mm and an alumina loading ball of ϕ 19.05 mm (Fig. 2b). The mechanical strength of the short PZT stacks at three temperatures (25, 100, 200°C) was studied, each with 24 specimens.

2.2 Electric fatigue responses

Electric cycle tests were performed on both EPCOS and NOLIAC stacks. The EPCOS stacks were prototypical stacks with the specifications 12 × 12 × 54 mm, 16.15 μF, 160 V, and 2500 N. All the stacks were uncapsulated and were supplied by Cummins. The stacks were examined, and those that had good insulation were screened out for testing. The selected stacks were then wired. The original ORNL piezo stack fatigue setup was modified to accommodate the large stack, including the transmitting rod, guiding rods, and target rods. The test facility was upgraded with high-frequency amplifiers (410-XS-6WB, 6 kHz, Capacitec).

A piezodilatometer (Fig. 3) was also used in testing PZT actuators with small capacitance. NOLIAC CMAP09 stacks (10 × 10 × 2 mm, 400 μF, 200 V) were used in this study. A new high-voltage amplifier, the Trek PZD2000A was used in the cycle test: ±2 kV, ±400 mA.

All of the PZT materials evaluated in FY2012 were summarized in Table 1. The details of test samples configuration and specifications were also provided for reference.

Results

1. Piezoceramics Characterization

The PZT specimens were grouped into four different humidity aging conditions: no treatment (G1 to 3), 10 days (G4 to 6), 30 days (G7 to 9), and 164 days (G10 to 12). Each condition consisted of 3 groups for 3 electric conditions, and each group consisted of 12 specimens. The specimens were weighed in batches. It was found out that aging in 85% RH and 25°C conditions even after 164 days did not introduce significant changes in weight, which suggested there was little or no absorption of moisture into the PZT specimens

After 164 days of humidity aging, the mechanical strength did not change significantly (Fig. 4). The mechanical strength was found to be similar to that of unaged specimens, and confidence ratio rings were overlapping to a large extent for a given electric condition. Under the condition of P (positive electric field), the characteristic strength seemed to drop slightly after 5 months of humidity aging. It was also seen that all the flexural strengths of the PZT were within the same levels as the data sets generated in previous tests [1, 2] under the same test conditions.

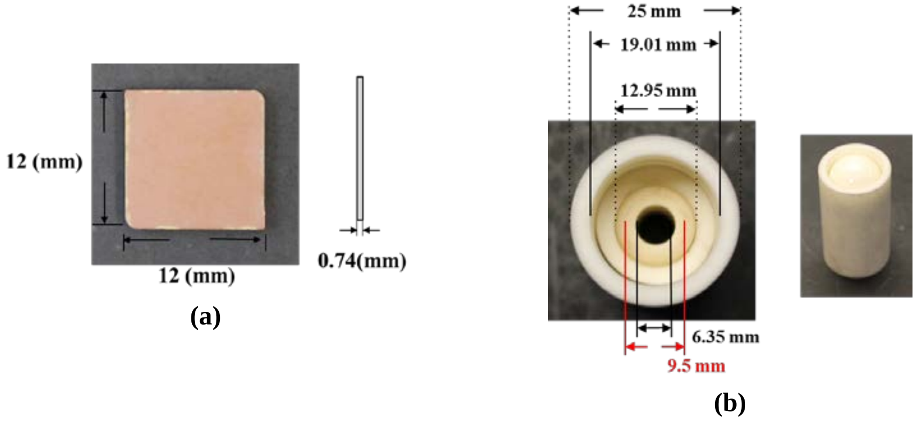

(a)

(b)

Fig. 2. (a) PZT short stacks or plates extracted and (b) triple alumina tube support and alumina loading ball for BoR tests at different temperatures.

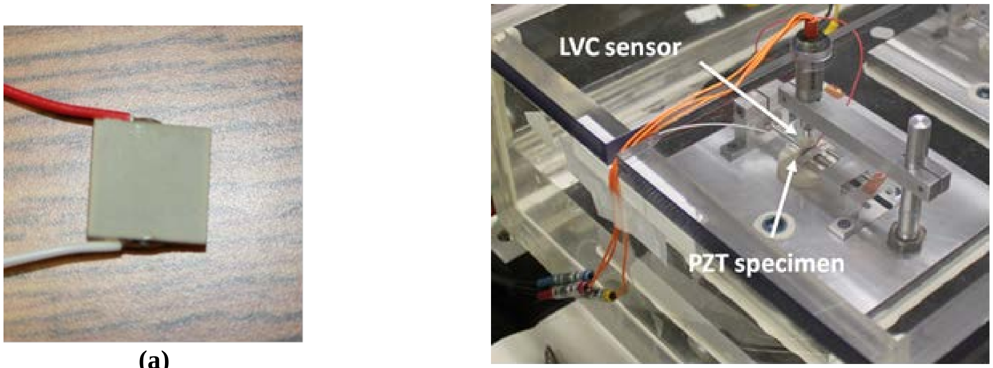

(a) **(b)**

Fig. 3. (a) PZT short stacks or plates, and (b) piezodilatometer used in electric cycle test with FC-40 as surrounding medium.

Table 1. PZT materials, which were purchased from commercial suppliers and provided Cummins, were evaluated in FY2012

No.	**PZT Material suppliers**	**Specimen geometries and main specifications**	**Test methods**
1	Piezo System, Inc., PSI-5A4E, PZT-5A	Single-layer plates; 10mm x 10mm x 0.267mm; Ec = 1.2 kV/mm; Tc = 350°C	Ball-on-Ring mechanical test
2	Short stacks, NOLIAC, CMAP09	Multilayer plates; 10mm x 10mm x 2mm; 400 nF, 200V	Electric cycle test
3	EPCOS short stacks supplied by Cummins Inc.	10-layer plates; 12mm x 12mm x 0.74mm; prepared from EPCOS prototypical stack 12mm x 12mm x 54mm: 16.15 mF, 160 V, 2500N	Ball-on-Ring mechanical test
4	EPCOS stacks supplied by Cummins Inc.	Bend bar specimens; 2.5mm x 3.5mm x 30mm; prepared from EPCOS prototype stack 12mm x 12mm x 54mm: 16.15 mF, 160 V, 2500N	4-point bending mechanical test
5	EPCOS stacks supplied by Cummins Inc.	12mm x 12mm x 54mm; 16.15 mF, 160 V, 2500N	Electrical cycle test w/ mechanical preload

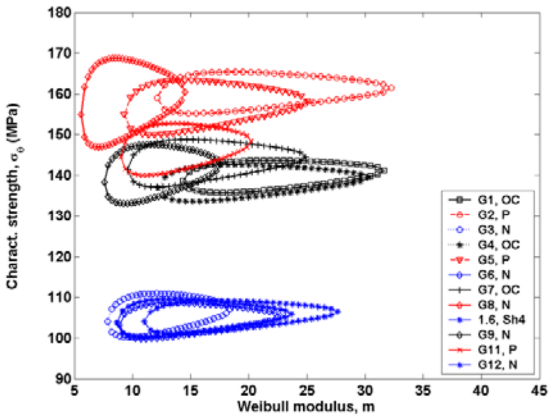

Fig. 4. Confidence ratio rings of mechanical strength of PZT based on BoR tests. OC: open circuit. P: 1 Ec applied parallel to specimens' polarization. N: 1 Ec applied anti-parallel to specimens' polarization.

2. PMLA Characterization

2.1 Size and temperature effect on mechanical strength

BoR tests on the first batch of 12 × 12 × 0.74 mm 10-layer specimens demonstrated that the flexural strength was lower than that of 10-layer PZT plates of 7 × 7 × 0.74 mm (extracted via the use of the chemical solution DYNASOL750). Therefore, the effect of size on the strength of PZT plates is apparent and significant.

Temperature effect studies were carried out on an in-house-built testing BoR frame equipped with a high-temperature furnace. A 20 minute period of soaking in air was provided before the mechanical loading. The pre-load force was 5 N and the loading rate was 0.001 mm/s. The results indicated that the effect of temperature was statistically significant (Fig. 5). There was a 13–26 MPa decrease in BoR strength as the temperature increased from room temperature to 100°C and then from 100 to 200°C. Agglomerates in the PZT layer were observed as a dominant failure origin of the PZT stacks at three temperatures (as shown in Fig. 6).

2.2 Failure of 4-point bending bar

Sixteen flexural bend bar specimens were prepared from as-received EPCOS PMLA stacks from Cummins, and 12 useful data points were obtained from 4-point bending tests. The specimens were usually broken into 2 to 4 pieces. The characteristic strength and Weibull parameters of the 12 specimens were 27 and 3.28, respectively. The characteristic strength appeared to be 8 MPa lower than that of stacks (7 × 7 × 30 mm) purchased in 2008.

It has been further observed that the failure of bar specimens mostly occurred on the plate-to-bonding-layer interface as a result of delamination. The PZT layer-to-internal electrode interface thus had a higher mechanical strength. However, an inter-PZT layer rupture was also observed, along with delamination at the interfacial porous layer (Fig. 7). Thus the surface flaws of the PZT layer influenced the fracture path in this case, also.

2.3 Electric cycle test of EPCOS stack

The test on an EPCOS stack without polymer encapsulation was conducted with electric loading of 160 V, 20 Hz. The electric cycling resulted in immediate surface dielectric breakdown. The breakdown was localized to the middle lateral area of the stack. The damaged stacks still delivered some stroke, but the stroke was substantially lowered so that the stack could not function properly. Therefore, an electronic fluid as a surrounding insulation medium was then employed for the electric cycle test to prevent electric discharge and arcing during the high electric loading condition. An electronic fluid such as FC-40 generally has a relative high dielectric strength and thus can mitigate the partial discharges related to the test setup.

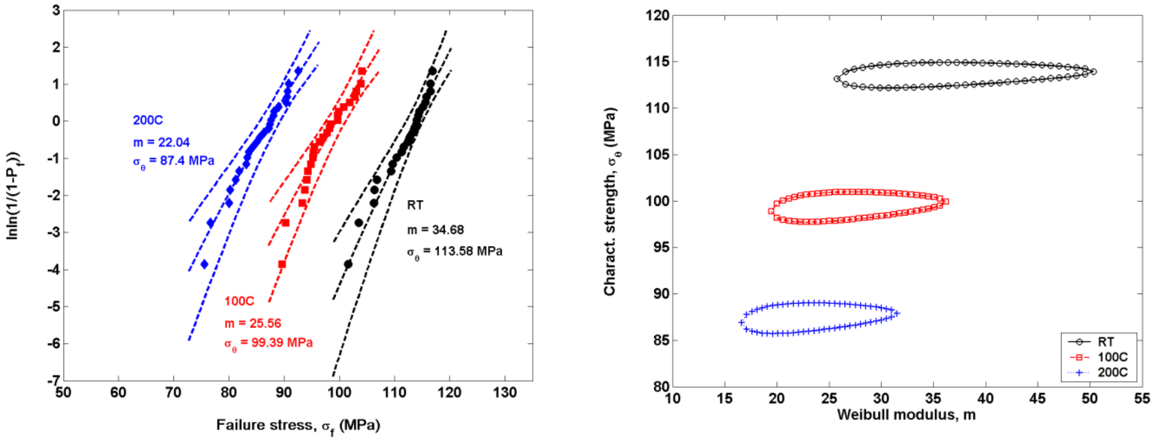

(a) **(b)**

Fig. 5. (a) Weibull plots of mechanical strength and (b) confidence ratio rings. The results were based on BoR tests with triple alumina tube support and alumina loading ball.

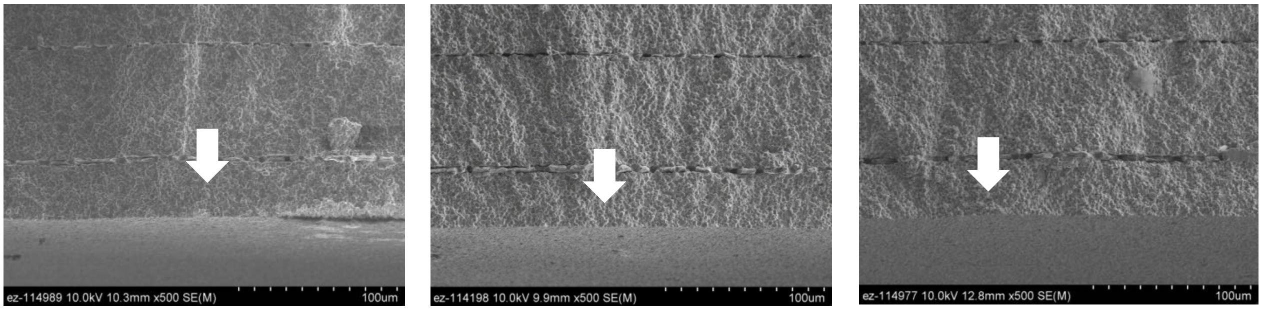

(a) **(b)** **(c)**

Fig. 6. Fracture surfaces of specimens failing at (a) 25, (b) 100, and (c) 200°C. Arrows indicate the fracture origin of agglomerates.

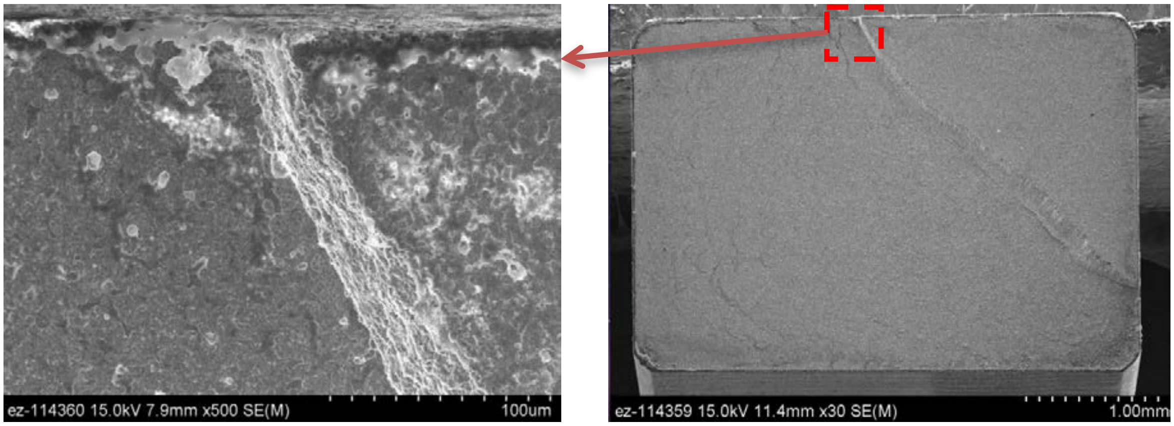

(a) **(b)**

Fig. 7. Fracture surface featuring an inter-PZT layer rupture along with delamination: (a) is a local area of step near the edge of fracture surface (b).

2.4 Electric cycle test of NOLIAC stacks

The commercial CMAP09 stacks manufactured by NOLIAC, Denmark were tested at two electric field levels: 6 and 3 kV/mm, 100 Hz. Unless the specimen failed, the cycling process was interrupted to perform the measurements at a specific number of cycles: 10^0, 10^3, 10^5, 10^6, 10^7, 3 × 10^7, 8 × 10^7, and

10^8. Five specimens tested at 6 kV/mm were found to have failed from 4.33×10^5 to 1.00×10^6 cycles. The other four specimens at 3 kV/mm finished 10^8 cycles.

Unipolar large signal measurement was conducted using two waveforms: a 0.1 Hz triangular wave and a 50 Hz sine wave. The first wave was designed to measure the mechanical displacement, and the second wave was to measure the electric current. The measurement of the PZT plate's properties was, therefore, accomplished through two measurement steps. In the 6 kV/mm tests, the field ranges of 0–3 Ec and 0–6 Ec were used, whereas in the 3 kV/mm tests, only the field range of 0–3 Ec was applied. For each session, there was a wait of one hour before the measurement in order to minimize the effect of cycling-induced heat. Descriptions of the data processing method for large signal measurement can be found elsewhere [3, 4, 5].

Mechanical strain–electric field loops and charge density–electric field loops for specimen CMAP09-01 at two measurement field levels are shown in Figs. 8 and 9, respectively. The variations of mechanical strain and piezoelectric hysteresis for specimen CMAP09 -01 prior to the failure are shown in Fig. 10. Both strain and hysteresis show a decreasing trend with the number of cycles. The piezoelectric coefficient and loss tangent exhibit a similar trend, as shown in Fig. 11. Note that the p_{31} has a negative sign, and the absolute value of p_{31} measures the piezoelectric effect arising from the polarization. Therefore, the results in Fig. 11 agree with those in Fig. 10. It is shown that the loss tangent became lower after 10^3 cycles but started increasing afterward. More fatigue data for the NOLIAC CMAP09 series can be found elsewhere [6].

A Solartron impedance/gain-phase analyzer 1260 was used to examine the health condition of the stacks. The measurement condition in this process was sine waves with amplitude of ±50 mV, and scan frequencies were from 10 to 400 kHz. The data acquisition was set as 20 intervals per frequency decade. The spectra of conductance and the Z-plots for three PZT stacks are given in Fig. 12.

It can be seen that the measurements captured the resonant peak of the stacks near 159 kHz. Both the as-received and 3 kV/mm fatigued stacks exhibited the resonant peak, whereas the broken stack no longer did so. At the same time, the broken stacks tested at 6 kV/mm exhibited the Z-plot curve with much more deflection than those of the other two stacks in as-received condition and after testing at 3 kV/mm. It is thus seen that a lower resistance was related to the broken PZT stack.

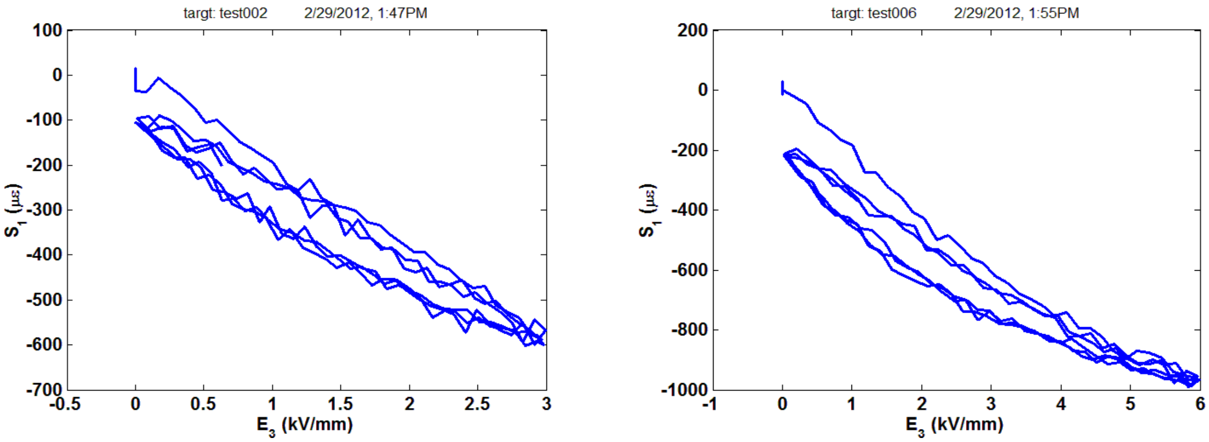

(a) **(b)**

Fig. 8. Strain –electric field curves for (a) test at 3 kV/mm, and (b) 6 kV/mm for CMAP09-01.

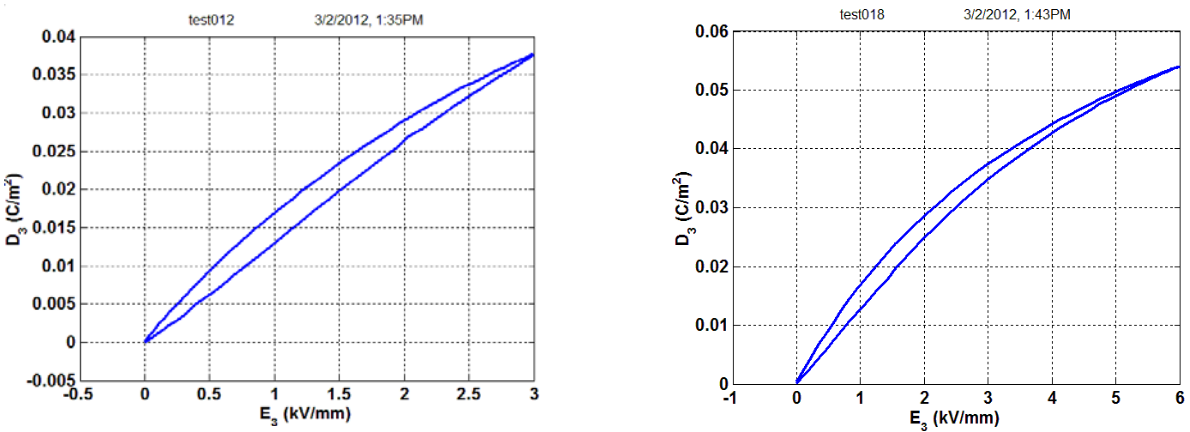

(a) **(b)**

Fig. 9. Charge density–electric field curves for (a) test at 3 kV/mm, and (b) test at 6 kV/mm for CMAP09-01.

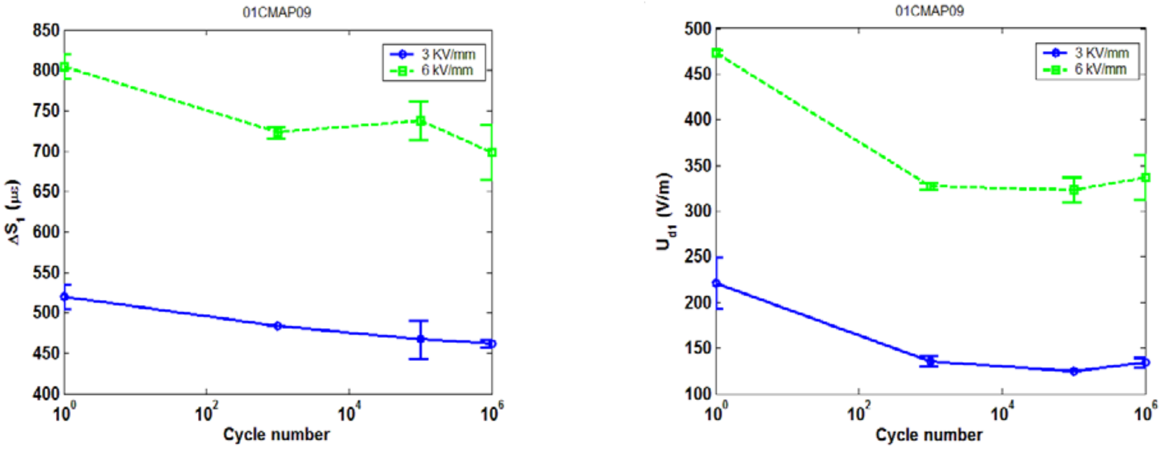

(a) **(b)**

Fig. 10. (a) Variation of mechanical strain with cycle number and (b) variation of piezoelectric hysteresis with cycle number for CMAP09-01.

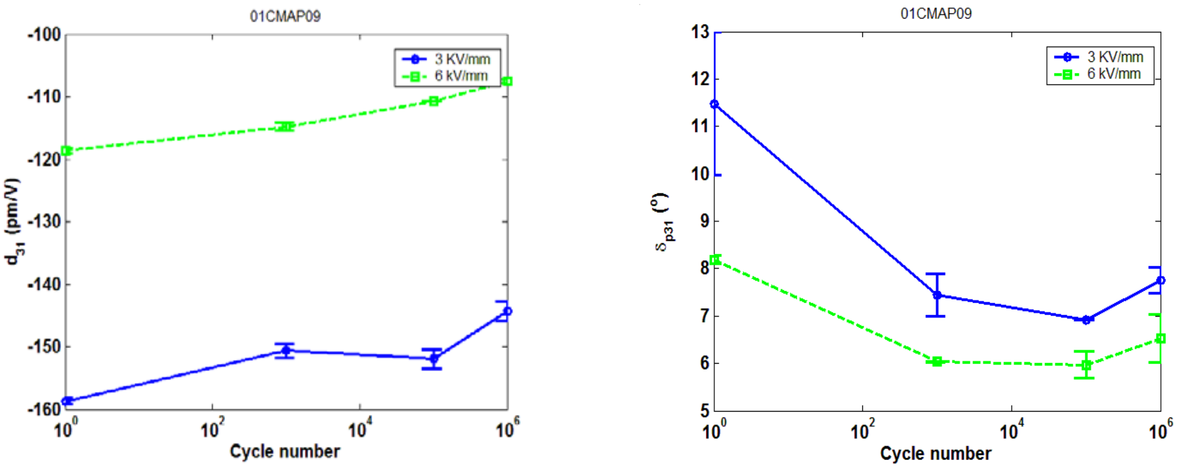

(a) **(b)**

Fig. 11. (a) Variation of piezoelectric coefficient with cycle number and (b) variation of loss tangent with cycle number for CMAP09-01.

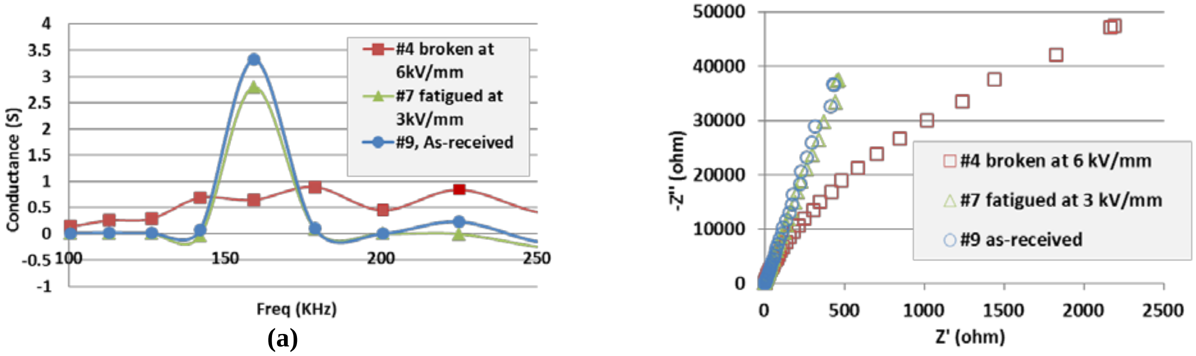

(a) **(b)**

Fig. 12. The effect of fatigue and damage resulting from the cycle test on (a) conductance response and (b) Z-plot is obvious. Measurements were made with a Solartron impedance analyzer 1260.

A scanning acoustic microscope (SAM, ULTRAPAC) was used subsequently to analyze structural damage. At each point, the SAM depends on a pulse and its echo to resolve the underlying damage or defects. A gate based on the time of flight is needed to image the internal structure of an object at a specified depth. The images corresponding to four gates of the ultrasonic signature are shown in Fig. 13 for specimen CMAP09-01. The fractures are shown as curly dark lines and delaminations are displayed as gray patches. These features provided the guidelines for further examination.

The specimen (CMAP09-01) was sectioned subsequently between two wires, polished, and etched to investigate the damage imaged from the SAM analysis. It was shown that fracturing indeed took place on the cross section of the stack at the corresponding location. Scanning electron microscopy further revealed that substantial damage occurred, including delamination between PZT layers and internal electrode layers, and cracks, as shown in Fig. 14.

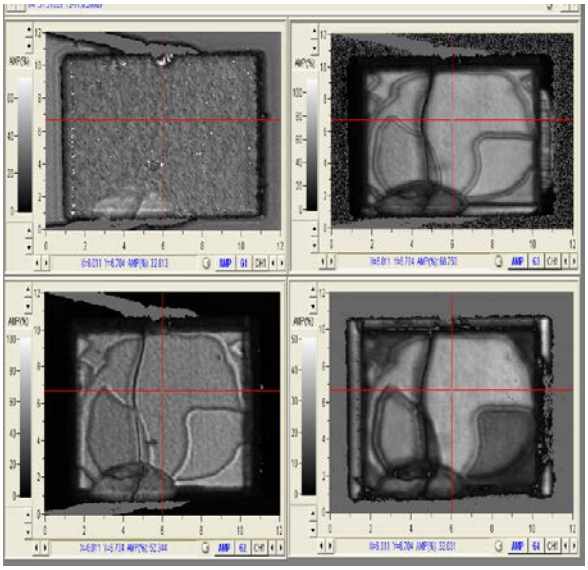

Fig. 13. An electrically broken stack was imaged using SAM (ULTRAPAC): CMAP09-01 with four gates that had an increasing time of flight from the specimen surface [7].

Conclusions

1. Environmental Effect on Mechanical Strength of PZT

Environmental effects on the mechanical strength of PZT were studied, including humidity and temperature. The effect of humidity was investigated by pretreating the PZT for a specified period of time, and the effect of temperature was studied by using a test frame equipped with a high-temperature furnace. Evaluations of mechanical strength were conducted using a BoR setup. The following conclusions can be drawn:

1) For the 5 months of pretreatment at 85% RH and 25°C, no significant change was found in the mechanical strength of the PZT specimens.
2) The use of low-profile PZT stacks or 10-layer plates for testing the mechanical properties of the PZT was demonstrated to be an effective approach.
3) The mechanical failure of the test specimens captures the collective response of the individual PZT and electrode layers that are the key components of the stacks.
4) The effectiveness of mechanical testing can be seen from the size and temperature effects captured by the mechanical strength measurements. The size scaling effect on mechanical strength is a probabilistic effect of ceramics.
5) As the temperature increased from room temperature to 100 and then to 200°C, the mechanical strength decreased by about 13–26 MPa at each step.

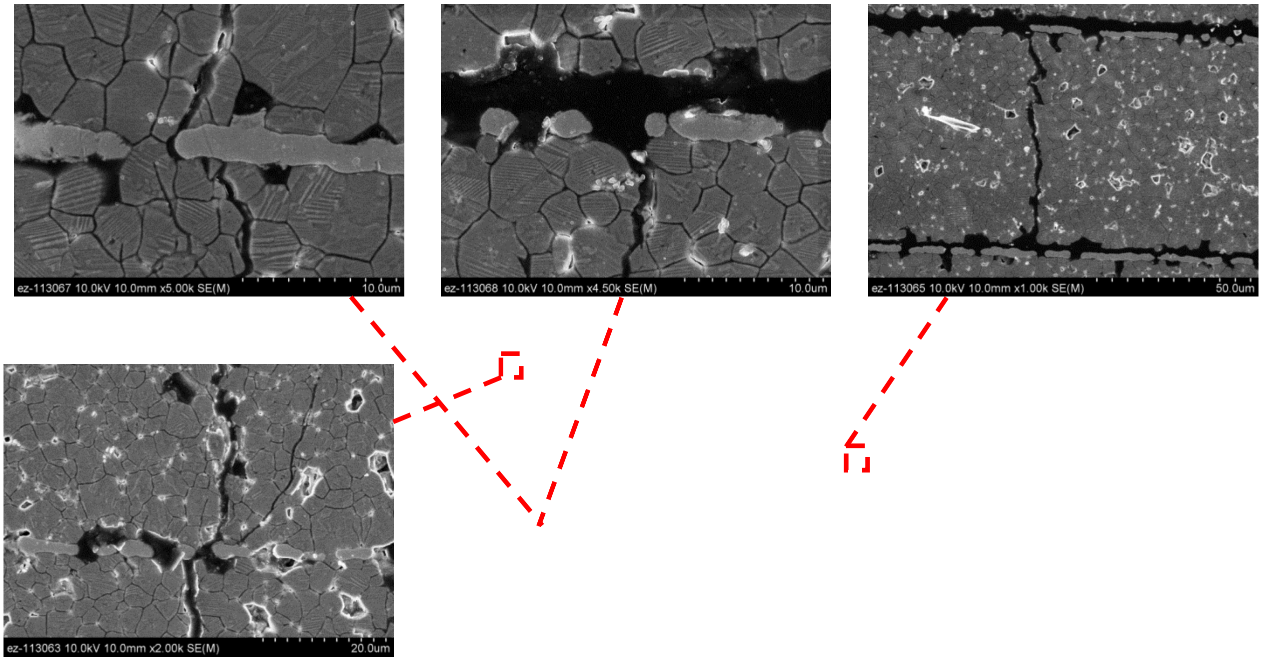

Fig. 14. Fractures on the section of tested stack (CMAP09-01) shown to cross and coalesce internal electrode layers.

2. Cyclic Fatigue of PZT Stack

Electric cycle tests were conducted on low-profile PZT stacks or plates. Specifically, the NOLIAC CMAP09 series was tested using the ORNL piezodilatometer. The following conclusions can be drawn from the tests:

1) Given such capacitance of the PZT stack, electric cycle tests can be conducted using the upgraded high voltage amplifier.
2) The piezoelectric response of the PZT stacks can be tested equivalently through the piezoelectric

coefficient effect by using the current testing stage in piezodilatometer.

3) The upgraded high-voltage amplifier, supplied with voltage and current monitoring channels, can measure the electric displacement of the stack once the measurement condition is defined.
4) The impedance analysis can serve as an important technical approach for small signal measurement as demonstrated on the PZT stacks with various damage/fatigue states. Data interpretation of impedance spectra and Z-plot remains to be developed and linked to the degradation mechanisms within the PZT stack.
5) SAM is effective in imaging the underlying damage introduced by the electric cycling, including cracks and delamination. The current SAM setup is mostly applicable to offline test and characterization of the PZT stack.
6) The fatigue of the stacks at 6 kV/mm was accelerated; the stacks broke in fewer than one million cycles. The fatigue at 3 kV/mm was limited with some fluctuation. Results and understanding developed from testing the NOLIAC specimens shall provide guidance in interpretation of the EPCOS stack.

Future Work

1. Complete a study of the effects of humidity and temperature (80% RH, 85°C) on the mechanical properties of supplied down-selected and equivalent PZT ceramics with and without an applied electric field of up to three times the coercive field. The database generated will enable the design of an optimized HDD fuel injector system that can withstand a fuel injection pressure of up to 45,000 psi.
2. Complete study of cyclic fatigue of short PZT stacks (typical of PZT plates consisting of 10 PZT layers) in a high-temperature environment (100 to 200°C).
3. Complete study of cyclic fatigue and thermal response of down-selected prototype PZT stacks in high-field cycling (up to two times the coercive electric field) with mechanical preload.
4. Conduct work on the finite element analysis to incorporate data generated by the projects mentioned above into the probabilistic design for the recommended stack configurations.

References

[1] Wang, H., and Wereszczak, A. A., Effects of electric field and biaxial flexure on the failure of poled lead zirconate titanate, IEEE Trans. Ultras. Ferroelec. Freq. Contr., 55 (12), 2008, 2559–2570.

[2] Wang, H., Lin, H.-T., and Wereszczak, A. A., Strength properties of poled lead zirconate titanate subjected to biaxial flexural loading in high electric field, J. Am. Ceram. Soc., 93 (9), 2010, 2843–2849.

[3] Wang, H., Matsunaga, T., Lin, H.-T., and Mottern, A. M., Piezoelectric and dielectric performance of poled lead zirconate titanate subjected to electric cyclic fatigue, Smart Mater. Struct., 21, 2012, 025009.

[4] Wang, H., Wereszczak, A. A., and Lin, H.-T., Fatigue response of a PZT multilayer actuator under high-field electric cycling with mechanical preload, J. Appl. Phys., 105 (1), 2009, 014112.

[5] Wang, H., Cooper, T. A., Lin, H.-T., and Wereszczak, A. A., Fatigue responses of lead zirconate titanate stacks under semi-bipolar electric cycling with mechanical preload, J. Appl. Phys., 108 (8), 2010, 084107.

[6] Zeng, F.-W., Wang, H., and Lin, H.-T., Fatigue and failure responses of lead zirconate titanate stack under unipolar electric cycling, in preparation, 2012.

[7] Ferber, M. K., unpublished, 2012.

Presentations and Publications

Publications

1. Zhang, K., Zeng, F.-W., Wang, H., and Lin, H.-T., Biaxial flexural strength of poled lead zirconate titanate in high electric field with extended field range, Ceram. International, in press, 2012.
2. Zhang, K., Zeng, F.-W., Wang, H., and Lin, H.-T., Strength properties of aged poled lead zirconate titanate subjected to electromechanical loadings, Smart Mater. Struct., 21, 2012, 117001.
3. Wang, H., Matsunaga, T., Lin, H.-T., and Mottern, A. M., Piezoelectric and dielectric performance of poled lead zirconate titanate subjected to electric cyclic fatigue, Smart Mater. Struct., 21, 2012, 025009.

Agreement 15054 - Fatigue Enhancements by Shock Peening

Principal Investigators: Mark T. Smith and Elizabeth V. Stephens
Energy Materials Group
Pacific Northwest National Laboratory
P.O. Box 999, MS K2-03
Richland, WA 99352
(509) 375-4478; fax: (509) 375-4448; e-mail: mark.smith@pnnl.gov
(509) 375-6836; fax: (509) 375-4448; e-mail: elizabeth.stephens@pnnl.gov

Yong-Ching Chen
Cummins, Inc.
(812) 377-8349; e-mail: yong-ching.c.chen@cummins.com

DOE Technology Manager: Jerry L. Gibbs
(202) 586-1182; fax: (202) 586-1600; e-mail: jerry.gibbs@ee.doe.gov
Field Technical Manager: Dean Paxton
(509) 375-2620; fax: (509) 375-2186; e-mail: dean.paxton@pnnl.gov

Contractor: *Pacific Northwest National Laboratory*
Contract No.: *DE-AC05-76RL01830*

Objectives

- Evaluate the capability for surface-modification techniques such as laser shock peening (LSP), water jet peening (WJP), and friction stir processing (FSP) to improve the fatigue performance of steel, aluminum, and cast-iron engine components.
- Evaluate the fatigue performance impact offered by these surface treatments to induce compressive residual stresses and to modify microstructure in the surface of aluminum, steel, and cast-iron engine components.
- Compare fatigue performance and thermal stability of these novel surface- treatment approaches to traditional shot peening methods.

Accomplishments

- Friction stir processed A354 in the as-cast and T6 condition and completed processing evaluations.
- Completed final project work.
- Completed final Cooperative Research and Development Agreement (CRADA) project reporting.

Introduction

Fatigue performance is an important factor in propulsion materials, especially for fuel system components such as cylinder heads and blocks. Faster injection response and higher pressures (for better control of combustion events) in modern engines have significantly increased cam stresses, leading to reduced contact and flexural fatigue life. Enhancing component fatigue life is a critical enabler in improving efficiencies for compression-ignition, direct-injection (CIDI)/homogeneous charge compression-ignition (HCCI) engines.

Thus, a CRADA was established between Pacific Northwest National Laboratory (PNNL) and Cummins Inc. with a primary objective of using surface-modification techniques to improve the overall durability of reciprocating parts. Surface-modification techniques (i.e., LSP, WJP, and FSP) were evaluated on their ability to improve the fatigue performance of steel, aluminum, and cast-iron engine components. In addition, the fatigue performance impact offered by these surface-modification techniques was investigated.

In this research, the materials of interest were 52100 steel, cast-aluminum alloy A354-T6, and gray cast iron ASTM A48 Grade 40. LSP was applied to 52100 steel and A354 rotating-beam specimens, WJP was applied to A354 rotating-beam specimens, and FSP was applied to Grade 40 cast iron and A354 plates. Characterization techniques (e.g., fatigue tests, residual stress measurements, surface roughness measurements, tensile tests, and microstructural analysis) were used to evaluate the surface-modified specimens.

Because this project concluded in FY12, the following sections describe the deliverables and technical approach and provide high-level summaries of the project research and key conclusions.

Deliverables and Technical Approach

The following deliverables were established towards the goal of improving the overall durability of steel, aluminum, and cast-iron engine components through surface-modification techniques and evaluating the fatigue performance impact offered by these techniques:

- Demonstrate fatigue enhancements achieved by LSP and WJP for steel and aluminum components as compared to traditional shot peening approaches
- Demonstrate enhancements achieved by FSP for cast-iron components
- Prototype a full-scale component enhanced by a promising surface-modification technique for evaluation.

To achieve the objectives and deliverables of the research, two approaches were implemented: 1) technology development and 2) technology transfer and commercialization. Technology development focused on the following goals for fatigue enhancements in steel and aluminum and FSP development for cast iron and aluminum:

- demonstrate use of surface treatments to induce deep subsurface compressive residual stresses in test specimens
- characterize stress distribution in test specimens and compare post-treatment to that of control specimens; characterize post-treatment surface roughness
- evaluate the mechanical properties of surface-modified bar specimens using rolling contact fatigue (RCF) and rotating beam fatigue (RBF) tests methods
- evaluate the thermal stability of surface-modified specimens
- demonstrate use of FSP on cast iron and aluminum.

Technology transfer and commercialization goals included the following:

- demonstrate LSP and WJP surface-modification approaches on a full-scale steel and/or aluminum components using engine systems qualification tests (Cummins Inc.)
- disseminate technology benefits to product design and development groups (Cummins Inc.)

Results and Discussion

Laser Shock Peening of Steel and Aluminum: LSP surface treatments were applied to evaluate the capability of the process to induce compressive residual stresses and enhance the fatigue properties of 52100 steel and A354-T6 cast aluminum. LSP was observed to induce deep compressive stresses that allow post-peening surface finishing and improve the fatigue life of these materials.

In the 52100 specimens, deep stresses (60,000 – 70,000 psi) remained at 0.020 in. of depth after surface grinding. In comparison to shot peening, no residual stress was observed at this same depth indicative of shot peening being a shallow peening method. In addition, fatigue life of LSP and ground 52100 specimens showed significant increase in RBF life in comparison to the control and shot-peened specimens (in both low-cycle and high-cycle fatigue) (Figure 1). At 10 million cycles, statistical analysis showed a 12 percent increase in RBF life and a 50 percent increase in RCF life for 52100 in comparison to the control. In the thermal stability tests, no relaxation of stresses was observed in the LSP 52100 specimens when exposed for 2 h at 141°C; however, when exposed for 2 h at 246°C, relaxation of stress was observed. Greater degradation of the residual stress field was observed in the shot-peened specimens when exposed to the same temperatures and duration.

In the A354 specimens, deep compressive stresses ~20,000 psi also remained at 0.020 in. of depth after surface grinding. Although, an improvement at 10 million cycles was observed in the LSP A354 specimens in comparison to the control (Figure 2), no significant difference was observed at 100 million cycles. Additional optimization of LSP processing parameters on cast aluminum may further enhance the fatigue life of A354.

Enhancements observed in the 52100 fatigue properties prompted Cummins Inc. to identify and process three fuel system components via LSP for component-level fatigue evaluations.

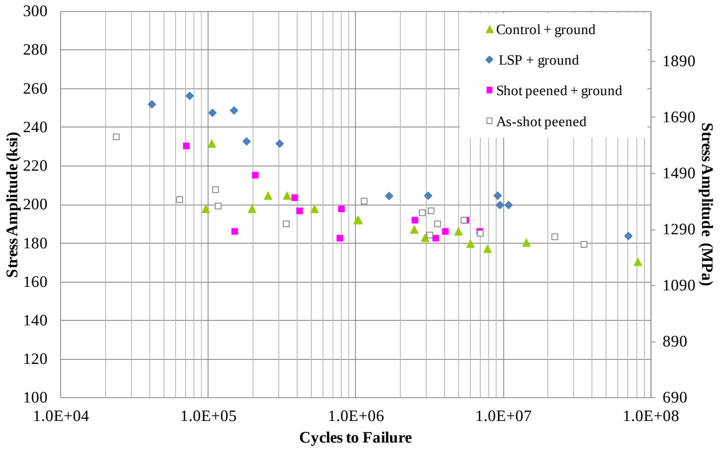

Figure 1. Fatigue test results of the LSP surface-modified 52100 specimens

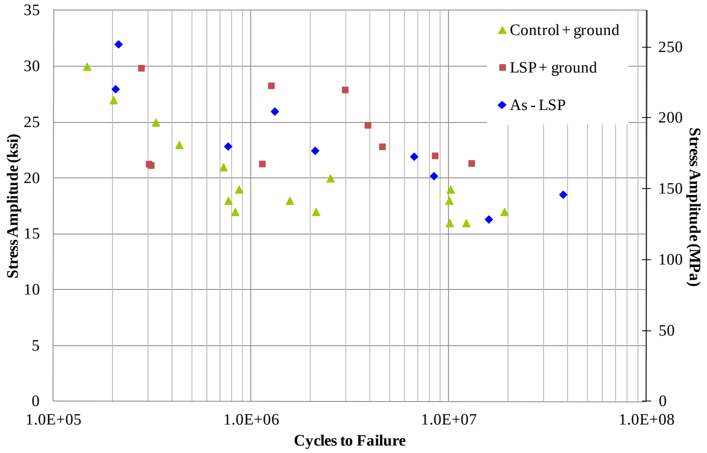

Figure 2. Fatigue test results of the LSP surface-modified A354-T6 cast aluminum specimens.

Waterjet Peening of Aluminum: WJP surface treatments were applied to evaluate the capability of the process to induce compressive residual stresses and enhance the fatigue properties of A354-T6 cast aluminum. WJP of A354 aluminum, regardless of peening method applied, can produce surface compressive residual stresses while maintaining a required surface finish. No secondary machining was required. In the processed specimens for fatigue evaluations, deep compressive stresses were observed ranging from 32.7 to 38.2 ksi with stress-field depths ranging from 0.001 to 0.005 in. Resulting surface roughness after processing ranged from 0.88 to 1.77 μm. In addition, WJP of cast-aluminum alloy A354 specimens showed a significant improvement in fatigue life ranging from 40 to 50 percent in comparison to the control (Figure 3). In addition, two of the processing conditions were applied 2 and 4 in. away from the specimen surface, allowing greater flexibility in processing components in hard-to-reach areas.

Enhancements observed in the A354 fatigue properties prompted Cummins Inc. to identify and process a component via WJP for component-level fatigue evaluations.

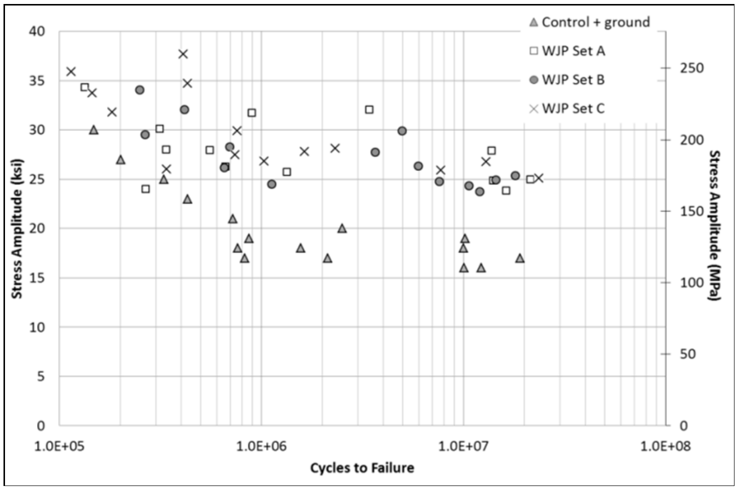

Figure 3. Fatigue test results of the WJP surface-modified A354-T6 cast aluminum specimens.

Friction Stir Processing of Cast Iron: This subtask focused on evaluating challenges of FSP/W cast iron and investigating potential solutions to overcome these challenges. Once plasticization of cast iron was achieved, work progressed towards consolidated, translating welds and then to developing process parameters for longer welds.

The most successful welds were made with a standard PCBN tool and a 304L shim with a 0.0625-in.-thick copper cover plate on the cast iron (Figure 4). This combination resulted in a well-consolidated nugget when processed at 1000 to 1200 RPM at 0.5 inches per minute (IPM). The weld nugget was shown to be softer than the base material in copper-rich areas, but harder than the base material in other areas. In addition, the longitudinal, weld tensile strength observed (33 ksi) was greater than 80 percent of the parent material ultimate tensile strength (UTS); although the welds had no strength in the transverse direction due to alignment of graphite flakes near the weld nugget. The success of using of cover plates with cast iron led to the filing of an invention report.

Friction Stir Processing of Aluminum: FSP was used to process as-cast and T6 heat-treated A354 aluminum. Initial processing evaluations in the as-cast 354 showed that 500 RPM/3 IPM could be used to homogenize the microstructure and hardness, reduce the size of primary silicon dendrites, and eliminate porosity in A354.

A second 1000 RPM/6 IPM condition appeared to have similar benefits but resulted in a hardening of the as-cast material. The two processing conditions were successfully used to process defect-free welds in A354-T6 plates that resulted in refined microstructures. However, both processing conditions appeared to reduce hardness in comparison to the base material, resulting in a reduction of strength and an increase in elongation (Table 1). This project ended prior to determining if these FSP conditions, or others, will enhance the fatigue life and wear behavior of A354-T6 aluminum castings. Further characterization and/or development in optimizing processing parameters for A354-T6 are needed.

Figure 4. Image of a 7.5 in. weld translation of cast iron.

Table 1. Summary of the tensile test results of the processed A354-T6 plates.

A354-T6 Specimen Population	Ave. YS (ksi)	Ave. UTS (ksi)	Ave. % Elongation
Baseline	34.1 ± 1.7	42.2 ± 5.0	4.0 ± 3.0
FSP 500 RPM/3 IPM	23.6 ± 0.6	40.4 ± 1.9	10.6±3.4
FSP 1000 RPM/6 IPM	27.7 ± 0.6	40.3 ± 6.2	7.5 ± 3.3

Note: All castings were made and heat treated by PNNL. Differenced in the baseline strength in comparison to A354 in the literature may be due to processing variations.

Conclusions

The overall objective of this research was to improve the overall durability of steel, aluminum, and cast-iron engine components through surface-modification techniques and to evaluate the fatigue performance impact offered by these techiniques. Fatigue enhancements achieved for steel (via LSP), aluminum (via LSP, WJP, and FSP), and cast iron (via FSP) components were to be demonstrated. In addition, a component was to be prototyped by a promising surface-modification technique and evaluated. In this research the following conclusions were derived:

- LSP induced deep, compressive subsurface stresses that allowed post-peening surface finishing in both 52100 steel and A354 aluminum specimens.
- LSP enhanced the fatigue properties of 52100 surface-ground steel specimens. A 12 percent increase in RBF and a 50 percent increase in RCF were observed in comparison to control and shot peened specimens.
- LSP improved the fatigue properties of A354 specimens at 10 million cycles; however, no significant difference was observed at 100 million cycles. Additional optimization of the LSP processing parameters may further enhance the fatigue life of A354 aluminum.
- WJP induced deep compressive surfaces stresses while maintaining the required surface finish in A354 aluminum. No secondary machining/surface finishing was required.
- WJP enhanced the fatigue properties of A354 aluminum. Two methods and three processing parameters were evaluated, where regardless of the condition applied, a 40 to 50 percent increase

in fatigue life at 10 million cycles was observed in comparison to control specimens.

- Thermally stable, well-consolidated welds were achieved (with the use of cover plates and no pre-heating) with FSP/W of Grade 40 cast iron. However, graphite alignment needs to be minimized to increase weld strength before enhancements in material properties may be realized.
- FSP can refine the microstructure, homogenize the hardness, reduce the size of primary silicon dendrites, and eliminate porosity in A354 aluminum. However, decreased strengths with increased ductility were observed in comparison to the parent material. Further processing parameter optimization is needed before enhancements in material properties are achieved.

The promising results in LSP and WJP prompted Cummins Inc. to identify and process several components that would benefit from these surface-modification techniques. However, due to internal priorities, component-level testing was not performed by the end of this research project. Regardless, these surface-modification techniques have proven to be critical enablers in supporting advanced combustion. By improving the fatigue performance of engine component materials, these surface-modification techniques may enable lower cost materials to meet or exceed the performance of higher cost materials, thereby enabling cost-effective and widespread introduction of more efficient engine systems.

Presentations/Publications/Patents

Cummins Internal Project Review, November 2011.

DOE Hydrogen Program and Vehicle Technologies Program Annual Merit Review, May 2012.

Acronyms

CIDI	compression ignition direct injection
CRADA	Cooperative Research and Development Agreement
FSP	friction stir processing
HCCI	homogeneous charge compression-ignition
IPM	inches per minute
Ksi	kilo-pound-force per square inch
LSP	laser shock peening
MPa	megapascal
PNNL	Pacific Northwest National Laboratory
WJP	waterjet peening

Agreement 17257 – Materials for Advanced Turbocharger Designs

P. J. Maziasz and A. Shyam
Materials Science and Technology Division
Oak Ridge National Laboratory
P.O. Box 2008, MS-6115
Oak Ridge, TN 37831-6115
(865) 574-5082; fax: (865) 576-6298; e-mail: maziaszpj@ornl.gov

K. Pattabiraman
Global Materials Engineering Manager
Honeywell – Turbo Technologies
3201 W. Lomita Blvd.
Torrance, CA 90505
(310) 571-1616; fax: (310) 539-7061; e-mail: kalathur.pattabiraman@honeywell.com

DOE Technology Manager: Jerry L. Gibbs
(202) 586-1182; fax: (202) 586-1600; e-mail: jerry.gibbs@ee.doe.gov
ORNL Technical Advisor: J. Allen Haynes
(865) 576-2894; fax: (865) 241-0112; e-mail: haynesa@ornl.gov

---

Contractor: Oak Ridge National Laboratory, Oak Ridge, Tennessee
Contract No.: DE-AC05-00OR22725

Objectives

- CRADA NFE-08-01671 – Provide the critical test data for new, improved materials, which in turn will enable the design of advanced turbocharger systems with upgraded performance, durability and reliability relative to conventional systems.

Approach

- CRADA NFE-08-01671 – This is now a 5 year project (3 years + 2 years extension) designed to consider both materials for the turbine and compression sections, and to consider turbochargers for both passenger/gasoline and commercial/diesel engines. Honeywell assesses and prioritizes the components that benefit most from materials upgrades or alloy development. ORNL works with Honeywell materials/component suppliers to obtain new materials for testing and evaluation.

Accomplishments

- ORNL and Honeywell completed neutron-scattering residual stress measurements, finding tensile stresses for turbine wheel/shaft components. Long-term creep and oxidation evaluation of CF8C-Plus cast stainless steel continued for diesel and automotive turbine housing applications.
- Honeywell is taking the first steps to evaluate CF8C-Plus as the turbo-housing material for the Ford V-6 3.5L twin-turbocharged EcoBoost gasoline engine used in light trucks.

Future Direction

- CRADA – Upgrade materials for wheel, shaft and housing of the turbine portion of the turbocharger will continue to be assessed. Supporting the Honeywell commercialization of CF8C-Plus for light duty truck and automotive turbine housing applications will be a priority.

Introduction

This ORNL CRADA project with Honeywell, NFE-08-01671 (DOE/EERE/OVT Agreement 17257) addresses the limitations of lifetime or use-temperature for the various components (casing, wheel, shaft, bearings) of both the turbine and compressor parts of the turbocharger system. Turbochargers are an attractive way to boost engine power to increase fuel efficiency. This year, the project also involved neutron scattering experiments at ORNL/HTML Neutron Residual Stress Facility 2 (NRSF2) at HFIR. Requests for more detailed information on this CRADA project should be directed to Honeywell, Inc.

Approach

The CRADA project, which began several years ago, extends for 5 years, and covers several different tasks. The first task assesses and prioritizes the various components that need or would most benefit from materials upgrades to increase temperature capability and performance, as well as durability and reliability. The next tasks examine current performance and degradation modes of wheel/shaft assemblies for turbines and compressors, and turbine housings, particularly for automotive applications. New materials will then be obtained and tested to verify upgraded performance and benefits.

Technical Progress

This CRADA project began several years ago, and is comprised of six tasks, which will span the duration of this project. ORNL and Honeywell discussed the priority of the various tasks and turbocharger components for materials upgrades at a kick-off meeting held in Torrance, CA.

Figure 1 – Honeywell turbocharger wheel/shaft assembly used for neutron-scattering experiments, consisting of a Ni-based superalloy turbine wheel welded to a steel shaft.

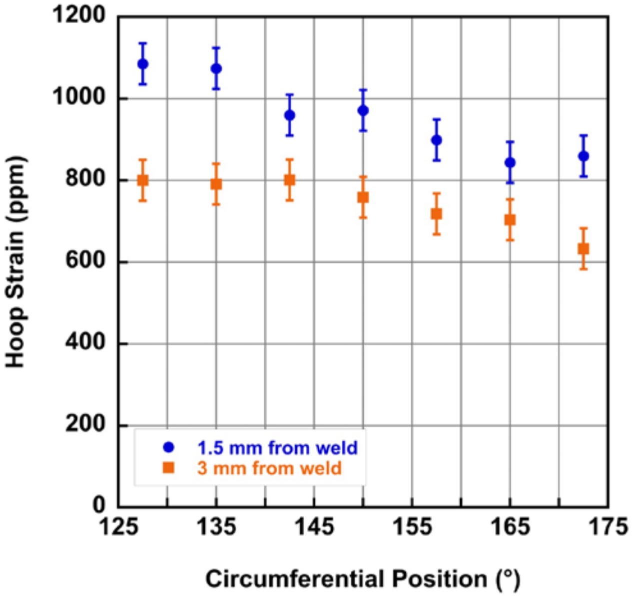

Figure 2 – Neutron scattering results show an asymmetric tensile hoop strain near the weld joint of the wheel/shaft assembly with no heat-treatment after welding. These experiments were run by Tom Watkins and Cam Hubbard of the Residual Stress User Center at the NRSF2 at the HFIR.

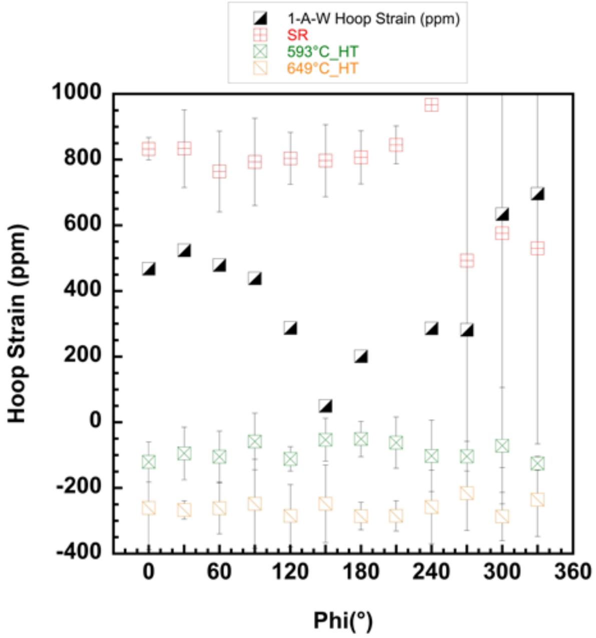

Figure 3 – Neutron hoop strain maps versus circumferential angle of wheel/shaft assemblies in 4 different conditions, as-welded, stress relieved via fast induction coil heating, and conventional furnace stress relief heat treatments at 593 and 649^{o}C. Error bars represent multiple measurements. Furnace stress relief at 593^{o}C reduces the residual stresses and their asymmetry.

Figure 4 – A typical diesel turbocharger housing made of SiMo cast iron.

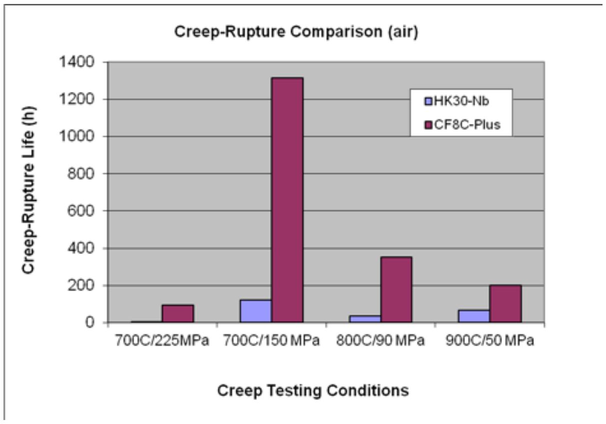

Figure 5 – Comparison of creep-rupture lifetimes for CF8C-Plus and HK-30Nb cast stainless steels tested at 700-900^{o}C.

The turbine wheel-shaft assembly (WSA) was chosen as the first component for analysis of residual stresses near the weld-joint of the Ni-based superalloy wheel to the steel shaft, using neutron-scattering at the HFIR reactor at ORNL. These wheel/shaft assemblies can develop vibrations if there is any asymmetry in the weld-joint. A typical wheel/shaft assembly used for the ORNL residual stress measurements is shown in Figure 1. Several sets of experiments were completed this year, and show that there is an asymmetry in the residual hoop stress circumferentially in the as-welded condition, as shown in Figure 2.

This year, additional measurements were done on larger WSA components with stainless steel shafts, and the asymmetric residual hoop stresses present after welding are shown in Figure 3. Stress relief of the welded regions was done with fast induction-coil heating, and two conventional furnace heat-treatment conditions at 593 and 649^{o}C. It is clear from Figure 3 that the induction coil stress relief (SR) does not reduce the tensile residual stresses or remove their asymmetry. By contrast, the conventional furnace heat-treatment at 593^{o}C is relatively effective at removing both the residual stresses and their asymmetry. These results should be a factor in Honeywell optimizing manufacturing processes to maximize WSA component performance and lifetime.

Materials testing was done in support of advanced materials for turbocharger housings. A typical diesel turbocharger housing is shown in Figure 4. Additional testing was done to extend previous work by ORNL and Honeywell comparing the new CF8C-Plus steel to HK30-Nb, a standard commercially available upgrade material for turbochargers for heavy-duty truck diesel engines when temperatures exceed the limitations of SiMo cast iron. Previous work clearly showed that CF8C-Plus had better yield strength at 800 and 900^{o}C than HK30Nb. Creep-testing at several different conditions at 700-900^{o}C also clearly showed that CF8C-Plus steel had better creep-resistance than the HK30-Nb alloy, as shown in Figure 5.

Additional creep-testing was done on the CF8C-Plus steel at 600 to 750^{o}C this year. At 600^{o}C, one creep test at 275 MPa failed after 7300 h, while another one at 180 MPa has exceeded 16,000 h without rupture. A creep rupture test at 700^{o}C and 135 MPa lasted 3212 h. Another creep test at 750^{o}C and 100 MPa lasted for 1784 h. All of these tests exceeded expectations, and failed with >25 % rupture ductility. Materials comparisons and additional testing will be included to enable CF8C-Plus steel to be evaluated for turbine housings for passenger vehicle gasoline engines.

Finally, Honeywell is considering commercialization of CF8C-Plus steel for a Ford gasoline engine light-truck application and several automotive applications. CF8C-Plus steel could be used as the turbo-housing material for the 3.5L V-6 twin-turbo EcoBoost engines for the Ford light-truck series. CF8C-Plus steel could also be the turbocharger material for Ford and GM automotive applications. This effort will continue next year.

Conclusions

The benefits of CF8C-Plus steel relative to HK-30Nb steel at 700-900^{o}C were defined for diesel turbocharger housing applications, and additional long-term creep-testing of CF8C-Plus at 600-700^{o}C continued. Neutron-scattering residual stress experiments were completed for the welded region of turbine wheel/shaft assemblies for passenger vehicle turbochargers, and these showed tensile hoop strain and circumferential asymmetries in the as-welded condition. New results this year showed certain heat-treatments can relieve those residual stresses and their asymmetries.

Publications/Presentations

None

Special Recognitions and Awards/Patents Issued

None

Agreement 18570 – Engine Materials Compatibility with Alternate Fuels

S. J. Pawel, J. K. Thomson, D. F. Wilson, H. M. Meyer, and M. D. Kass*
** Corrosion Science and Technology Group*
Oak Ridge National Laboratory
1 Bethel Valley Road, Bldg. 4500-S, MS-6156
Oak Ridge, TN 37831-6156
(865) 574-5138; fax: (865) 214-0215; e-mail: pawelsj@ornl.gov

DOE Technology Manager: Jerry L. Gibbs
(202) 586-1182; fax: (202) 586-1600; e-mail: jerry.gibbs@ee.doe.gov
ORNL Technical Advisor: James A. Haynes
(865) 576-2894; fax: (865) 574-4913; e-mail: haynesa@ornl.gov

---

Contractor: Oak Ridge National Laboratory, Oak Ridge, Tennessee
Prime Contract No.: DE-AC05-00OR22725

Objectives

- Conduct a systematic assessment of engine materials corrosion in ethanol fuel blends to develop a mechanistic understanding of performance boundaries and material selection requirements.
- Seek to relate forensic analysis of materials returned from field exposures (samples created from actual engine operation) with laboratory corrosion test results to develop a rapid corrosion assessment technique.

Approach

- Evaluate corrosion patterns and surface films on components returned from vehicles (engines tests, actual service) via forensic analysis and compare with similar results generated in laboratory testing.
- Investigate possibilities for in-situ extraction and analysis of liquid/gas constituents from internal threads, pockets, or crevices, as examples of the corrosive environment generated during engine testing.
- Gather laboratory test data to enable mechanistic assessment of corrosion of engine materials as a function of fuel blend, temperature, and fuel contaminants as well as alloy composition and structure.

Accomplishments

- Analysis of cylinder heads for evaluation of structure and corrosion products is complete; the cylinder heads for analysis were selected from among engines exposed to variable degree of test operation.
- Gas and fluid specimens have been successfully collected for analysis from an operating engine through a capillary tube inserted into the combustion chamber. Specimens representing engine operation with E0 and E85 were collected for comparison.
- The redesigned laboratory test stand for evaluation of engine material corrosion as a function of alloy composition/structure and fuel blend variables is fully operational and generating extensive data. Aluminum corrosion is quite sensitive to fuel blend composition and particularly water and oxygen content of the fuel.

Future Direction

- Contingent on the availability of close-out funds, perform battery of corrosion tests on aluminum-base alloys, and other relevant engine materials in methyl, propyl and butyl alcohol fuel blends of variable composition and environmental conditions in order to elucidate alcohol corrosion mechanism.

Introduction

The ever increasing rate of fossil fuel consumption coupled with the desire for energy independence has influenced the United States to enact legislation to integrate renewable biofuels such as ethanol into the nation's fuel supply [1]. As of 2012, over 95% of standard refueling stations distribute gasoline blended with up to 10% fuel-grade ethanol, often termed E10. Due to various national policy goals and initiatives to pursue energy independence, there is mounting pressure to increase the ethanol content of transportation fuels to levels of 15-20% ethanol (E15-E20) in the near future, and flex-fuel vehicles capable of utilizing E85 (85% ethanol) fuel blends are in production by many manufacturers.

The addition of ethanol to gasoline is expected to be a source of concern for increased corrosion in two primary ways. Firstly, compared to gasoline, ethanol has significant affinity for water. Thus, additions of ethanol to transportation fuel invite the possibility of aqueous corrosion of all materials in contact with the fuel, including vehicle fuel systems and engines as well as the infrastructure for distributing and dispensing the fuel. Due to the hygroscopic nature of ethanol, absorbed water can phase separate from the organic fuel phase leading to a number of potential issues with fuel and containment corrosion [2]. Secondly, ethanol is orders of magnitude more electrically conductive than gasoline [3], so even modest additions of ethanol can contribute to corrosion possibilities in ethanol fuel blends, such as galvanic attack, that are not observed in ethanol-free gasoline.

This investigation systematically examined the potential impact of changing fuel compositions on fuel compatibility with materials of interest for lightweight engine materials. The focus of the effort has been on aluminum and its alloys, primarily because it is lightweight and is used extensively in automotive engines as a piston and head material for fuel-efficient vehicles. There are mixed reports suggesting variable degrees of corrosion susceptibility of aluminum in ethanol [4-11]. Inconsistencies exist possibly as a result of variations (intended or not) in critical exposure variables and/or incomplete interpretation of the results. An overview of several experiments demonstrating the unique vulnerabilities of aluminum alloys to corrosion in ethanol is presented.

Results and Discussion

Galvanic Coupling

Karl Fischer titration showed that the water content pre- and post-test was less than 100 ppm in all cases. The corrosion results are summarized in Figures 1a and 2a, which pictorially indicates that uncoupled (stand-alone) aluminum specimens corroded to an essentially identical degree to the aluminum exposed in each galvanic couple. Further, the end of the aluminum specimen physically in contact with each coupled material revealed no more or less corrosion than the rest of the specimen, again suggesting no effect of electrochemical potential for these exposure conditions. In all cases, whether exposed as part of a couple with aluminum or as individual specimens, the other materials – copper, cartridge brass, mild steel, and 304 stainless steel – were found to be completely immune to corrosion under these conditions.. The mass loss of aluminum material in each case was approximately 20±3%. The corrosive attack on aluminum appears to initiate at discrete locations as rather intense general corrosion. These areas of intense corrosion have some similarities to pitting, but the corroded area spreads laterally at a similar rate to penetration, and ready overlap of corroded areas suggests no electrochemical protection of areas adjacent to those areas that are actively corroding. The experiment was repeated under similar test conditions with a 0.5% by weight water addition in E100. This resulted in a test fuel with a higher electrical conductivity; however, corrosion of the aluminum was suppressed due to the presence of the water. Results for this experiment are shown in Figures 1b and 2b.

Water Content and Temperature

Results on the effect of water content and temperature on aluminum corrosion in ethanol are summarized in Table 1. In these tests, if the reaction initiates at all, it proceeds quite rapidly. The reaction is accompanied by a rapid increase in pressure and temperature as hydrogen gas is generated and the exothermic reaction accelerates. Gas samples were collected through a release valve into a Teflon sample bag and analyzed by a gas chromatograph/mass spectrometer (GC/MS). It was determined that hydrogen gas was the only gaseous reaction product. Samples of the post reaction liquid fuel were also analyzed by GC/MS and aside from the original fuel constituents, ethanol, toluene and iso-octane, no evidence was found of other compounds as reaction products. In the cases where the reaction initiates, the aluminum specimen is quickly consumed leaving a bright white powder interspersed with gray particles as solid corrosion product. For specimens tested in water concentrations below 0.1%, post experiment Karl Fischer titrations demonstrated significantly decreased water concentration levels indicating that water is consumed in the reaction. The solid corrosion product was analyzed by Scanning Electron Microscopy (SEM) and Energy Dispersive X-ray spectroscopy (EDX), and X-Ray Diffraction (XRD) and is thought to consist of a combination of amorphous aluminum oxide, aluminum hydroxide and aluminum oxy-hydroxide.

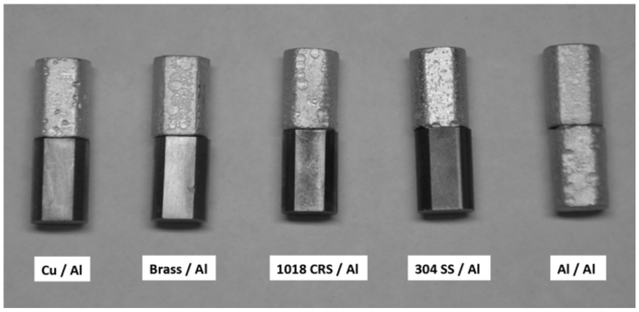

Figure 1a *Galvanically coupled aluminum specimens and stand alone aluminum specimen exposed to anhydrous ethanol E100 for a period of 24 hours at 78°C.*

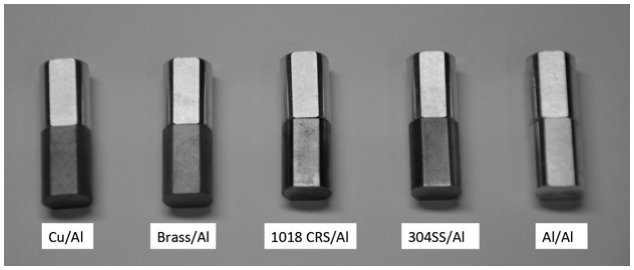

Figure 1b *Galvanically coupled aluminum specimens and stand alone aluminum specimen exposed to ethanol E100 with 0.5% water for a period of 24 hours at 78°C.*

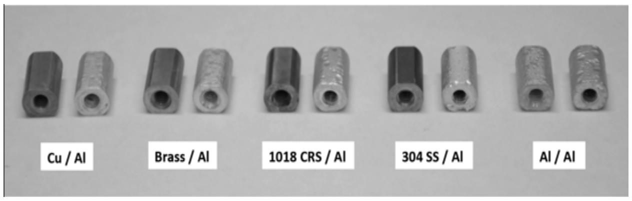

Figure 2a. *Separated galvanic couples of Al 1100 with copper, cartridge brass, 1018 carbon steel and 304 stainless steel after exposure to anhydrous ethanol E100 for a period of 24 hours at 78°C.*

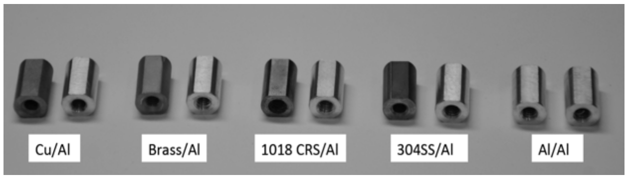

Figure 2b. *Separated galvanic couples of Al 1100 with copper, cartridge brass, 1018 carbon steel and 304 stainless steel after exposure to ethanol E100 with 0.5% water for a period of 24 hours at 78°C.*

Due to rapid reaction progression under these conditions, an attempt to quantify corrosion rates would not be very useful. Therefore, test outcomes are reported in a binary 'yes' or 'no' format. In the case of a 'yes' result, for all intents and purposes, the aluminum sample was heavily attacked in a 24 hour time period. In the case of a 'no' result, no appreciable corrosion was observed. Experience in this laboratory has shown that if the reaction does not initiate in the first 24 hours, then it likely will not initiate on a much longer time scale. The data presented in Table 1 are specifically for type 1100 aluminum, but it should be noted that similar results were obtained for a series of several cast aluminum alloys as well. This observation indicates that the specific structure (wrought vs. cast, presence of largely un-attacked second-phase particles of much different composition than the base alloy) is not very important to the corrosion mechanism(s). Rather, it appears that aluminum is fundamentally incompatible with dry ethanol.

Table 1 *Temperature and water concentration corrosion dependence of Al 1100 in E100 over a 24 hour time period. 'Yes' indicates rapid aluminum corrosion under designated conditions, whereas 'No' indicates no appreciable corrosion observed.*

Temperature (°C)	**Water Content**						
	≤50ppm	**200ppm**	**0.1%**	**0.5%**	**1%**	**5%**	**10%**
20	**No**	**No**	**No**	**No**	**No**	**No**	**No**
40	**No**	**No**	**No**	**No**	**No**	**No**	**No**
60	**No**	**No**	**No**	**No**	**No**	**No**	**No**
80	**Yes**	**Yes**	**No**	**No**	**No**	**No**	**No**
100	**Yes**	**Yes**	**Yes**	**No**	**No**	**No**	**No**
120	**Yes**	**Yes**	**Yes**	**No**	**No**	**No**	**No**
160	**Yes**	**Yes**	**Yes**	**Yes**	**Yes**	**No**	**No**
200	**Yes**	**Yes**	**Yes**	**Yes**	**Yes**	**No**	**No**

Ethanol Concentration

Increasing concentrations of ethanol in the anhydrous synthetic fuel blend resulted in increasingly rapid rates of corrosion. As depicted in Figure 3, aluminum is essentially immune to corrosion in E0 for the conditions of this experiment. In E5, there are isolated, shallow indications of corrosion initiating on the surface. In E10, there are multiple, shallow areas of attack on the surface. In E15, the areas of attack are widespread, with increasingly large sections of the surface area being affected, and areas of corrosion are substantially overlapping. In E20, the entire surface layer has been attacked and aluminum is dissolving at a high and generally uniform rate. In addition to the results depicted here, examinations were also conducted in E50, E85 and E100, all of which resulted in even more extensive corrosion of the metallic specimen. Several cast aluminum alloys were also tested; all yielded generally similar results. Reaction products included hydrogen gas, an amorphous combination of aluminum oxide, aluminum hydroxide and aluminum oxy-hydroxide, as well as metallic second phase particles from the cast alloys, which were verified by SEM, EDX and XRD experiments.

Figure 3. *Corrosion of aluminum in increasing concentrations of dry ethanol synthetic fuel blend C at 120°C for a 24 hour time period.*

Pretreatment

Representative results for three of the eight aluminum alloys receiving pretreatments and subsequently tested for corrosion susceptibility in ethanol are shown in Figure 4. In all cases, the treated alloys fared better than the untreated alloys. In general, the treated alloy exhibited less coverage of active corrosion for a fixed exposure period than did the untreated specimen. It should be noted that when the corrosion occurs on the treated alloys, it progresses in a similar fashion to the untreated alloys albeit with a longer incubation period. In general, treated alloys with low levels of copper, manganese and zinc exhibited higher levels of immunity from corrosive attack. In some cases, the reaction product, after saturating the limited solution volumes, would precipitate on available surface, including that of the specimen, and the reaction rate would rapidly decrease due to a lack of available reaction sites. This phenomenon will be explored further in the next section.

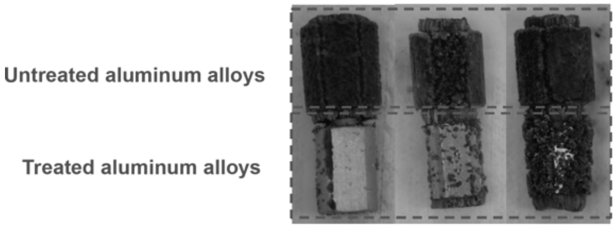

Figure 4. *Aluminum alloys exhibiting corrosion in treated and untreated conditions. Pretreatment included immersion in dilute acid followed by boiling in purified water. Specimens were exposed to anhydrous E100 at 78°C for 72 hours.*

Corrosion Mechanism

According to the open literature on the subject, aluminum can corrode in alcohol in either a 'wet' pathway or a 'dry' pathway. [5-7] Depending on environmental conditions such as temperature, water concentration, exposure time, etc., one reaction may dominate over another, i.e., these reactions do not necessarily occur sequentially. The wet and dry family of reaction pathways is:

Wet Corrosion (passivating)

$$4Al_{(s)} + 3O_{2(g)} \longrightarrow 2Al_2O_{3(s)}$$

$$Al_2O_{3(s)} + nH_2O_{(bulk)} \longrightarrow xAlO(OH)_{(s)} + yAl(OH)_{3(s)}$$

$$Al_{(s)} + 3H_2O_{(bulk)} \longrightarrow Al(OH)_{3(s)} + 3/2\ H_{2(g)}$$

Dry Corrosion (destructive)

$$Al_{(s)} + 3C_2H_5OH_{(l)} \longrightarrow Al^{3+}{}_{(dissolved)} + 3C_2H_5O^{-}{}_{(dissolved)} + 3/2\ H_{2(g)}$$

$$Al^{3+}{}_{(dissolved)} + 3C_2H_5O^{-}{}_{(dissolved)} \rightleftarrows Al(C_2H_5O)_{3(s)}$$

$$Al(C_2H_5O)_{3(s)} + 3\ H_2O_{(trace)} \longrightarrow Al(OH)_{3(s)} + 3C_2H_5OH_{(l)}$$

When metallic aluminum contacts either oxygen or water it will rapidly passivate forming a protective oxide layer on the aluminum surface. Under dry ethanol conditions, when the underlying metallic aluminum becomes exposed (through mechanical, chemical or other means), the metal cannot reform a passive layer due to the absence of oxygen and water, and corrosion proceeds unabated. As temperature increases, it is postulated that the mismatch of the thermal expansion coefficients for aluminum and aluminum oxide/hydroxide cause the outer passivated surface layer to crack, exposing metallic aluminum below the surface. Yoo et al., has suggested that the presence of anhydrous ethanol may also serve to dehydrate the passive film, leading to further cracking. [5] The corrosion reaction initiates at these discrete microcrack locations, gradually enlarging as metallic aluminum dissolves and hydrogen is generated. As the areas subject to corrosion increase, the reaction quickly accelerates leading to rapid general corrosion over the entire surface of the metal. Before the general corrosion can occur, there is a finite incubation time, typically on the order of a few hours, during which the passive layer becomes undermined possibly via coalescence of microcracks.

In aluminum alloys, second phase material does not dissolve as the reaction proceeds and remains behind in the growing areas of corrosion. The corroded surface turns black and becomes quite porous as aluminum continues to rapidly dissolve. Figure 5 demonstrates how the corrosion reaction proceeds under dry ethanol conditions for an aluminum alloy at 78°C. Figure 6 shows high magnification SEM images of the reaction sequence for the specimens depicted in Figure 5. During the first 12 hours, the sample loses mass as aluminum attack spreads over the exposed surface. General corrosion spreads from the initiation point in all directions and corrosion proceeds until the entire surface becomes active. At some point beyond 12 hours, the specimen starts to regain mass as corrosion product, presumably aluminum ethylate, $Al(C_2H_5O)_3$, begins to precipitate on the metal surface. The precipitation of corrosion products appears to slow the reaction rate considerably. This result appears to be an effect of using a small volume of test fuel, which becomes saturated with dissolved species from the corrosion reaction. Under test conditions at higher temperatures or in larger solution volumes, this decrease in reaction rate was not observed. At temperatures above 100°C, a very drastic and sudden spike in pressure (~500 psi) and temperature is observed after an incubation time typically between 3 to 5 hours. For the volume of solution used and size of the reaction vessel, this rapid pressure spike signals the reaction is nearing completion; in most cases the remaining metal is completely consumed over a period of less than a minute from the onset of the pressure spike. The rapid generation of hydrogen at the microcracks in the oxide layer serves to further disrupt the passive oxide layer. This sudden spike in temperature and pressure is likely the culmination of all the discrete initiation points coalescing into a single monolith of exposed metallic aluminum.

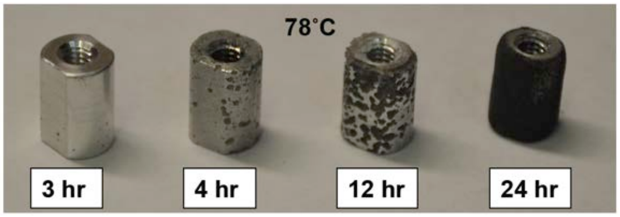

Figure 5. *Aluminum alloy corrosion progression over a 24 hour time period. Specimens were exposed to anhydrous E100 at 78°C.*

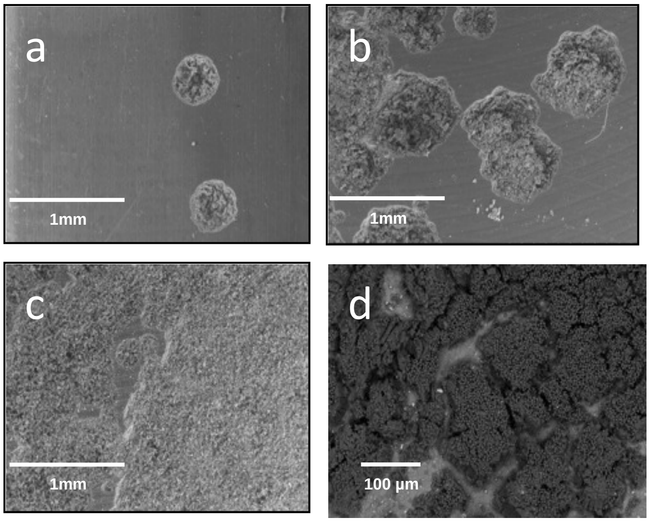

Figure 6. *SEM images of aluminum alloy exposed to anhydrous E100 at 78°C for time periods a) 3 hours b) 4 hours c) 12 hours and d) 24 hours, corresponding to the specimens in Figure 5.*

Conclusion

On-going investigation of aluminum compatibility with ethanol containing fuels has shown that aluminum and dry ethanol are fundamentally incompatible. It has been demonstrated that aluminum is most vulnerable to extensive corrosion in ethanol environments having trace water concentrations, at elevated temperature, and after exposure times on the order of hours. Fortunately, most real-world aluminum ethanol contact does not happen under conditions that allow for “dry” corrosion in ethanol to occur. The present study was carried out under tightly controlled laboratory conditions, using reagent grade simulated fuel. Therefore, the effect of impurities from the field is currently unknown and worthy of future study. Observations of aluminum/ethanol corrosion from the field appear to be isolated to areas where uncombusted fuel is allowed to pool and stagnate. Aluminum alloy engines running on E85 have been in operation for over 10 years and have shown very minimal susceptibility to this type of corrosion in ethanol. What has been learned in the present study can summarized as follows: on exposure to dry ethanol, aluminum exhibits a finite incubation period during which time the passive oxide layer is penetrated, exposing the reactive base metal to ethanol with which it rapidly reacts. The reactivity rate is strongly dependent on the concentration of water in the ethanol fuel. At water concentrations below 1%, aluminum is susceptible to rapid rates of corrosion at temperatures above 80°C. High levels of water suppress aluminum reactivity with ethanol, by allowing the passive aluminum oxide or hydrated aluminum oxide layer to remain protective or to reform if penetrated. Viable routes for investigation to mitigate this reactivity/corrosion problem include: (a) the development of an aluminum alloy composition that allows for a more tenacious, less defective, passive oxide layer and/or a more rapid reforming of a protective layer, especially at lower water levels; and (b) development of an additive package that is compatible with engine performance and fuel economy that decreases aluminum reactivity in the presence of ethanol. The former approach, alloy development, would start with modeling of the alloy with computational thermodynamics to reduce the design space. The latter, an additive package, might begin with the inclusion of known aluminum passivating agents, or at the very least, setting a lower bound for acceptable water concentration in ethanol containing fuels.

REFERENCES

[1] The Energy Policy Act of 2005 (EPAct 2005, P.L. 110-58), The Energy Independence and Security Act of 2007 (P.L. 110-140, H.R. 6) See http://www.ethanol.org/index.php?id=78.

[2] Vargel C. Corrosion of aluminum. Oxford: Elsevier Ltd: 2004.

[3] Kirk DW. Conductivity of gasoline ethanol water mixtures. Fuel 62 (1983) 1512–3.

[4] Niven, R.K. Ethanol in gasoline: environmental impacts and sustainability review article. Renewable and Sustainable Energy Reviews 9 (2005) 535-555.

[5] Yoo, Y.H.; Park, I.J.; Kim, J.G.; Kwak, D.H.; Ji, W.S. Corrosion characteristics of aluminum alloy in bio-ethanol blended gasoline fuel: Part 1. The corrosion properties of aluminum alloy in high temperature fuels. Fuel 90 (2011) 1208-1214.

[6] Scholz M, Ellermeier J. Corrosion behavior of different aluminum alloys in fuels containing ethanol under increased temperatures. Mat –wiss U Werkstofftech 2006:37: 842-51.

[7] Kruger, L.; Tuchscheerer, F.; Mandel, M.; Muller, S.; Liebsch, S., Corrosion behavior of aluminum alloys in ethanol fuels, J Mater Sci, (2012) 47: 2798-2806.

[8] Pawel, S.J.; Kass, M.D.; Janke, C.J.; Preliminary Compatibility Assessment of metallic dispenser materials for service in ethanol fuel blends. ORNL/TM-2009/286.

[9] Nie, X.; Li, X; Northwood, D. Corrosion Behavior of metallic materials in ethanol-gasoline alternative fuels. Materials Science Forum Vols. 546-549 (2007) 1093-1100.

[10] Kane, R.D.; Maldonado, J.G. Stress Corrosion Cracking in Fuel Ethanol: a Newly Recognized Phenomenon. NACE Corrosion 2004 Paper No. 04543.

[11] Nakaguchi, G.M.; Keller, J.L.; Wiseman, E.L., Ethanol Fuel Modification for Highway Vehicle Use Final Report. Union Oil Company of California, ALO-3683-T1, 1979.

[12] The Engineering Society for Advancing Mobility Land Sea Air and Space, “Gasoline, Alcohol, and Diesel Fuel Surrogates for Materials Testing”, SAE J1681 Revised Jan 2000.

[13] Harrigan, M.J.; Banda, A.; Bonazza, B.; Graham, P.; Slimp, B. A Rational Approach to Qualifying Materials for Use in Fuel Systems. SAE 2000-01-2013.

[14] Pawel, S.J.; Manneschmidt, E.T., Journal of Nuclear Materials 318 (2003) 355-364.

Agreement 18571 – Materials Issues Associated with Exhaust Gas Recirculation Systems

M. J. Lance, M. K. Ferber, C. S. Sluder, J. M. E. Storey*, Samuel A. Lewis Sr.*, and H. Z. Bilheux*[#]
Ceramic Science and Technology Group
Oak Ridge National Laboratory
P.O. Box 2008, MS 6068, Bldg. 4515
Oak Ridge, TN 37831-6068
(865) 241-4536; fax: (865) 574-6098; e-mail: lancem@ornl.gov
** Fuels, Engines and Emissions Research Center, ORNL*
 # Neutron Scattering Science Division, ORNL

DOE Technology Manager: Jerry L. Gibbs
(202) 586-1182; fax: (202) 586-1600; e-mail: Jerry.gibbs@ee.doe.gov
ORNL Technical Advisor: J. Allen Haynes
(865) 576-2894; fax: (865) 574-4913; e-mail: haynesa@ornl.gov

Contractor: Oak Ridge National Laboratory, Oak Ridge, Tennessee
Prime Contract No.: DE-AC05-00OR22725

Objectives

- Provide information to industry specialists about fouling deposit properties so as to enable improved models and potential design improvements to reduce fouling and its impact on the performance of EGR (exhaust gas recirculation) coolers.

Approach

- Assemble EGR engineers from member companies of the Diesel Crosscut Team to serve as an advisory board for this project.
- Develop a bench tube reactor for aging EGR deposits in a controlled environment.
- Obtain and evaluate EGR coolers from industry members that exemplify plugging failure.

Accomplishments

- Demonstrated a densification of the deposit through water condensation which led to an improvement of the thermal effectiveness of the model cooler tube.
- Characterized industry-provided deposits that exhibited the plugging failure mode.
- Investigated sample preparation methods for forming wavy model cooler tubes.

Future Direction

- The 2nd round of industry-provided coolers will continue to be characterized mainly using neutron tomography.
- Further use the exhaust sampling system to generate PM deposits that will be aged in controlled conditions using a bench tube reactor so as to evaluate the effects of water, hydrocarbon and cycling on deposit properties.
- Investigate the role of cooler geometry on deposit formation and removal.

Introduction

High-pressure exhaust gas recirculation (EGR) is the dominant NO_X-reduction technology used by the diesel engine community today. EGR reduces NO_x emissions by both lowering the oxygen present in the combustion chamber available to oxidize nitrogen, and by increasing the thermal mass of the intake charge due to the presence of CO_2 and H_2O in the exhaust which have higher specific heats than air. Cooling the exhaust gas through a heat exchanger (cooler) further increases the beneficial effects of EGR. Unfortunately, the recirculated gas also contains particulate matter (PM) and hydrocarbons (HCs) that may deposit on the inside of cooler through thermophoresis and condensation, respectively. Owing to the string-of-pearls nanostructure of PM, the deposit that forms has a porosity that exceeds 95% resulting in an extremely low thermal conductivity, only slightly higher than stagnant air [1]. Depending on the hydrocarbons present in the exhaust and the temperature of the EGR coolant, HCs will also condense inside the cooler.

In February of 2009, a team consisting of engineers responsible for EGR systems was assembled from nine diesel engine manufacturers: Caterpillar, Cummins, Detroit Diesel, Ford, GM, John Deere, Navistar, PACCAR (now DAF Trucks), Volvo/Mack and one heat exchanger supplier, Modine. They were asked what the biggest problem is facing EGR cooling systems and the clear winner was fouling. Over the course of this project, the EGR team has been notified of results generated and have contributed coolers for forensic analysis and have provided real-world coolers for analysis [2]. During this fiscal year, a second round of coolers was analyzed that tended to exhibit the plugging failure mode whereby the gas passages in the cooler become partially occluded due to a dense tar-like or lacquer-like deposits. In addition, model deposits generated by an engine recommended by the EGR team were aged using a bench tube reactor in order to establish a refreshment strategy whereby the thermal effectiveness of the cooler may be improved during use.

Results

Laboratory-Generated Deposits

A GM 1.9 L engine on a Drivven controller was used to foul model cooler tubes under both a light-duty and a heavy-duty condition. The tube sampler is based on a previous sampling system designed at ORNL that directs exhaust gas through square tubes that are externally-cooled to temperatures similar to those existing in actual EGR coolers.

Following deposit formation using the engine and tube sampler, a bench tube reactor is used for accelerated aging of deposits at controlled temperatures and gas composition. This allows for the characterization of microstructural changes that occur in the deposits due to engine transients, and water/HC condensation without the use of a full-scale engine and all the costs that come with it. This tube reactor (shown in Figure 1) was significantly redesigned this year to correct problems encountered with the temperature control and water content. The furnace was placed much closer to the heat exchanger which significantly lowered the heat loss and allows inlet temperatures up to 450°C to be reached. The heat exchanger is on a moveable track which makes it easier to remove and replace the tubes in the heat exchanger. The water coolant is flowing from the bottom of the heat exchanger to the top which ensures the tube is completely immersed in coolant at all times. The outlet gas temperature is now measured exactly at the end of the tube at the center of the tube cross-section. The previous approach placed the outlet thermocouple within a marmon cap which measured temperatures a few millimeters away from the tube outlet. Also, the marmon cap at the inlet has been removed and the entire heat exchanger shortened so that the inlet side of the model tube is swaged directly on to the tube from the furnace which greatly reduces leaks. The absence of leaks was confirmed by measuring the actual flow using a gillibrator and comparing it to the flow rate programmed into the mass flow controller. The lack of the marmon cap also aids in controlling and measuring the gas temperature entering into the heat exchanger. The system is equipped with multiple thermocouples to monitor gas temperature before and after the cooled tube and the coolant entry and exit temperatures as well as the furnace temperature.

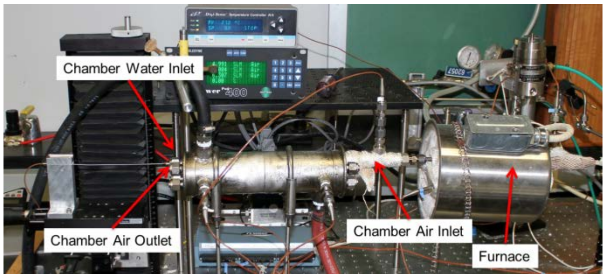

Figure 1. The bench tube reactor system used for aging deposits.

The most important improvement to the bench tube reactor design was the use of a water pump to saturate the inlet gas with water shown in Figure 2. The previous approach used a mass flow controller and bubbler but the bubbler was unable to handle the large flow rates required with this system. This approach injects water at a controlled volume into a tube wrapped with heat tape that turns the water into steam. This steam supply line is connected to the dry air supply line. The water pump allows one to saturate the inlet gas with water at flows up to 20 SLM.

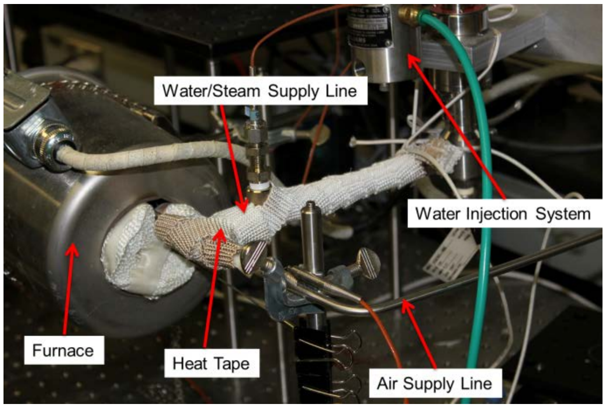

Figure 2. Details of the water injection system.

The effectiveness (ε) of a heat exchanger is defined as the actual heat transfer divided by the maximum possible heat transfer. This can be further defined in terms of temperatures according to Equation (1):

$$\varepsilon = (T_{Gas\ In} - T_{Gas\ Out}) / (T_{Gas\ In} - T_{Coolant\ In}) \qquad (1)$$

The effectiveness, then, is the ratio of the actual change in temperature of the EGR gas stream divided by the maximum change in temperature that the EGR gas stream could have experienced by being cooled to the temperature of the coolant. Since actual heat transfer rate for a given heat exchanger depends upon the flow rates and properties of the gases and coolants, effectiveness also varies with these characteristics independent of fouling. Nevertheless, it is a useful measure of performance as it is easily calculated from measurable quantities.

The tube reactor is now completely controllable using a LabView interface shown in Figure 3. This allows one to control the inlet and coolant temperatures and the flow rate while measuring the temperatures at 7 locations in the system.

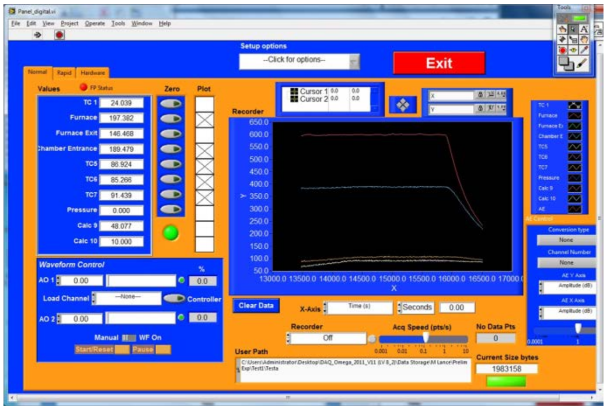

TC 1 24.039
Furnace 197.382
Furnace Exit 146.468
Chamber Entrance 189.479
TC5 86.924
TC6 85.266
TC7 91.439
Pressure 0.000
Calc 9 48.077
Calc 10 10.000
AO 1 0.00 % 0.0
Load Channel --None-- Controller
AO 2 0.00 % 0.0
X-Axis Time (s) Seconds 0.00
Recorder Off
Acq Speed (pts/s)
No Data Pts 0
User Path C:\Users\Administrator\Desktop\DAQ_Omega_2011_V11 (LV 8_2)\Data Storage\M Lance\Prelim Exp\Test1\Testa
Current Size bytes 1983158
Conversion type None
Channel Number None
AE Y Axis Amplitude (dB)
AE X Axis Amplitude (dB)

Figure 3. LabView virtual instrument used to control and measure the tube reactor.

The effectiveness of the heat exchanger during a water condensation experiment is shown in Figure 4. Here, the effectiveness starts at ~80% but after injecting 10 vol % water, it increases to ~85%. This change is due to the water in the gas condensing on the cold metal wall (which was cooled to 10°C) and collapsing the soot porosity, thereby increasing its thermal conductivity. This experiment supports our proposal that water condensation can be used as a method to refresh the EGR cooler during use by altering the deposit thermal properties.

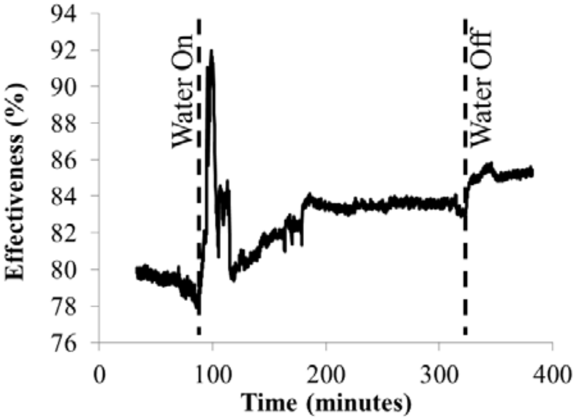

Figure 4. The effectiveness of a fouled tube during a water condensation experiment.

The effect of water condensation on the deposit microstructure can be seen by comparing the deposit surface near the inlet of the tube where no water condensed (Figure 5A) to the outlet where water had condensed (Figure 5B). Deposits appeared much denser and less uniform near the outlet. This suggests that the water is collapsing the PM nanostructure causing it to densify which in turn increases its thermal conductivity. Since the deposit is >95% porous, there is the potential to greatly improve its thermal properties by collapsing the PM nanostructure through water condensation. These results show the potential of refreshing the EGR cooler by changing the engine operating conditions so as to condense water or HC on the deposit.

Industry-Provided Samples

In a first round of testing, eight companies provided twelve coolers for forensic analysis of the cooler deposits, the results of which were published in Ref. 2. A criticism of that work was that little information was provided about the operating conditions of the engines that produced the EGR coolers came from. Therefore, a second round of coolers was requested except this time with more information about the origins of the coolers. Specific operating conditions were requested that would represent common fouling conditions of coolers. Most of the coolers represented low temperature idling conditions (typical of a school bus, for instance) which tend to produce a plugging failure mode.

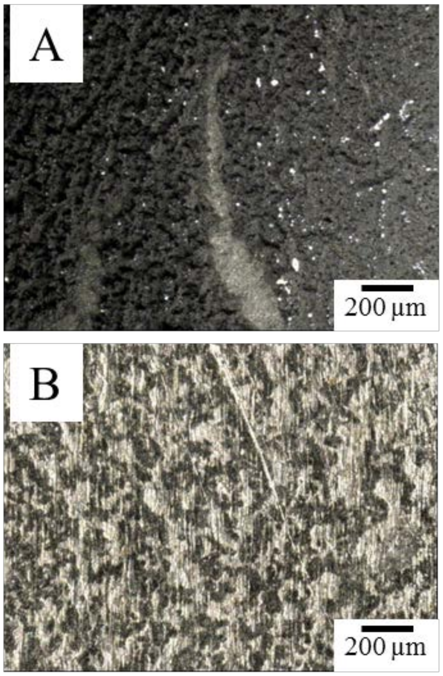

Figure 5. The deposit surface near the inlet (A) and the outlet (B) following the water condensation test shown in Figure 4.

Figure 6 shows the weight of the deposit relative to the surface area for both the first and second round of coolers. The plugging of these coolers is reflected in Figure 6 by heavier deposit masses compared to the first round of coolers. Figure 7 shows the volatile fraction which is also higher in the 2nd round of coolers which suggest that they were produced during lower temperature combustion regimes which would leave partially burned fuel in the exhaust available for condensation. Four of the coolers in Figures 6 and 7, indicated by the arrows and blue colored bars, clearly exhibited plugging and were analyzed in more detail.

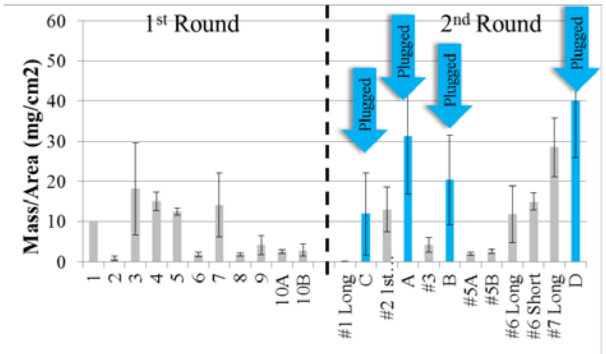

Figure 6. Mass per area (mg/cm^2) of deposit on industry-provided coolers.

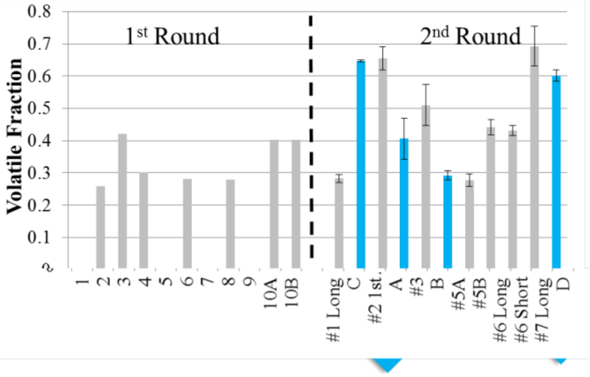

Figure 7. Volatile fraction of deposit from industry-provided coolers.

Of the four coolers that were plugged, coolers A and B were both lacquer-like and had the lowest ash content as shown in Table 1. The lacquer deposit was brittle and lustrous, which is highly unlike the soft friable deposit typically seen in EGR coolers. Cooler C burned at a low temperature, had lower volatile content and showed exothermic spikes during oxidation. Cooler D was very wet and oily and contained the most ash which suggests that it formed due to a failure in a lubricant seal and was not caused by normal operation.

Table 1. The volatile and ash content for the four plugged coolers measured by thermogravimetry.

Cooler	Volatile	Ash	Description
A	78%	0%	Shiny Brittle Lacquer
B	55%	1%	Lacquer and soot
C	26%	8%	Dry, Crumbly
D	59%	13%	Oily, wet

Pyrolysis GC-MS revealed the composition of the lacquer-like deposits (coolers A and B) to be variants of 2 to 5-ring polycyclic aromatic hydrocarbons (PAHs) and oxygenated PAHs with a narrow range of melting points and no fuel or paraffin species. These "proto soot" compounds that have not lost all of the hydrogen necessary to become particulate carbon condense to form a brittle deposit at room temperature but will readily melt and coat the metal surface at temperatures expected within the EGR cooler during operation as shown in Figure 8. These observations compare well to recent work that found that lacquer deposits in EGR coolers formed from resinification of phenols through contact with formaldehyde and high amounts of NOx which produces nitric acid that acts as a catalyst for the reaction [3]. Maintaining the EGR wall temperatures above the dew points of the PAHs in the gas is critical for preventing the formation of the lacquer.

Figure 8. The image on the left is a lacquer-like deposit from cooler A at 25°C. On the right, the same deposit at ~140°C after melting. Image width is 9 mm.

Neutron tomography was also used to characterize the lacquer deposit from cooler A. Since neutrons transmit through metal and are attenuated by hydrogen, hydrocarbon in the deposit will preferentially block neutrons from transmitting to the detector. One ¾ inch segment of cooler A was rotated and 360 images collected and reconstructed to provide a 3-D tomograph of the sample as shown in Figure 9. In between the wavy fins of the heat exchanger the deposit can be seen occluding the gas passages. The deposit contains closed porosity, or bubbles, that will have the effect of increasing the volume of the deposit making the plugging problem even worse. These bubbles were also observed as the deposit was heated in air.

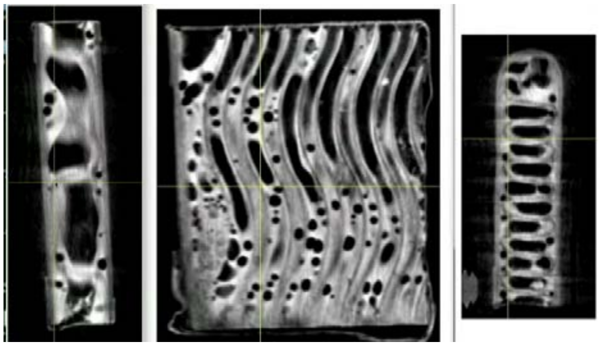

Figure 9. Three orthogonal views of cooler A from a neutron tomograph.

The thermal conductivity of the deposit from cooler A was measured to be 0.11 W/mK which was not as low as the fluffy deposit typically seen during stabilized effectiveness loss [1] but was still low enough to severely degrade the thermal effectiveness of the cooler.

Cooler C was also plugged but had much lower amounts of HC present and appeared dry and crumbly with no lacquer present. It contained similar HC species (as measured with pyrolysis GC-MS) to coolers A and B but at far lower concentrations and more dispersed by PM. It is speculated that the PM may be hindering the gas-liquid phase reaction that produces lacquer. ***Cooler Geometry***

In previous work conducted on this project [2], deposit removal on industry-provided coolers was observed to occur on the leading edges of turbulation structures like the sinusoidal fin shown in Figure 9. In order to better understand how the cooler geometry influences both deposit formation and removal, a foot-long model cooler tube was fabricated out of titanium with an electron beam using additive manufacturing. Figure 10 shows the CAD drawing that was used to design the tube geometry and the resulting fabricated tube. This is just the first attempt at forming tubes in this way but we anticipate that we will be able to use additive manufacturing to investigate geometry effects on fouling using our own engine and tube sampler.

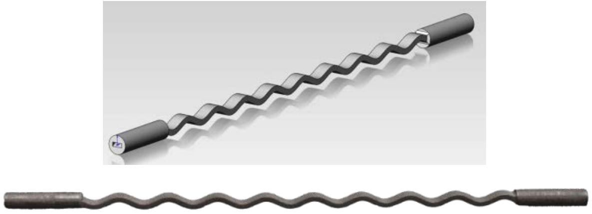

Figure 10. CAD drawing (top) and manufactured wavy tube (bottom) that simulates a single channel in a heat exchanger.

In addition to the experimental work described above, three new pieces of equipment were installed during this fiscal year; a Keyence digital microscope and optical profiler, a TA Instruments Q5000IR thermogravimetric analyzer (TGA) and a Pfeiffer mass spectrometer (MS) attached to the TGA. It is anticipated that these tools will help us to better characterize EGR deposits in the future.

Conclusions

- A team of industry advisors has been assembled that will help guide future research directions of this pre-competitive research.
- Laboratory-generated deposits were successfully densified through water condensation thereby improving the thermal conductivity of the deposit and the thermal effectiveness of the cooler tube.
- Forensic analysis of a second round of cooler deposits that exhibited plugging showed the presence of lacquer-like deposits that are formed during engine operation by a reaction between condensed PAHs and aldehydes in the exhaust.
- The first wavy tube that will be used to study geometry effects on cooler fouling was fabricated using additive manufacturing.

References

1. Michael J. Lance, C. Scott Sluder, Hsin Wang, John M.E. Storey, "Direct Measurement of EGR Cooler Deposit Thermal Properties for Improved Understanding of Cooler Fouling," SAE 2009-01-1461.
2. Michael Lance, Charles Scott Sluder, John M.E. Storey, and Samuel A. Lewis "Characterization of Field-Aged EGR Cooler Deposits," SAE 2010-01-2091.
3. N. Furukawa, et al., "On the mechanism of exhaust gas recirculation valve sticking in diesel engines," *International Journal of Engine Research*, September 2012.

Publications and Presentations

- J.M.E. Storey, C.S, Sluder, M.J. Lance, D. Styles, and S. Simko, "Exhaust Gas Recirculation Cooler Fouling in Diesel Applications: Fundamental Studies, Deposit Properties and Microstructure," in press Heat Transfer Engineering (2012).
- Michael J. Lance, C. Scott Sluder, Matt K. Ferber, John M.E. Storey and Hassina Bilheux, "Materials Issues Associated with EGR Systems," Advanced Engine Cross-cut Team Meeting, March 15, 2012.
- Michael J. Lance, John M.E. Storey, C. Scott Sluder, Samuel A. Lewis Sr., and Hassina Bilheux, "Plugging of Exhaust Gas Recirculation Coolers," 2012 DEER Conference.

Agreement 19192 - Titanium for Vehicle Propulsion Applications

Principal Investigators: Curt A. Lavender and Vineet Joshi
Energy Materials Group
Pacific Northwest National Laboratory
PO Box 999, MS K2-44
Richland, WA 99352
(509) 372-6770; fax: (509) 375-2186; e-mail: curt.lavender@pnl.gov
(509)372-6211; fax (509)375-2186; e-mail: vineet.joshi@pnl.gov

Yong-Ching Chen
Cummins Inc.
(812) 377-8349; e-mail: yong-ching.c.chen@cummins.com

Vladimir Moxson
ADMA Products Inc.
(330)650-4000; e-mail: moxson@admaproducts.com

DOE Technology Manager: Jerry L. Gibbs
(202) 586-1182; fax: (202) 586-1600; e-mail: jerry.gibbs@ee.doe.gov

Field Technical Manager: Dean Paxton
(509) 375-2620; fax: (509) 375-2186; e-mail: dean.paxton@pnl.gov

---

Contractor: *Pacific Northwest National Laboratory*
Contract No.: *DE-AC05-76RL01830*

Objective

- Increase the efficiency of vehicle engines by reducing the mass of rotating and reciprocating components through the use of titanium and titanium alloys.
- Increase the efficiency of vehicle engines by increasing the operating temperature of selected components through the use of titanium and titanium alloys.
- Predict the engine efficiency improvements made possible through the use of titanium.

Approach, Including Industrial Partner/Collaborator and Path to Technology Transfer and Commercialization

- Develop, prototype, and evaluate the performance of components at Cummins Inc. to ensure that components developed produce the predicted performance improvements in actual engine systems.
- Use suppliers to fabricate most titanium components to ensure that processing used is prototypic of a full-scale production process.

Milestone, Metrics and Accomplishments

- The Ti6Al4V alloy produced from TiH_2 powder was hot-worked in the alpha plus beta phase field and heat treated to produce a highly refined duplex structure. The fatigue life from the Ti6Al4V was measured and matched the wrought processed handbook values for the alloy.
- The low-cost beta titanium alloy Ti1Al8V5Fe processing schedule was enhanced and exhibited fatigue properties equal to the reported values from wrought processing.

- Two engine components have been identified for further development and ultimately systems testing at Cummins Inc.

Future Direction

- Complete fabrication of forge blanks of low-cost Ti6Al4V from titanium hydride for rotating component applications.
- Complete fabrication of bar stock of low-cost Ti1Al8V5Fe from titanium hydride for reciprocating component applications.
- Complete cost analysis of the ADMA Products Inc. process for Ti6Al4V and Ti1Al8V5Fe production.

Introduction

This project is a collaborative effort between Cummins Inc., ADMA Products Inc., and Pacific Northwest National Laboratory (PNNL) focused on the development and evaluation of low-cost titanium components produced by emerging low-cost titanium production technologies.

Over the past 30 years, many original equipment manufacturers, researchers, and titanium companies have demonstrated titanium's ability to increase internal combustion engine efficiency. However, titanium has only been used in a limited number of production applications and sometimes only over limited production periods. Even though performance benefits resulting in engine efficiency improvements of as much as 20 percent have been demonstrated, the high cost of producing titanium components using current technologies has been a limiting factor.

In recent years, the Department of Defense (DOD) and the commercial aerospace industry (the largest consumers of titanium) have become increasingly reliant on titanium to meet performance needs. A study commissioned by the Defense Logistics Agency revealed that not only was the titanium raw material costly, but the manufacturing processes used to produce titanium components often had production yields of 5 percent, meaning that the DOD was buying as much as much as 20 times the titanium as was used in the final application. To address this cost, the Defense Advanced Research Projects Agency (DARPA) began an activity to reduce titanium component cost. DARPA started many titanium-related activities and new low-cost-titanium development projects, and stimulated titanium production activity throughout the world—with as many as 20 production methods under development.

In prior reporting periods, this project was focused on assessing "emerging" low-cost development activities by using technical evaluation and cost modeling to analyze the products for suitability in vehicle and engine applications. It was determined that two of the processes, developed by International Titanium Powder and ADMA Products Inc., could produce titanium raw materials at costs that approach those needed to achieve widespread titanium usage and have an impact on the overall fuel economy in the United States.

The next step for these emerging processes is to identify applications and create a demand for the titanium to move them from development to full-scale production, thus meeting the cost projections associated with high-volume production.

The purpose of this project is to identify and demonstrate applications within the vehicle propulsion system which, when titanium is used, would produce an increase in engine and vehicle efficiency. The project will be performed in three topical areas: the first is focused on vehicle propulsion system modeling, the second is focused on technical development of the titanium semi-finished products, and the third is focused on technical demonstration of the components in systems-level tests.

The goal of the project is to use titanium, where appropriate, to increase the efficiency of vehicle propulsions systems. This report summarizes progress toward that goal.

Approach

This project will increase vehicle efficiency through use of titanium by 1) using vehicle system models to identify critical components to be made from titanium that will impact efficiency, 2) demonstrating that those critical components can be made from emerging low-cost processing, and 3) demonstrating efficiency improvements through systems-level tests at Cummins Inc.

Cummins Inc. identified components of interest and property targets for both the Ti6Al4V (alpha-beta) and Ti1Al8V5Fe (beta) alloys. In the current work, semi-finished components were produced and the effect of microstructure on the mechanical properties in the beta alloy was studied.

Results and Discussion

Ti6Al4V Component Forging and Fatigue Testing: During the previous reporting period, the hot forming process of Ti6Al4V was developed and initial mechanical tests and microstructural characterization were consistent with industry standards and conventional wrought processing for bar stock. This indicated that Ti6Al4V could be processed by TiH_2 powder metallurgy and produce wrought-like properties at 50 percent of the cost.

To capture additional potential automotive applications, a “blockier” product that can be machined into a final component is desirable. Typically, powder metallurgy parts are small and limited to non-fatigue-rated applications. However, due to the unique characteristics of the TiH_2 powder and titanium sinterability, it may possible to make large components from a powder metallurgy (P/M) compact and achieve fatigue performance. If demonstrated, the cost savings could be much greater than the previously demonstrated 50 percent. A simple P/M compact could be produced at 100 percent yield from a lower cost feedstock, replacing a forging produced at less than 50 percent yield, from a lower cost feedstock.

Therefore, the current work uses P/M compacts (billets) that were synthesized using powder produced using the ADMA process. The billets were then subjected to hot isostatic processing (HIP) and then hot-forged to produce semi-finished blanks that can be machined into automotive components. Mechanical tests on the billets were performed to evaluate the versatility of this novel process.

As per the requirements of Cummins Inc., the semi-finished billets were to measure 6 in. in diameter (ϕ) × 3.5 in. in length. Two sets of billets were produced:

1. Die pressed and sintered billets 6 in. in diameter × 3.5 in. in length.

2. Cold isostatically pressed and sintered billets with varying dimensions. The varying sizes were produced so that after forging the desired ϕ 6 in. × 3.5 in. in length billets were produced. The following dimensions were produced:
   a. ϕ 3.22 in. × 7.50 in. length
   b. ϕ 5.55 in. × 5.50 in. length
   c. ϕ 3.22 in. × 12.0 in. length

The samples a, b, and c were produced to undergo hot forging to get a reduction of 25, 50, and 75 percent in length, respectively, to produce the desired semi-finished dimensions.

The samples produced via die-pressing and sintering showed significant cracking. The low height to diameter ratio resulted in bending associated with spring-back upon ejection from the die. This bending resulted in cracking near the center of the compact, as shown in Figure 1a. The applied pressure was increased from 413 MPa (30 tons per square inch [tsi]) to 690 MPa (50 tsi) to reduce spring-back. However, this did not eliminate the cracking. The cracking was not healed during sintering and cracking was present in the sintering pressings as shown in Figure 1b. The die-pressing process was discontinued and the project is now focused on cold isostatic pressing (CIP) and sintering.

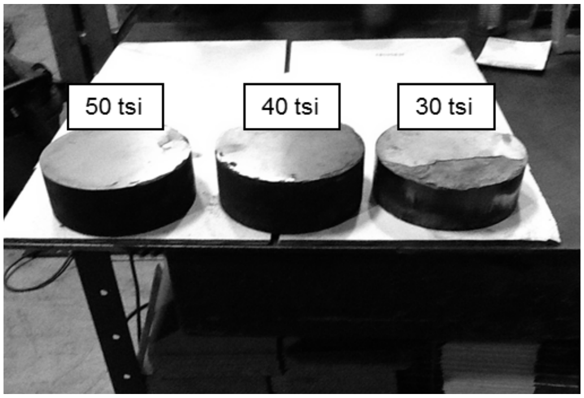

(a)

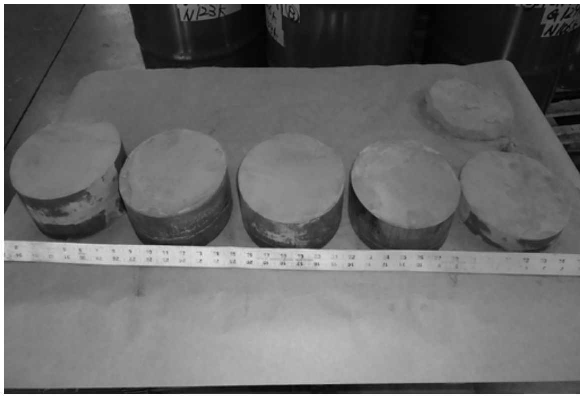

(b)

Figure 1: (a) Effect of uniaxial pressing on the Ti6Al4V green and (b) sintering.

Billets were produced by CIP in polyurethane tooling (Figure 2a) and sintered horizontally (Figure 2b). It should be noted that the billets were sectioned to the required length after sintering to the diameters described above. Billet densities were in excess of 93 percent of the theoretical density. No cracks were visible upon sintering.

Microstructural characterization of the as-sintered billets was performed and showed that the Ti6Al4V had a lamellar microstructure with grain size less than 150 µm (Figure 3). The lamellae were approximately 10 µm in width. The porosity was located at the grain boundaries. The chemistry of the billets was consistent with American Society for Testing Materials (ASTM) B348 standard requirements and described in Table 1. These results are consistent with FY11 work.

(a)

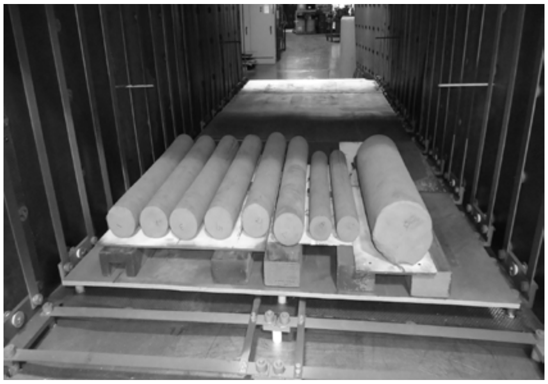

(b)

Figure 2: (a) The polyurethane tooling used for CIP operation. (b) The billets upon sintering in the furnace.

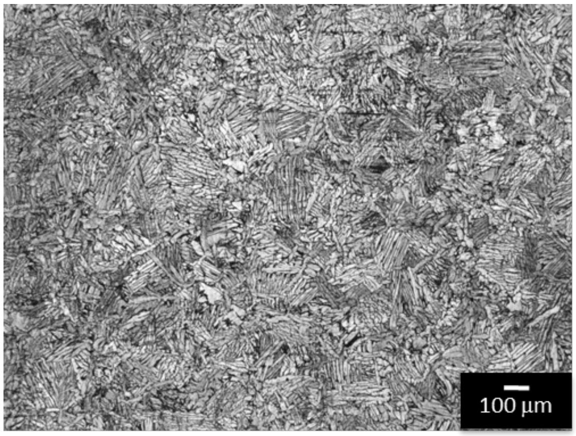

Figure 3: The microstructure of the Ti6Al4V billets after sintering.

Table 1: Chemistry of the as-cold isostatically pressed and sintered billets.

Grade	C	O	N	H	Al	V	Fe	Ti
Ti64	0.02	0.2	0.02	0.01	6.0	4.0	0.1	Bal

To reduce the porosity and improve the density of the as-sintered billets, it was decided that the billets undergo HIP prior to the forging operation. This was done to minimize the porosity in the samples, which would deteriorate the mechanical properties if persistent after forging. Thus, all material underwent HIP at Bodycote Inc. at 100 MPa pressure for 2 h at 950°C.

The next steps are to assess the density and microstructure of the hot isostatic processed samples and initiate forging operations, which will be followed by fatigue testing and component fabrication and testing.

Ti1Al8V5Fe Microstructure Property Evaluation: The mechanical properties of the Ti1Al8V5Fe were evaluated in FY11 and found superior to those described in the Materials Properties Handbook - Titanium Alloys of the American Society for Materials. Due to the novelty of the way in which the alloy was developed using the low-cost TiH_2 powder feedstock and the lack of any systematic investigations on the alloy properties in the literature, it was decided to correlate the mechanical properties with the microstructure. For this, a proposal was submitted to the national user facility (Environmental and Molecular Sciences Laboratory at PNNL) to conduct transmission electron microscopy (TEM) and atom probe tomography (APT) studies on the heat-treated Ti185 samples.

Figure 4 shows the effect of heat treatment on the tensile properties of Ti185. The elongation was between 4 and 8 percent in all samples. The samples with lowest and highest strength were specifically chosen for TEM and APT analysis. Figure 5a and b show backscattered electron (BSE) scanning electron microscopy (SEM) images. The microstructure of the sample solution treated at lower temperature (704°C) had a larger fraction of alpha than the ones treated at higher temperature (787°C). This indicates that the relatively coarse primary alpha formed during solution heat treat was not an effective strengthener.

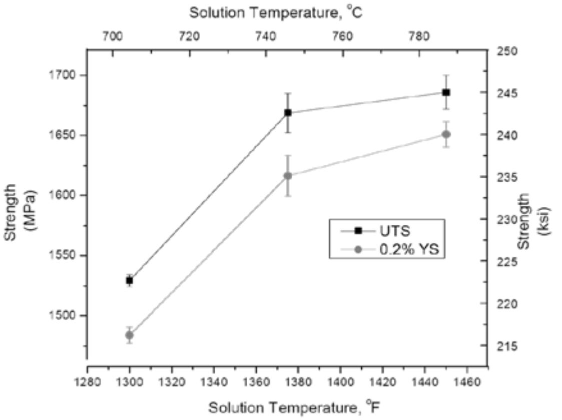

Figure 4: Tensile properties of Ti1Al8V5Fe as a function of solution treatment. (Note that all samples were later aged at 482°C for 2 h).

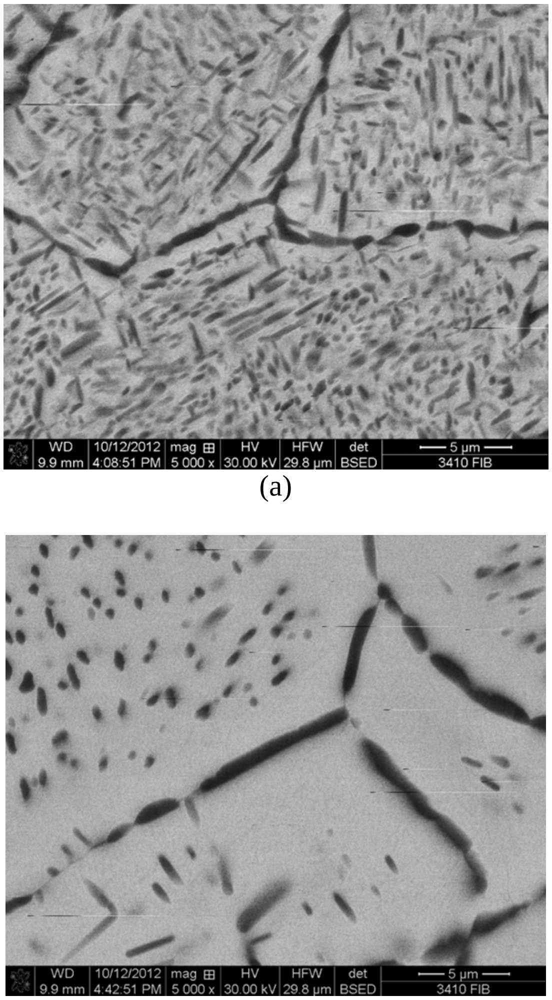

(a)

(b)

Figure 5: BSE-SEM images of samples solution treated at (a) 704°C and (b) 787°C.

TEM analysis of aged samples was performed and showed the presence of fine microstructural features as indicated by Figure 6. This feature is likely to be transformed beta (or secondary alpha, α_s). It was observed that the α_s phase in the 704°C heat treatment was up to 100 nm in width and 500 nm in length whereas when heat treated at 787°C the α_s was 25 nm in width and 100 nm long. More α_s appeared present in the 787°C heat treatment, which is likely due to the larger fraction of metastable beta available for transformation to α_s. In addition, APT analysis of the α_s in both samples revealed a similar chemical composition, indicating that α_s was likely the same phase for each heat treatment and that size and fraction was controlling strength of the Ti185 alloy.

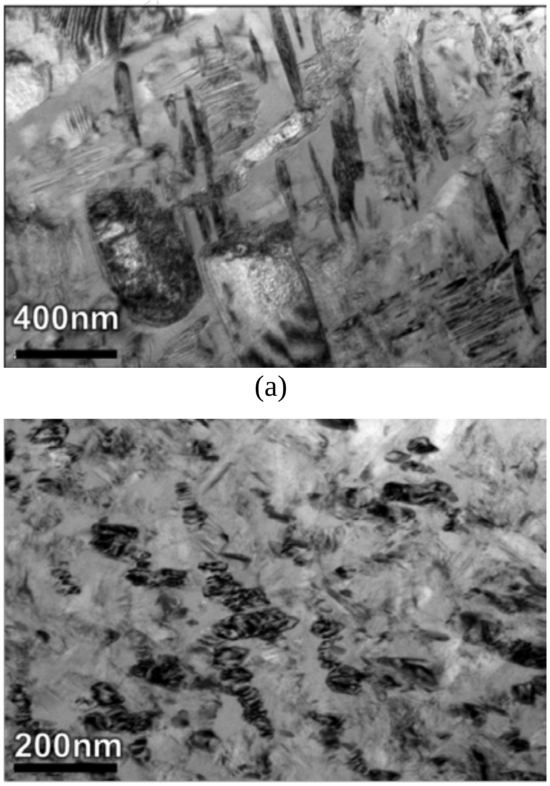

(a)

(b)

Figure 6: Bright field TEM image of an intra-granular region in a sample solution treated at (a) 704°C and (b) 787°C.

Therefore, the presence of smaller and high-volume fraction of α_s was responsible for the high strength, whereas the presence of large size and low volume fraction of α_s in the samples solution treated at lower temperatures was responsible for the lower strength.

Conclusions

During this reporting period, the following conclusions were reached:

- Ti64 billets were produced to develop the desired parts as requested by Cummins Inc.
- Detailed microstructural characterization of Ti185 was performed and analyzed.

Publications/ Contributions

Development of Ti-6Al-4V and Ti-1Al-8V-5Fe Alloys Using Low Cost TiH_2 Powder Feedstock
Vineet V. Joshi, Curt Lavender, Vladimir Moxson, Vlad Duz, Eric Nyberg, K. Scott Weil, Journal of Materials Engineering and Performance, DOI: 10.1007/s11665-012-0386-x, 2012.

Low Cost Titanium-Propulsion Applications
Lavender CA, YC Chen, and VS Moxson. 2011. "Low Cost Titanium – Propulsion Applications." Presented by Curt Lavender (Invited Speaker) at DOE-VTP Merit Review, Washington DC, DC on June 10, 2010. PNNL-SA-72900.

Development of High Strength Titanium Alloy Bar Stock from TiH_2 Powder
Curt Lavender (Invited Speaker); Elizabeth Stephens, Eric Nyberg; Vladimir Moxson; Volodymr Duz
Presented at TMS annual Meeting Seattle WA, February 2011.

Development of β and α+βTitanium Alloys Using a Low Cost TiH_2 Powder Feedstock
Vineet Joshi, Curt Lavender, Valdimir Moxson, Vlad Duz and Eric Nyberg. MS&T 2011
Conference & Exhibition, October 16-20, 2011
Columbus, Ohio.

Keywords

Titanium, titanium alloys, solid state consolidation, rod-rolling, beta titanium alloys, cold isostatic press and sinter, titanium alloy, and heat treatment.

Brief Description of Report

This report describes progress in the development of low-cost titanium for vehicle and propulsion system applications

Agreement 19202 – Titanium Friction and Wear: Surface Engineering of Connecting Rods and Other Bearing Components

Peter J. Blau
Oak Ridge National Laboratory, P. O. Box 2008, Mail Stop 6063, Oak Ridge, TN 37831-6063
(865) 574-5377; fax: (865) 574-4913; e-mail: blaupj@ornl.gov

DOE Technology Manager: Jerry L. Gibbs
(202) 586-1182; fax: (202) 586-1600; e-mail: Jerry.gibbs@ee.doe.gov
ORNL Technical Advisor: J. Allen Haynes
(865) 865-576-2894; fax: (865) 574-4913; e-mail: haynesa@ornl.gov

---

Contractor: Oak Ridge National Laboratory, Oak Ridge, TN
Prime DOE Contract Number DE-AC05-00OR22725

Objectives

- To increase the vehicle freight efficiency by substituting lightweight titanium (Ti) alloy moving parts and bearing surfaces into diesel engine and drivetrain components like connecting rods.
- To identify novel surface engineering approaches, including combinations of mechanical and diffusion treatments that can reduce friction and wear of commercial Ti alloys.

Approach

- Conduct friction and wear screening of candidate commercial and experimental surface treatments for Ti alloys (Phase 1), then down-select the most promising ones for further investigation under more simulative, load-varying, lubricated conditions (Phase 2).
- Design and build a computerized, variable load bearing test apparatus (VLBT) to apply the kinds of transient lubrication conditions that connecting rod large end bearings experience when in operation.
- Based on the results of Phase 1 and Phase 2 experiments, and using the VLBT, identify the best candidate surface treatments for Ti alloy connecting rods and similar applications. Prepare a final report summarizing experimental results and recommending an approach to enable the use of Ti alloys in friction and wear critical components in diesel engines.

Accomplishments

- More than 20 candidate surface engineering treatments and coatings from both commercial and experimental sources were selected and friction/wear screened under lubrication by diesel engine oil. Performance was ranked, communicated to industry, presented at an international conference, and published in an archival journal.
- A novel variable-load bearing test (VLBT) apparatus was built and used to rank the tribological performance of pre-screened surface treatments under transient bearing pressures like those in an engine.
- Relationships between applied bearing load and frictional behavior under transient lubricating conditions were determined. Comparison was made between VLBT results for the mixed and full-film lubrication regimes to Phase 1 results that emphasized material durability. A conserve, bearing insert-based approach for using Ti-alloy connecting rod large end bearings has been recommended.

Future Directions

- This project ended in September 2012 with the preparation of a final report and two journal publications. Surface engineering treatments continue to evolve, and new variants could be tested using the VLBT apparatus in collaboration with industry should the opportunity arrive.

Introduction

The Department of Energy's heavy vehicle research and development plan targeted a 50% increase in freight efficiency (measured in ton miles per gallon). A combination of approaches is being used to achieve this goal. This includes a reduction in parasitic losses (e.g., engine and drivetrain friction, aerodynamic drag, etc.), reduced tire rolling resistance, and the use of lightweight structural materials.

Properly processed and treated, titanium (Ti) based alloys are strong, corrosion-resistant, and lighter in weight than similarly sized steel or cast iron parts. Once used mainly in marine and aerospace components, Ti's use has expanded into areas as diverse as human joint replacements, dental implants, and sports equipment. Recent developments in processing raw materials promise to make Ti alloys more affordable and could expand their use into fuel-efficient heavy vehicles.

Despite their advantages, Ti alloys have a propensity to scuff, gall, and exhibit adhesive wear. Lubricant formulations designed for ferrous alloys do not work on bare Ti surfaces. If, however, the friction and wear of Ti alloys could be improved by surface engineering, there would be new opportunities to use them for pistons, cam shafts, valves, valve guides, crank shafts, and connecting rod bearing surfaces.

Approach

A two-phase approach was taken in this work:

Phase 1: Using an aggressive ASTM friction and wear test, pre-screen candidate surface engineering treatments and coatings.

Phase 2: Build a variable load connecting rod bearing simulator to study effects of transient normal force on down-selected surface treatments and coatings.

Having carried through this approach, a final report (ORNL Tech Report) was prepared. It contains recommendations on the advisability of using engineered Ti alloy surfaces for lubricated connecting rod bearings and other engine components subjected to sliding contact.

Progress in FY 10-11.

Screening of candidate surface treatments and coatings. Following a comprehensive literature review and discussions with suppliers, more than 24 candidate surface treatments and coatings for Ti ally Ti-6Al-4V were considered. About 20 were screened using a modified ASTM G133 reciprocating sliding friction and wear test. Publications listed at the end of this report describe the sources of the materials and the test results. Candidate treatments whose average friction coefficients (when lubricated by used oil) were below 0.15, and which survived a 400 m sliding distance were designated as 'passed.' In addition to a reference alloy (CDA 932 leaded bearing bronze), the following passed: a diamond film coating, a TiN hard coating, a CrN hard coating, oxygen-diffusion treated Ti alloy, and a nitrided Ti alloy.

Progress in FY 12

Effects of work hardening combined with diffusion treatments. Experiments probed the effects of combining mechanical treatments like shot peening or hammer planishing with diffusion treatments like nitriding and oxygen diffusion in order to determine whether synergistic benefits could be derived. Other than a temporary reduction in friction coefficient when sliding began, the effects of such treatments were short-lived and not felt worthy of further consideration. Details will be presented in an international wear of materials conference (see the Publications list).

Variable load friction experiments. Evaluation of the materials, coatings, and surface treatments that passed Phase 1 screening continued during FY12 using a custom-designed variable load bearing tester (VLBT). A schematic diagram of the apparatus is shown in Figure 1. A 25.4 mm diameter alloy steel rod that simulates an engine crankshaft rotates under a set speed while a variable load is applied to a 25 x 25 mm flat test surface from underneath. A metered peristaltic pump drip feeds diesel oil (15W40) to the cylinder-on-flat sliding couple. Friction force, normal force, and motor speed are recorded using a program developed by D. Bansal and D. Erdmann using LabView™ software.

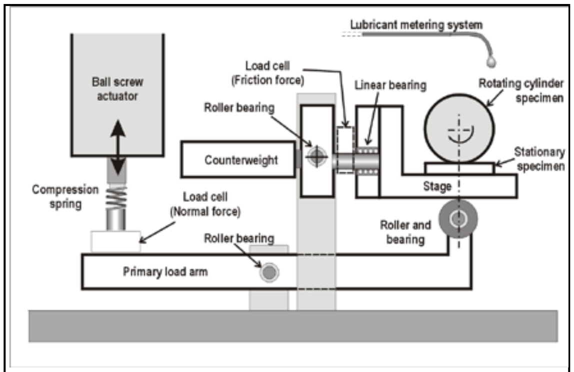

Figure 1. Component parts of the VLBT test apparatus.

Initial VLBT trials on bare Ti-6Al-4V indicated that the wear loss and friction coefficients obtained in variable load tests were not equal to those using the average load and the same sliding distance. This supports the need for better test simulations in order to select materials for components like engine bearings that normally do not operate at constant load. During initial tests, the diamond coating which passed Phase 1 wore through quickly and was deleted from further consideration. Also, to investigate whether the two different types of screening tests (Phases 1 and 2) would rank surface treatments differently, two treatments that failed Phase 1 criteria were carried over into Phase 2. Candidate treatments ranked in a different order with respect to friction level depending on which test method was used. In programming the VLBT, literature data depicting the load changes on a connecting rod bearing were used and scaled to the operating range of the test device. This load spectrum, from a test on bronze, is shown in Figure 2.

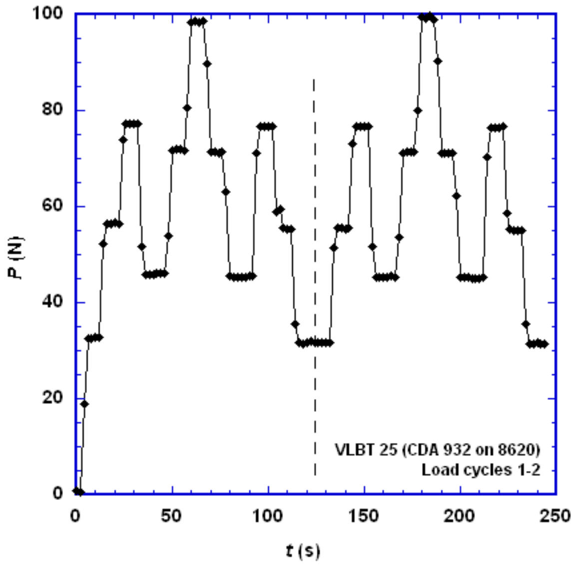

Figure 2. Variation in load (P) that was applied in VLBT tests to simulate the load spectrum when a connecting rod big-end bearing rotates.

Summary of frictional behavior of the candidate treatments and baseline alloy. The Stribeck curve, which plots friction coefficient versus a normalized parameter containing the variables of sliding velocity, lubricant viscosity, and inverse applied load, is commonly used in the analysis of lubricated bearings. Therefore, it was useful to plot VLBT test results as friction coefficient versus the inverse of applied load. This method was used to portray test results for the tenth, post-wear-in load cycle of all candidate materials. A typical curve of this type is shown in Figure 3. The shape of the curve and the low level of the measured friction coefficient suggest that the 15W40 oil was operating in a near full-film lubrication regime in which solid/solid contact is rare. That lubricated cylinder-on-flat testing configuration was not as hard on the surfaces as were the contact stresses imposed during the reciprocating pin-on-flat tests in Phase 1, but it is closer to the contact condition in connecting rod big end bearings.

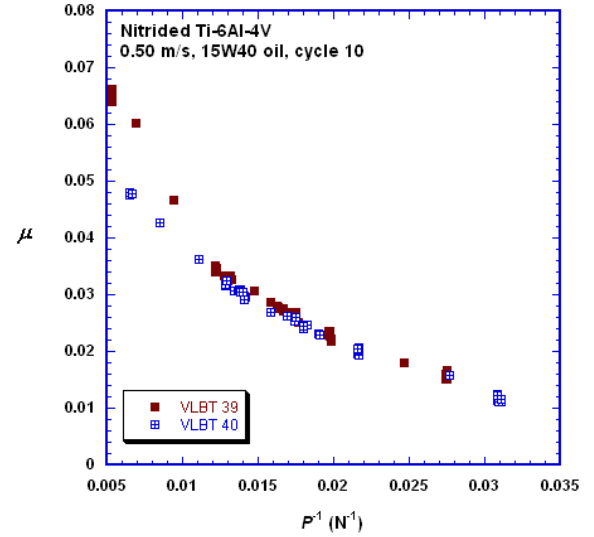

Figure 3. Relationship between kinetic friction coefficient (μ) and inverse applied load (P) during the tenth cycle of a VLBT test on nitrided Ti-6Al-4V.

Friction coefficients corresponding to the high and low loads in the applied load range were extracted from data such as that in Figure 3 and used to compare the candidate surface treatments and coating options (see Figure 4).

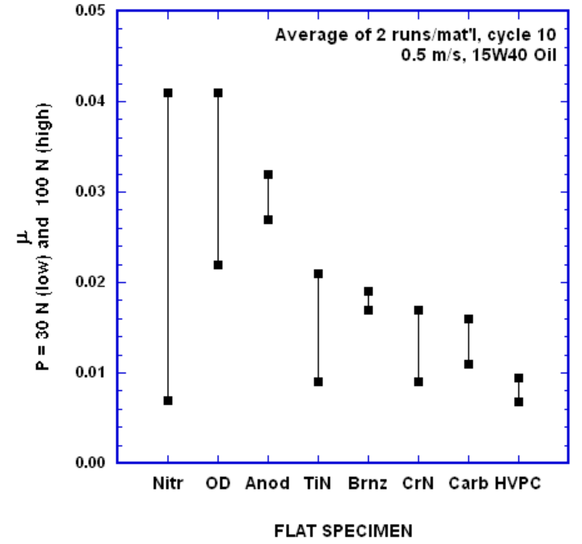

Figure 4. Range of friction coefficients during the tenth cycle of loading, indicating both magnitude of friction under oil-lubricated conditions and sensitivity to load changes.

The shorter the length of the vertical bars in Figure 4, the less susceptible was the system to changes in the applied load, and the lower the minimum μ, the more beneficial the materials would be in reducing friction relative to the baseline bronze ('Brnz'). The best performing material in Phase 2 was a high velocity powder consolidation (HVPC) coating comprised of nickel metal and boron nitride, produced by Prof. A. Segall's group at Pennsylvania State University. Rankings of the surface treatment options differed between reciprocating tests in Phase 1 and VLBT tests in Phase 2.

Overall, the HVPC coating, the carburized treatment (which failed Phase 1 test criteria), and a CrN commercial coating called Fortiphy™ looked most promising to protect Ti surfaces, but only if there is an adequate lubricating film, a situation that is not guaranteed in all friction- and wear-critical engine components.

Despite being state-of-the-art, none of the diffusion treatments tested was sufficiently promising in terms of their long-term wear and frictional behavior to be confidently recommended for service in a diesel engine; however, several of the surface treatments seemed suitable for lightly loaded, well-lubricated applications. Two of the coatings offer some promise because they can be made thicker (larger wear allowance). Still, the Achilles' heel of the material system is the poor wear resistance of the underlying Ti alloy base, which is a concern should the surface treatment or coating wear through to expose it. Consequently, a conservative approach would be to use inserts of conventional bearing materials in titanium connecting rods, rather than to attempt to substitute surface treated or coated Ti in such applications.

Future Work

- New coatings and surface treatments for Ti alloys continue to be developed, and the VLBT is available to test these. A follow-on effort would be to compare the leading coatings and surface treatments identified in work on the VLBT to results from a fired engine in a dynamometer test cell.

Summary and Conclusions

- Over 20 candidate surface treatments and coatings for Ti alloys were selected, obtained, and evaluated using two test methods. Candidates ranked differently between the two methods, one of which stressed material durability under severe, point-loaded conditions, and the other lubricated behavior under simulative bearing conditions.
- None of the candidate coatings and surface treatments for Ti-6Al-4V alloy demonstrated the kind of superior friction and wear performance that would evoke high confidence in their being able to survive in connecting rod large end bearings for at least 500,000 miles of road service. Instead, a more conservative approach of using conventional bearing inserts into Ti connecting rods seems more reasonable in the near term.

Publications/Presentations

Publications

1) D. G. Bansal, O. L. Eryilmaz, and P. J. Blau (2011) "Surface engineering to improve the durability and lubricity of Ti-6Al-4V alloy," *Wear*, Vol. 271, pp. 2006-2015.
2) D. G. Bansal, M. Kirkham, and P. J. Blau' "Effects of combined diffusion treatments and cold working on the sliding friction and wear behavior of Ti-6Al-4V," paper submitted to *Wear* journal, 2012.
3) P. J. Blau, K. M. Cooley, D. Bansal, I. Smid, T. J. Eden, M. Neshastehriz, J. K. Potter, A. E. Segall, "Spectrum loading effects on the running-in of lubricated bronze and surface-treated titanium against alloy steel," paper submitted to *Wear* journal, 2012.
4) P. J. Blau, K. M. Cooley, and M. J. Kirkham, and D. G. Bansal (2012) "Investigation of Surface Treatments to Improve the Friction and Wear of Titanium Alloys for Diesel Engine Components," ORNL Technical Report TM-2012/506, 49 pp. (in press)

Presentations

1) D. G. Bansal, O. L. Eryilmaz, and P. J. Blau (2011) "Surface engineering to improve the durability and lubricity of Ti-6Al-4V alloy," presented at the 18th International Conference on Wear of Materials, Philadelphia, PA, April 3-7.
2) D. G. Bansal and P. J. Blau (2011) "Tribological Behavior of Oxygen Diffusion Treated Ti-6Al-4V with Different Cooling Rates," presented at ASM International, Materials Science and Technology 2011 Conference, Oct. 17-21, Columbus, OH.
3) D. G. Bansal, M. Kirkham, and P. J. Blau, "Effects of combined diffusion treatments and cold working on the sliding friction and wear behavior of Ti-6Al-4V," accepted for presentation at the19th International Conference on Wear of Materials, Portland, OR, April 14-18, 2013.
4) P. J. Blau, K. M. Cooley, D. Bansal, I. Smid, T. J. Eden, M. Neshastehriz, J. K. Potter, A. E. Segall, "Spectrum loading effects on the running-in of lubricated bronze and surface-treated titanium against alloy steel," accepted for presentation at the19th International Conference on Wear of Materials, Portland, OR, April 14-18, 2013.

Agreement 23284 – Friction Reduction Through Surface Modification: Integrated Surface Texturing and Coating

Peter J. Blau and Stephen M. Hsu*[#]
** Oak Ridge National Laboratory, P. O. Box 2008, Mail Stop 6063, Oak Ridge, TN 37831-6063*
(865) 574-5377; fax: (865) 574-4913; e-mail: blaupj@ornl.gov
 # George Washington University, Exploration Hall, 20101 Academic Way, Ashburn, VA 20147
(703) 726-8365; e-mail: stevehsu@gwu.edu

DOE Technology Manager: Jerry L. Gibbs
(202) 586-1182; fax: (202) 586-1600; e-mail: Jerry.gibbs@ee.doe.gov
ORNL Technical Advisor: J. Allen Haynes
(865) 865-576-2894; fax: (865) 574-4913; e-mail: haynesa@ornl.gov

Contractor: Oak Ridge National Laboratory, Oak Ridge, TN
Prime DOE Contract Number DE-AC05-00OR22725

Objectives

- To develop and demonstrate surface engineering methods to apply friction-reducing micro-scale patterns (textures) to the sliding surfaces of diesel engine components.
- To document and optimize frictional benefits of surface texturing on curved surfaces like those on piston rings and cam lobes, and to provide usage guidelines to engine makers.

Approach

- Fabricate and optimize integrated surface texture designs for diesel engine piston rings, simulated cam lifters, and plain bearing surfaces.
- Using two types of laboratory friction tests, determine the efficacy of surface texturing produced by micro-lithography (GWU) and by compression texturing (ORNL).
- Compare the benefits of textured surfaces for oscillating motion and unidirectional rotation.

Accomplishments

- Published an annotated and indexed literature review on the production and use of patterned surfaces to control friction and wear.
- Using a customized variable load bearing test system (VLBT), investigated the effects of feature size, coarseness of dimple spacing, and pattern depth on compression textured bearing bronze surfaces (ORNL).
- Demonstrated the ability to pattern curved piston ring surfaces and discovered an optimal shape factor for achieving lowest friction with circular and elliptical dimples (GWU).

Future Directions

- Complete work and provide guidance to engine makers on friction reduction by texturing.

Introduction

The U.S. Department of Energy has undertaken a portfolio of research and development efforts to achieve a goal of 50% increase in freight efficiency (measured in ton miles per gallon) for heavy vehicles. This multi-pronged approach includes a reduction in parasitic losses (e.g., friction, aerodynamic drag, etc.), more efficient designs, novel waste heat recovery systems (thermoelectrics), and the use of lightweight materials, both metals and non-metallics. The project reported here is aimed at reducing rubbing friction losses in diesel engines by applying micro-scale features to lubricated moving surfaces.

Sliding contacts, notably the piston ring and cylinder bore, are responsible for as much as 40 – 50% of the total engine friction losses, depending on engine speed and design. Options for reducing frictional losses in moving parts include: advanced lubricant formulations, reduction in churning losses (low viscosity oils), tighter manufacturing tolerances on bearing components, and surface engineering. Here, ‘surface engineering’ (SE) refers to the design of chemical, physical, metallurgical, and/or geometrical features of solid surfaces in order to achieve desired functional characteristics like low friction and low wear.

Recent years have witnessed impressive advances in SE technology. Among the most promising is the application of patterned features (sometimes called surface textures). Figure 1, from a recent review [1], illustrates some design aspects of textured surfaces.

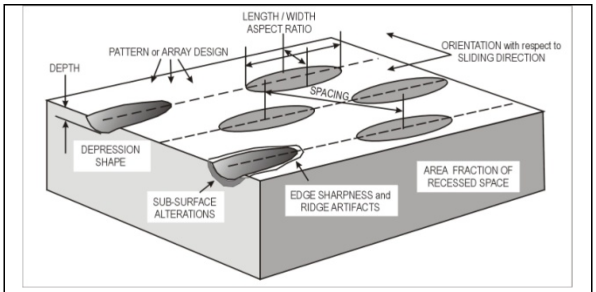

Figure 1. Schematic representation of a textured surface. Variations in size, shape, spacing, and combinations of different features are practically limitless and must be optimized for each system.

Friction-controlling features work by altering the flow of lubricants through the confined interface and by trapping harmful debris particles. Textures can be produced in numerous ways, including micro-machining, laser ablation, roll-forming, and photo-lithography [1]. Two promising methods are being investigated in the current project.

Approach

This team effort draws on the texturing expertise of a sub-contractor (Prof. S. M. Hsu, George Washington University), the advice of a diesel engine manufacturer, and ORNL’s experience in materials tribology.

SE of engine component surfaces and test coupons will be conducted by two methods: photo-lithography (GWU), and compression texturing (ORNL). Friction reducing effects will be validated by two laboratory test methods: reciprocating sliding friction, as would be experienced by a piston ring, and unidirectional sliding friction, as would be experienced by a cam lifter or a connecting rod bearing insert.

Confirmatory tests of laboratory results will be performed under an agreement between GWU and a U.S. diesel engine maker.

Progress During FY 2012.

An annotated literature review, with an appendix grouped by type of application and method of texturing, was prepared to summarize the variety of methods used to produce texture bearing surfaces. It was published in FY 2012 [1]. The primary finding was that patterns and processes must be matched to the application. Otherwise there may be no benefit, and even negative effects on friction and wear.

Compression texturing (CTx) of metal bearing surfaces. In FY 2011 an initial set of friction experiments was performed on an off-set square pattern of diamond-shaped microindentation hardness impressions produced by a computer-controlled Vickers hardness tester. Since only a small reduction in friction was obtained, that approach was discontinued after the initial study (see the FY 2011 Annual Report for details).

In FY 2012, a new method of compression texturing by rigid wire grids was explored. Wire grids of a high hardness alloy were impressed on a bearing bronze surface using a servo-hydraulic testing machine under controlled loading rates. Locations where the wire strands crossed produced a series of dimples separated by shallower troughs (e.g., Fig. 2). Coarse and fine wire mesh was used to create CTx patterns, and detailed measurements of surface details were made with 3D interference microscopy (Fig. 3).

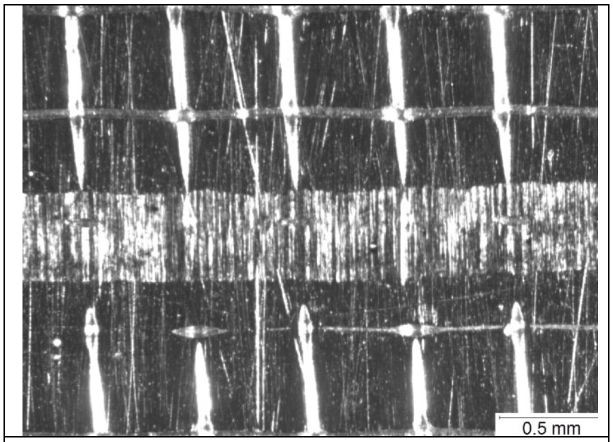

Figure 2. CTx pattern on bearing bronze with a wear track aligned across the center of the fine grid.

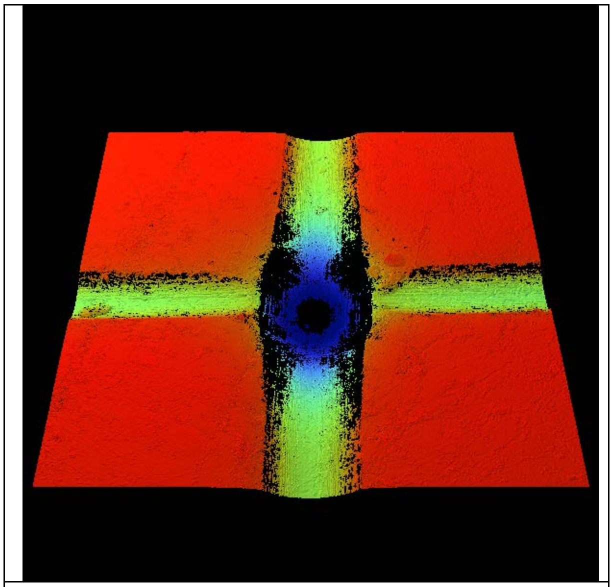

Figure 3. Height-coded 3D image of a cross-over point used to measure feature sizes produced by CTx of Cu-Pb bronze (50x50/inch, coarse grid).

CTx surfaces were then friction tested using a variable load bearing tester (VLBT) to simulate the changing loads on engine connecting rod bearing components. (The details of the VLBT apparatus are described in the annual report for Agreement 19202 "Titanium Friction and Wear.") Effects of CTx on 15W40 diesel oil lubricated surfaces are shown in Figure 4 where the friction coefficient is plotted versus the reciprocal of the applied load. The coarser grid pattern produced higher friction, but the finer pattern produced a friction reduction of as much as 50% relative to a polished flat surface (see Fig 2). In FY 2013, other patterns will be tested in order to optimize CTx for friction reduction.

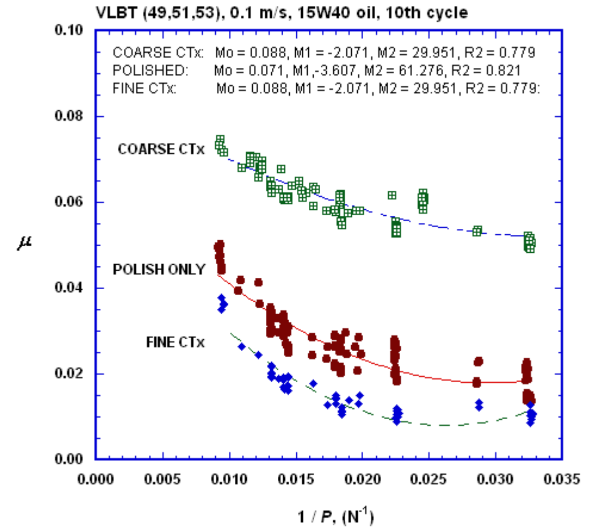

Figure 4. Grid spacing on CTx surfaces can affect the friction coefficient-normal load relationship under lubricated sliding conditions.

Progress at George Washington University (GWU). Progress was made in two areas under the subcontract to GWU. The first advance was to show that controlled dimple textures could be formed on the curved surfaces of piston rings, and the second concerned how the relative dimensions of multiple shapes (circles and ellipses) could be optimized to achieve minimum friction coefficient during reciprocating, lubricated sliding contact.

1) Progress in texturing. Diesel engine piston rings have high curvatures and complex surface compositions (e.g., tapered and crowned rings). When using microlithography to create textures, curvature and composition influence both the UV exposure time and photo-resist adhesion during processing. To address these issues, GWU designed a fixture with a circular metal polished mirror placed beneath the ring to reflect UV light directly onto the contact surface. After calibration and adjustments, the system was able to texture the entire circumference of a piston ring. A second component, a bronze roller pin, was also successfully textured after modifying the electrochemical etching technique to account for the different surface composition. This new method overcame a major hurdle and brings the texture concept closer to diesel engine testing.

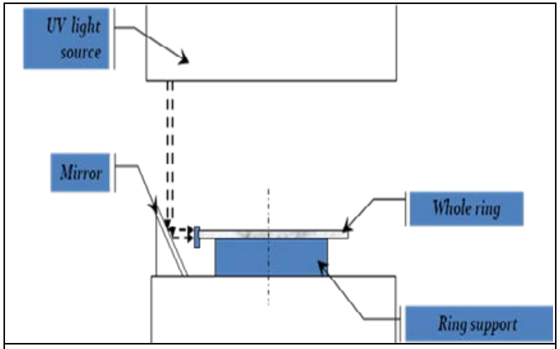

Figure 5. Arrangement for UV illumination of a piston ring contact surface (GWU).

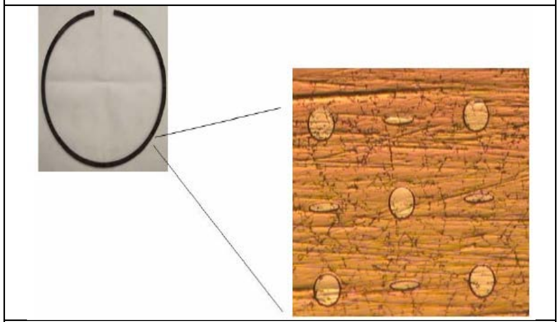

Figure 6. Pattern of rounded and elongated shapes on a piston ring surface.

2) Progress in pattern optimization. A variety of combinations of circles and ellipses having various aspect ratios were investigated and proven to be effective in reducing lubricated friction. Current studies are aimed at optimizing that pattern design to find the best ratio (D) of the circle diameter to the ellipse minor axis. A series of piston ring samples was fabricated with different circle diameters and friction-tested using a commercial reciprocating apparatus at 24 Hz, and over a range of step-loads from 20-240 N. Additive-stabilized mineral oil was used as the lubricant. Results, shown in Figure 7, indicated that not all textured patterns are equally effective, and that the difference between the optimum pattern and others can be very large. Additional tests of textured GWU piston rings are underway at ORNL using ASTM G181, a standard intended to measure piston ring/cylinder liner friction.

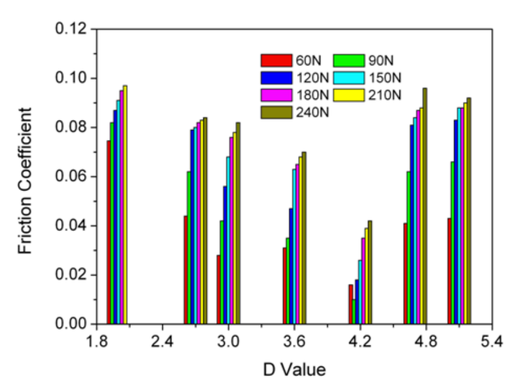

Figure 7. Effect of D ratio on friction coefficient during lubricated tests run at a series of loads.

Future Work

- Lubricated sliding experiments will continue at ORNL and GWU. Their goal is to optimize the frictional benefits of texturing the surfaces of piston rings and cam lifters.
- ORNL will further investigate the effects of compression texturing on the achievable degree of friction reduction under simulated connecting rod bearing conditions.

Summary and Conclusions

- The use of microlithography to texture entire piston rings has been demonstrated under a subcontract to GWU.
- Combinations of circles and ellipses can be optimized for friction reduction as much as 60%, but achieving the benefits of textures requires optimization of dimple shapes and sizes for each given application.
- Compression texturing by fine mesh imprints can reduce friction over polished surfaces in variable load, lubricated tests. Coarser patterns actually increased friction, confirming the need to optimize designs. The requirement to match texture designs to the specific components of interest agreed with

similar findings from GWU experiments on micro-lithographically produced textures.

- In FY 2013, research will extend texturing methods to compare the effects of texturing on surfaces that either oscillate (like piston rings) or rotate in one direction (cam lobes and connecting rod big end bearings).
- Findings of this work will be summarized in a final report and communicated to the diesel industry.

Publication

1. P. J. Blau (2012) *Use of Textured Surfaces to Mitigate Sliding Friction and Wear of Lubricated and Non-Lubricated Contacts*, ORNL Tech Report ORNL/TM-2012/20, 19 pp.

Agreement 23725 - Tailored Materials for Improved Internal Combustion Engine Efficiency

Principal Investigator: Glenn J. Grant
Energy Materials and Manufacturing
Pacific Northwest National Laboratory
902 Battelle Blvd., K2-03
Richland, Washington 99356
(509) 375-6890; fax: (509) 375-4448; e-mail: glenn.grant@pnnl.gov

Blair E. Carlson
Manager, Lightweight Materials Processing
General Motors R&D
30500 Mound Rd.
Warren, MI USA 48090
e-mail: blair.carlson@gm.com

Rajiv S. Mishra
University of North Texas
Professor, Department of Materials Science and Engineering
Site Director, NSF IUCRC for Friction Stir Processing
1155 Union Circle #305310
Denton, Texas 76203-5017
(940 565-2316; Fax: (940) 565-4824

DOE Technology Manager: Jerry L. Gibbs
(202) 586-1182; fax: (202) 586-1600; e-mail: Jerry.gibbs@ee.doe.gov

Field Technical Manager: Dean Paxton
(509) 375-2620; fax (509) 375-2186; e-mail: dean.paxton@pnnl.gov

Contractor: *Pacific Northwest National Laboratory*
Contract No.: *DE-AC05-76RL01830*

Objective

- Develop friction stir processing (FSP) to tailor the properties of conventional, low-cost engine materials (cast iron, alloy steels, and aluminum alloys) with the goal of increasing their high-temperature performance, durability, and thermal properties.
- Deploy friction stir processed components that enable energy-efficient combustion strategies, especially those that will require higher peak combustion pressure or higher temperature operation where component durability is the primary barrier to the use of efficient combustion strategy.

Approach

- Develop surface modification techniques, modified materials, and components. The project is a collaboration with General Motors (GM), with GM providing in-kind and materials (i.e., aluminum castings, cylinder heads, engine components, and testing).
- Investigate FSP, a new technology that can produce functionally graded surfaces with unique and tailored properties that will allow propulsion materials to withstand higher temperatures and pressures without appreciably losing strength, hot hardness, or wear resistance and improve their resistance to thermal fatigue.
- Evaluate and test friction stir processed components through industry collaborators to demonstrate efficiency benefits and potential commercial applications.

Milestones, Metrics, and Accomplishments

- **Milestone**: Demonstrate property improvements from FSP that can reach the following metrics established by the project team: minimum two-fold improvement in fatigue life, and 20 percent improvement in average failure stress level at N cycles.
- **Milestone**: Demonstrate consolidated FSP regions in aluminum and ferrous materials typical of cylinder head, cylinder liner, block, crankshaft, rod, piston, and bearing materials on a subscale two-dimensional shape relevant to real part geometry (TRL 3 to 4 transition).
- **Milestone**: Demonstrate and document the energy savings potential of a friction stir processed prototype part with improved durability and high-peak combustion pressures (PCP).

Introduction

The purpose of this project is to improve the durability and thermal properties of conventional, low-cost materials so they can withstand the increased level of mechanical performance required in new combustion strategies such as homogenous charge compression ignition (HCCI), low temperature combustion, and other conditions where higher PCPs are anticipated. HCCI, premixed charge compression ignition (PCCI), low temperature combustion, and other strategies can produce higher specific power levels which allow engine downsizing and decreased fuel consumption; however, increases in PCP often result. One barrier to fully realizing these energy-efficient strategies can be the engine component materials themselves. Increasing the durability of engine components can increase the operational envelopes of the engine, allowing designers of the combustion process to access areas of engine control where increased specific power and low emission levels are found, but where high PCPs can create reliability problems.

The proposed project aims to achieve U.S. Department of Energy (DOE) goals for increased fuel and thermal efficiency in both light- and heavy-duty engines by developing and deploying FSP, a new surface modification technology that has been shown to significantly improve the strength and durability of current engine materials. This project proposes to experimentally develop the FSP process required to engineer the surface of propulsion materials for improved properties, then fabricate prototype parts for in-engine testing by project partners. The microstructural modification created by FSP is expected to lead to a set of materials with enhanced surface properties that can handle increased combustion pressures, resulting in improved engine efficiency.

Purpose

This project proposes to further develop and implement concepts validated in the previously funded Vehicle Technology Program-Propulsion Materials project, “Tailored Materials for Advanced CIDI Engines.” The current project will prototype and test up to four separate internal engine components expected to have limited durability at very high PCPs or high load-rise times during engine operation. These components will have FSP processing selectively applied to the regions of the part where durability issues are either found or anticipated. Example components will be cylinder heads, blocks, and potentially components in the rotating assembly, including, but not limited to, crankshafts and camshafts.

A number of different localized material durability issues that limit highly efficient engine design have been identified and include resistance to thermal fatigue, improved hot strength, improved resistance to erosive or adhesive wear in piston ring grooves, and improved performance and strength in aluminum blocks and cylinder heads of small displacement turbo gas and turbo diesel engine materials. These durability issues have been identified as potential opportunities where friction stir processing may be able to produce property improvements.

The link between improved material properties and increased engine efficiency is obvious empirically. For example, higher combustion pressures are needed for high efficiency combustion, but if engine internals do not have the performance needed, the higher pressure combustion cannot be implemented. The goal of this project is to establish a quantitative link between improved properties and increased efficiency.

Background

Almost since the inception of internal combustion engines, there has been a steady rise in specific power (SP) output (i.e., the power per liter of engine displacement). Higher SP correlates to efficiency and is the combined effect of optimization of combustion, fuels, engine materials and design, reduction in parasitic losses, and improved heat management. Figure 1 shows that SP has steadily increased from 1970 to 2001. After 2001, the SP levels dropped due to emission and after-treatment devices and controls mandated by federal legislation (primarily increased exhaust gas recirculation rates and particulate filters). The drop in SP from 2001 to ~2003 would have been greater if not for significant advances in engine management, computer control, injection pressures, etc., made during this period to compensate for the power losses. However, around 2003, another restriction on combustion process optimization began to force diminishing returns. The restriction is illustrated in Figure 1 as the PCP plot. As the peak pressure increases, more work can be done by the piston as it is forced downward in the bore, resulting in a higher SP.

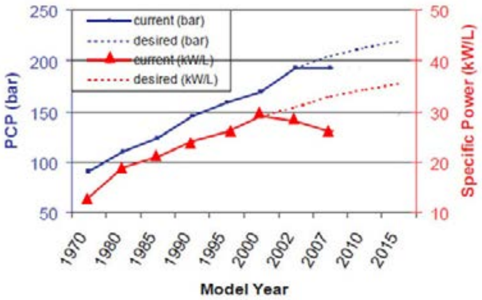

Figure 1. Plot showing the increase in SP and PCP for typical heavy-duty diesel engines over the last 38 years (figure modified from the Southwest Research Institute website at www.swri.org)

Since 2003, PCP has leveled out around 190 to 200 bar. Above this level, conventional engine materials in pistons, cylinder liners, and cylinder heads will be beyond strength and fatigue limits.[1] To increase efficiency further, either unconventional, expensive materials (i.e., nickel alloys, titanium, compacted graphite iron, nodular iron, or micro-alloyed steels) must be used or conventional materials must be modified in a way that increases their durability. New energy-efficient combustion strategies, especially HCCI, could increase PCP above 220 bar. Accordingly, materials must be improved to enable this process.

One of the major challenges for conventional materials under increasing peak pressure environments is resistance to thermal-fatigue failure. Pistons and cylinder heads are particularly vulnerable to this failure mode because of the cyclic nature of the loading and temperature changes in the combustion chamber. Figure 2 shows failures of pistons in the bowl rim area when subjected to high PCP over time.

Rather than substitute a potentially high-cost, high-temperature, monolithic material, one low-cost strategy to enable higher PCP involves using techniques to improve the thermal-fatigue performance of current materials. In the case of thermal fatigue in the bowl rim area, the

---

[1] Figure 1 represents data primarily from medium-duty to heavy-duty diesel engines. Production automotive diesel engines (light-duty, high-speed) now achieve SP levels up to 75 kW/L in turbocharged and intercooled configurations.

technique only needs to be applied to the narrow area around the bowl rim itself because failures of this area drive the overall material selection.

FSP is a new technology that can be used to create engineered regions on selective areas of a part. In recent years, the Pacific Northwest National Laboratory (PNNL) has developed techniques and tools that allow FSP to be accomplished in steel, cast iron, and aluminum. FSP is an outgrowth of friction stir welding, which was invented 20 years ago by TWI, Ltd. (Figure 3). It has been recognized that the same techniques and processes used in friction stir welding could be used to process a material for enhanced properties. The process can be selectively applied to the surface of a material, altering the microstructure through severe plastic deformation in the processed zone.

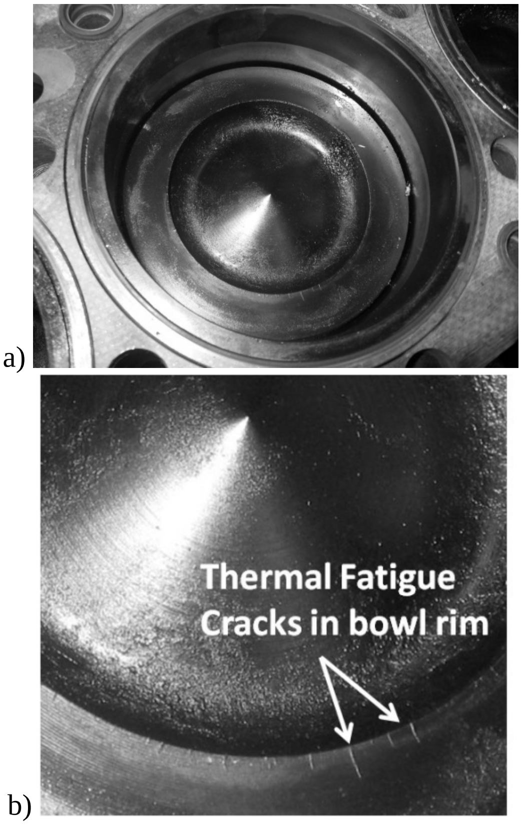

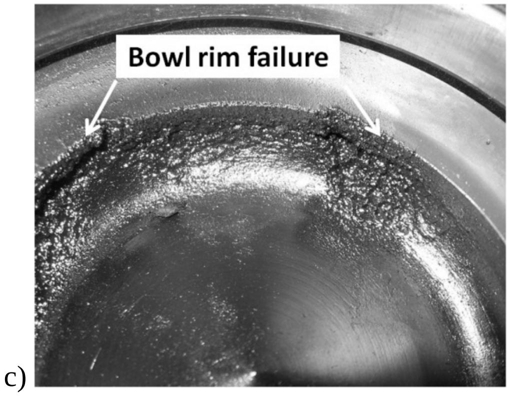

Figure 2. a) Piston in bore; b) cracks on inside edges of bowl rim; c) bowl rim failure

FSP can create a robust and graded structure with fundamentally different properties than the underlying surface. It has been shown to produce surface regions with improved fatigue life, ductility, and strength.

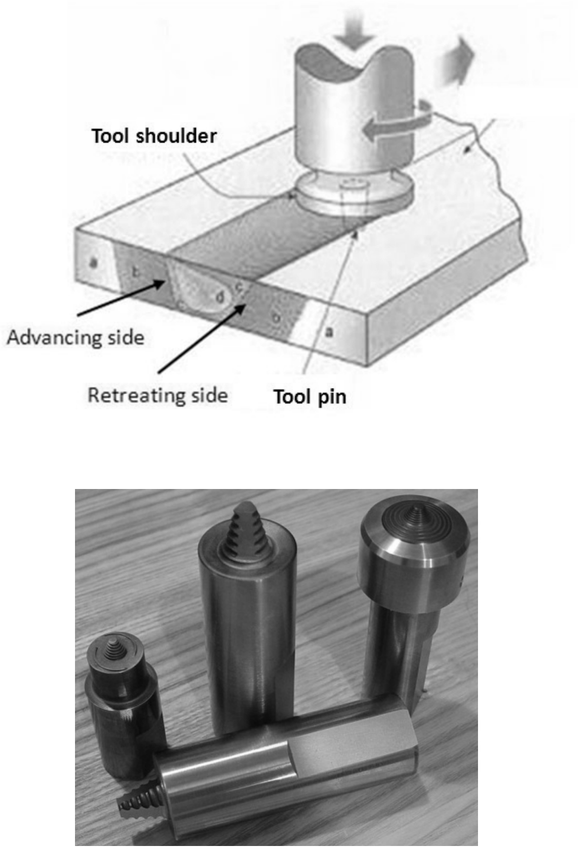

Figure 3. FSP illustration (top) and typical friction stir tools

FSP produces a surface-modified region that is different from a coating. Commonly, surface treatments designed to enhance wear or thermal performance include various coating methods or fusion-welded hard facings. Most of these processes are liquid state and often result in detrimental temperature effects on the base material. Heat-affected zones in the base metal and various deleterious high-temperature reactions can create a coated part with less-than-desirable properties.

In addition, traditional thin coatings can suffer from issues involving the nature of the interface between the coating and the base material (e.g., spalling, debonding, and cracking on the interface), especially under high-stress, gouging wear conditions, or cyclic-thermal conditions where coefficient of thermal expansion mismatch is an issue. Further, failure of a coating under high-loading conditions can occur when the substrate below a thin, hard coating fails by plastic deformation. Regions treated with FSP can be significantly more robust than traditional coatings for two reasons: 1) FSP produces a modified region that transitions to the base material without a sharp interface (Figure 4) and 2) the modified region is generally thicker and the transition region wider than traditional coating because the plasticized region depth is related to the tool geometry, specifically the depth and size of the pin.

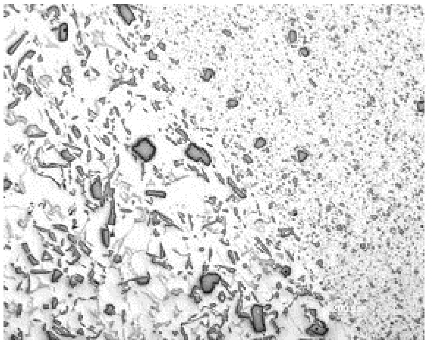

Figure 4. Micrograph of the edge of a stirred zone showing particle refinement in the processed region. (FSP can close porosity in castings and decrease both size and aspect ratio of particles, thus producing better fatigue performance).

FSP can be used to alter the original microstructure, create surface composites and new alloys, and potentially produce selective areas of improved material performance. This project will investigate several opportunities for FSP to improve engine materials to enable increases in engine efficiency.

The current project is a continuation from work done during 2008–2010 in the project "Tailored Materials for Advanced CIDI Engines," which demonstrated that FSP, a new surface engineering process can show 5 to 15 times fatigue life improvement over as-cast material. In addition, FSP-processed materials can show up to 80 percent improvement in fatigue strength across a wide range of maximum stress levels. These improvements were demonstrated at the coupon scale and were demonstrated in aluminum materials in common usage for piston applications in medium duty diesel engines.

The previous project developed the FSP process in specific aluminum alloys and documented the microstructures and mechanical performance of the processed zone. However, moving this technology towards implementation requires engine component prototyping and testing, which is the focus of this project. The current project proposes to take the techniques and FSP process knowledge developed in the previous work, and, by working with an original equipment manufacturer partner, apply the techniques to actual engine components.

Approach

The project will develop and use FSP to produce surface-modified regions on parts composed of conventional engine materials to address barriers related to durability at high PCPs without incurring increased raw material costs associated with using exotic or expensive materials.

- The project will develop the FSP manufacturing parameters and select and evaluate proper tool materials and techniques needed to produce defect-free FSP regions. The project will leverage a large amount of process knowledge gained from the earlier project on heavy-duty diesel engine materials.
- Coupon-level testing and evaluation of the thermal and mechanical properties will be conducted, focusing on specific performance

targets identified by project partners. If performance metrics are met for sample friction stir processed materials, additional research will develop and demonstrate the appropriate method to apply the process to the two- and three-dimensional geometry of the selected parts.

- After process schedules are established, prototype parts will be fabricated to the specifications provided by project partners and relevant part testing will be completed (i.e., in-engine or other tests specified by partners).
- Project tasks will be divided by part or application. The physical parts to be tested are expected to define several primary tasks surrounding the development of FSP for that part and the actual test runs in realistic environments.

Task 1: Cylinder Head Thermal-Fatigue Life Improvement

- Subtask 1a – Chill casting of A356 plate stock for experimental trials
- Subtask 1b – FSP trials for thermal aging studies
- Subtask 1c – FSP trials for stable microstructure (resistance to abnormal grain growth [AGG])
- Subtask 1d – Room temperature fatigue studies on FSP coupons (miniature fatigue testing)
- Subtask 1e – Elevated temperature fatigue testing of FSP coupons
- Subtask 1f – Translating the process to a three-dimensional part and producing a processed region on an actual head or head analog
- Subtask 1g – Operating-temperature, cylinder head thermal shock testing (conducted by GM).

Task 2: Block and head casting FSP to close near surface porosity for improved strength and durability

- Subtask 2a – FSP trials on block materials in plate form for thermal aging studies
- Subtask 2b – FSP trials for stable microstructure (resistance to AGG)
- Subtask 2c – Room temperature fatigue studies on FSP coupons (miniature fatigue testing)
- Subtask 2d – Translating process to a three-dimensional part and producing a processed region for microstructural examination and testing

Task 3: Fillet, oil hole, or flange fatigue performance improvement on rotating shafts

- Subtask 3a – FSP trials on steel alloy plate for process parameter development
- Subtask 3b – Mechanical and toughness testing of FSP coupons
- Subtask 3c – Room temperature fatigue studies on FSP coupons (rotating beam fatigue on subscale specimens)
- Subtask 3d – Translating process to a three-dimensional part and producing a processed region on an actual rotating shaft assembly
- Subtask 3e – In-engine testing

The current project will prototype and test up to four separate internal engine components that are expected to have limited durability at very high PCPs or high load-rise times during engine operation. These components will have FSP selectively applied to the regions of the part where durability issues are either found or anticipated.

Technology transfer both during and at the end of this project will be directly through GM (and potentially a Tier 1 supplier), which will implement the technology.

Results

During fiscal year (FY) 2012 work focused primarily on Tasks 1 and 2, FSP trials on cast materials used for cylinder head and block castings. A total of 15 cast A356 plates were received from GM. This is a typical cylinder head material and the plates were cast so that their microstructures were similar to what should be expected near the roof of the combustion chamber. The plates were chill cast, and modified with the addition of strontium (Sr). Chill casting leads to small secondary dendrite arm spacing (SDAS), while Sr modification results in fibrous and refined morphology in the eutectic silicon (Si) particles. The microstructure of the cast plates was examined and the details are shown in Figure 5.

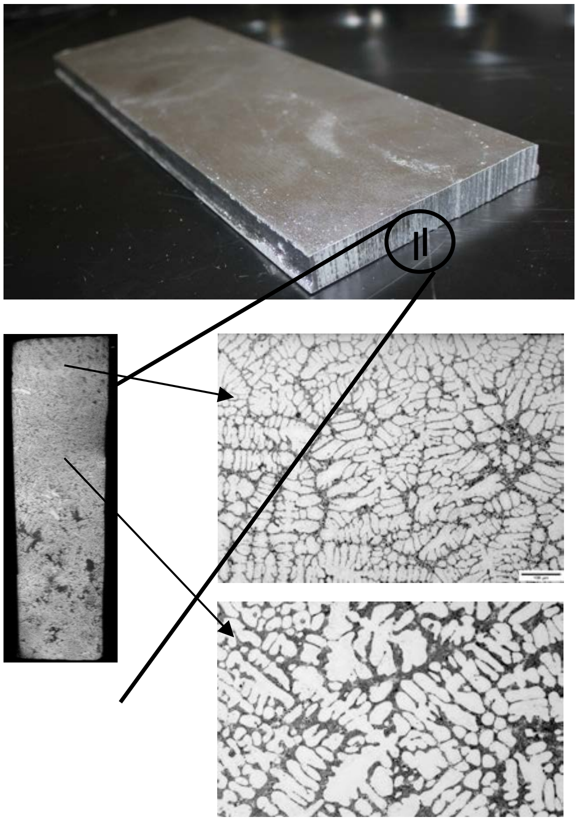

Figure 5. Microstructural details of the cast A356 plates. Small variation in SDAS occurs across the thickness of the cast plates.

A slight variation in SDAS occurs across the thickness of the cast plates, which is related to the chill casting process. The average SDAS is ~25 µm. Figure 6 plots the SDAS and hardness variation along the thickness of the as-cast plates. The hardness values decrease as the SDAS increases from the top of the plate to the middle of the plate. However, such variation in hardness is eliminated after the cast plates are subjected to a T6 heat treatment. T6 heat treatment leads to the formation of strengthening precipitates, and as a result, SDAS size-related hardness variation is eliminated. The hardness plot after T6 treatment is shown in Figure 7. The initial microstructures obtained by the casting and heat-treating process will be tested alongside the FSP-processed material during this project to quantify the benefits of FSP.

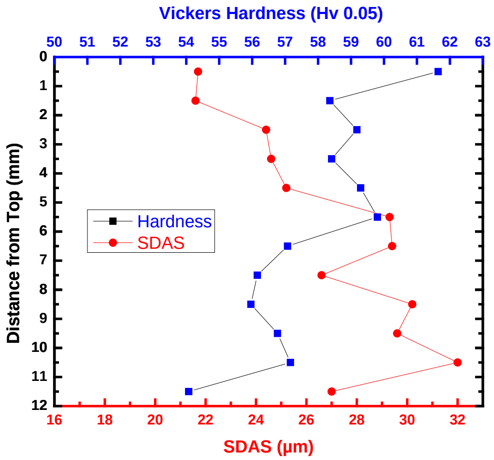

Figure 6. SDAS and hardness variation along the thickness of the cast plate, from top to middle.

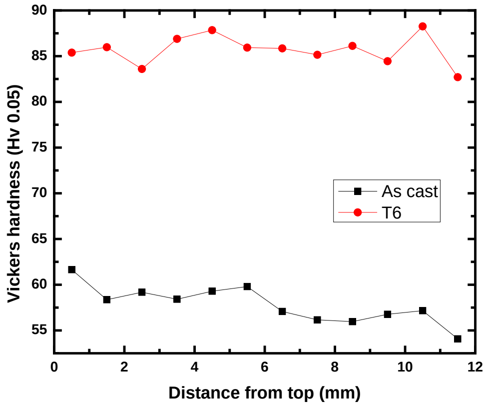

Figure 7. Hardness variation along the plate thickness after T6 treatment.

Material durability at higher combustion pressures is one major barrier to more efficient combustion strategies. The thermal-fatigue behavior of conventional engine materials at higher PCPs is one performance limiting example. FSP has been shown to dramatically improve fatigue performance; however, one concern raised has been whether or not these improvements will be realized at the high operating temperatures experienced by parts such as pistons and heads. For example, at elevated temperatures, some of the metallurgical properties that define fatigue crack mechanisms do not operate. Elevated temperature conditions may produce durability concerns more closely related to creep-fatigue mechanisms than to fatigue alone.

In addition, the stability of a FSP-produced microstructure at elevated temperature may be a concern. FSP leads to significant microstructural refinement (e.g., eutectic Si particle, grain size), removal of casting porosity, and breakdown of dendritic structure. However, some FSP microstructures can undergo excessive grain coarsening (i.e., AGG) when exposed to elevated temperatures. It is not yet known if AGG will produce a microstructure with lower thermal-fatigue performance, but it is known to restrict ductility at room temperature. Because the processed part will be exposed to elevated temperature, it is imperative to learn what controls AGG during FSP of A356 alloy.

Earlier studies have shown that both FSP parameters and the nature of the constituent and secondary particles play a key role in AGG. In recent studies (Sato et al 2007; Attallah and Salem 2005) the occurrence of AGG has been found to be related to process parameters. In both these studies, friction stir processed material was subjected to a post-weld heat treatment (PWHT) and then examined for AGG. A wide range of processing conditions was explored. Microstructural examination revealed that high rotation per minute (RPM) and intermediate travel speeds led to more stable microstructures that did not experience AGG.

Material flow and repeated mixing has been found to be another important criterion that controls AGG. If a linear FSP region is created in a substrate, followed by a second FSP pass directly over the same region, the resulting material is resistant to AGG. In a study on A357 alloy (Al-7Si-0.6Mg), the amount of nugget overlap played a critical role in determining the extent of AGG during PWHT (Jana et al. 2010).

FSP likely causes some non-uniformity in the microstructure that can be minimized by repeated material mixing by overpassing a previously processed region.

During the last quarter of FY 2012, a series of FSP experimental trials explored the role of various process parameters on AGG. The initial focus was on the following:

- Tool RPM
- Tool design
- Process configuration (e.g., single pass, multiple pass)

Initial FSP trials used four RPM conditions (300, 700, 1200, 1500) and a constant travel speed (4 in./min). Two tool designs (Figure 8) were used; one with a stepped spiral pin feature and no flats and one with stepped spiral pin and three flats. Both tools used a concave shoulder design

Figure 8. Tools used in the current FSP trial

Single pass FSP runs were made in position control mode. Processed plates are shown in Figure 9.

A thermocouple, embedded in the tool, was used to record processing run temperatures. Figure 10 plots the tool temperature data as a function of time. The tool temperature during each run stayed fairly constant with a slight rise during the run. The average tool temperatures for each run at different process parameters show a strong increase with increasing RPM. However, the largest change in average tool temperature occurred between 300 and 700 RPM (Figure 11).

Figure 9. Friction stir processed Cast A356 plates

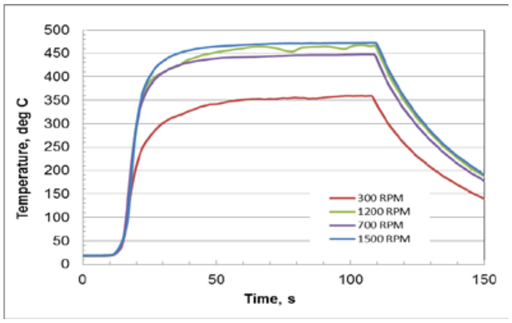

Figure 10. Temperature profile of the tool during processing (tool with no “flats” on the pin)

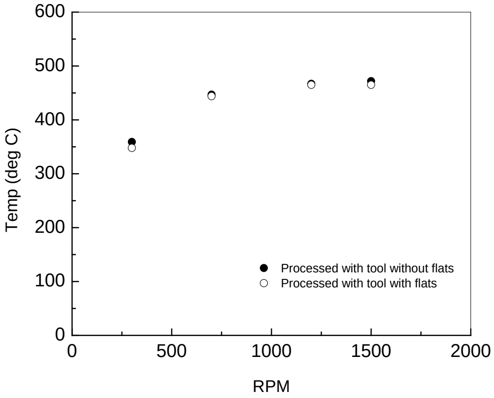

Figure 11. Tool temperature as a function of tool RPM

The microstructures within the processed zone show a breakdown of the dendritic structure, uniform distribution of Si particles, and a refinement in the particle size (Figure 12). Although not shown, the grain size in the nugget region increased with tool RPM.

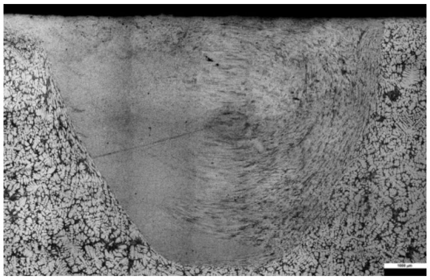

Figure 12. Fully consolidated weld nugget

The FSP trials have resulted in a wide range of microstructures that will be tested during the first quarter of FY 2013 for their propensity to develop AGG and their durability with respect to thermal fatigue.

Conclusions

The goal of this project is to develop friction stir processed components that can enable energy-efficient combustion strategies, especially strategies that will require higher PCP or higher temperature operation. FSP produces selected, graded structures that have shown increased strength and durability in fatigue. Surface modification through FSP may address some emerging material problems seen in very high combustion pressure systems such as HCCI engines.

This project leverages the discoveries made on the FY 2008–2010 project “Tailored Materials for Advanced CIDI Engines,” which focused on mid-size and heavy-duty diesel engines. This project will apply the lessons learned to smaller on-road turbo gas and diesel engines found in typical passenger car and light truck applications. The project will demonstrate property improvements available from FSP. Functionally graded materials can be anticipated through this solid-state process that cannot be fabricated any other way. This project will develop a set of tools and techniques that can be used by designers who require materials that can operate at ever-increasing stresses and temperatures where part durability is the primary barrier to increased engine efficiency.

References

Sato, Y.S.; Watanbe, H.; and Kokawa, H. Grain growth phenomena in friction stir welded 1100 Al during post-weld heat treatment. *Sci. Technol. Weld. Joining*, **2007**, *12*, pp. 318–323.

Attallah, M.M. and Salem, H.G. Friction stir welding parameters: a tool for controlling abnormal grain growth during subsequent heat treatment. *Mat. Sci. Eng. A*, **2005**, *391*, pp. 51–59.

Jana, S.; Mishra, R.S.; Baumann, J.A.; Grant, G.; Effect of process parameters on abnormal grain growth during friction stir processing of a cast Al alloy. *Mat. Sci. Eng. A,* **2010**, 528 (1), pp. 189-199.

Agreement 24034 - High Strength and High-Temperature Materials for Heavy Duty Engines

Principal Investigator: Mark T. Smith, PNNL
Energy Materials Group
Pacific Northwest National Laboratory
P.O. Box 999, MS K2-03
Richland, WA 99352
(509) 375-4478; fax: (509) 375-4448; e-mail: mark.smith@pnnl.gov

Yong-Ching Chen
Cummins, Inc.
(812) 377-8349; e-mail: yong-ching.c.chen@cummins.com

DOE Technology Manager: Jerry L. Gibbs
(202) 586-1182; fax: (202) 586-1600; e-mail: jerry.gibbs@ee.doe.gov
***Field Technical Manager**: Dean Paxton*
(509) 375-2620; fax: (509) 375-2186; e-mail: dean.paxton@pnnl.gov

Contractor: *Pacific Northwest National Laboratory*
Contract No.: *DE-AC05-76RL01830*

Introduction

Aluminum alloys that possess strengths approaching of 300 MPa at 300°C have been produced in small quantities by numerous mechanical attrition (MA) methods. Although MA can produce unique combinations of properties, MA processing approaches have not been able to meet the requirements for low-cost, high-volume production. The purpose of this project is to demonstrate that MA alloys can be produced with adequate high-temperature mechanical properties through the development of a low-cost, high volume, rapid solidification (RS) production process.

MA aluminum alloys with strengths approaching 300 MPa at 300°C have been produced by adding alloying elements with very low solubility and that form intermetallic dispersions (e.g., Fe, Ti, Cr, Mn and Zr) to the aluminum matrix. Milling cycles can require hundreds of hours to adequately homogenize the alloy, which produces a large amount of oxide, limiting production and ductility, respectively. In the past, the Pacific Northwest National Laboratory (PNNL) has worked with melt-spinning methods to produce alloys by RS using a process that produces a low surface area particulate (flake). The RS flake can be consolidated by elevated temperature extrusion. This project intends to use the RS flake/extrusion process to produce an aluminum alloy with increased elevated temperature strength that can be used in diesel engine service environments up to 300°C.

Approach

<u>High Strength and High-Temperature Aluminum Alloy Development</u>

1. Produce the rapidly solidified alloy compositions using the PNNL pilot flake system. The PNNL flake melt spinning machine can produce limited quantities of experimental alloys in the form of rapidly solidified flake. After melt spinning aluminum flakes, the following subtasks will be initiated:
    a. Conduct a comprehensive technology review of prior high-temperature and high-strength aluminum alloy development, including alloys developed by Allied Signal and the University of Connecticut (UConn).

   b. Select three alloy compositions, two similar to the early Allied Signal Al-Fe-X compositions the third the Al3Fe2Cr2Ti previously developed by MA.

2. Consolidate flake materials via extrusion using laboratory-scale extrusion tooling at PNNL and/or Kaiser EP (under subcontract to PNNL). Rapidly solidified flake will be consolidated using the canning and upset extrusion process previously developed by PNNL. To produce extruded product of sufficient dimensions, PNNL will work with Kaiser EP to process materials.
3. Measure elevated temperature mechanical properties and compare to baseline materials. Elevated temperature tensile tests of sample materials will be conducted to establish temperature-strength behavior for the materials.
4. Produce larger quantities of flake (via Transmet [under subcontract to PNNL] using the production melt spinning system. The downselected alloy composition(s) will be made into master alloy feedstock and provided to Transmet for melt spinning into rapidly solidified feedstock. Quantities of several hundred pounds are anticipated, depending on the alloy systems selected.
5. Consolidate the production flake by canned and can-less powder extrusion at Kaiser. The flake feedstock will be supplied to Kaiser for canning and extrusion at larger billet diameters. Processing will simulate anticipated full-scale production methods.
6. Test full-scale component using the appropriate test system at Cummins, Inc. Cummins, Inc. will select components that will benefit from the high-temperature aluminum properties and process the materials supplied by PNNL/Kaiser into full-scale test components.
7. Perform engine testing at Cummins, Inc. if component test is successful. Established rig-testing will be conducted to establish performance and mass reduction benefits.

The primary deliverables from the project will be:

- The development and production of high-temperature aluminum alloys by rapid solidification.
- Characterization of the RS alloys and baseline materials for elevated temperature fatigue strength.
- Cost analysis of the process to produce full-scale extrusions.
- Full-scale component testing to validate performance of the alloys.

Results and Discussion

Work on this project began in May 2011, conducted under a Cooperative Research and Development Agreement (CRADA) between Cummins, Inc. and PNNL. The first phase of the effort has focused on identification of candidate aluminum alloy systems that can provide higher strengths (300 MPa) at elevated temperatures of approximately 300^{o}C. In FY12, a series of three alloy compositions were evaluated along with two different consolidation and extrusion processes. All alloys contain iron (Fe) as a key alloy addition along with smaller additions of silicon, Ti-Cr-V, and manganese. With the exception of silicon, alloy additions were chosen for their low solubility in aluminum and ability to form stable second-phase particles. Evaluated alloy compositions are listed in Table 1. The first two alloys contain Si and V, while the aluminum-iron-chrome/titanium (AFCT) alloy contains a lower level of Fe, combined with higher weight percentages of Cr and Ti. The aluminum-iron-manganese (AFM) alloy was developed at PNNL in FY12.

Table 1. Initial High Temperature High-Strength Aluminum Alloys

Alloy Designation	Fe	Si	V	Cr	Ti	Mn
Al-12Fe	12.4	2.3	1.2			
Al-8.5Fe	8.5	1.7	1.3			
AFCT	6.0			3.4	3.2	
AFM-11	11.4	1.8	1.6			0.9
AFM-13	13.2	2.6	.50			0.9

The first three alloys have been previously produced in small quantities and tensile tested at a range of temperatures. Tensile strengths for these alloys at 300°C have been reported in the 250 to 300 MPa range, close to, or meeting the property goals.

The processing steps that were selected for this project include induction melting to produce suitable feedstock alloys that approximate the compositions of the alloys listed in Table 1, analysis of actual compositions and the alloy melting characteristics, induction re-melting of the alloys, and melt spinning to produce rapidly RS flake materials for subsequent processing. Figure 1 shows the RS flake material and the melt spinning equipment used to produce it.


(a) (b)

Figure 1. (a) Picture of the PNNL flake melt spinning machine with the front chamber removed and (b) typical RS flake product produced with the melt spinning equipment.

The second focus of the project was the development of laboratory-scale extrusion tooling to be used in the consolidation and extrusion of the RS flake materials to produce a wrought extruded rod. The extruded rod material provides sufficient material for machining of tensile specimens for room temperature and elevated (300°C) tensile. Two processing approaches were developed for preparing the RS flake material for extrusion into the wrought rod product. The first approach involved cold (room temperature) pressing of the RS flake into an aluminum can, followed by weld-sealing the can under vacuum conditions. The sealed can was heated and extruded to the rod product using a 19:1 extrusion ratio. In the second approach, the canned flake was placed in a vacuum hot press at 450°C and pressed to pre-consolidate the RS flake to approximately 90 percent theoretical density. The canned and consolidated billet was then extruded into rod using the same 19:1 extrusion ratio. Figure 2 shows an example of the canned billet (50 mm diameter) and the resulting extruded rod (11.4 mm diameter).

Following extrusion of the RS flake materials, the extruded rods were cut into lengths and machined into round ASTM sub-sized tensile specimens with a gage length of 25 mm and a gage diameter of 6.4 mm. Approximately 150 mm of the nose and tail of the extrusion were discarded to minimize non-uniform material. Machined tensile specimens were then tested at room temperature and at an elevated temperature of 300°C. A minimum of three tests were conducted at each temperature. Results of the tensile tests for the various aluminum alloys are shown in Table 2 (room temperature) and Table 3 (300°C).

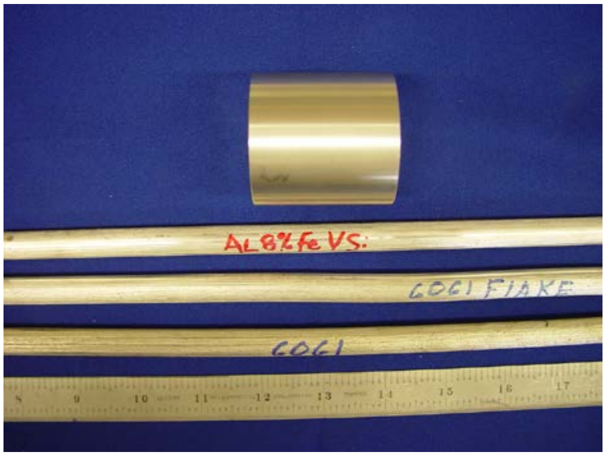

Figure 2. Photograph of the canned RS flake billet (top) and the extruded rod.

Table 2. Room temperature tensile test results for candidate high temperature extruded aluminum alloys.

Alloy Designation	Extrusion Temperature(°C)	Elastic Modulus (GPa)	Tensile Yield Strength(MPa)	Tensile Strength (MPa)	Failure Strain (%)
Al-8.5Fe - EB	450	83.5	345.0	390.4	19.1
Al-8.5Fe - EB	500	84.2	331.2	389.4	18.0
Al-8.5Fe - HP	500	86.9	338.1	384.9	18.3
AFCT - HP	500	95.9	400.2	448.6	12.2
AFM-11-HP	500	96.0	427.8	493.6	7.2
EB= vacuum electron beam welded can without hot press HP= vacuum hot pressed billet. Failure strains measured using an extensometer.					

Table 3. Elevated temperature (300°C) tensile test results for candidate high temperature extruded aluminum alloys. Notes: yield strength and ultimate strength are the same at the 300 C test temperature. Extension at failure calculated from gage section measurements.

Alloy Designation	Extrusion Temperature(°C)	Elastic Modulus (GPa)	Tensile Yield/Ultimate Strength(MPa)	Failure Strain (%)
Al-8.5Fe - EB	450	74.5	210.9	25.1
Al-8.5Fe - EB	500	76.6	208.2	21.7
Al-8.5Fe - HP	500	71.8	204.2	18.4
AFCT - HP	500	80.7	226.7	18.8
AFM-11-HP	500	91.1	256.8	17.0

The goal of this project is to approach a tensile strength of 300 MPa at 300°C test temperature. As shown in Table 3, the AFM-11 alloy comes the closest to meeting that goal. Based on the initial results for the candidate alloys, further processing of the AFCT and AFM-11 alloys has been initiated, and a new version of the AFM-series of alloys, (i.e., AFM-13 [with a higher Fe content]), has been included in the next phase of material processing. In addition to the elevated temperature strength goal, elevated temperature (300°C) fatigue strength is an important material performance property for heavy-duty engine applications. A key goal for FY2013 is to scale-up the RS flake and extrusion processing steps so that larger diameter and longer extrusion can be produced. This will provide sufficient material to conduct the room temperature and elevated temperature fatigue test series.

Metallographic examination of the extruded materials was conducted along with x-ray diffraction and scanning electron microscopy analysis. All three alloys are characterized by having sub-micron grain size and an extensive distribution of sub-micron secondary phase particles. Both the AL-8.5Fe and the AFM alloys have areas of larger, less dense secondary particles, indicating some phase growth during processing. Figure 3 shows low magnification micrographs of the three extruded aluminum alloys. As indicated in Tables 2 and 3, all three alloy compositions show an increase in the measured elastic modulus of the materials, which is most pronounced in the AFCT and AFM-11 alloys.

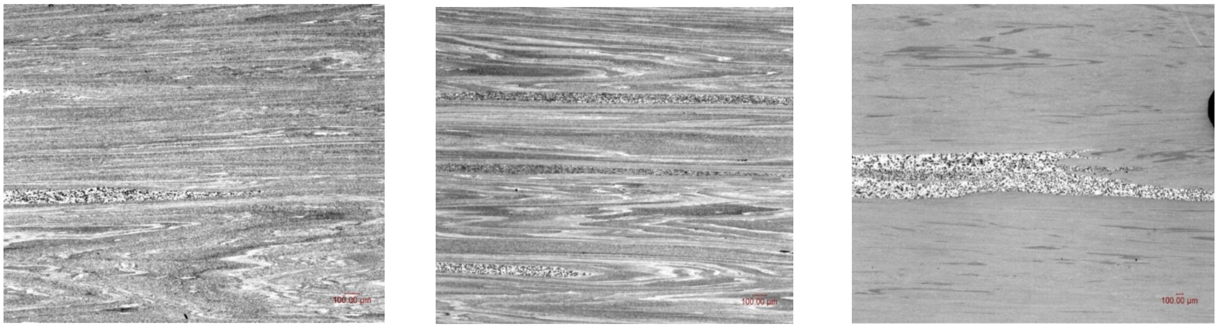

(a) (b) (c)

Figure 3. Low magnification micrographs of extruded aluminum alloys (a) AL-8.5Fe, (b) AFM-11, and (c) AFCT.

Technology Transfer

By participating in this CRADA, Cummins, Inc. will benefit by applying new technology to improve the high-temperature performance and life of engine combustion components, air-handling systems, and emission-control components. In addition, Cummins, Inc. benefits by coupling its own engineering production experience and know-how with the scientific expertise and technical capabilities of PNNL staff and U.S. Department of Energy (DOE) laboratories to solve relevant problems that benefit the industry and achieve DOE fuel economy goals.

Conclusions

The High Strength and High-Temperature Aluminum Alloys for Heavy Duty Engine Applications project started under a CRADA (agreement) in May 2011. The early phase of this project has evaluated potential high-temperature, high-strength aluminum alloy systems that can be produced by RS processing and subsequent processing into extruded or forged product forms. A group of candidate alloys have been selected for processing and characterization, and feedstock melting methods were developed. RS processing using the PNNL/Transmet melt spinning flake equipment has been completed. Laboratory-scale extrusion tooling was designed and fabricated and the tooling was used to consolidate flake materials into extruded wrought aluminum alloy rods. Extruded materials of the three alloy compositions were machined into tensile test specimens and tested at room temperature and at an elevated temperature of 300°C. Test results show that the AFCT and AFM-11 alloys have higher tensile strengths at the 300°C test temperature when compared with the Al-8.5Fe alloy, and that the AFM-11 alloy has a tensile strength exceeding 250 MPa. The focus of FY13 project work will be to optimize the alloy compositions focusing on the AFCT and AFM alloys and to scale-up processing methods to produce sufficient materials for fatigue testing and engine component fabrication.

Project 18519 - Materials for Control of Exhaust Gases and Energy Recovery Systems

Agreement 9130 - Development of Materials Analysis Tools for Studying NO_x Adsorber Catalysts (CRADA No. ORNL-02-0659 with Cummins Inc.)

Thomas Watkins, Larry Allard, Michael Lance and Harry Meyer
Oak Ridge National Laboratory
P.O. Box 2008
Oak Ridge, TN 37831-6064
(865) 387-6472; fax: (865) 574-4913; e-mail: watkinstr@ornl.gov

Krishna Kamasamudram and Aleksey Yezerets
Cummins Inc.
1900 McKinely Av., MC 50197
Columbus, IN 47201
(812) 377-4935; fax: (812) 377-7226; e-mail: Krishna.Kamasamudram@Cummins.com

DOE Technology Manager: Jerry L. Gibbs
(202) 586-1182; fax: (202) 586-1600; e-mail: jerry.gibbs@ee.doe.gov
ORNL Technical Advisor: J. Allen Haynes
(865) 576-2894; fax: (865) 574-4913; e-mail: haynesa@ornl.gov

---

Contractor: Oak Ridge National Laboratory, Oak Ridge, Tennessee
Contract No.: DE-AC05-00OR22725

Objective

- The objective of this effort is to produce a quantitative understanding of the process/product interdependence leading to catalyst systems with improved final product quality, resulting in diesel emission levels that meet the prevailing emission requirements.

Approach

- Characterize lab-engine tested samples with X-ray diffraction, spectroscopy, and microscopy. Correlate findings with Cummins data and experience.

Accomplishments

- XRD and FTIR results may suggest dealumination with hydrothermal aging.
- Microscopy observed Pt particle growth with increasing hydrothermal aging temperature.

Future Direction

- Continue in-situ AMOx catalyst characterization of a practically-relevant zeolite catalyst subjected to hydrothermal aging at elevated temperatures for lifetime prediction model input using x-ray diffraction or piezospectroscopy.

- Assist Cummins to competitively produce engines, which attain the required emission, levels while maintaining the advantage of the diesel's inherent energy efficiency.

Introduction

Commercial off-the-shelf aftertreatment technologies are now available to meet the 2010 US Environmental Protection Agency (EPA) emission requirements for diesel exhaust.[1] However, the performance of these technologies and their integration with engine control systems needs optimization. In particular, the catalytic materials can change or age with exposure to high temperatures and engine exhaust conditions. Consequently, Cummins Inc. is working to understand the basic science necessary to effectively utilize these catalyst systems. ORNL is assisting with the materials characterization effort. This report will focus on the study of materials used in ammonia oxidation.

Ammonia containing compounds may be added to diesel exhaust to reduce NO_x to N_2, as in selective catalytic reduction (SCR). The reductant reduces NO_x to H_2O and N_2.[2] Excess ammonia is often needed resulting in NH_3 escaping or "slip". This slip is a concern for sociability and environmental reasons. Although not regulated, proactive steps are taken to mitigate even small amounts of ammonia slip by employing a selective oxidation catalyst.

Oxidation catalysts are usually present in after treatment systems to oxidize ammonia that is not being oxidized upstream by the SCR catalysts. These oxidation catalysts ensure that ammonia slip to ambient is minimal and are referred to by several names: ammonia oxidation (AMOx) catalysts, selective catalytic oxidation (SCO) catalysts or ammonia slip catalysts (ASC). Candidate catalysts are typically zeolite-based, alumina-supported metal or alumina-supported metal oxide catalysts. Hydrothermal conditions, temperature and water content, strongly influence the functioning of these catalysts by changing or "aging" the catalytic materials. These changes and their impact on performance are not well understood.

Goal, Barriers, Relevance & Integration

In the study area of VT's Materials Technology subprogram, the Propulsion Materials Technology activity provides materials R&D expertise to enable advanced materials and supports the goals of several VT subprograms.[3] Within the Advanced Combustion Engine R&D activity, one primary R&D direction is to: Develop aftertreatment technologies integrated with combustion strategies for emissions compliance and minimization of an efficiency penalty.[3] Correspondingly, one *goal* is to: by 2015, improve the fuel economy of light-duty gasoline vehicles by 25 percent and of light-duty diesel vehicles by 40 percent, compared to the baseline 2009 gasoline vehicle. In support of these, this project addresses four *barriers* [3] related to the Emission Control: lack of cost-effective emission control, durability, cost (e.g., precious metal content) and improving market perception. This project is *relevant* to this goal as the understanding of the material aging underlying the Ammonia Oxidation (AMOX) catalyst performance degradation increases, efficient and durable AMOX with higher NOx conversion efficiencies can be attained. This minimizes constraints on engine-out NOx emissions and allowing engines to be tuned for optimal fuel efficiency, cost and durability. This project supports clean diesel, which increases acceptance by the public. Larger acceptance, in turn, results in larger percentages of conversion to diesel, with the resulting reduction in petroleum usage/dependency upon foreign oil. This project, similarly, also addresses three *barriers* [3] related to the Propulsion Materials Technology activity itself: Changing internal combustion engine combustion regimes, long lead times for materials commercialization and costly precious metal content. This project is *integrated* within Vehicle Technologies program as it utilizes characterization tools acquired and maintained by the High Temperature Materials Laboratory (HTML) Program.

Approach

The main focus of the CRADA in FY2012 was to continue the characterization of a practically-relevant zeolite AMOx catalyst, which was subjected to hydrothermal aging for lifetime prediction model input. The technical approach will be as before: experimentally characterize materials, supplied by Cummins, from all stages of the catalyst's lifecycle: fresh, de-greened, aged, regenerated, on-engine and off-engine, etc. The crystal structure, morphology, phase distribution, particle size, and surface species of catalytically active materials supplied by Cummins were characterized using transmission electron microscopy (TEM), X-ray diffraction (XRD), X-ray photoelectron spectroscopy (XPS), and FTIR. Ultimately, an understanding of the thermal and hydrothermal aging processes and other degradation mechanisms is sought throughout the lifecycle of the catalytic material. {Acronyms are used liberally through out this report and are defined in Table I.}

Results

While the nominal operating temperatures for diesel engines are less than 600°C, high temperature excursions may occur. As such, new samples were hydrothermally aged for 1 and 2 h at 600, 650, 700, 800, 900°C in air with 7% H_2O to study accelerated aging and then characterized at ambient.

XRD and FTIR

The brown zeolite and washcoat was easily separated from the cordierite substrate. A small section was collected from each sample, placed on a zero background plate and examined using XRD. Figure 1 shows a brown catalyst section from a 900°C – 2-h sample, completely separated from the cordierite substrate. A slight grey film appeared on the back side where it was attached to the cordierite substrate, while the bulk of the section has the same brown color as the outer/top surface.

Figures 2 shows the 3-D overlays of all the 1-h and 2-h XRD patterns. For a particular time, the x-ray patterns were nearly identical and therefore appear to be independent of temperature. Comparison to the as-received condition was not presently possible given that the sample preparation was not the same as prior work [6] (i.e., here powder was removed from the substrate). Qualitatively though, the prior work also showed only slight changes between the as-received sample peaks and the aged, which is consistent with what is observed here. Given the similarities are independent of temperature, Figure 3 is a summation of all of the 1-h and all of the 2-h scans to assist in peak identification. There are distinct differences in the two sets of patterns. A shift in the low angle peak after 2 hours, the appearance of two new peaks, and the reduction in intensity of the major peak between 23° to 24° 2θ are observed. The new peak near 28.5° 2θ is located where the major peak of silicon is observed, and the new peak near 24° 2θ, is located where a peak for hematite (Fe_2O_3) is observed. It is speculated that the changes in the peaks at 7.8 and 22.5° 2θ are due to dealumination of the zeolite structure. A crude Rietveld refinement of the two zeolite-beta phases was undertaken using HighScore Plus,[4] and the quantitative estimates can be seen in Figures 4 and 5. Table II lists the unit cell parameters for the 1-h and 2-h summation scans in Figure 3.

A Nicolet 670 Fourier Transform-Infrared Spectrometer (FTIR) with a diamond ATR (attenuated total reflectance) cell was used to measure the change in vibrational frequency of the zeolite structure of an AMOx catalyst wash coat caused by hydrothermal aging in 7% H_2O at temperatures from 600ºC to 900ºC. The best spectra were obtained by pressing the wash coat surface directly against the ATR diamond, which eliminated the cordierite peaks from the final spectrum.

Spectra were collected from samples aged for 1 and 2 hours at 600, 650, 700 800 and 900ºC. Only the 900ºC sample differed from the other specimens. Figure 6 shows the skeletal modes of the zeolite framework[5] that occur below 1400 cm^{-1} for the as-received, the 600ºC 1-h and the 900ºC 2-h samples. The large peak around 1050 cm^{-1} is produced by the Si-O stretching vibration. There is no significant difference between the as-received sample and the 600°C 1-h sample. The shift to higher frequencies seen in the 900ºC spectrum may indicate more network bonding of the O-Si-O units, which causes them to vibrate at a higher frequency. This shift may also be caused by dealumination of the structure resulting in more Si-O bonding.

Figure 7 again compares the three samples in the frequency range from 2400 to 4000 cm^{-1}. The broad peak from 2800 to 3600 cm^{-1} is from OH groups, which seems to decline in abundance following hydrothermal treatment. In addition, the sharp peaks around 2900 cm^{-1} produced by C-H bonding appear in the 600ºC sample and then disappear in the 900ºC sample. These peaks could be from residual hydrocarbon species that oxidize at 900ºC.

Microanalysis of AMOx Catalyst Materials

Selected samples were characterized using several techniques of electron microscopy. Bulk cross-sections of the catalyst monolith structures were prepared by standard metallographic techniques of mounting in epoxy and polishing, and these samples were examined first in the scanning electron microscope (Hitachi S-4800) primarily in secondary electron (SE) imaging mode. These cross-sections have typically been used in past work to make thin sections of a “cross” of the monolith, giving the potential for having an electron transparent area through both the cordierite monolith and the washcoat layer. This allows the components of the structure to be observed with their spatial relationships maintained. Also the components of the washcoat powder are typically examined and characterized.

Samples were prepared for observation in the ORNL JEOL 2200FS aberration-corrected STEM/TEM instrument (ACEM), which is equipped with a Bruker-AXS silicon-drift energy-dispersive spectrometer (EDS) for analysis of the chemistry of phases observed with scanning transmission dark-field and bright-field images. Powder was scraped from the inner surfaces of channels in a fractured section of monolith, ground and dry-dispersed onto a holey carbon film which was supported on a Be TEM grid (to minimize the contribution of Cu, an element of interest, in the EDS spectra collected). Images in the ACEM were recorded simultaneously using a high-angle annular dark-field (HAADF) detector and a bright-field (BF) detector. The HAADF images show contrast related primarily to atomic number, where the high atomic number (Z) species are brighter in contrast, with the contrast related roughly to Z^2. This latter technique was used for most of the results, but a new method for making the electron-transparent thin section was tried for the first time. Here a focused ion beam milling instrument (Hitachi NB-5000) was used to prepare a sample from the metallographic mount, and the excellent results of this technique are highlighted in the following.

The microstructures of samples hydrothermally treated for 1 and 2 hours at 600°C and 900°C were selected to show the general trend of changes in morphology with the treatment times and temperatures. Figure 8 shows an SE image of a polished section of the AMOx-600C-1h specimen; the interface between the cordierite monolith, an inner coating of alumina (shown also to support Pt catalyst particles, per coming figures), and a layer composed of particles of alumino-silicate zeolite structure compatible with the mineral “chabazite” can be seen. The chabazite particles were typically in the range of 0.1-0.5 microns. Figure 9a shows an oblique view with an initial slice shown partly milled in the bulk cross-section mount. This sample was site-selected to run from the edge of the cordierite monolith, across the alumina (AlOx) inner layer and into the zeolite outer washcoat layer. Figure 9b shows a perpendicular view of the nearly final thinned section, with the thin section mounted onto a special FIB mount (not shown on the left edge of this image). The AlOx and Zeolite regions are labeled, and in this sample, an area filled in with the epoxy mounting medium is also shown.

In Figure 10, the HAADF image shows zeolite particles on the left side, and the alumina layer on the right side. HAADF images show contrast related to atomic number, with brighter areas comprising elements of higher average atomic number than darker areas. Within the alumina layer, the very bright particles are Pt. Figure 11 shows the primary elemental distribution from the area of Figure 10. These “Hypermaps” or elemental maps were acquired on the ACEM using a Bruker silicon-drift detector (SDD) system, in which the sample area of e.g. 256 x 256 pixels is scanned with the electron beam for a period of time (e.g. 25 minutes) and spectra are acquired for every point in the image. Post-processing allows all the spectra composing pixels in any chosen area to be summed, and the elements in that area identified. A coating on the zeolite particles composed of Fe and Al oxides is indicated by the elemental maps, and confirmed by the elemental spectra from these areas (not shown). A similar intergranular coating was seen on the chabazite zeolite washcoat materials analyzed in earlier work.[6]

Figures 12 and 13 show the alumina area in HAADF mode and the elemental maps from this region, respectively. The bright particles show a range of Pt particle sizes from smaller than 1nm to about 15nm. Even the smallest bright “specks” in the HAADF image are all Pt. Interestingly, a full spectrum from the entire area (not shown) indicated a minor peak at the position of Zr, and the map for just Zr shows a few very small areas with strong contrast, suggesting a tiny bit of Zr-rich particles exist in the alumina layer. Zr was not typically seen in other mapped areas from this and others of the sample suite, so the role of Zr is not clear. As will be shown below, ZrO_2 and alumina may have been added to surfaces of the zeolite to improve the zeolites stability.[7]

In Figure 14, the Pt distribution in the 600°C 1-h sample is shown. The smallest bright specks in the HAADF image map to the bright intensity in the Pt map, in which the contrast has been enhanced to better show the very fine Pt particles. A typical Pt particle that is well oriented to the electron beam direction (looking down a <100> (cube edge) crystallographic zone axis) is shown in Figure 15 and its inset. This figure also has some bright intensity shown in areas circled, suggesting the presence of very small clusters of Pt atoms. Details of the presence of Pt distribution down to the single-atom level are given in the description below of the washcoat powder sample from the 600°C 2-h hydrotreatment.

Powder from the AMOx-600°C 2-h sample was mounted on a holey-carbon film supported on a beryllium TEM grid (to minimize contributions from the support grid on an EDS spectrum). The powder was composed primarily of the zeolite phase, which comprises the majority volume of catalyst on the monolith. But with careful “hunting” on the grid, examples of a thin flakes of the Pt-containing alumina phase were located. The roughly cube-shaped zeolite particles coated with the Al-FeOx material are seen in Figure 16 with the very fine-grained alumina flake circled was magnified (Figure 17). The distribution of Pt particles is in bright contrast. A typical single-crystal Pt particle in the AMOx-600°C 2-h sample is shown at higher magnification in Figure 18, with again some suggestion of additional Pt species seen in the several slightly higher intensity areas above the particle. This area is shown in further detail in the contrast-enhanced image of Figure 19. This image shows that in addition to the discrete Pt nanoparticles in the washcoat. There is also a collection of disordered “rafts” or clusters of Pt atoms still coating the surfaces of the alumina aggregates, and even many single atoms still present, even after the 2-h hydrothermal aging at 600°C. This important observation is shown at even greater detail in a similar sample area shown in Figure 20. Recall that because of the small depth of focus in the aberration-corrected microscope, sample areas separated by small height differences can vary greatly in focus. Figure 20a shows a disordered raft of Pt atoms in sharp focus, in which several individual or pairs of atoms are circled in addition to the cluster. Note that the variation in contrast of the “atoms” in the cluster is likely due to atoms of Pt “sitting” one atop another, although a full double layer is not formed in this cluster. Figure 20b shows in sharp focus the fuzzy area that is arrowed in 20a, while the original raft of 20a is out of focus, indicating that the cluster in Fig. 20b is at a different height. Several individual atoms are also seen around this cluster; this suggests that in addition to the disordered clusters, individual Pt atoms are prevalent on the alumina surfaces.

After deposition onto a carbon-coated TEM grid, washcoat powders from the samples hydro thermally treated at 900°C for 1 and 2 hours were also examined. Figure 21 shows an individual flake of alumina material with Pt particles that are much larger (20X) and more widely separated than those in the 600°C samples. One of these particles is shown in the inset, illustrating that no individual Pt atoms are seen in the region, and is the typical observation in both the AMOx-900°C 1-h and 2-h samples. Figure 22 shows a flake of alumina washcoat in the 900°C 2-h sample. The Pt particles circled in both figures are reversed in focus between the figures; this allows showing the presence of most of the Pt particles in the flake. The relative size and distribution of Pt particles in all of the hydrotreated specimens in the AMOx series will be more accurately assessed statistically by images made from FIB-processes thin sections, and will be reported in a future quarterly report.

Microanalysis of Cu-Zeolite SCR Catalyst Materials

Advanced electron microscopy methods are being used to characterize the structure, morphology and microchemistry of a new series of commercial copper-based zeolite selective-catalytic-reduction (SCR) catalyst materials provided by Cummins. The catalysts were provided typically as wash-coated monoliths in an as-coated or fresh condition (i.e. the monoliths had not been used or treated in any way). Six different zeolite SCR catalysts are being studied; typical results from characterization of one of the as-prepared materials, identified as "Cu-F" are given as follows. Effects of hydrothermal aging treatments at various times and temperatures on the remaining fresh materials are also being characterized and will be reported later, as appropriate.

Figure 23 shows HAADF-BF images of the general morphology of the Cu-F zeolite sample. There are two distinctly different characteristics of the powder: one component is composed of rounded, equiaxed particles 50-150nm in size with generally smooth surfaces, such as the area shown in the inset box A, and the second major component is a very fine-grained aggregation of nanoparticles such as the area shown in the inset box B. This area was used to generate a "hypermap" of EDS data for further compositional analysis. The hypermap generates individual elemental spectra, pixel by pixel, so that any area of the elemental map selected, after its accumulation, will show the sum of all the spectra within the area. This allows *a posteriori* determination of the elemental distributions in chosen areas. The elemental map data for a selected group of elements is shown in Figure 24. General inspection of the individual elemental maps suggests that the rounded particles are primarily an aluminosilicate composition, and the fine powder contains Zr as well as Al and Si. These results are consistent also with the spectra generated from the areas A and B in Figure 23, and shown in Fig. 25a and b. The high Si-O peaks in area B likely are contributed to some extent by excitation of the nearby bulkier aluminosilicate particles, but there is also the potential that some fraction of the fine particulate, likely ZrO_2, phase also has a silica component. As mentioned before, ZrO_2 and alumina may have been added to surfaces of the zeolite to improve the zeolites stability.[7] Mo in the spectrum is a system contaminant, probably from Mo in the collimator of the silicon drift detector system. The Cu elemental map suggests an overall distribution of Cu in the aluminosilicate particles, but this might also originate from spurious x-rays generated by electron scattering onto Cu-bearing components of the microscope. To test this, we used the same specimen holder and a Be grid with SiO_2 particles, and collected the spectrum shown in Figure 25c. The spectrum was collected from 1-10 keV in energy, and so is adjusted relative to the spectra from areas A and B to match the energy scales. It also shows a small Cu peak, the height of which relative to Si is lower than the Cu peak from area B, but about the same as the Cu peak from Area A. This suggests that there is a component of Cu, likely Cu oxide, also in the fine powder material. But since the hypermap of Cu shown in Figure 24 indicates the possible presence of Cu in (or on) the bulk aluminosilicate particles, another powder area was analyzed.

Figure 26 shows a HAADF-BF image pair of a nearly "clean" aluminosilicate particle. Several bright spots are clearly seen in profile on the surface are indicated by arrows, indicating heavy metal species. Two of the bright spots are labeled Cu, as they match the hypermap data shown in Figure 27, which indicates a non-uniform concentration of both Zr and Cu on (or in) the particle. The Cu concentrations on the surface corresponding to those labeled in Figure 26 are also shown by arrows on the ADF image and Cu map of Figure 27. Since the fine powder phase is primarily Zr-based, it is logical that the Zr distribution shown in Figure 27 on the aluminosilicate particle is primarily on the surface. Cu is not in a uniform dispersion throughout the particle, and it is reasonable to presume that Cu is present as an oxide species also primarily on the surface of the zeolite, particularly since Cu species can be positively identified on the surface as per Figure 27. These results are an example of the kinds of information available on the structure, chemistry and morphologies seen in the set of commercial zeolite SCR catalysts presently being analyzed on the CRADA project.

Summary

AMOx and SCR catalysts have been characterized. For the AMOx catalysts, the XRD patterns for all the hydrothermal aging temperatures were very similar. That is, for a particular time, the x-ray patterns were nearly identical and therefore appear to be independent of temperature. This suggests the material aged quite quickly above 600°C in 7% H_2O. There were difference between the 1- and 2-h aging times with new phases appearing after two hours. It is speculated that the changes are due to dealumination of the zeolite structure, based in part on crude Rietveld refinements.

In contrast, the FITR spectra were collected from samples aged for 1 and 2 hours at 600, 650, 700 800 and 900ºC in 7% H_2O. Only the 900ºC sample differed from the other specimens. It was speculated that a shift to higher frequencies of the Si-O stretching vibration may be caused by dealumination of the structure resulting in more Si-O bonding.

Microscopy techniques examined a selection of specimens from the AMOx suite of catalysts. The primary observation is that the catalyst comprises a two-layer system, with a Pt/AlOx-based inner layer and a zeolite particle outer layer. In the sample hydrothermally aged at 600°C (both 1 and 2 h) in 7%H_2O, the Pt particles range in size from 15nm at the largest down to smaller than 1nm, and there exists in addition a dispersion of disordered rafts of atoms. Also single atom species were observed over the surfaces of the alumina support. However, after a 900°C hydrothermal aging temperature, no similar atoms and clusters or rafts were seen, and the Pt particles were much larger and more widely dispersed. In possible contrast with XRD and FTIR results, initial observations of the zeolite phase in the 600°C and 900°C specimens did not show any readily apparent differences in morphology between those extremes in treatment.

Both the size and distribution of the Pt particles are critical to catalytic function. Pt rafts were not observed in prior work for as-received/no hydrothermal aging samples.[6] Well dispersed PT particles ~5nm in size were also seen.[6] Hydrothermal aging at 600 in air with 7% H_2O showed Pt rafts/clusters of individual PT atoms and larger partially facetted Pt particles, ~12 nm in size. Hydrothermal aging at 900 in air with 7% H_2O showed widely dispersed larger facetted Pt particles, >20 nm in size. As larger Pt particles are found to be less catalytically active, engine excursions above 600°C need to be minimized to reduce or slow Pt coalescence.

Microscopy techniques also examined a selection of specimens from the SCR suite of catalysts. Cu and Zr were observed on the surface of the zeolite. The copper is consistent with the type of zeolite. The Zr (ZrO_2) may be present to help stabilize the zeolite.

References

1. United States Code of Federal Regulations 40 CFR 86 (7–1–10 Edition), pp. 144-722.
2. I. Chorkendorff and J. W. Niemantsverdriet, Concepts of Modern Catalysis and Kinetics, Wiley-VCH Verlag GmbH & Co. KGaA, Weinheim, 2003, pp. 395-400.
3. Multi-Year Program Plan 2011-2015, Vehicle Technologies Program, EERE, DOE, December 2010, pp. 2.3-1, 2 ; 2.5-8. (http://www1.eere.energy.gov/vehiclesandfuels/resources/fcvt_plans_roadmaps.html).
4. High Score Plus (2009). High Score Plus, version 3.0 (computer software), PANalytical B.V., Amelo, The Netherlands.
5. Paze´ et al., J. Phys. Chem. B **101** 4740-4751 (1997).
6. 2011 Propulsion Materials Annual Progress Reports, Vehicle Technologies Program, US DOE, Energy Efficiency and Renewable Energy, Office of Vehicle Technologies, www.ornl.gov/sci/propulsionmaterials/Reports.html.
7. X. Wei and S.A. Roth, Surface-coated zeolite materials for diesel oxidation applications, US Patent Application No.2012/0079817.

Table I - Acronyms

ACEM	aberration-corrected electron microscope
AMOx	ammonia oxidation
ASC	ammonia slip catalysts
ATR	attenuated total reflectance
BF	bright-field
BSE	back-scattered electron
EDS	Energy dispersive spectroscopy
EPA	Environmental Protection Agency
FIB	Focused Ion Beam (microscopy)
FTIR	Fourier Transform-Infrared Spectroscopy
HA-ADF	high-angle annular dark-field
HTML	High Temperature Materials Laboratory
NOx	Nitrogen and Oxygen containing compounds
ORNL	Oak Ridge National Laboratory
SCO	selective catalytic oxidation
SE	secondary electron
(S)TEM	scanning transmission electron microscopy
XPS	X-ray photoelectron spectroscopy
XRD	X-Ray Diffraction

Table II. A list of the refined unit cell parameters for the 1-h and 2-h scans.

Sample	Compound	Wt %	Space Group	a	b	c
				α	β	γ
Summation of 1-h Scans	Zeolite beta Monoclinic	52	Monoclinic	17.606	17.656	14.336
			C 1 2/c 1 (15)	90	113.84	90
	Zeolite beta Tetragonal	48	Tetragonal	12.464	12.464	26.223
			P 41 2 2 (91)	90	90	90
Summation of 2-h Scans	Zeolite beta Monoclinic	38	Monoclinic	17.547	17.620	14.369
			C 1 2/c 1 (15)	90	113.76	90
	Zeolite beta Tetragonal	40	Tetragonal	12.438	12.438	26.166
			P 41 2 2 (91)	90	90	90
	Hematite Fe_2O_3	10	Rhobohedral	5.029	5.029	13.79
			R -3 c (167)	90	90	90
	Silicon	12	Cubic	5.429	5.429	5.429
			F d -3 m (227))	90	90	90

Figure 1. *The brown catalyst section separated from the cordierite surface for sample AMOX2 900°C – 2 h and was collected for XRD examination. The slight grey on the brown scale is where it was attached to the cordierite surface, while the brown surface is the outer surface as seen when attached to the tan cordierite substrate.*

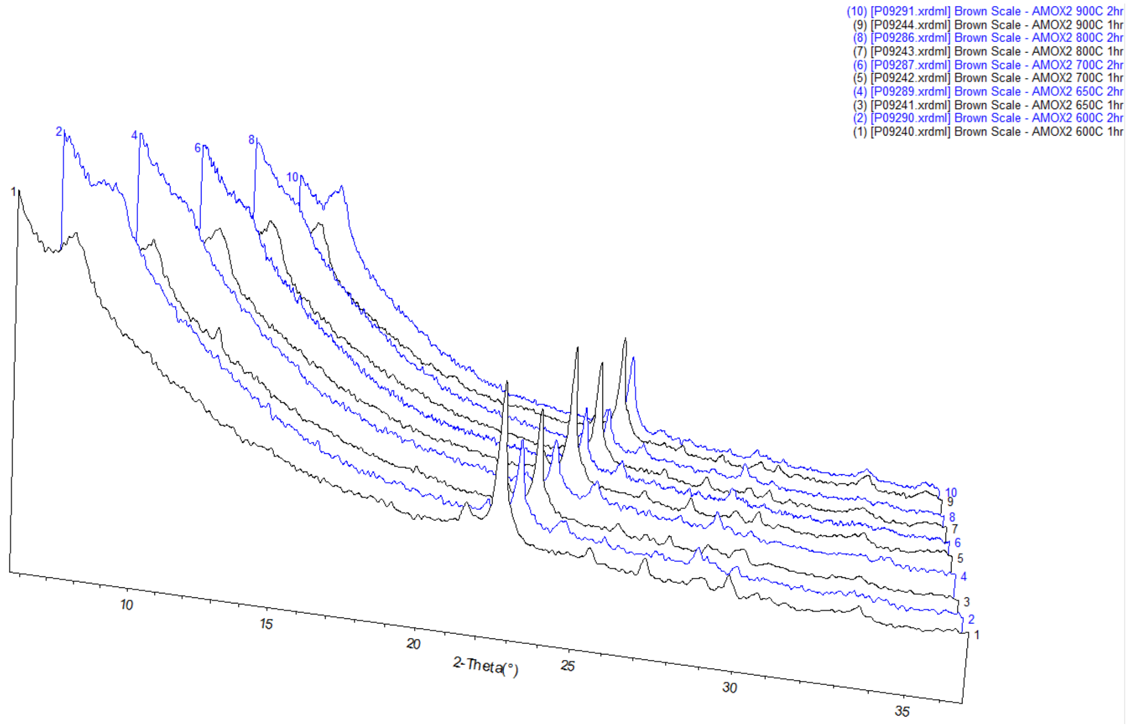

Figure 2. *A 3-D overlay of all the XRD patterns sorted by time (one hour black and two hour blue) and temperature as seen in the key at top right.*

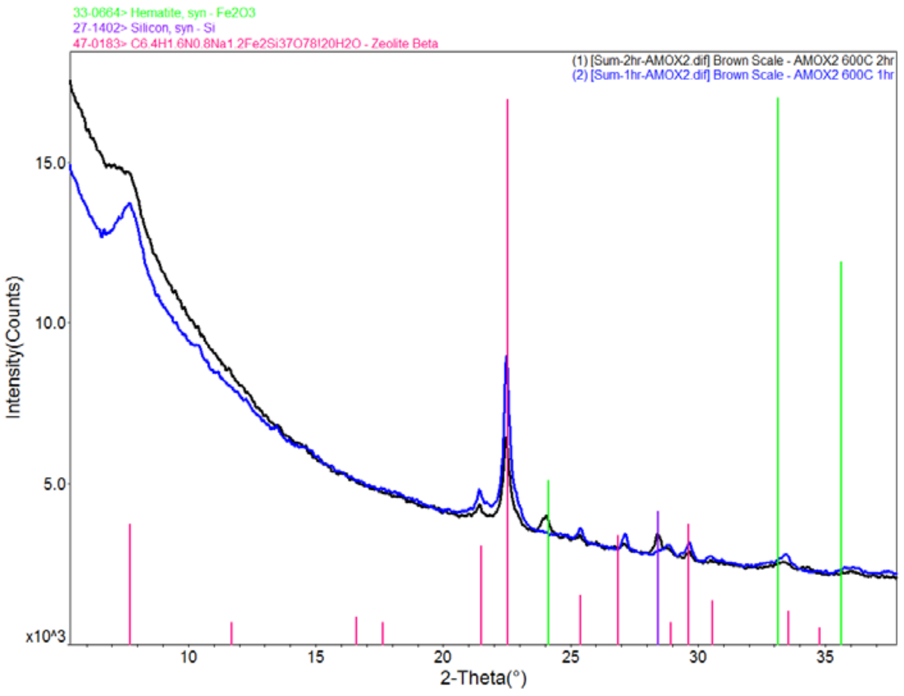

Figure 3. *The location and intensity for Zeolite-beta (red), silicon (purple) and hematite (green) are superimposed on a plot of summations of the 1h (blue) and the 2h (black) scans. The changes between the one and two hour sets can be seen to correspond with the location of major peaks of silicon, a peak of hematite and zeolite-beta.*

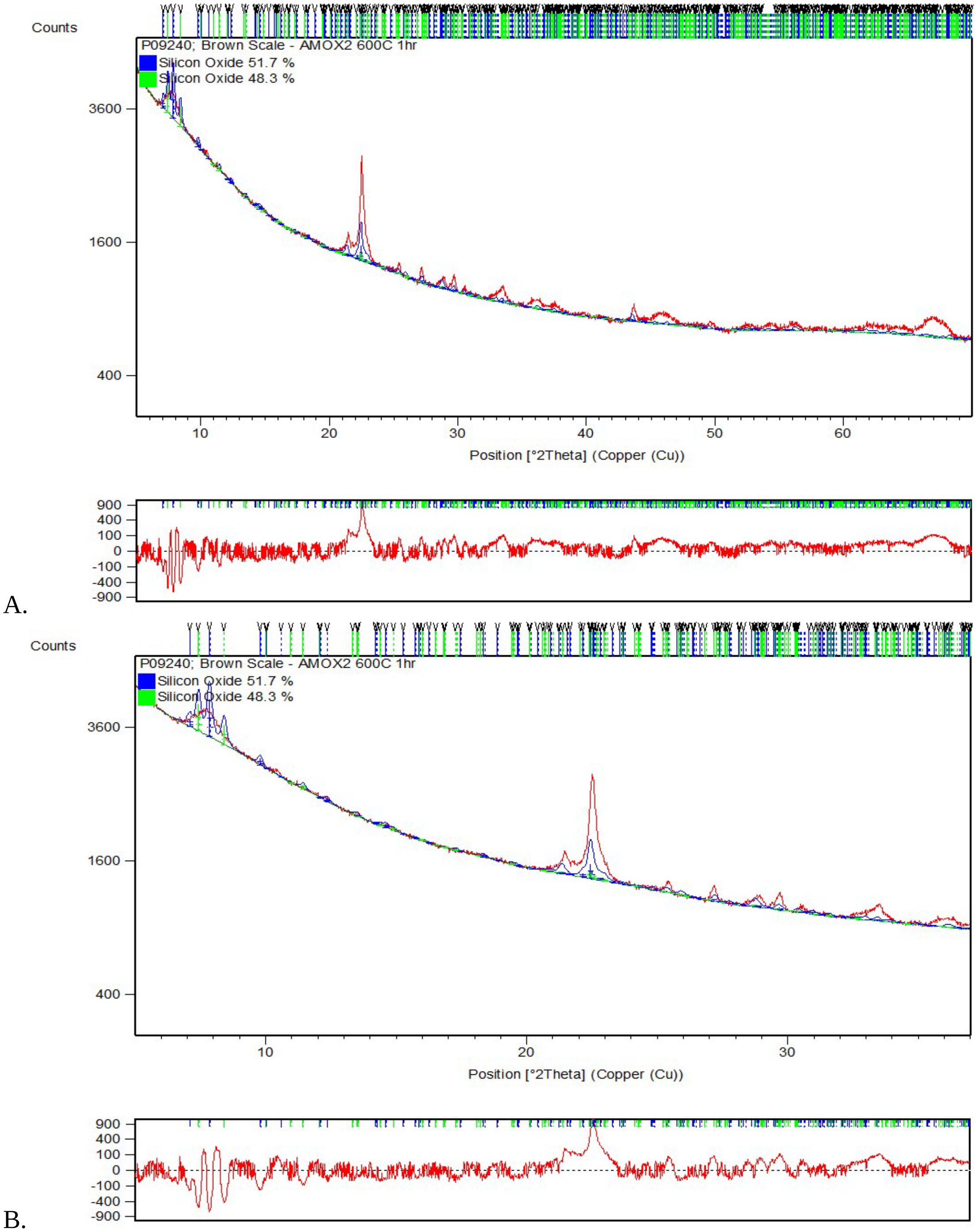

Figure 4. *A. For the summation of the 1h scans, the calculated structure refinement (blue line – calculated pattern) is plotted along with the observed XRD data (red) in the top section. In addition, the location of the refined peak position is marked with the same colored lines as noted in the color key. The difference between the observed and calculated patterns (red) is plotted in the bottom portion of the figure. B. An enlargement of A in the low 2*θ *region.*

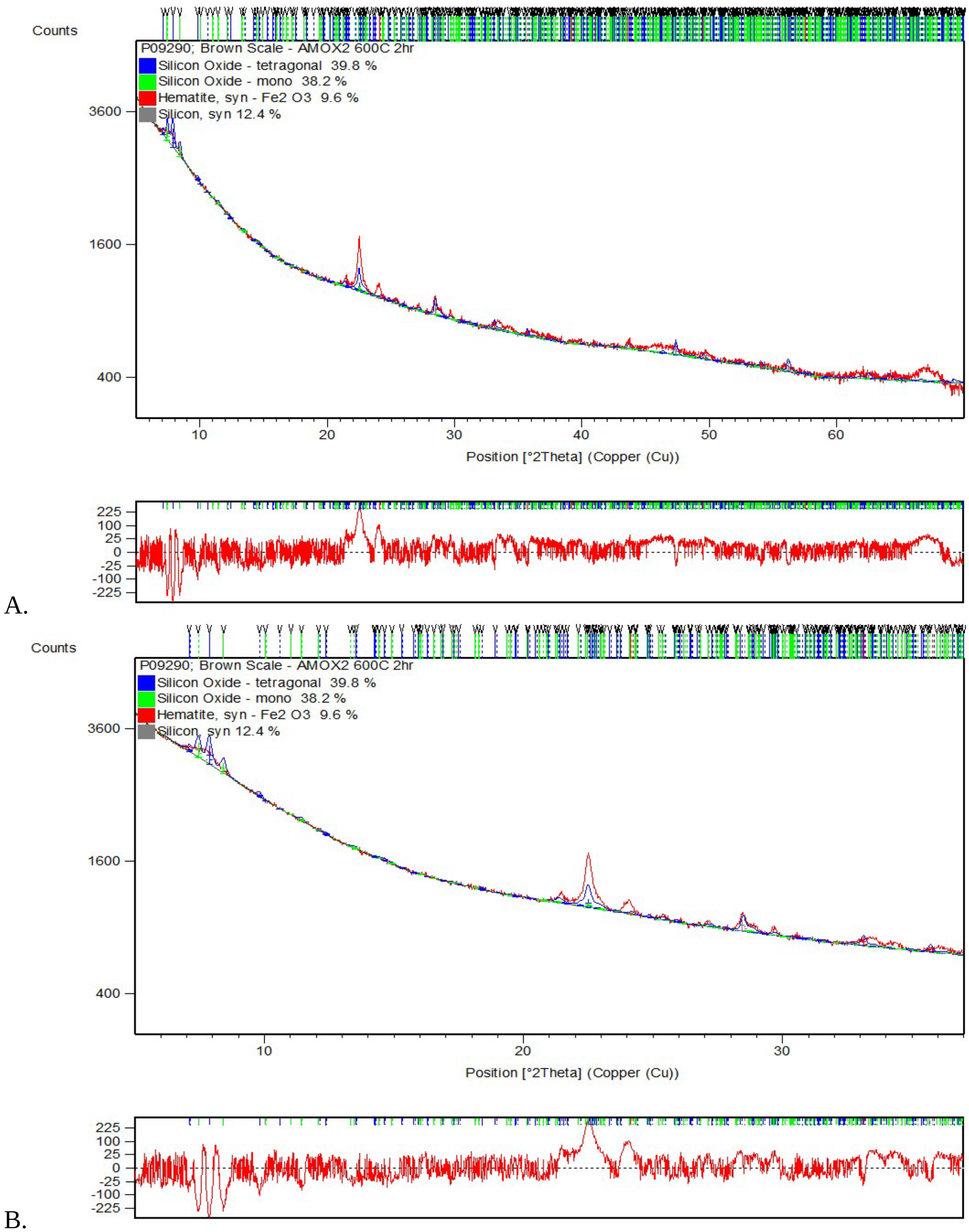

Figure 5. *A. For the summation of the 2-h scans, the calculated structure refinement (blue line – calculated pattern) is plotted along with the observed XRD data (red) in the top section. In addition, the location of the refined peak position is marked with the same colored lines as noted in the color key. The difference between the observed and calculated patterns (red) is plotted in the bottom portion of the figure. B. An enlargement of A in the low* 2θ *region.*

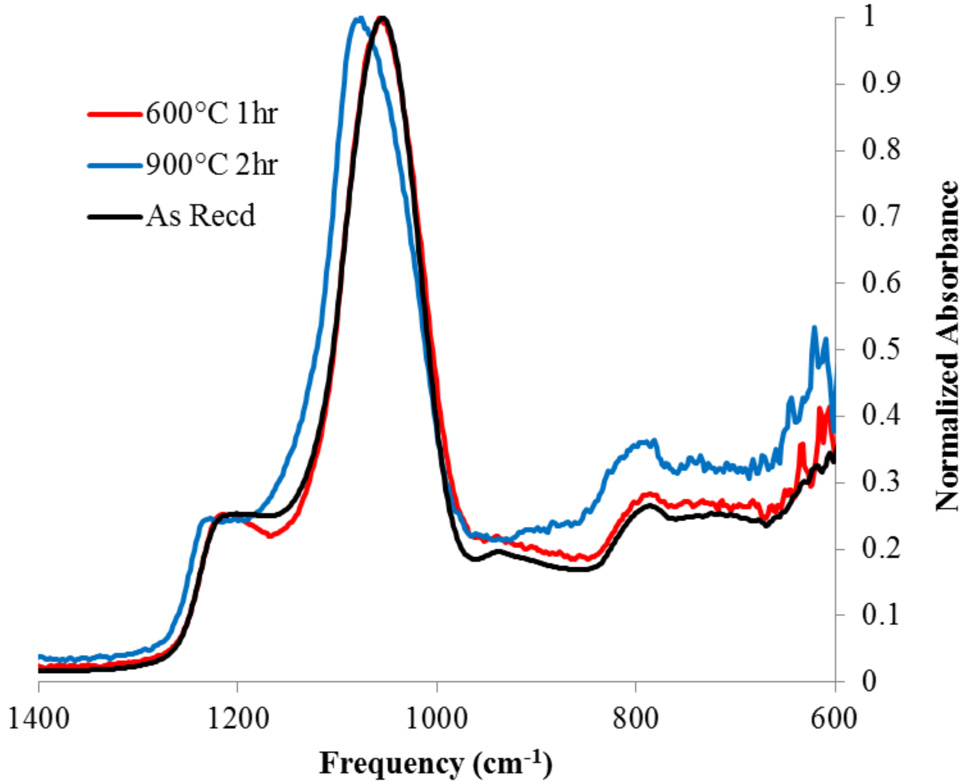

Figure 6. FTIR spectra showing the zeolite Si-O framework peaks.

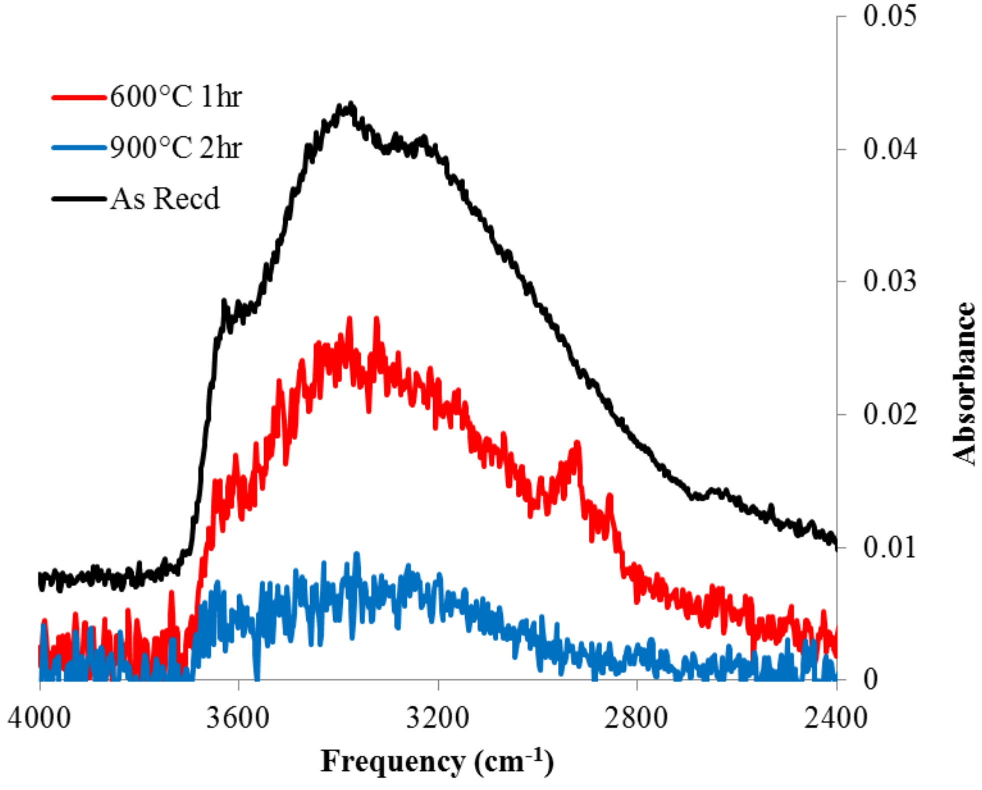

Figure 7. *FTIR spectra showing the broad –OH peak and peaks from C-H stretching vibration around 2900 cm*$^{-1}$*.*

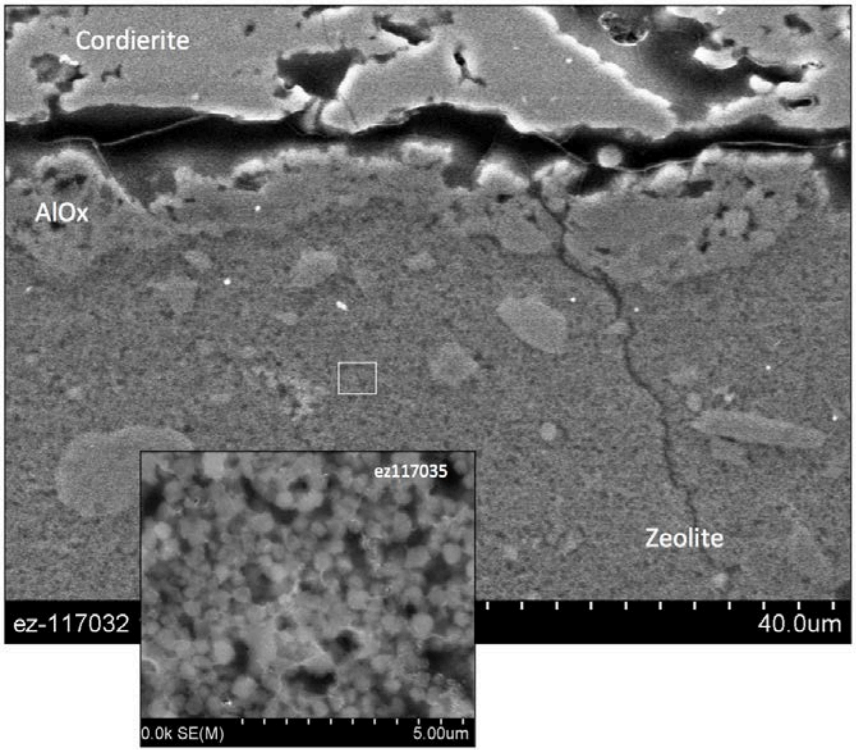

Figure 8. *SE image of a polished section of the AMOx-600C 1-h specimen. Inset: close up of zeolite layer.*

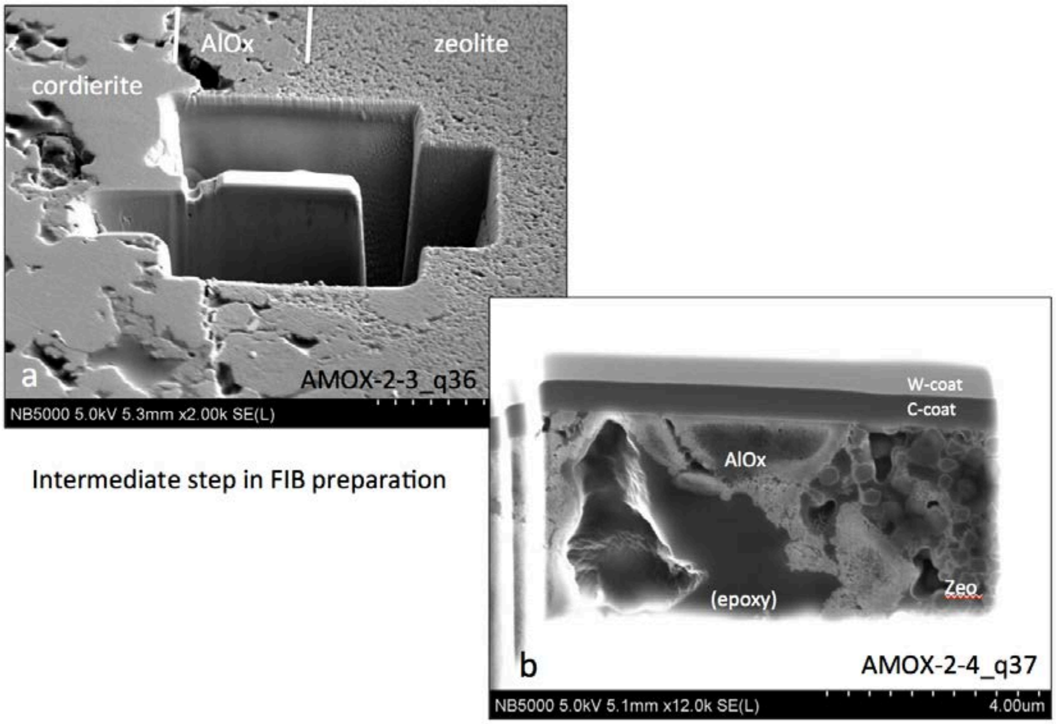

Intermediate step in FIB preparation

Near final thinning, perpendicular view

Figure 9. *The FIB-milled sample preparation technique is highlighted. Left: oblique view, Right: perpendicular view.*

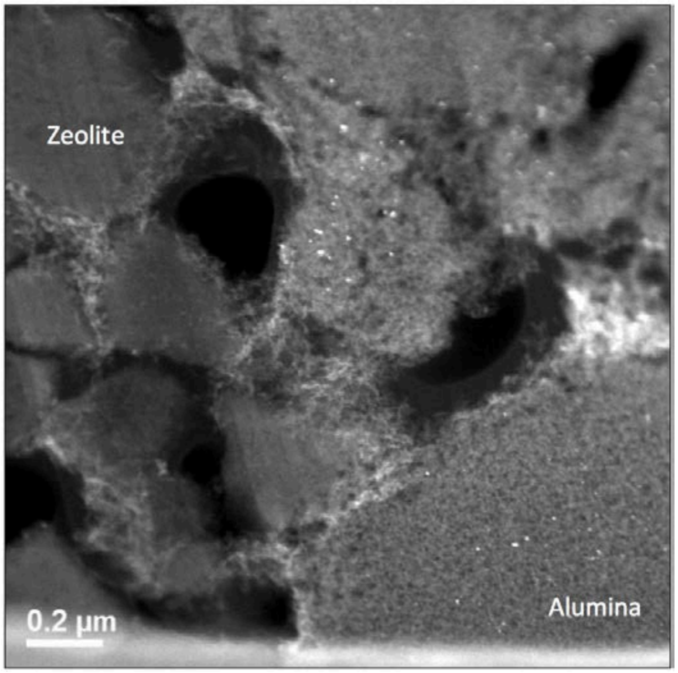

Figure 10. *The final electron-transparent section HAADF image of the AMOx-600C 1-h specimen.*

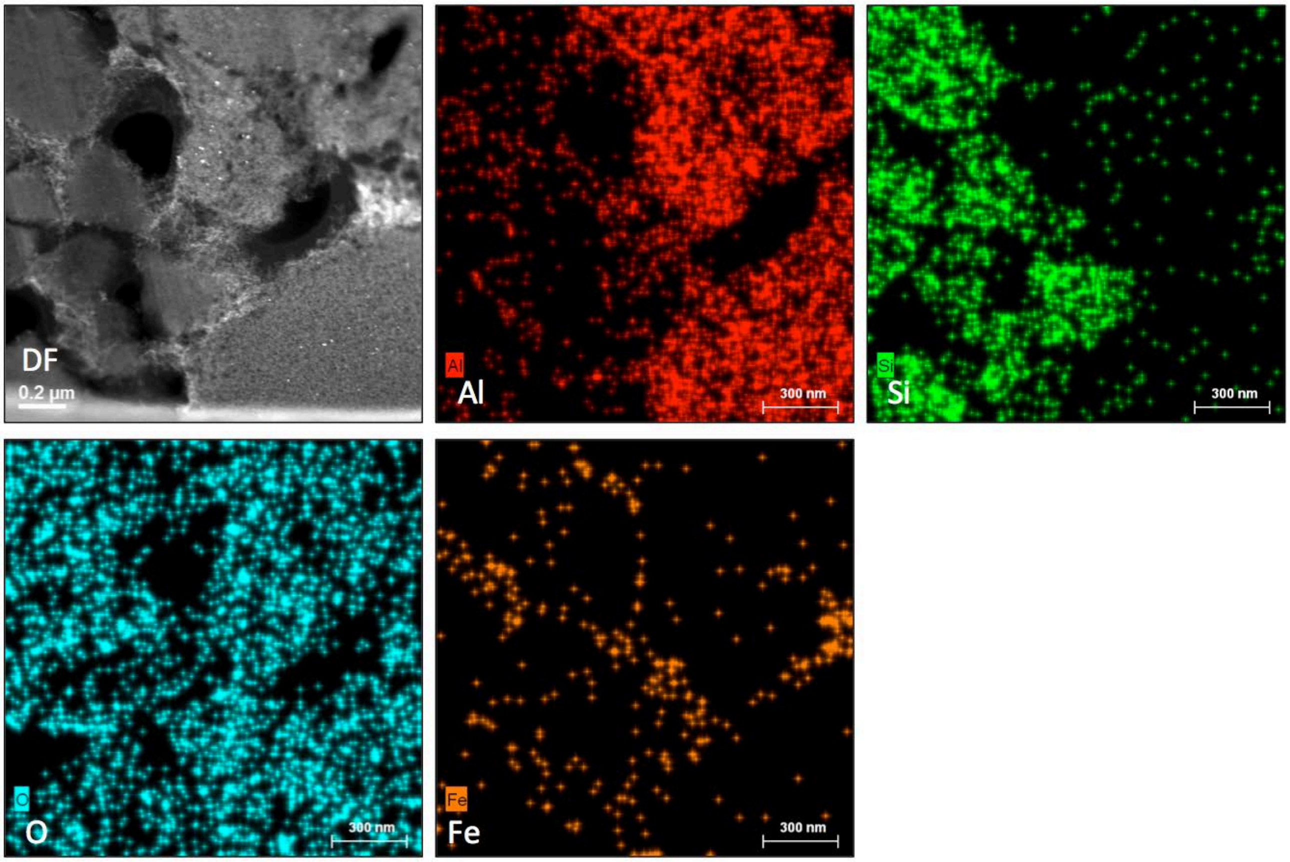

Figure 11. *The elemental maps of the region shown in the dark field image (upper left and in Figure 10) after 1 hour at 600°C in air with 7%* H_2O*.*

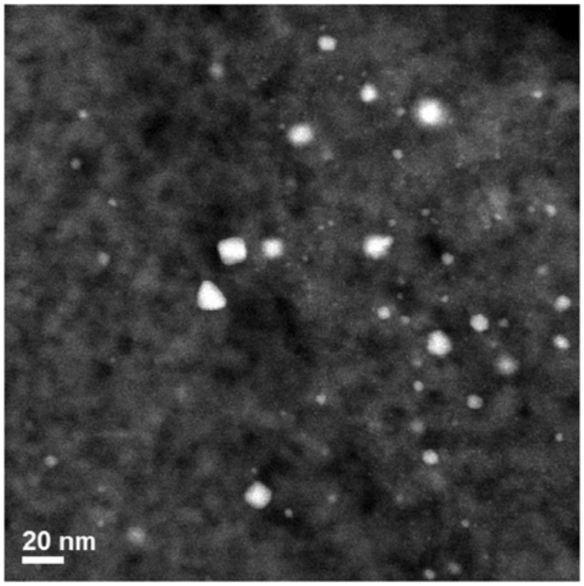

Figure 12. *The HAADF image of alumina layer showing Pt particles.*

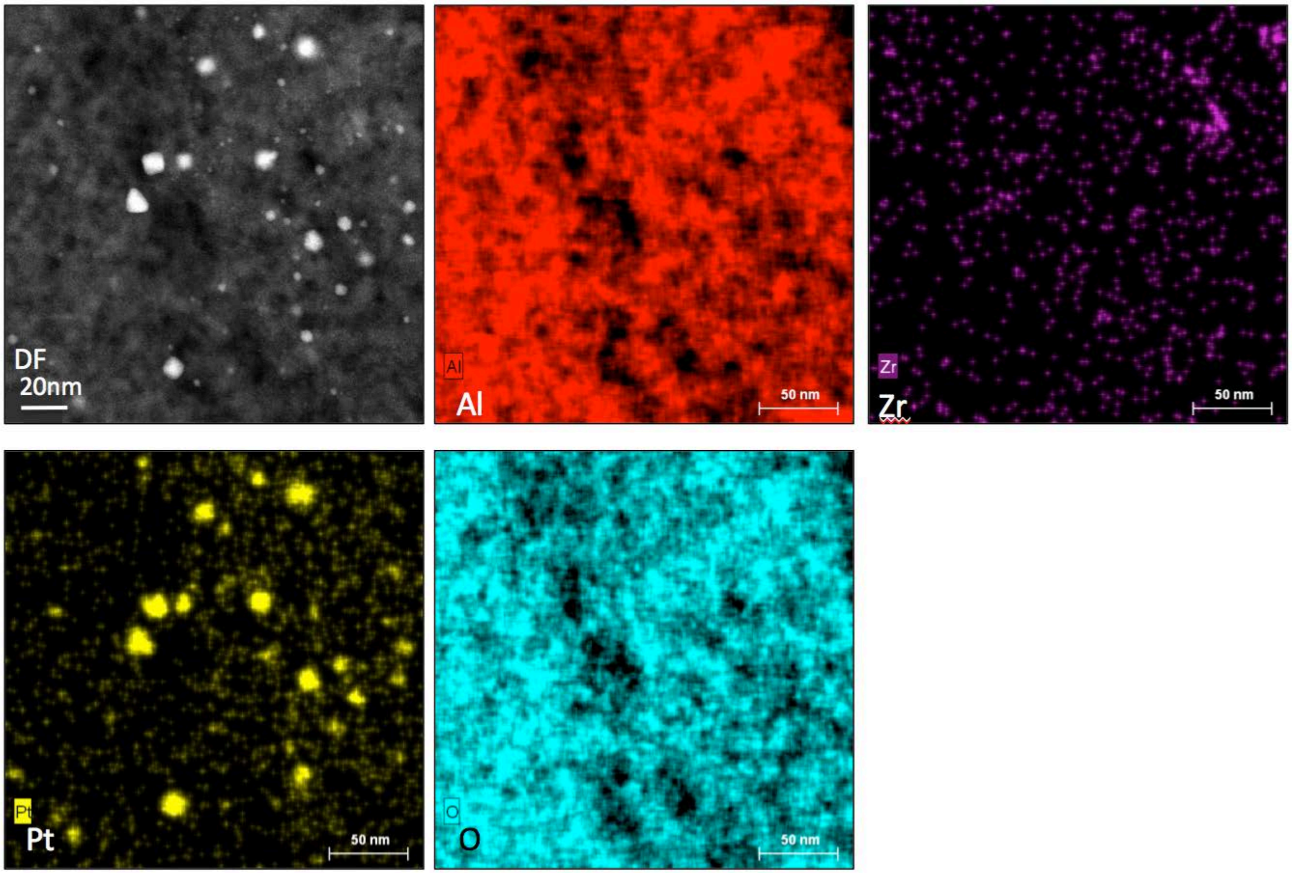

Figure 13. *The elemental maps of a region within the alumina layer shown in the dark field image (upper left and in Figure 12) after 1 hour at 600°C in air with 7%* H_2O.

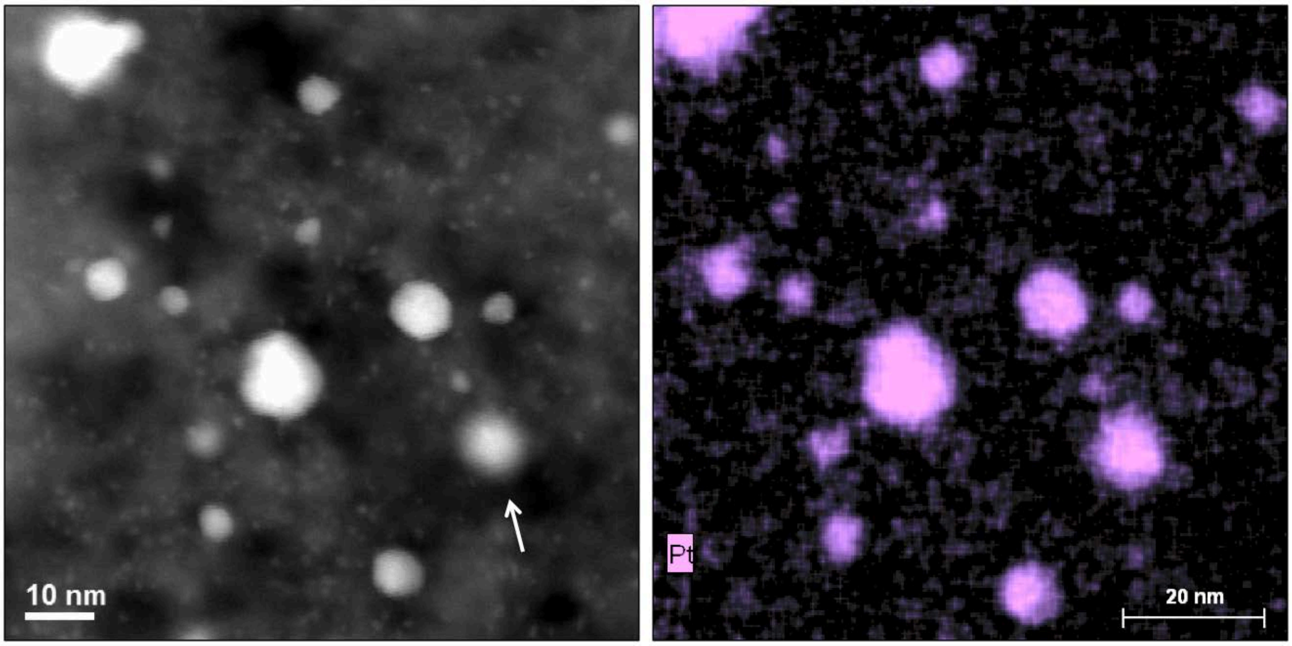

Figure 14. *A higher magnification HAADF image (left) of alumina layer showing Pt particles distribution in the AMOx-600C 1-h specimen, which is confirmed in the Pt elemental map (right). Note that in the HAADF image, some particles are in focus while others (e.g., arrow) are out of focus. This is because the focused probe in the ACEM has a relatively large convergence angle, and thereby a very small (~5nm) depth of focus. Thus, the particles in the FIB section (nominally ~50nm thick), that are more than 5nm from a given plane of focus, appear increasingly "fuzzy" in the HAADF image. The depth of focus issue does not affect the acquisition of the x-rays from the sample area, however.*

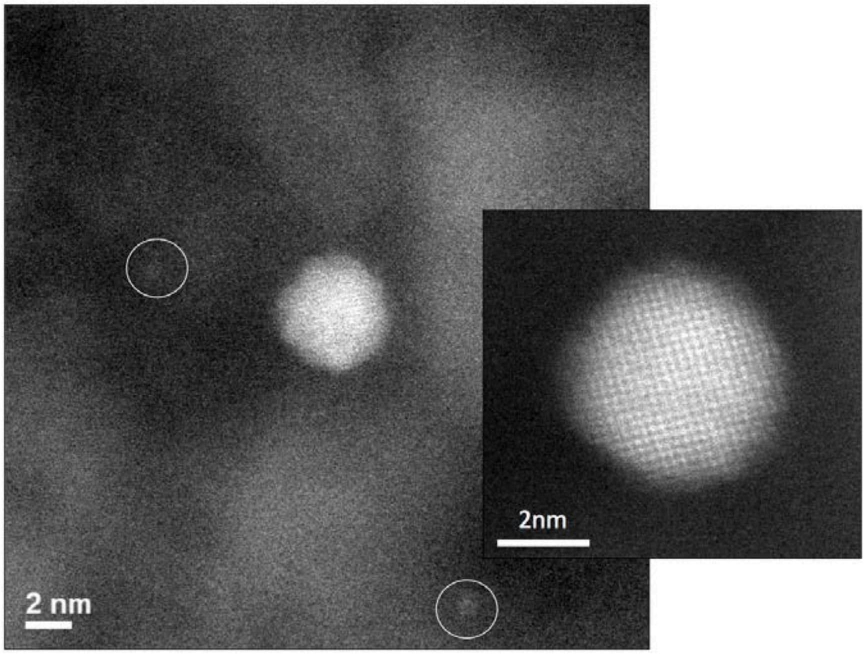

Figure 15. *A typical Pt particle that is well oriented to the electron beam direction (looking down a <100> (cube edge) crystallographic zone axis) from AMOx-600°C 1-h sample. Inset: Close up. The circled areas of bright intensity suggest the presence of very small clusters of Pt atoms.*

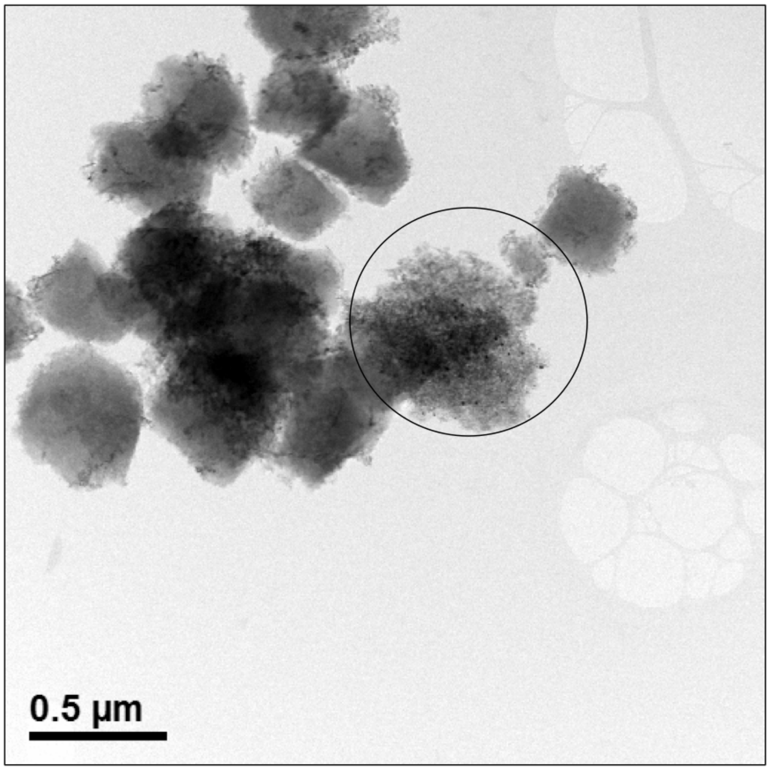

Figure 16. *A typical area of the powder is shown in a bright-field image from AMOx-600°C 2-h sample. The circled area shows a very fine-grained alumina flake.*

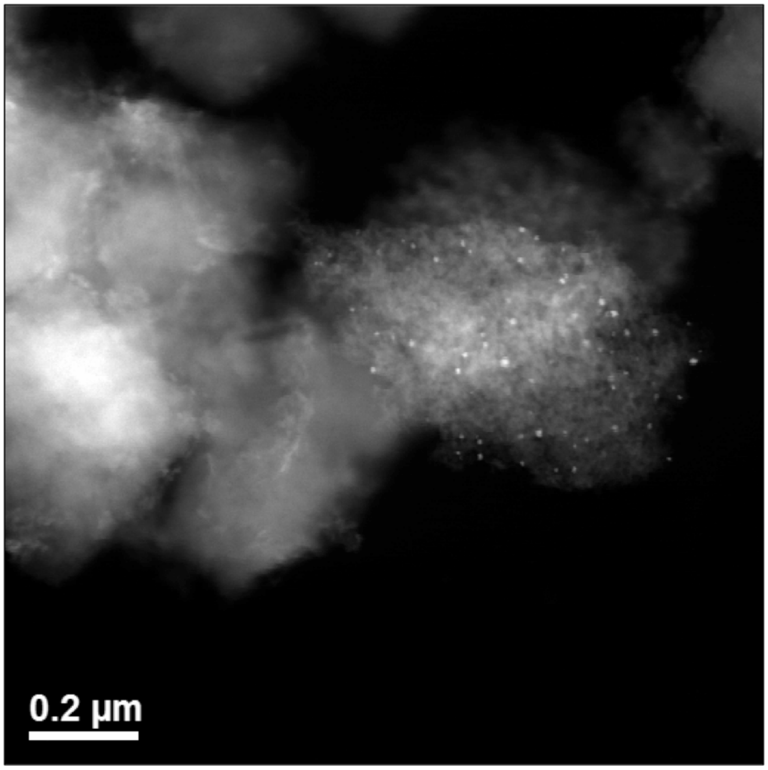

Figure 17. *Higher magnification image of Figure 16 showing the distribution of Pt particles in bright contrast.*

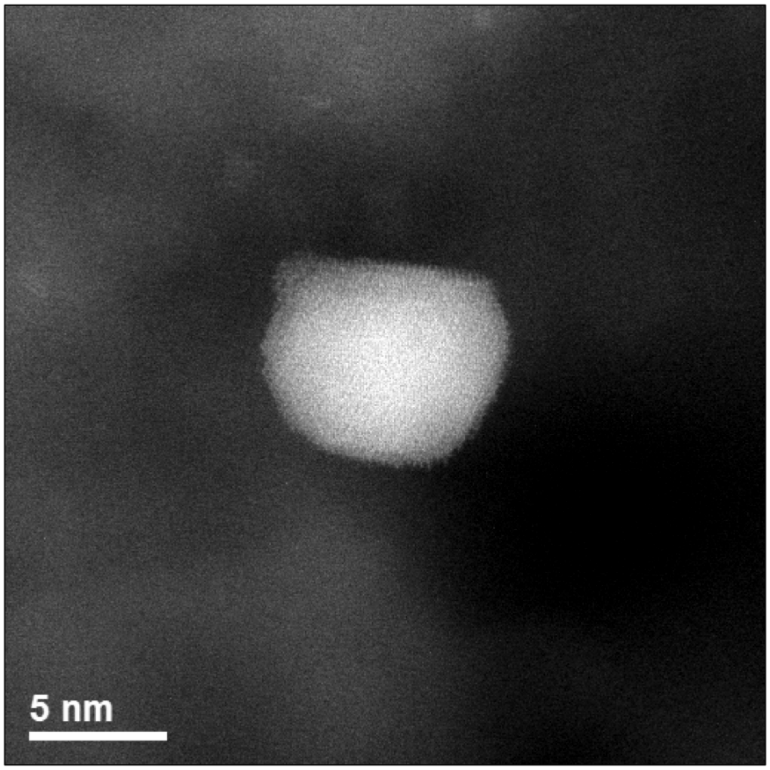

Figure 18. *A typical single-crystal Pt particle from the AMOx-600°C 2-h sample.*

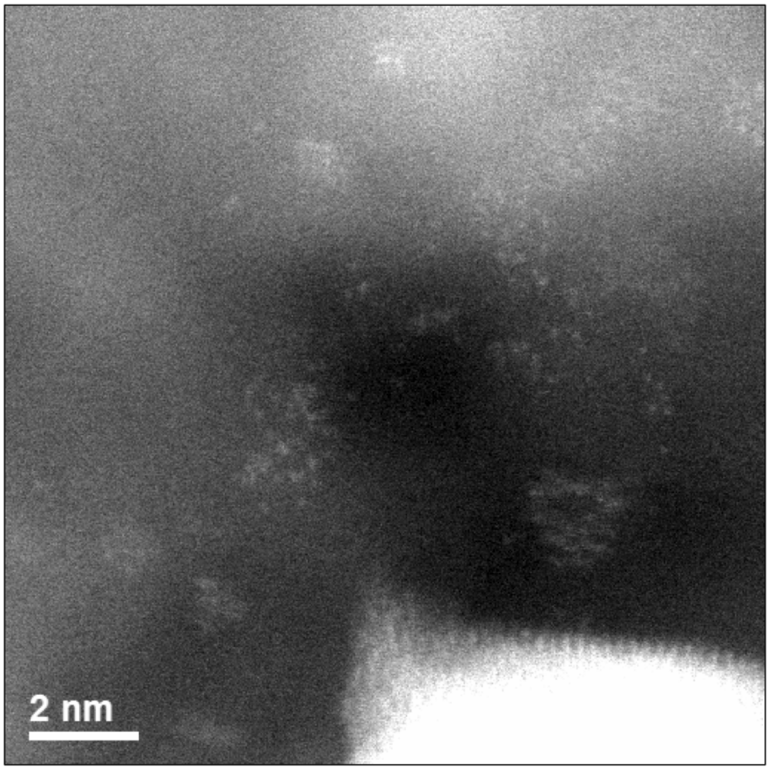

Figure 19. *A close up of the region above the Pt particle in Figure 18.*

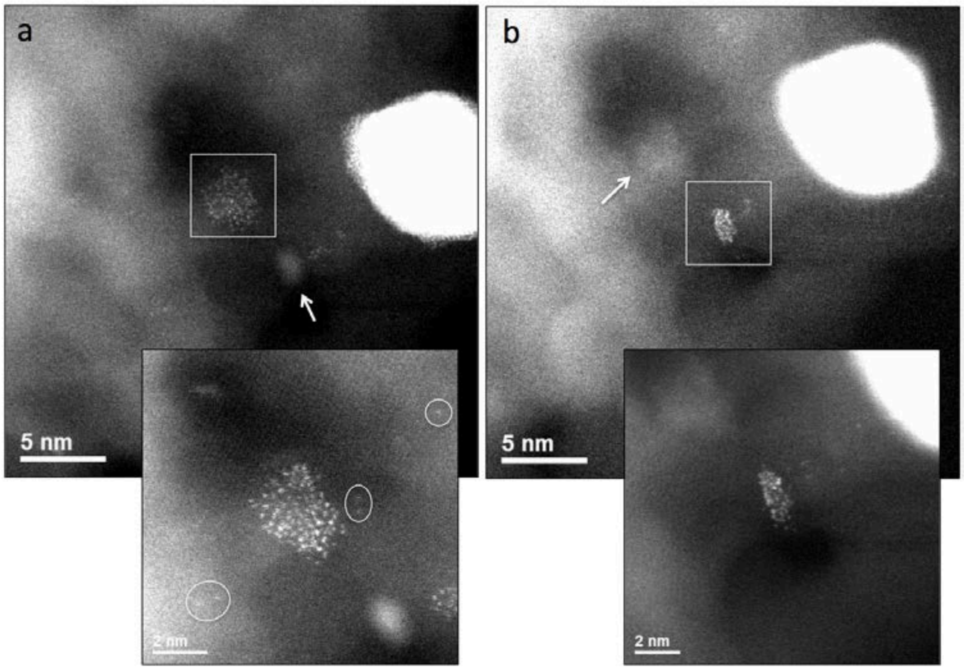

Figure 20. *a) A disordered raft of Pt atoms in sharp focus, especially in the inset of the figure, in which several individual or pairs of atoms are circled in addition to the cluster. b) The fuzzy area arrowed in 20a in sharp focus, especially in the inset of the figure. These are from the AMOx-600°C 2-h sample.*

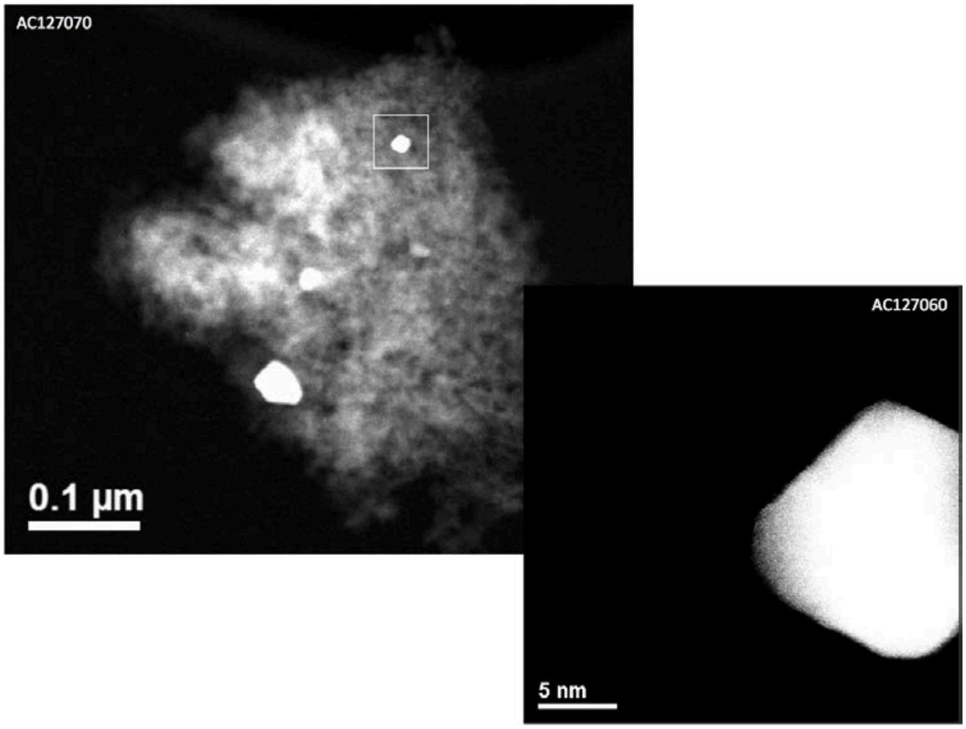

Figure 21. *Pt particles on an alumina flake and a close up of a facetted Pt particle from the AMOx-900°C 1-h sample.*

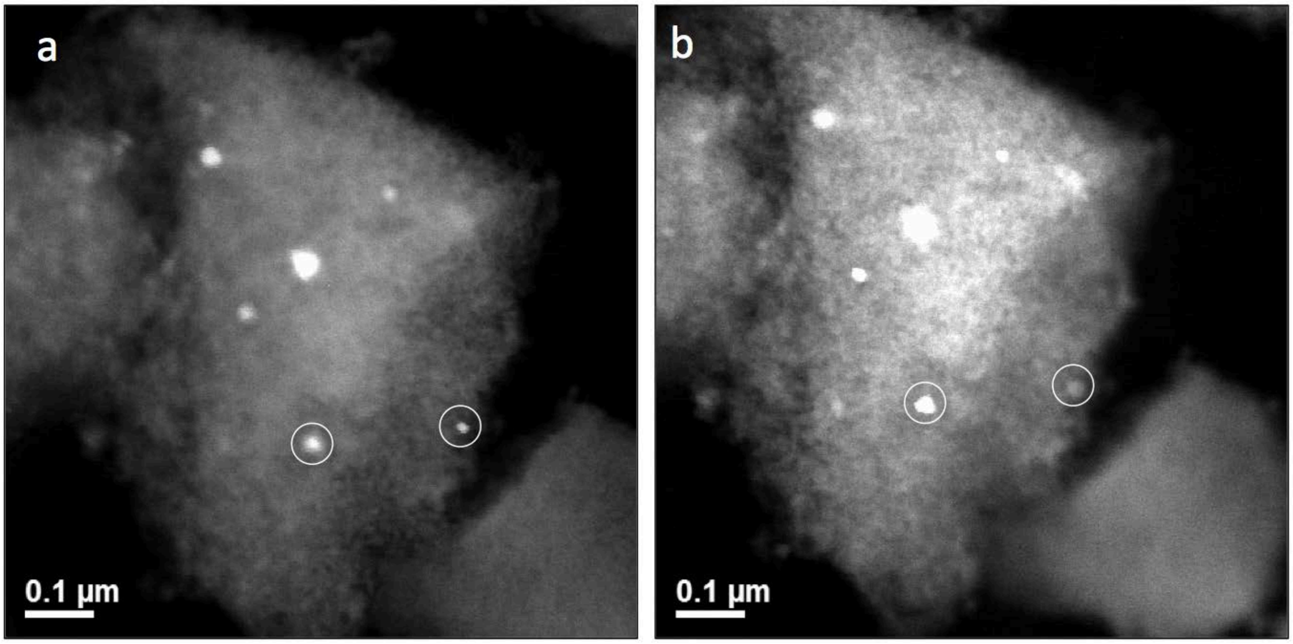

Figure 22. *A flake of alumina washcoat in the 900°C 1-h sample from the AMOx-900°C 2-h sample, where a and b are at different focus depths*

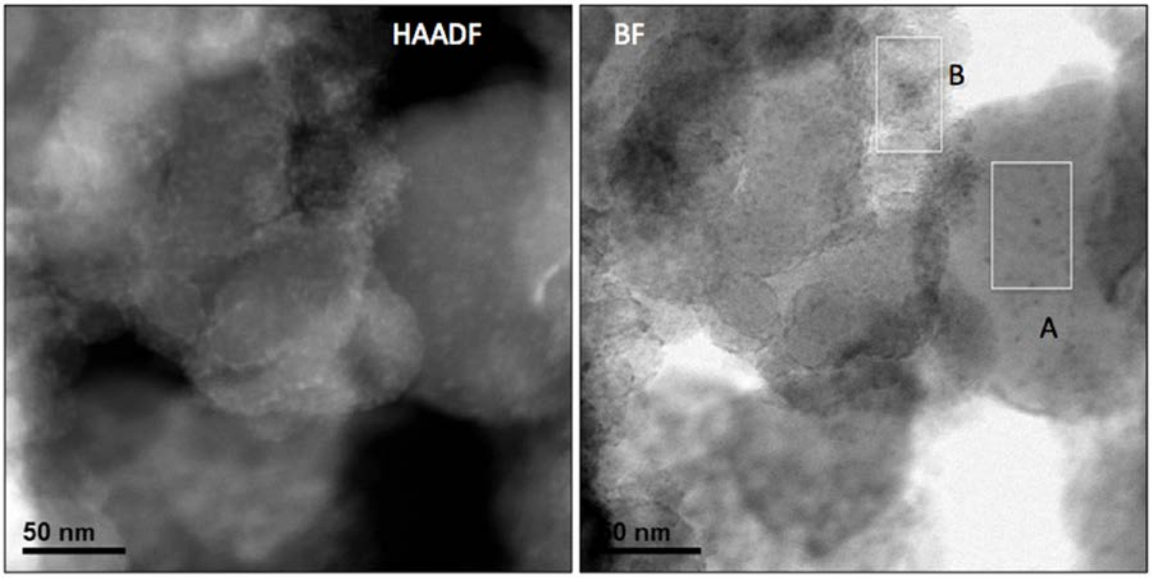

Figure 23. *HAADF-BF image pair showing general morphology of the Cu-F zeolite SCR catalyst. Smooth, equiaxed particles and a very fine-grained particulate aggregate are indicated in areas A and B, respectively. These areas were used to generate the spectra shown in Figure 25, acquired from the hypermap of this area shown in Figure 24.*

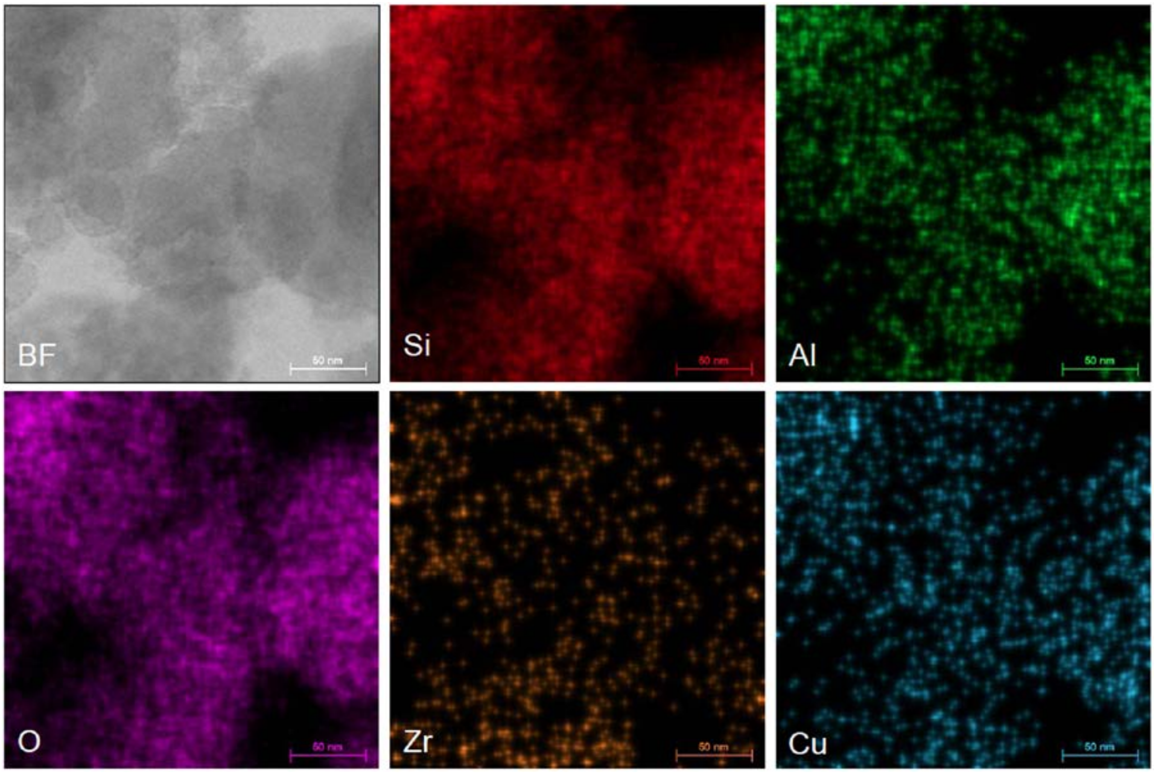

Figure 24. *Elemental maps from the area of the Cu-F catalyst shown in Figure 9. Spectra shown in Figure 25 were generated from analysis areas A and B, representing the two distinctive morphologies in this catalyst.*

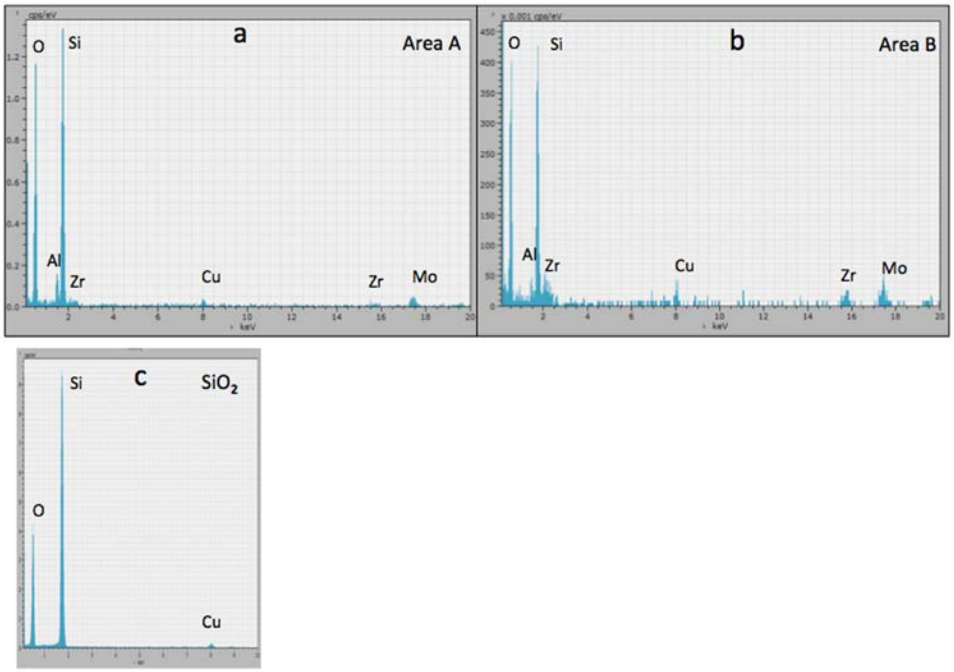

Figure 25. *a) and b) represent spectra generated from the inset areas A and B, respectively, in Figure 24. c) a spectrum from a particle of SiO_2, and shows the residual Cu peak that is due to excitation of microscope column components. Area B shows significant Zr relative to the smooth aluminosilicate particle of area A, and some Cu apparent also. Additional data on the distribution of Cu and Zr is shown in the next figures.*

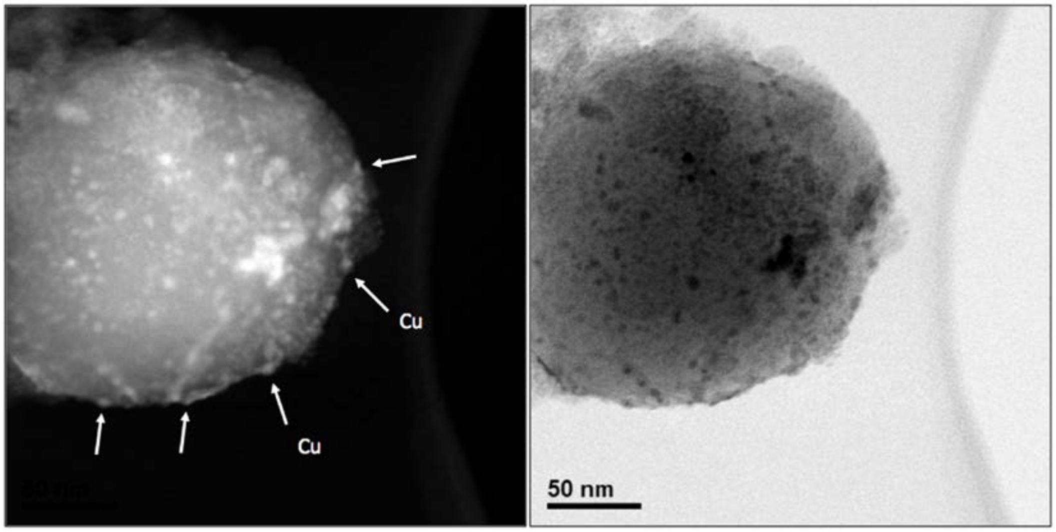

Figure 26. *HAADF-BF images of an isolated aluminosilicate particle, showing heavy metal species in bright contrast in the HAADF image. In the transmitted electron image, only species on the edge of the particle and seen in profile, such as at the arrows, can conclusively be determined to be on the surface of the particle. The elemental maps shown in Figure 27 allow identification of Cu on the surface in the spots labeled.*

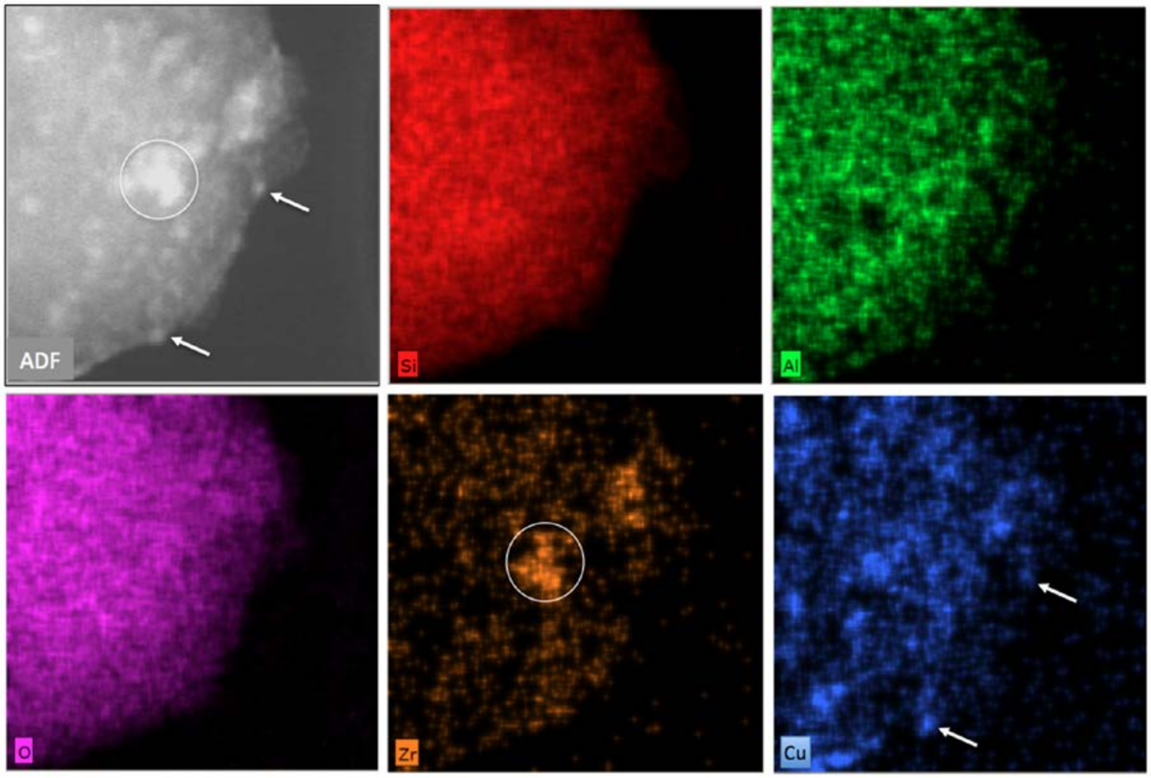

Figure 27. *Elemental maps from the particle of Figure 26. The non-homogeneous distribution of Zr and Cu on the surface is evident. Arrows locate at least two Cu-rich particles on the surface, and the circles show significant Zr present, likely also on the surface.*

Agreement 10461 - Durability of Diesel Particulate Filters (CRADA with Cummins Inc.)

Thomas R. Watkins, Amit Shyam, Amit Pandey and Hua-Tay Lin
Oak Ridge National Laboratory
P.O. Box 2008, MS-6064
Oak Ridge, TN 37831-6064
(865) 387-6472; fax: (865) 574-4913; e-mail: watkinstr@ornl.gov

Randall J. Stafford
Cummins Inc.
1900 McKinley Av., MC 50183
Columbus, IN 47201
(812) 377-3279; fax: (812) 377-7050; e-mail: randy.j.stafford@cummins.com

DOE Materials Engineer: Jerry Lee Gibbs
(202) 586-1182; fax: (202) 586-1600; e-mail: jerry.gibbs@ee.doe.gov
ORNL Technical Advisor: J. Allen Haynes
(865) 576-2894; fax: (865) 574-4913; e-mail: haynesa@ornl.gov

---

Contractor: Oak Ridge National Laboratory, Oak Ridge, Tennessee
Contract No.: DE-AC05-00OR22725

Objective

- To identify and implement test techniques to characterize the physical and mechanical properties of ceramic substrates used as diesel particulate filters (DPFs), to identify the mechanisms responsible for the degradation and failure of DPFs and to develop analysis tools for predicting their reliability and durability.

Approach

- Application of advanced characterization techniques to DPF ceramic substrates.
- Refinement of DPF service lifetime prediction models based on characterization of field returned filters.

Accomplishments

- Completed the determination of strength, fracture toughness, density/porosity/microstructure, and thermal expansion of coated DPFs as a function of time at elevated temperatures of 300, 500, 800 and 900°C for a second alternate substrate DPF material.
- Characterized the dynamic and static fatigue response of SiC DPFs
- Provided evidence of crack healing within thermal cycling in some DPF materials.

Future Direction

- Continue the study of microcracking in DPF materials with large CTE anisotropy.
- Determine the Young’s modulus of various DPF materials in tension.

Introduction

The EPA regulates the emissions of nitrogen oxides (NO_x) and particulate matter (PM) from diesels engines. Stringent regulation on PM went into effect in 2007. There are many technologies designed to reduce emissions from diesel engines; prominent among the technologies for PM control are diesel particulate filters (DPFs). A DPF is often a ceramic device that collects particulate matter in the exhaust stream. The high temperature nature of the ceramic withstands the heat of the exhaust and allows heating to break down (or oxidize) the particles inside. DPFs reduce emissions of PM, hydrocarbons, and CO by 60 to 90%.

Most DPFs consist of a ceramic honeycomb with hundreds of cell passages partitioned by walls (Figure 1). Each cell passage has a square cell opening at one end and is closed at the other end so that the cell passages are alternately closed at each end. The so-called checkerboard plugging structure forces the exhaust gases through the porous, thin ceramic honeycomb walls. When the gases carrying the PM flow through the fine pores of the walls, the PM is filtered out. High porosity values, in the range of 40-70%, heighten filtration efficiency to more than 90% and reduce gas-flow resistance for better engine performance.

The process of diesel PM collection continues while the engine is operating. The particles are collected on the ceramic walls and as a result, the backpressure of the system increases. The back pressure is reduced by oxidizing the trapped PM, aided by a catalytic reaction using exhaust gas heat at 400°C or more, into CO_2 and water vapor. This process, called regeneration, results in a cleaner filter. The regeneration process is dependent upon exhaust temperature, oxygen, NO_x content, time, and PM levels.

The *key* to the successful application of DPFs is to reliably regenerate the filter (e.g., to clean up the PM that the filter continues to trap or collect). Traditionally, combustion of soot is done in an oxygen atmosphere (air). In air, the soot will oxidize at ~500°C and up. However, this is not a typical operating temperature for diesel engine exhaust. Therefore, to oxidize soot in air, an active system—i.e., one that increases the temperature of the exhaust using some external heat source—is required. But if an active system is not carefully controlled, or if too much PM collects on the filter walls, the filters can experience an “uncontrolled regeneration” where the temperature increases to 600°C or more, resulting in damage to the filter element.

The objective of this project is to implement test techniques to characterize the physical and mechanical properties of different candidate substrate materials and to develop analysis and inspection tools for assessing the reliability and durability of DPFs. The developed tools, methods and properties would allow the design of more durable and reliable DPFs, particularly through the regeneration cycle.

Goals, Barriers, Relevance & Integration[1]

This work is in the study area of VT’s Materials Technology-Propulsion Materials Technology, and addresses the *goal* of: by 2015, develop materials that reduce the fuel economy penalty of particle filter regeneration by at least 25% relative to the 2008 baseline. This project addresses the three *barriers* within Propulsion Materials and four *barriers* within Advance Combustion Engine R&D-Combustion and Emission Control R&D: changing internal combustion engine combustion regimes, long lead times for materials commercialization, cost, lack of cost-effective emission control, lack of modeling capability for combustion and emission control, durability and cost (again), respectively. This project is *relevant* to the goal and barriers as the thrust is to characterize the material properties and improve the durability and lifetime prediction, resulting in the lowest overall cost while preventing emission release in service. This is achieved by understanding of the relationships of the material properties for the filter (and catalyst) substrates enables optimization of porosity, strength, elastic modulus, thermal conductivity, thermal expansion, etc. leading to thermal management and improved efficiency. This project supports clean diesel, which increases acceptance by the public. Larger acceptance, in turn, results in larger percentages of conversion to diesel, with the resulting reduction in petroleum usage/dependency upon foreign oil. This project is *integrated* within Vehicle Technologies program as DPF substrate material are used in both DPF and catalyst systems and as it utilizes characterization tools acquired and maintained by the High Temperature Materials Laboratory (HTML) Program.

Approach

The design process for making DPFs that are durable and reliable includes a complex materials property optimization and selection process.[2] For example, the porosity of DPFs, which allows the removal of PM from the exhaust gas stream, has a deleterious effect on their mechanical and fracture strength. A higher porosity, though, decreases the engine backpressure and increases efficiency of the diesel engine. Designing mechanically reliable DPFs is important because these components will experience demanding thermo-mechanical conditions during service. These include, for example, thermal shock resulting from rapid heating/cooling and thermal stresses that arise from temperature gradients.

Techniques to assess the elastic and fracture properties of virgin or unexposed DPF substrates have been identified, implemented and reported earlier.[3] The test techniques were applied to rank the suitability of common candidate substrates for application in DPFs. The developed test techniques were applied to characterize field returned DPFs. The material properties responsible for the thermal shock resistance and mechanical property degradation in the various stages of the bathtub curve were determined. These properties include thermal expansion, thermal conductivity, heat capacity, density, porosity, elastic properties, strength, fracture toughness, and environmentally assisted crack growth at ambient and elevated temperatures, in air and in relevant environments.

The information generated has in turn been input into predictive models. Such service life predictions are based on a combination of experimentally determined strength data, stress analyses of the component using a finite-element analysis, and selection of appropriate failure criteria. The durability (service life) of the component can also be predicted using this framework by considering the mechanisms that are responsible for the degradation of material strength, such as slow crack growth or creep.

Results-SiC

A new SiC-based DPF material continued to be characterized. The DPF honeycomb monoliths were sectioned, and samples were machined as before.[5] A quantitative XRD analysis was performed using the Reitveld method[4] on an X-ray diffraction pattern of powder from a crushed piece of the SiC-based material (see Figure 2). Since ~20 v% of the solid (excluding porosity) is silicon (8.3 v% Si if porosity is included), this material can be considered a siliconized silicon carbide (Si/SiC) or a reaction-bonded silicon carbide (RBSC).

Some of the measured properties of this SiC-based material are listed and compared to literature references in Table I. The skeletal densities are all within 13% of the dense literature reference values, indicating that there is at most 13 % closed porosity. The skeletal density of the SiC based material will obviously vary with free Si content and is comparable to values for reaction-bonded silicon carbide (RBSC). I Table II, the Young's moduli are quite low relative to the values for dense materials, which is directly related to the high porosity. There is some variability (factors 2-4X) of Young's moduli values amongst the available measurement techniques: load deflection, resonant ultrasound spectroscopy (RUS), pulse echo and dynamic mechanical analysis (DMA, reported here). Understanding this variability is the subject of an on-going study.

Double torsion fracture toughness testing was performed at RT, 300, 500, 800 and 900 °C as described elsewhere.[5] The double torsion plate samples were sectioned from larger monoliths (see Figure 3) and were 40 x 20 mm (L x W) in size. The sample thicknesses were governed by the starting wall thickness of the honeycomb monoliths; after machining, typical double torsion sample thicknesses was ~0.28 mm for the SiC-based materials. Figure 3 shows the experimental set-up of the double torsion testing. The sample is carefully mounted in the double torsion jig; the jig with sample is then gingerly lowered into position within the furnace. The tube and much of the insulation is in place prior to the required precracking. A successfully fractured test specimen is defined as one where the crack propagates to the opposite/far end of the sample and is displayed in Figure 3. The fracture surfaces of successfully tested double torsion samples were examined using the SEM (see Figure 5). In examining these micrographs, it is often difficult to discern pre-fracture/pre-existing surfaces from post-failure fracture-related surface features. During sample machining, the samples were held with a vacuum chuck for dry grinding which likely pulls in grinding debris. As such, a lack of debris highlights fracture sites on internal ligaments/struts. The fracture features of all the samples do not look appreciably different with temperature; the Si/SiC is fracturing transgranularly without any ligamentation. Unlike the double torsion fracture surfaces of the cordierite and AT-based materials, which possessed numerous microcracks, the SiC-based material had only an occasional microcrack. These are thought to originate from the fracture process itself. Oxidation/glass formation is evident at the highest temperatures.

Figure 6A shows typical the fracture behavior in the double torsion experiments. The double torsion method was selected to measure apparent fracture toughness as crack length not needed for determination.[12] This is important given the large amount of engineered porosity and honeycomb structure as well as microcracks in the DPF materials. Here, the maximum load was used to calculate K_{IC}. The non-zero start-finish of K_I is due to weight of the double torsion jig top, which pre-loads the sample, and is included in the K_{IC} calculation. The slopes in Figure 6A suggest that the moduli are the same or slightly lower at elevated temperature. In Figure 6B, the average fracture toughnesses, K_{IC}, are shown to increase with testing temperature. It can be seen that there is a significant difference between the RT value and the 800 or 900°C values. In contrast, the increase in temperature had a negligible effect on the fracture toughness of cordierite and AT-based DPF materials. It is speculated that the mechanism for this increase in toughness is due to increased ductility of the free Si nodules.

In the RBSC and Si/SiC literature, reports of strength and toughness increasing with temperature are common for dense materials with volume fractions of free silicon ranging from 8 to 49 v% tested at temperatures greater than 1000°C. For example, Huang and Zhu[9] observed increases in strength and fracture toughness of RBSC starting at 1000°C and continuing to 1330°C. They observed that the material was transitioning from transgranular to intergranular failure and speculated that this was due to a change in the bond strength between the Si and SiC grains. Various toughening mechanisms have been attributed to the observed strength and toughness increases with temperature, but all ultimately originate in the plastic/softening behavior of free Si. These mechanisms include crack tip blunting or healing,[13,14] stress redistribution due to grain cluster movement,[13-18] grain boundary softening or sliding,[9,15-17,19,20] creep cavitation (hard to see in highly porous DPF materials),[13-17] oxidation and/or possibly glass formation to close or fill in cracks/flaws.[9,21] These behaviors are dependent upon volume fraction of Si, temperature, time at temperature and stress level.[13,14,22]

In a simple experiment, half of a double torsion specimen was dead loaded, heated up to 900°C for 24 hours then furnace cooled. Upon removal from the furnace the sample was permanently bent, confirming some sort of creep or deformation had occurred. Subsequent SEM work did not find any definitive surface features (e.g. ligamentaion nor stretched Si nodules) suggesting a toughening mechanism. Likewise, XRD pattern did not display any evidence of a glassy phase. In the absence of significant amounts of a glassy phase and the fact that SiC is a refractory material, it would appear that the permanent deformation, and perhaps the toughness increase, is related to the free silicon.

Dynamic fatigue testing was also conducted on the SiC-based DPF material. In static fatigue, samples are simply loaded with a constant stress (e.g., dead weight) and monitored for time to failure (see Figure 7). Dynamic fatigue provides an accelerated means, relative to static fatigue, to evaluate the mechanical reliability of ceramics[23-25] and is shown schematically in Figure 7. Fast fracture is considered to be inert as there is not enough time for strength degradation mechanisms to occur. As the loading/stressing rate slows, environmental factors, such as stress assisted corrosion cracking, can occur resulting in slow crack growth (SCG). As such, dynamic fatigue is used to evaluate time and environmentally dependent mechanisms, such as SCG, strength degradation, creep effects, oxidation effects as well as checking repeatability. Figure 8 schematically shows a dynamic fatigue curve plotting the natural log of the failure strength as a function of the stressing rate. The slope of this line is equivalent to 1/(N+1). When N is large, the material does not exhibit susceptibility to SCG. As N decreases, the SCG susceptibility of the material increases. N can be used to estimate the static fatigue lifetime, t_{est_df}, as follows:

$$t_{df} = \frac{\sigma_f}{\dot{\sigma}} \; .$$

Substituting N and t_{df} into:

$$t_{est\_sf} = \frac{t_{df}}{(N+1)} \; .$$

Figure 9 compares the dynamic fatigue responses of SiC DPF samples with 4x3 and 6x3 cell size. The result shows that there is no size effect on the measured strength for the types of samples used in this study. The dynamic fatigue results at elevated temperatures also showed that the flexural strength of SiC DPF materials was insensitive to the cell size as well. Mechanical results at 600°C for both sizes of SiC DPF samples showed that there was no stressing-rate dependence of flexural strength (from 3 MPa/s to 3 x 10^{-6} MPa/s). However, there was a minor increase in flexural strength with decreasing stressing rate (from 3 MPa/s to 3 x 10^{-4} MPa/s) for temperature at 800 and 900°C, while there was little change in measured fracture strength from 3 x 10^{-4} MPa/s to 3 x 10^{-6} MPa/s. This is atypical. Normally, the strength either remains constant (no environmental effect) or decreases with slower stressing rates due to the extra time allowing environmentally assisted mechanism to occur. Further when tested at 0.003 MPa/s, the strength data at 800 and 900°C are consistently stronger than the 600°C data suggesting some sort of thermally activated strengthening mechanism. Several studies in the literature show the fracture strength of Si/SiC increasing with testing temperature up to ~1200°C [9,13,14,18-21] and have attributed this to varied strengthening mechanisms as discussed above. An SEM study was carried out to provide insight into the effect of test temperature and stressing rate on flexural strength at higher temperatures. In Figure 10, an apparent increase was observed in the thickness and extent of the oxide (SiO_2) scale due to increased oxidation of SiC at higher temperature (e.g., 600 vs. 900°C). The increased oxidation reaction may promote the sealing or blunting of defects such as pores and cracks present in SiC DPF; thus resulting an increase in fracture strength. Also, some plastic behavior of the free Si metal may also contribute. In FY2013, more SiC DPF bend bars would be tested at these three loading rates and test temperatures in order to obtain better statistic results.

Results-Microcracking

In addition to the ~50% porosity in DPF materials, microcracking also plays an important role in their mechanical behavior. The unusual thermal expansion and high temperature elastic behavior of porous cordierite have been attributed to microcrack healing and re-initiation as a result of heating and cooling.[26] While this is an accepted mechanism, few researchers have provided evidence for crack healing at elevated temperatures in low thermal expansion ceramics. Here, the mechanical behavior of cordierite, aluminum titanate (AT)-based material and a β-eucryptite based material was investigated with respect to crack healing. This was accomplished by an iterative method, wherein, images of specific microstructural regions of a sample were recorded repeatedly after subsequent thermal treatments. After the initial SEM observation of a region, the specimen was heated at to 1100^{o}C, held for 24 hours and then subsequently cooled to room temperature. The sample was replaced in the SEM. The same areas were relocated and imaged before and after the thermal cycle with the aid of fiducial features on the surface of the specimen. The observation of crack healing was performed, *ex-situ*. The changes in microcrack populations were recorded using backscattered SEM images in six regions of the specimen before and after heat treatment and again after a second identical thermal treatment.

Explicit evidence of change in crack population as a result of heating the DPF specimens to 1100^{o}C is provided in Figures 11-13. The images on the left indicate the as-processed surface, and the corresponding image on the right is the same surface after the heat treatment. Images of the same area were taken after a second thermal cycle but are not shown. The grain-size range for the porous cordierite, AT-based and β-eucryptite based materials were measured to be 1.5-3, 5-10, and 1.5 - 7 μm by optical microscopy, respectively.

Figure 11 demonstrates that a microcrack in cordierite specimen present on the as-processed specimen surface has completely healed, and a new one has formed nearby with a small change in its orientation as a result of the thermal cycle. Similarly, Figure 12 shows a set of microcracks in the β-eucryptite based material where the larger cracks appear more open and the smaller cracks seem to close. In the center region of Figures 11A and B, an exhibition of crack healing and formation due to the thermal cycle is displayed. Likewise in Figure 13, a microcrack present in the as-processed aluminum titanate based material is completely healed in the upper left of the image. Taken together, the results in Figure 11-13 provide compelling evidence of microcracks healing, evidence of change in microcrack population since new populations of microcracks have emerged as a result of elevated temperature exposure and subsequent cooling. Furthermore, it was observed that the second thermal cycle had a smaller effect on the microcrack distribution of cordierite materials as compared to the first cycle. These results are in consistent with the Young's modulus dependence on thermal cycling where the largest decrease in Young's modulus is observed after the first thermal cycle.[26]

Summary

Mechanical and thermal shock characterization test procedures developed earlier were employed to measure properties in SiC DPF materials, the focus here. The fracture toughness of the SiC DPF was measured using the double torsion technique and found to increase from room temperature to 900°C. The fracture strength was measured as a function of stressing rate, sample size and temperature; the strength was observed to increase with temperature. The mechanism for this is thought related to the softening of the free silicon and/or glassy phase. The importance of reliable input data was demonstrated with predictive simulations of the number of regeneration cycles to component failure.

The role of microstructure is discussed with the thermal and elevated temperature mechanical properties of porous cordierite. Temperature cycling to 1000°C led to explicit evidence of microcrack healing and reopening for the porous cordierite, AT-based and β-eucryptite based materials.

References

1. Multi-Year Program Plan 2011-2015, Vehicle Technologies Program, EERE, DOE, December 2010, pp. 2.3-4; 2.5-7, 8. (http://www1.eere.energy.gov/vehiclesandfuels/resources/fcvt_plans_roadmaps.html).
2. J. Adler, "Ceramic Diesel Particulate Filters," International Journal of Applied Ceramic Technology, **2** [6] 429-39, 2005.
3. Propulsion Materials Annual Progress Reports, Vehicle Technologies Program, US DOE, Energy Efficiency and Renewable Energy, Office of Vehicle Technologies, www.ornl.gov/sci/propulsionmaterials/Reports.html.
4. R.A. Young, editor. The Rietveld Method, International Union of Crystallography, Oxford University Press, New York (1995).
5. A. Shyam, E. Lara-Curzio, T. R. Watkins and R. J. Parten, "Mechanical Characterization of Diesel Particulate Filter Substrates," *J. Am. Ceram. Soc.*, **91** [6] 1995–2001 (2008).
6. ASTM D3766, Standard Terminology Relating to Catalysts and Catalysis, ASTM International, West Conshohocken, PA 2008.
7. CRC Handbook of Chemistry and Physics, Edited by R. C. Weast, CRC Press, Inc., Boca Raton, FL 33431, p. B-121 (1980).
8. S. Aroati, M. Cafri, H. Dilman, M.P. Dariel, N. Frage, "Preparation of reaction bonded silicon carbide (RBSC) using boron carbide as an alternative source of carbon," J. Euro. Ceram. Soc. 31 841–845 (2011).
9. Q-W. Huang and L-H. Zhu, "High-temperature strength and toughness behaviors for reaction-bonded SiC ceramics below 1400 °C," Mat. Let. **59** 1732–5 (2005).
10. T. R. Watkins, D. J. Green, and E. Ryba, "Determination of Young's Modulus in Chemically-Vapor-Deposited SiC Coatings," *J. Am. Ceram. Soc.*. **76** [8] 1965-68 (1993).
11. P. G. Karandikar, G. Evans, S. Wong S, M. K. Aghajanian, M. Sennett, "A Review of Ceramics for Armor Applications," pp. 163-175 in Advances in Ceramic Armor IV, Ceramic Engineering and Science Proceedings, V. 29 [6]. Edited by L.P. Franks, T. Ohji, A. Wereszczak, Wiley, Hoboken, NJ 2009.
12. A. Shyam and E. Lara-Curzio, "The Double-Torsion Testing Technique for Determination of Fracture Toughness and Slow Crack Growth Behavior of Materials: A Review," J. Mater. Sci **41** 4093–4104 (2006).
13. D. F. Carroll and R. E. Tressler, "Time-Dependent Strength of Siliconized Silicon Carbide under Stress at 1000° and 1100°C," *J. Am. Ceram. Soc.*, **68** [3] 143-146 (1985).
14. T. Darroudi, R. E. Tressler and M. R. Kasprzyk, "Low-Cost Melt-Formed Siliconized Silicon Carbide Radiant Tube

Materials," *J. Am. Ceram. Soc.*, **76** [1] 173–79 (1993).

15. S. M. Wiederhorn, D. E. Roberts, T-J. Chuang and L. Chuck, " Damage-Enhanced Creep in a Siliconized Silicon Carbide: Phenomenology," *J. Am. Ceram. Soc.*, **71** [7] 602-608 (1988).
16. B. J. Hockey and S. M. Wiederhorn, "Effect of Microstructure on the Creep of Siliconized Silicon Carbide," *J. Am. Ceram. Soc.*, **75** [7] 1822-30 (1992).
17. B. A. Fields and S. M. Wiederhorn, "Creep Cavitation of a Siliconized Silicon Carbide Tested in Tension and Flexure," *J. Am. Ceram. Soc.*, **79** [4] 977-86 (1996).
18. K. Breder, "Time-Dependent Strength Degradation of a Siliconized Silicon Carbide Determined by Dynamic Fatigue," *J. Am. Ceram. Soc.*, **78** [10] 2680-84 (1995).
19. D. C. Larsen and J. W. Adams, "Property Screening and Evaluation of Ceramic Turbine Engine Materials," Technical Report AFWAL-TR-83-4141, Materials Laboratory, Wright-Patterson AFB, Ohio, (1983).
20. D. C. Larsen, "Property Screening and Evaluation of Ceramic Turbine Engine Materials," Technical Report AFML-TR-79-4188, Air Force Materials Laboratory, Wright-Patterson AFB, Ohio (1979).
21. W. J. Tomlinson, S. Khela, C. A. Jasper and S. J. Matthews, "Flexural Strength of Lapped and Oxidized Siliconized Silicon Carbide," *J. Mat. Sci.*, **27** 3372-78 (1992).
22. O. P. Chakrabarti and P. K. Das, "High Temperature Load-Deflection Behaviour of Reaction Bonded SiC (RBSC)," *Ceram. Int.*, **27** 559-63 (2001).
23. ASTM Standard C 1368 entitled "Standard Test Method of Determination of Slow Crack Growth Parameters of Advanced Ceramics by Constant Stress-Rate Flexural Testing at Ambient Temperature," ASTM International, 2006.
24. A. A. Wereszczak, H. -T. Lin, T. P. Kirkland, M. J. Andrews, and S. K. Lee "Strength and Dynamic Fatigue of Silicon Nitride at Intermediate Temperatures," *J. Mater. Sci.* **37** 2669-2684 (2002).
25. H. T. Lin, M. K. Ferber, T. P. Kirkland, and S. M. Zemskova, "Dynamic Fatigue of CVD-Mullite Coated SN88 Silicon Nitride," ASME GT2003-38919, published in the Proceedings of at 2003 ASME TURBO EXPO: Power for Land, Sea & Air 2002, June 16-19, Atlanta, GA.
26. A. Shyam, E. Lara-Curzio, A. Pandey, T. R. Watkins, K. L. More, "The Thermal Expansion, Elastic and Fracture Properties of Porous Cordierite at Elevated Temperatures," *J. Am. Ceram. Soc.*, **95** [5] 1682–1691 (2012).

Presentations:

Invited Presentation: T.R. Watkins, K.J. Wright, A. Shyam, H.T. Lin, M.K. Ferber, R. Stafford, "Fracture Toughness and Dynamic Fatigue of Porous SiC at Elevated Temperature," presented at the 36th International Conference on Advanced Ceramics and Composites Meeting held in Daytona Beach, FL, January 24, 2012.

RELATED Presentation**: R. J. Stafford, K. Golovin, A. Dickinson, T. R. Watkins, A. Shyam, "Elastic Modulus of Porous Cordierite by the Flexure Test Method Compared to Sonic/Resonance Test Methods," presented at the 36th International Conference on Advanced Ceramics and Composites Meeting held in Daytona Beach, FL, January 24, 2011. **(Work funded by the HTML User Program).

T. R. Watkins, A. Shyam, H.T. Lin, E. Lara-Curzio, A. Pandey, R. Stafford, "Durability of Diesel Engine Particulate Filters," presented at the DOE 2012 Vehicle Technologies Annual Merit Review and Peer Evaluation Meeting, Washington, D.C., May 15, 2012.

Publications:

A. Shyam, E. Lara-Curzio, A. Pandey, T. R. Watkins, K. L. More, "The Thermal Expansion, Elastic and Fracture Properties of Porous Cordierite at Elevated Temperatures," J. Am. Ceram. Soc., 95 [5] 1682–1691 (2012).

Table I – Young’s modulus and various measures of density of the SiC DPF material studied. Density definitions are given in ASTM D3766.[6]

Property/Material	SiC
Literature density (g/cc)	3.217 [§,7], 2.85-3.10 [§§,8], 3.11 [§§§,9], 2.98 [§§§§,9]
Bulk (g/cc)*	1.18(0.03) **
Skeletal (g/cc)[¥]	2.83(0.05)
Relative ρ (%)[Ø]	41.7
Porosity (%)	58.3
Literature polycrystalline Young’s Modulus for dense material (GPa)	420 [∞,10], 320-340 [∞∞,8], 359-407 [11]
Young’s Modulus (GPa)***	20(2.5)

* Geometric volume: includes solids plus all open and closed porosity of plate samples, i.e., no channels

** () values = standard deviation

[¥] He pycnometry: volume includes solids plus all closed porosity

[Ø] Relative density (ρ_{bulk}/ ρ_{skel} *100)

[§] 0 v% free Si;[§§] 15-35 v% free Si; [§§§] 12 v% free Si; [§§§§] 26 v% free Si in RBSC

*** Dynamic Mechanical Analysis (DMA); MOI corrected; 2-5 samples, Each remounted >5 X

[∞] CVD β-SiC, no free Si, [∞∞] 15-35 v% free Si

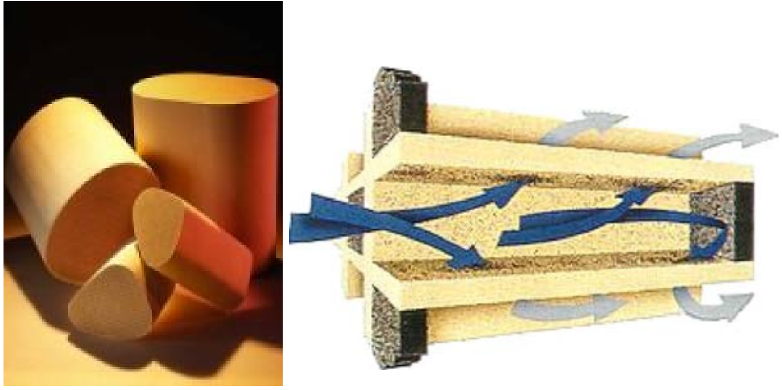

Figure 1. Cordierite-based DPFs.

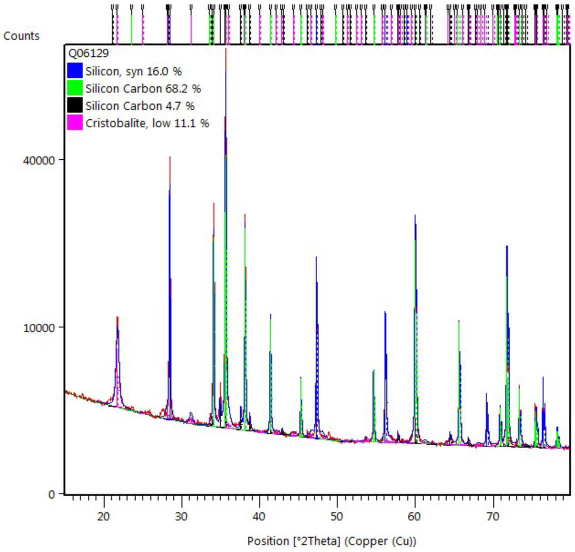

Figure 2. The X-ray diffraction pattern the SiC-based DPF material. Quantitative X-ray diffraction revealed that there is about 16 wt % Si, 73 wt % SiC and 11 wt % Cristobalite (SiO_2) in the solid, excluding porosity.

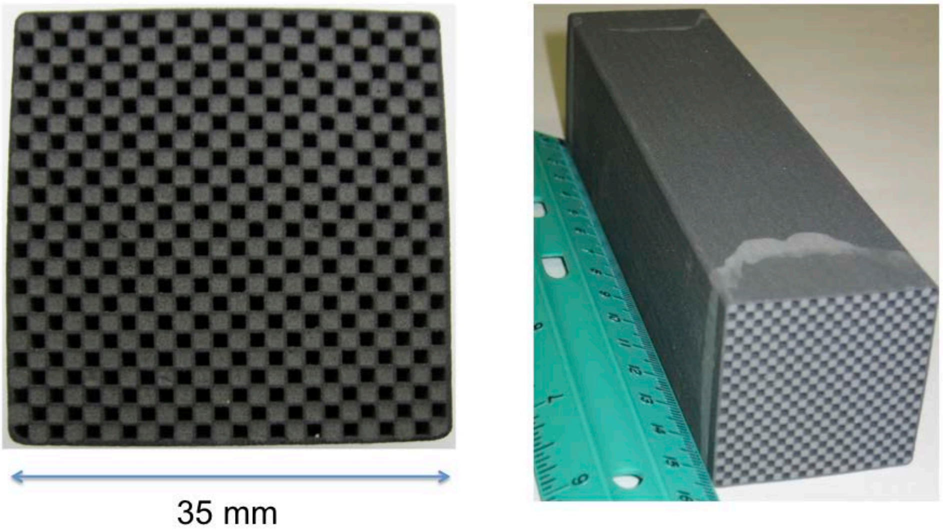

Figure 3. The SiC-based DPF material comes in segments (35 X 35 x 153 mm) that may be joined together to form a larger DPF. The cell size is roughly 1.1 square with nominal wall thickness of 400 microns.

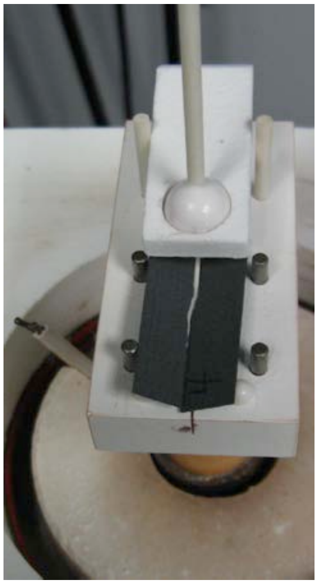

Figure 4. A "successfully" fractured double torsion SiC-based sample and jig without furnace. A thermocouple is seen to the left and the Al_2O_3 push rod comes down from the top. Successful means that the crack propagates from the precracked notch tip to the far side of the sample as shown.

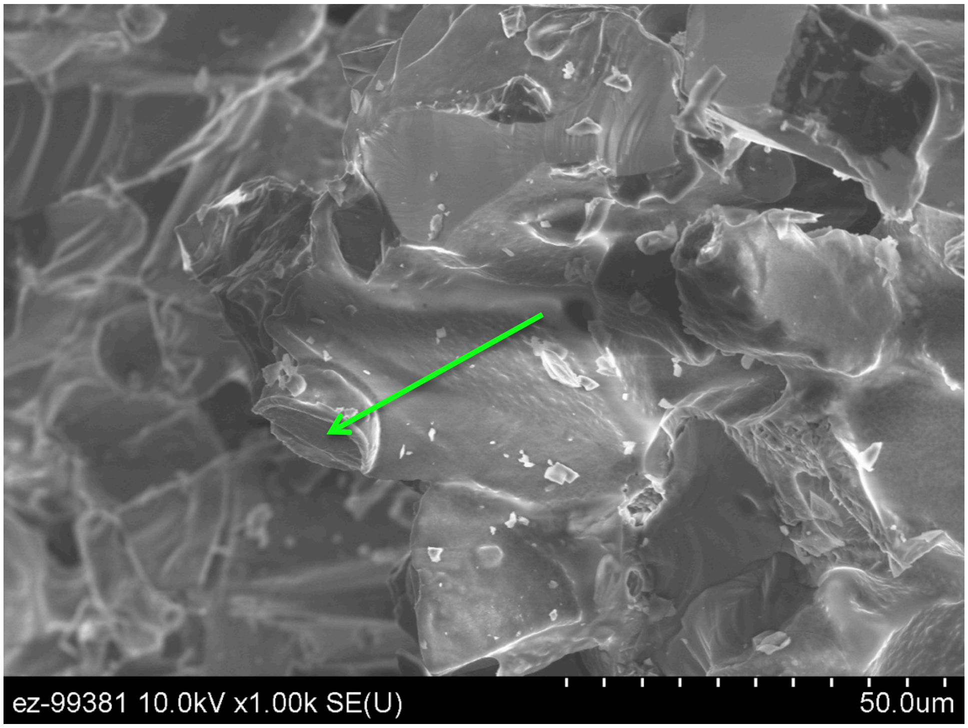

Figure 5. SEM micrograph of a double torsion fracture surface of a SiC-based DPF material tested at room temperature. The green arrows indicate Si-rich nodules (per EDS).

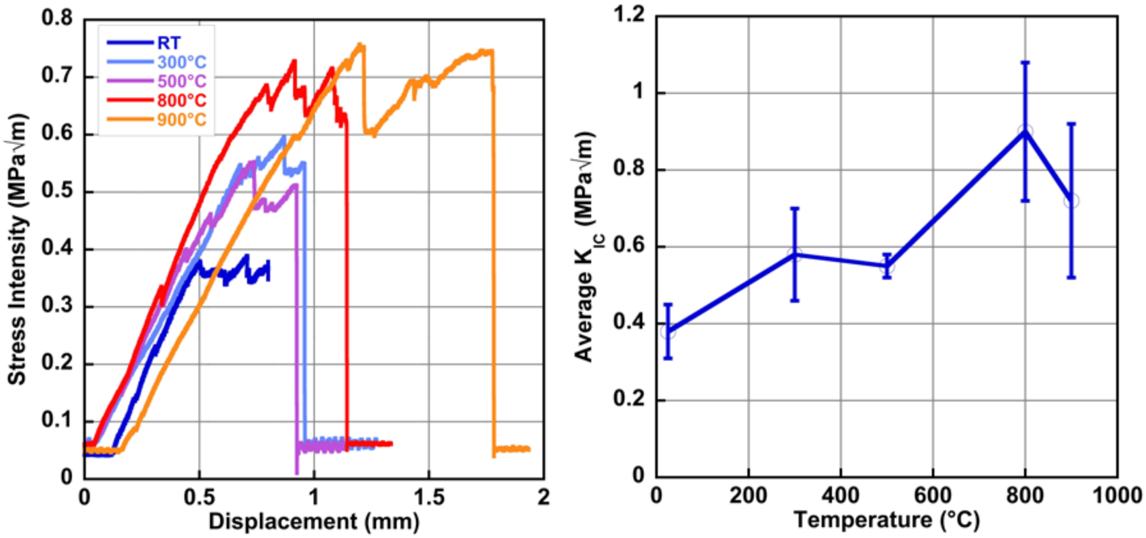

A. B.

Figure 6. A.) Typical stress intensity as a function of displacement for double torsion samples of silicon carbide based DPF materials, B.) The average fracture toughness as a function of temperature for the silicon carbide based DPF materials. The standard deviation of the K_{IC} measurements is plotted with the error bars.

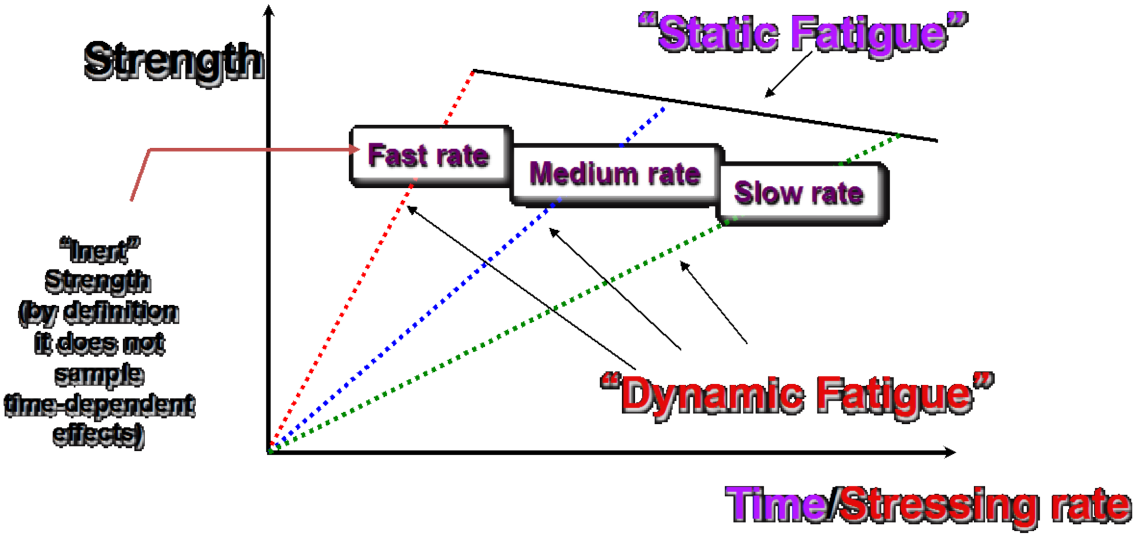

Figure 7. A schematic comparing dynamic and static fatigue. Purple lettering refers to static fatigue and red dynamic.

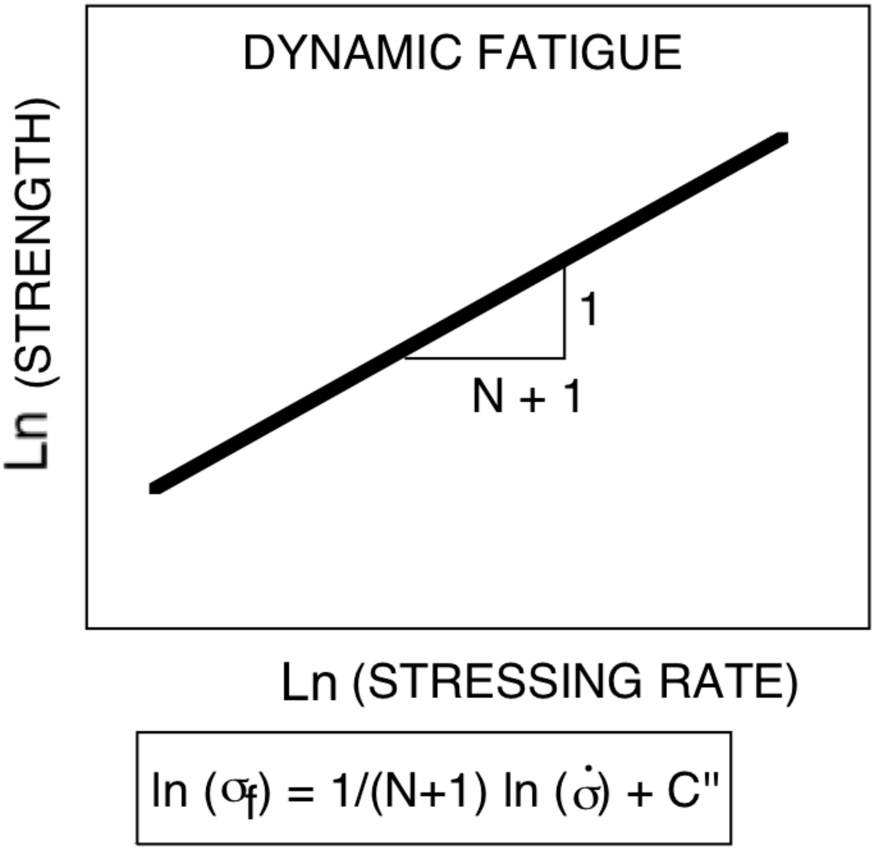

Figure 8. A schematic of a dynamic fatigue curve, where σ_f, $\dot{\sigma}$, N and C" are the failure strength, stressing rate and environmentally dependent constants, respectively.

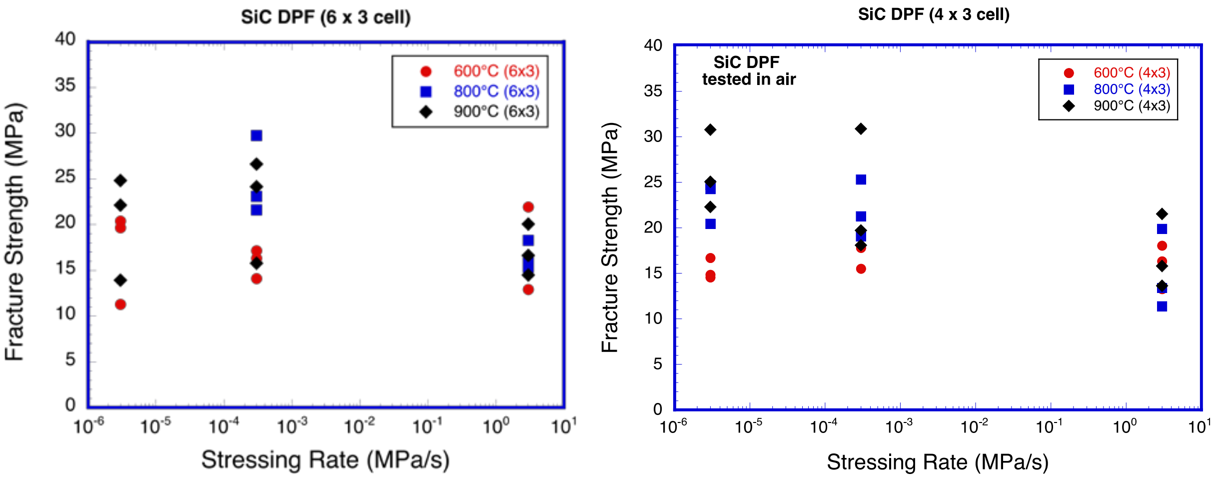

Figure 9. The flexural strength of SiC DPF materials as a function of stressing rate (time), temperature and cross-sectional size. Note that the room temperature fracture strengths of 4x3 and 6x3 cell size sample are 13.9±3.3 and 13.5±2.6 MPa, respectively.

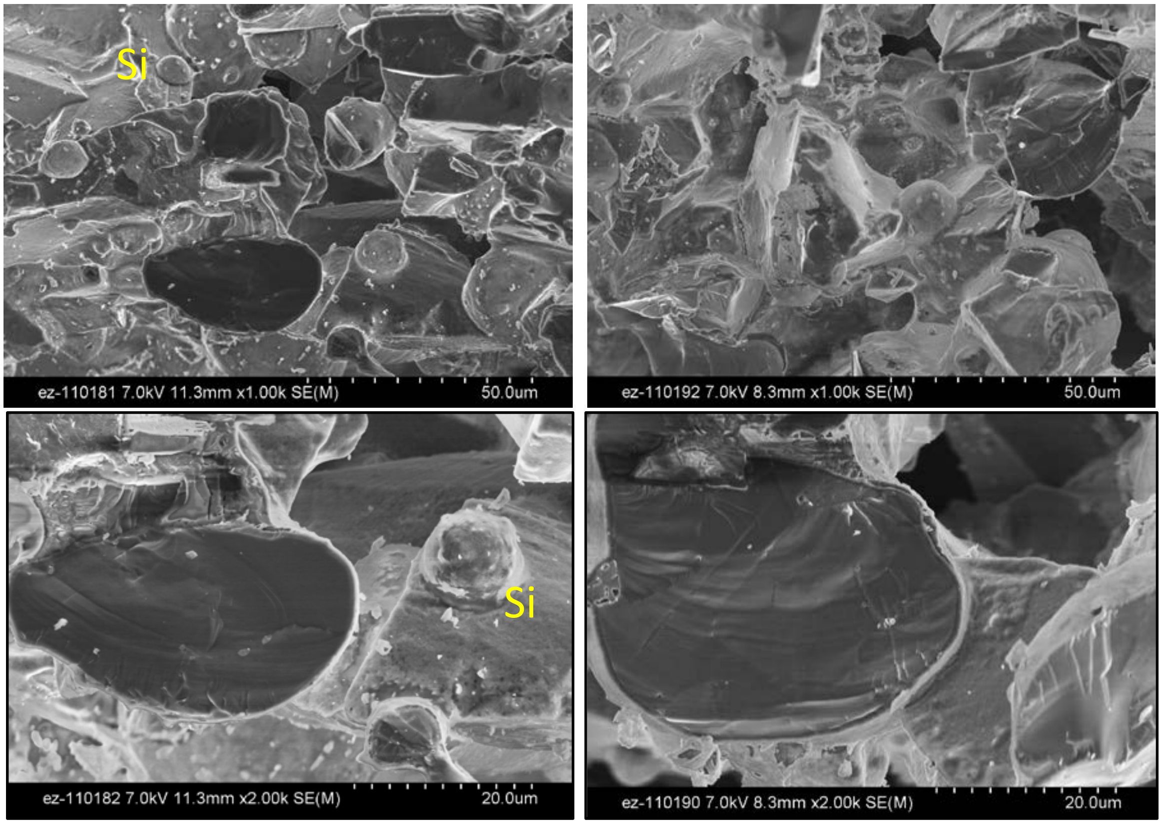

600°C **900°C**

Figure 10. The fracture surfaces of SiC DPF tested at 600 and 900°C at $3x10^{-6}$ MPa/s loading rate.

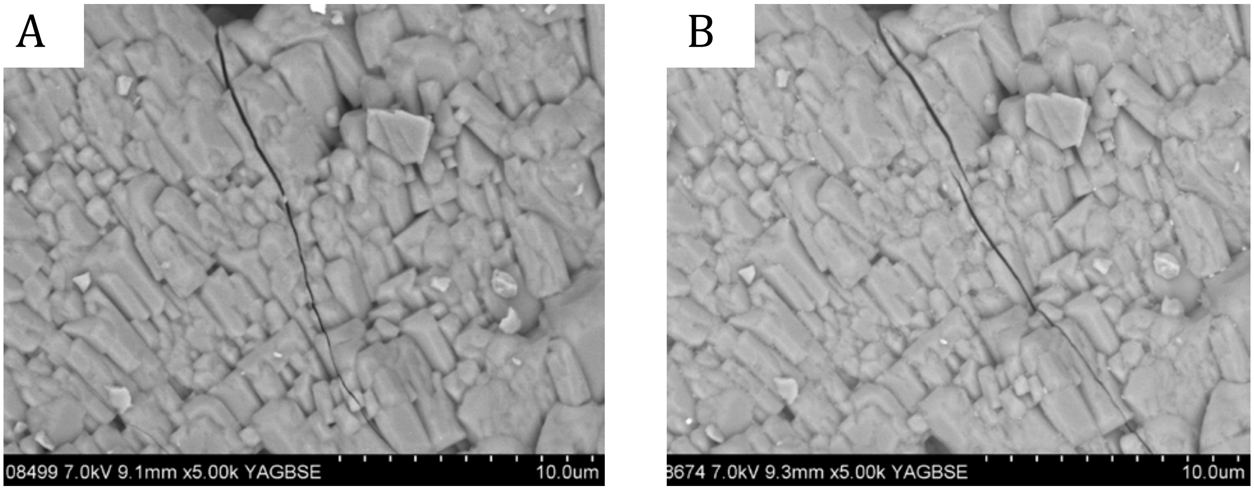

Figure 11. SEM micrograph of Cordierite A) before and B) after thermal cycling.

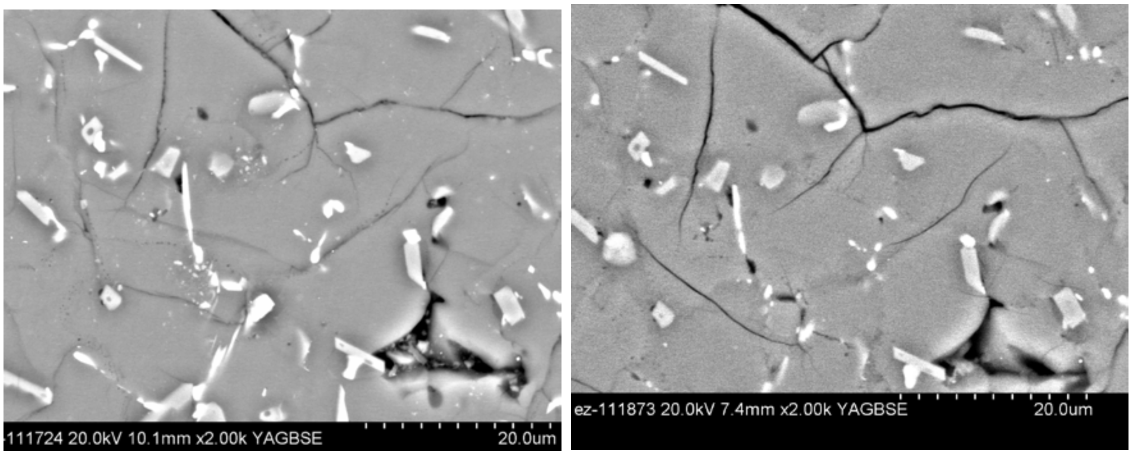

A.) B.)

Figure 12. SEM micrograph of β-eucryptite A.) before and B.) after thermal cycling.

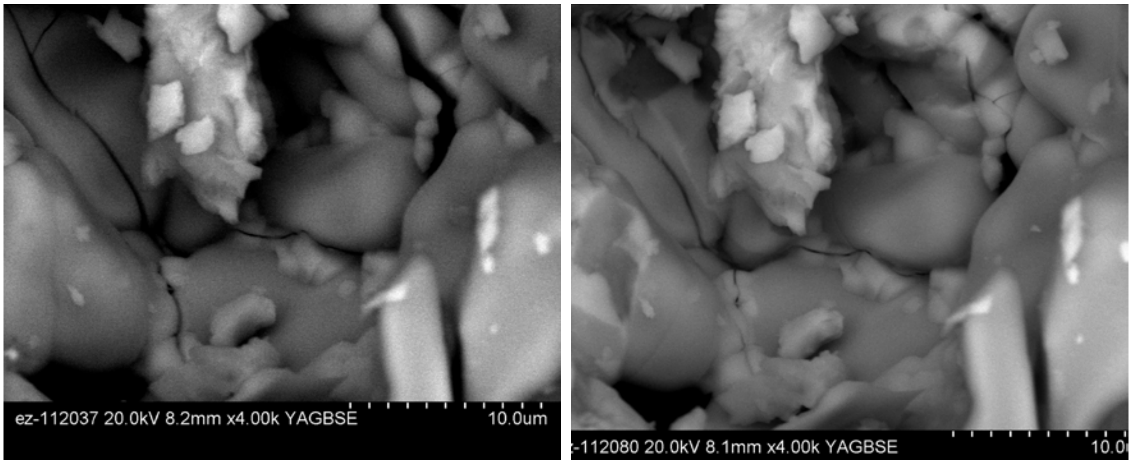

A.) B.)

Figure 13. SEM micrograph of Aluminum titanate based DPF A) before and B) after thermal cycling.

Agreement 10635 - Catalysis by First Principles

C. K. Narula, M. Moses-DeBusk, M. Stocks, X. Yang
Oak Ridge National Laboratory
P.O. Box 2008, MS 6133
(865)574-8445, narulack@ornl.govl

DOE Technology Manager: Jerry L. Gibbs
(202) 586-1182; fax: (202) 586-1600; e-mail: Jerry.gibbs@ee.doe.gov
Field Technical Manager: James A. Haynes
(865) 574-2894; fax: (865) 574-4913; e-mail: haynesa@ornl.gov

---

Contractor: Oak Ridge National Laboratory, Oak Ridge, Tennessee
Contract No.: DE-AC05-00OR22725

Objectives

- The objective of this work is to search for durable emission treatment catalysts including lean NOx traps (LNT), three-way catalyst (TWC), oxidation catalyst (OC), and Selective catalytic reduction catalyst (SCR) from a protocol based on
  - an integrated approach between computational modeling and experimental development,
  - design and testing of new catalyst materials to rapidly identify the key physiochemical parameters necessary for improving the catalytic efficiency of these materials.

Approach

- Theoretical and Experimental Studies of
  - Pt clusters supported on alumina and metal exchanged zeolites. Interaction of CO, NO_x, and HC with Pt clusters supported on alumina and NO_x reduction on zeolites
  - Understand non-structural changes in catalyst under operating conditions and correlating the changes to performance.

Accomplishments

- We have shown by theoretical models that single atoms of Pt on θ-alumina are catalytically active. We synthesized and characterized single atoms of Pt on θ-alumina and experimentally validated the proposal by carrying out CO oxidation.
    - Theoretical studies suggest CO oxidation on single atoms of supported platinum is possible through a modified Langmuir-Hinshelwood scheme.
- We have shown that 2, 3, and 4 atom Pt clusters are energetically favored over 2, 3, and 4 isolated atoms on θ-alumina surface providing driving force for agglomeration and sintering.
- We have shown that Pd prefers surface over core even for a 4-atom Pt3Pd supported cluster. The experimental studies show agglomeration and sintering of Pt-Pd core-shell structure occurring via a reverse mitosis type mechanism leading to merging of core and shell.
- We completed characterization of CuFe-SSZ-13 which is a low-temperature NO_x reduction catalyst.

Future Direction

- Guided by our results, the synthesis and evaluation of new durable supported catalysts for lean NO_x catalysts and other systems such as TWC, OC for diesel etc.

- Focus on low temperature NOx catalyst that is effective even under standard NOx reduction catalyst
- Scale up and preparation for engine testing of CuFe-SSZ-13 catalyst as a low temperature NOx reduction catalyst for diesel engines.

Introduction

This research focuses on an integrated approach between computational modeling and experimental development, design and testing of new catalyst materials, that we believe will rapidly identify the key physiochemical parameters necessary for improving the catalytic efficiency of these materials.

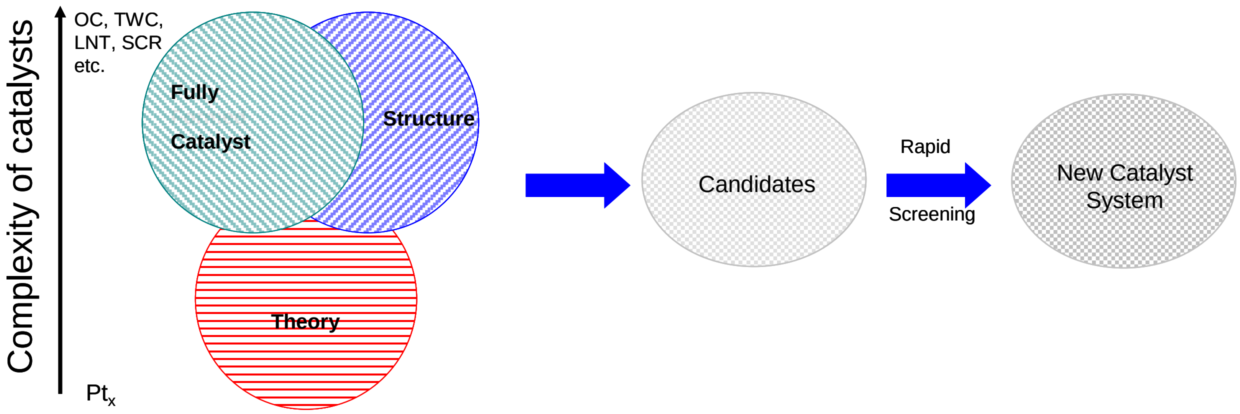

The typical solid catalyst consists of nanoparticles on porous supports. The development of new catalytic materials is still dominated by trial and error methods, even though the experimental and theoretical bases for their characterization have improved dramatically in recent years. Although it has been successful, the empirical development of catalytic materials is time consuming and expensive and brings no guarantees of success. Part of the difficulty is that most catalytic materials are highly non-uniform and complex, and most characterization methods provide only average structural data. Now, with improved capabilities for synthesis of nearly uniform catalysts, which offer the prospects of high selectivity combined with state-of-the science characterization methods, we have compelling opportunity to markedly accelerate the advancement of the science and technology of catalysis.

Computational approaches, on the other hand, have been limited to examining processes and phenomena using models that had been greatly simplified in comparison to real materials. This limitation was mainly a consequence of limitations in computer hardware and in the development of sophisticated algorithms that are computationally efficient. In particular, experimental catalysis has not benefited from the recent advances in high performance computing that enables more realistic simulations (empirical and first-principles) of a large ensemble of atoms including the local environment of a catalyst site in heterogeneous catalysis. These types of simulations, when combined with microscopic and spectroscopic characterization of catalysts, can lead to a much deeper understanding of the reaction chemistry that is difficult to decipher from experimental work alone.

Thus, a protocol to systematically find the optimum catalyst can be developed that combines the power of theory and experiments for the atomistic design of catalytically active sites and can translate the fundamental insights gained directly to a complete catalyst system that can be technically deployed.

Although it is beyond doubt computationally challenging, the study of surface, nanometer-sized, metal clusters may be accomplished by merging state-of-the-art, density-functional-based, electronic-structure techniques and molecular-dynamic techniques. These techniques provide accurate energetics, force, and electronic information. Theoretical work must be based on electronic-structure methods, as opposed to more empirical-based techniques, so as to provide realistic energetics and direct electronic information.

Thus it is conceivable that “computationally complex but experimentally simple” system can be examined by both theoretical models and experimental work to forecast improvements to obtain optimum catalyst systems.

Approach

The theoretical modeling is based on DFT studies of Pt supported on θ-alumina. We are completing DFT study of large clusters of Pt supported on θ-alumina. Our experimental studies suggest that CO oxidation is identical on both Pt supported on γ-alumina and θ-alumina. This suggests that the catalyst site structure is probably identical in both catalysts.

Experimentally, we have synthesized and characterized single atoms of Pt supported on alumina and shown them to be catalytically active. We notice some stabilization of platinum in Pt-Pd nanoparticles since very large clusters (~300-500nm) seen upon sintering of Pt at 900C are not seen in TEM of Pt-Pd nanoparticles. Our studies of Pt-Pd clusters supported on alumina shows that the agglomeration of these cluster occurs without alloying below 750°C. Alloying begins at 750°C and is more pronounced at 900°C. Theoretical studies suggest that Pd of Pt-Pd sub-nanoclusters prefer the shell locations. The experimental data also show that the mechanism of Pt-Pd agglomeration is probably reverse mitosis type.

Finally, guided by the theoretical models of Pt-Pd, we are initiating a new set of catalyst materials with higher durability under operating conditions in FY12.

Results

Until recently, our theoretical studies have focused on supported noble metals. We have shown that single platinum atoms supported on θ-alumina slab are in the zero oxidation state. This result is very different from that reported in literature on single platinum atoms supported on α-alumina or simplified models of γ-alumina where a platinum atom generally has an unpaired electron. This also means that the mechanism of CO, NO_x or HC oxidation on Pt(0) will be different from that on Pt(I) or Pt(II). We plan to carry out first principle studies of CO oxidation on Pt atoms supported on θ-alumina slab.

Since our experimental work has already shown that the distribution of platinum on γ-alumina and θ-alumina is almost identical, and the surface properties and CO oxidation of both catalysts are identical, we propose that Pt supported on θ-alumina is a better model for Pt supported on γ-alumina than Pt supported on α-alumina or simplified models of γ-alumina. Unlike α-Al_2O_3, θ-Al_2O_3 is structurally similar to γ-Al_2O_3 because both phases have a combination of tetra- and octahedrally coordinated Al atoms and a fcc arrangement of the O ions.

We have also shown that incorporation of palladium in platinum particles at sub-nanometer scale is quite ineffective in improving the durability, however, large Pt-Pd nanoparticles tend to be more hydrothermally durable than pure Pt particles. We have synthesized Pt-Pd sub-nanometer and nanometer sized particles and carried out their agglomeration studies.

In this report, we describe our theoretical and experimental studies of catalysts by single atoms for CO oxidation on Pt/ θ-alumina. Preliminary work on CO oxidation was reported in the FY11 annual report. Now, we have completed the optimization of various intermediates and also synthesized and characterized catalysts with single Pt atoms supported on θ-alumina. We also summarize our results on agglomeration of Pt atoms supported on alumina with or without palladium.

We have also carried out the characterization of CuFe-SSZ-13, a new heterobimetallic zeolite that exhibits high NO_x conversion at 150°C under fast SCR conditions.

THEORETICAL STUDIES

CO Oxidation on Pt Single Atoms Supported on θ-Al_2O_3

We employed Vienna *Ab Initio* Simulation Package (VASP) to carry out first principle total energy calculation within the supercell DFT framework.[1-3] Generalized gradient approximation (GGA) in the Perdew-Wang-91 form was employed for electron exchange and correlations.[4,5] The Kohn-Sham equations were solved using the projector augmented wave (PAW) approach for describing electronic core states. [6,7] The plane-wave basis set was truncated at a kinetic energy cut-off of 500eV.

As mentioned in the previous reports, platinum supported on a θ-alumina (010) surface is in the zero oxidation state with a d^{10} structure and bonded to two oxygen atoms. The implication of this important result is that the mechanism of CO, NO or HC oxidation on sub-nanometer particles such as single atoms can be expected to be different from the large particles normally examined by DFT. Here, we present our results for the pathways of CO oxidation on a single Pt atom supported on θ-alumina [Figure 1].

While Pt on a dry θ-alumina surface can be stable for indefinite period under oxygen free conditions, it will oxidize readily if any oxygen is present. Since an experimentalist will start with oxidized sample, we explored platinum oxidation pathways before CO oxidation. Oxygen can bond to Pt in two possible ways – terminal or side-on. The energetics shows that the side-on configuration is lower in energy than the terminal one. Density of state analysis shows that $5d_{xy}$ of Pt and $2p_x$ of O_2 have no electrons. This suggests a d^8 oxidation state for Pt. This structure also draws support from organometallic chemistry where a platinum(0) in a sixteen electron complex, $(Ph_3P)_2Pt(O_2)$, has been shown to exhibit side on configuration by single crystal X-ray structure determination.[8] The absorption energy of O_2 on Pt on a dry θ-alumina surface is -43.20 Kcal/mole.

The oxygen on platinum in $(Ph_3P)_2Pt(O_2)$, has been suggested to dissociate to form Pt=O bond before reaction with CO or a SN2 type CO reaction can occur on Pt with CO bond formation resulting in the oxygen becoming terminally bonded. The formation of carbonate from this structure is quite likely and has been confirmed in the reaction of $(Ph_3P)_2Pt(O_2)$ with CO. The loss of CO_2 from this structure will generate intermediate species containing Pt=O bond which can react with another molecule of CO. This intermediate will form platinum(0) after CO_2 elimination. In analogy with this scheme in homogenous catalysis, we examined possible intermediates for CO oxidation over Pt on a dry θ-alumina surface.

On a reduced Pt surface, the CO absorption can occur with bond formation between Pt and the carbon of CO. There is no magnetic moment associated with this structure and the density of state analysis shows it to be in d^{10} oxidation state. All d orbitals of Pt are filled and bonding is through σ_C of C=O. The absorption energy of CO on Pt on a dry θ-alumina surface is -43.06 Kcal/mole. Since there is no significant difference between CO and O_2 absorption energy, CO and oxygen can compete for the platinum(0) site.

Regardless of whether the first species formed is Pt with O_2 absorbed on it or CO, the next intermediate forms with the bonding of both CO and O_2 on the same Pt atom. This intermediate formation involves breaking of one Pt-O bond with the surface. The intermediate is still a d^{10} system with magnetization at oxygen atoms of O_2 species. The absorption energy for oxygen is -45.79Kcal/mole. This intermediate undergoes rearrangement to form a carbonate species. The carbonate species is a d^8 species with no magnetization. DOS analysis shows no electrons in Pt $5d_{xy}$ and $C2p_z$. This species is analogous to an organometallic platinum(0) sixteen electron complex, $(Ph_3P)_2Pt(CO_3)$, which has been shown to exhibit CO_3 bonding via two oxygen atoms by single crystal X-ray structure determination.[9]

The elimination of CO_2 from the carbonate species forms a monoxide high spin d^8 species.

DOS shows Pt d_{xy}, Pt d_{yz}, O $1p_z$, and O $1p_x$ partially occupied. The DOS of p-orbitals of the alumina surface oxygen atoms bonded with platinum are shifted to lower energy and have features similar to parent compound.

The monoxide complex reacts with CO to form a new intermediate which eliminates CO_2 to regenerate the catalyst to enable a new catalytic cycle for CO oxidation.

Multiple Pt atoms and Agglomerates on θ-alumina (010) surface

The sintering of platinum particles has been extensively studied and some of the models developed for Pt particles also apply to Pt nanoparticles. Theoretical studies point to structures of various small clusters and show that oxidized Pt is more prone to sintering. However, the reasons for facile sintering of Pt particles are not well understood. It is in this context we started our work to understand the reason for sintering with the expectation that insights will help us design the catalyst materials that are less susceptible to sintering. We have completed the study of 2, 3, and 4-atom systems. We find that there is no significant difference between binding energy of two atom clusters and two independent atoms. For three-atom and four atom-clusters, the clusters are more energetically favored over independent atoms. These results show that increased stability of clusters over supported independent atoms provides the driving force for sintering. The results are summarized below:

Two-atom clusters: The total energy of two independent atoms on 010 surface of θ-Al_2O_3 is -3047.5495 eV. There are two possible locations of two atom Pt clusters are shown in Figure 2 (middle and right). The energy of the two atom clusters is -3047.8793 for the Pt configuration of the middle figure and -3047.7091 eV for the Pt configuration of the right figure in Figure 2. This suggests that 2 atom clusters are energetically favored by 0.3298 and 0.1596 eV (7.6 and 3.86 Kcal/mole). Although the difference in energy of independent atoms and 2-atom clusters is low, the results do point to the fact that there is no significant barrier to sintering of Pt when distributed atomically on alumina surface.

Three atom clusters: The total energy of three independent atoms on 010 surface of θ-Al_2O_3 is -3051.1554 eV. There are two possible locations of three atom Pt clusters are shown in Figure 3 (middle and right). The energy of the three atom clusters shown in Figure 3 is -3052.2214 and -3053.0851 eV, respectively. This suggests that 3 atom clusters are energetically favored by 1.066 and 1.9297 eV (24.59 and 44.51 Kcal/mole). The significant differences in energy of independent atoms and 3-atom clusters clearly show that the driving force for sintering is the energetics of clusters which is apparent even for a 3-atom system.

Four Pt atom clusters: The total energy of 4 atoms absorbed on θ-alumina 110 surfaces is -3054.4954 eV [Figure 4]. These four atoms are independent of each other and each of these atoms is located above aluminum and bonded to two oxygen atoms on the surface. All platinum atoms are d^{10} species. The four atom cluster, on the other hand is favored by 3.3976 eV (78.3 Kcal/mol) over four atoms adsorbed on θ-alumina 110 surfaces. Its total energy is -3057.8930 eV and all Pt atoms are d^9.

Pt-Pd/Alumina system:

We have previously shown that pre-formed Pt-Pd nanoclusters with Pt-Pd ratio of 3:1, 1:1, and 1:3 supported on γ-alumina are hydrothermally more stable than Pt/γ-alumina in 500-900°C range and do not form extra-large clusters of 300-400 nm commonly observed upon hydrothermal aging of Pt/γ-alumina. In order to explain the phenomenon, we carried out first principles modeling of a four atom cluster, Pt_3Pd/γ-alumina, and the optimized structures are shown in Figure 5.

The total energy of the Pt_3Pd/γ-alumina system where three platinum and one palladium atoms are adsorbed on θ-alumina 110 surfaces is -3054.4628 eV (A) and all atoms are d^{10}. In 4 -atom clusters where cluster bonding to the θ-alumina 110 surfaces occurs via one platinum and one palladium, the energies are -3055.7018 eV (B) and -3055.2498 eV. The energy of the four atom cluster with Pd atom not bonded to alumina surface is -3055.6357 eV. Finally, the energy of the cluster with Pd in core is -3054.7419 eV indicating that it is the least energetically favored of all four atom Pt-Pd clusters [Figure 5 (D)]. Energetically, the most favored structure is when the Pd atom of the Pt_3Pd cluster is bound to the alumina surface via two surface oxygen atoms and one Pt is bound via one oxygen atoms [Figure 5A].

This analysis suggests that Pd prefers a shell position over the core position even for a small cluster.

EXPERIMENTAL STUDIES

Single Pt atoms on θ-Al_2O_3

In order to validate the results of theoretical modeling studies, we synthesized Pt/theta-alumina with Pt distributed on alumina surface as single atoms. The samples were prepared by impregnation method with Pt loading of 0.18% and 1%. The electron microscopic images, obtained on an ACEM, show single atom distribution on 0.18% sample and 10-20 atom agglomerates in 1.0% sample [Figure 6]

The extended x-ray absorption fine structure (EXAFS) of our samples were recorded on fresh samples and after reducing them at 150°C under a flow of hydrogen [Figure 7]. The 0.18% sample shows peaks near 2Å for Pt-O bonds but there are no peaks at 2.8Å normally assigned to Pt-Pt bonds. The 1% sample does not exhibit Pt-Pt bonds either when fresh suggesting all Pt is oxidized. However, the reduction step leads to a new peak in the EXAFS near 2.8Å that is normally assigned to Pt-Pt bonds. The EXAFS studies suggest that the 0.18% sample is most probably comprised of single Pt atoms on the alumina surface. The EXFAS data also suggest that 10-20 atom agglomerates are prone to sintering even under relatively mild reducing conditions.

The light-off of CO oxidation on 0.18% Pt/θ-Al_2O_3 is at 191ºC and that on 1.0% Pt/θ-Al_2O_3 is at 167ºC [Figure 8]. This experiment clearly shows that single Pt atoms are catalytically active.

The CO absorption studies were carried out on a DRIFTS instrument [Figure 9]. First, the samples were heated under a flow of helium to remove surface impurities and then were exposed to a flow of CO at room temperature and at 170ºC. The 0.18% Pt/θ-Al_2O_3 exhibits a broad absorption for CO at room temperature while 1.0% Pt/θ-Al_2O_3 shows features for CO adsorbed in terminal and bridging mode (1850 cm^{-1}). The presence of bridging CO adsorption mode suggests the presence of Pt-Pt bonds in this sample.

The 0.18% Pt/θ-Al_2O_3 sample does show features for terminal adsorption of CO at 175ºC but no features for CO in bridging mode. The absence of CO adsorption in bridging mode is indicative of the absence of Pt-Pt bonds in conjunction with the results of EXAFS and ACEM data.

Sintering of Pt-Pd Nanoparticles

Freshly prepared samples with Pt_xPd_y particles have Pt cores and Pd shell particles. The loading of nanoparticles on alumina during synthesis does not deteriorate this structure. The STEM of the sample shows a Pt core and Pd shell structure.

The hydrothermal aging of Pt-Pd nanoparticles was studied by electron microscopy. Interestingly, we found two Pt core - Pd shell particles in the process of coalescing after hydrothermal aging at 500°C [Figure 10]. The image looks like that of a reverse mitosis process and Pd on both particles leaves the surface to allow Pt cores to coalesce. The resulting particle shows Pt cores and Pd shells merging.

Hydrothermal aging gradually starts converting Pt-Pd nanoparticles to alloys and aging at 900°C shows particles which are essentially Pt-Pd alloys.

Structural Characterization of CuFe-SSZ-13

Samples of the ORNL-designed catalyst material CuFe-SSZ-13 were prepared by ion exchange with iron nitrate at 80°C. CuFe-SSZ-13 exhibits high NO_x conversion activity at 150°C as compared with Cu-SSZ-13, a commercial urea-SCR catalyst [Figure 11]. The performance of CuFe-SSZ-13 is identical to that of Cu-SSZ-13 in the 200-650°C range. After hydrothermal aging, the new CuFe-SSZ-13 material retains its high NO_x conversion activity at 150°C.

The UV-Vis of Cu-SSZ-13 and CuFe-SSZ-13 is shown in Figure 12. The UV-Vis spectra of CuFe-SSZ-13 and Cu-SSZ-13 exhibit very intense absorptions from a d-d transition at ~ 210 nm and a broad peak at ~ 830 nm from the charge transfer band related to $O \rightarrow Cu$ transition from lattice oxygen to isolated Cu^{2+} ions. In addition, CuFe-SSZ-13 has two absorptions that can be attributed to isolated tetrahedral and octahedral Fe^{3+}, at 210 and 270 nm, respectively, which are also seen in Fe-ZSM-5 type structures. In general, absorptions of iron oxide clusters and iron oxide particles are believed to be above 400 nm and are not seen.

A new, intense absorption centered at ~ 350 nm is also present which could be assigned to octahedral Fe^{3+} in small oligomeric clusters and has previously been assigned to $[HO\text{-}Fe\text{-}O\text{-}Fe\text{-}OH]^{2+}$ cluster bound to the zeolite framework via iron oxygen bridges.

The Cu EXAFS and XANES of CuFe-SSZ-13 are identical to those of Cu-SSZ-13 and the data suggest Cu to be Cu(II) [Figure 13]. The Fe EXAFS and XANES of CuFe-SSZ-13 could not be compared to Fe-SSZ-13 but the data indicate a structure very similar to that of Fe-ZSM-5 and Cu-Fe-ZSM-5. These data point to a structure for the CuFe-SSZ-13 sample where Cu is in the ionic position in Cu-SSZ-13 and iron resides in the pores of Cu-SSZ-13 as an oligomeric cluster.

Conclusions

Theoretical studies show that CO oxidation can occur on single supported atoms without the involvement of support. The mechanism is a variation of Langmuir-Hinshelwood scheme and the proposed intermediates have analogues in organometallic chemistry. Experimentally, we synthesized single atoms of Pt supported on θ-alumina support, characterized by STEM and EXAFS studies and carried out CO oxidation. The results validate our theoretical study which suggested CO oxidation is possible on single atoms.

Our platinum-palldium analysis suggests that Pd prefers a shell position over the core position even for a small cluster. Experimentally, the hydrothermal aging of Pt-Pd nanoparticles leads to coarsening via a reverse mitosis process and Pd on both particles leaves the surface to allow Pt cores to coalesce. The resulting particle shows Pt cores and Pd shells merging. Hydrothermal aging gradually starts converting Pt-Pd nanoparticles to alloys and aging at 900°C shows particles which are essentially Pt-Pd alloys.

We also summarized our detailed characterization of CuFe-SSZ-13 which is a hydrothermally stable, low-temperature NO_x reduction catalyst (under fast SCR conditions).

Future studies will focus on scale-up and preparation for engine testing of the new CuFe-SSZ-13 catalyst material, which was designed as a low temperature (150°C) NO_x reduction catalyst for diesel exhaust treatment.

References

1. Kruse, G.; Hafner, J.; Phys. Revd., **1993**, 47, 558.
2. Kruse, G.; Hefner, J. Phys. Rev. B, **1993**, 48, 13115
3. Kruse, G. Hefner, J.; Phys. Rev. B, **1994**, 49, 14251

4. Perdue, J.P.; Chivalry, J.A.; Vodka, S.H.; Jackson, K.A.; Pederson, M.R.; Singh, D.J.; Phys. Rev. B.; **1992**, 46, 6671
5. Perdue, J.P.; Chivalry, J.A.; Vodka, S.H.; Jackson, K.A.; Pederson, M.R.; Singh, D.J.; Phys. Rev. B.; **1993**, 48, 4978.
6. Bloch, P.E.; Phys. Rev. B, **1994**, 50, 17953.
7. Kruse, G.; Jobber, D.; Phys. Rev B, **1999**, 59, 1758.
8. Cheng, P.T.; Cook, C.D., Nyburg, S.C., Wan, K.; Can. J. Chem., 49 (1971) 3772.
9. Scholz, S.; Lerner, H.W.; Bolte, M. Acta Cryst E62 (2006) m312-m313. Gregg, M.R.; Powell, J.; Sawyer, J.F.; Acta. Crystal. C44 (1988) 43-46
10. Qiao, B; Wang, A.; Yang, X.; Allard, L.F.; Jiang, Z.; Cui, Y.; Liu, J.; Li, J.; Zhang, T.; Nature Chem., 3 (2011) 634

Presentations and Publications (FY 12)

1. X. Yang, Z. Wu, M.M. DeBusk, D.R. Mullins, S.M. Mahurin, R.A. Geiger, M. Kidder, C.K. Narula, Heterometal Incorporation of M-Exchanged Zeolties enables low temperature catalytic activity of NOx reduction, J. Phys. Chem. C (in press)

2. C.K. Narula, M.G. Stocks, "Ab Initio Density Functional Calculations of Adsorption of Transition Metal Atoms on θ-Al2O3(010) Surface" J. Phys. Chem,. C, 2012, 116, 5628.

3. DeBusk, M.M.; Allard, L.F.; Mullins, D.R.; Stocks, G.M.; Yang, X.; Wu, Z.; Narula, C.K.; CO oxidation on supported single Pt atoms – experimental and ab initio density functional studies of CO interaction with Pt atom on θ-Al2O3(010), J. Am. Chem. Soc. (to be submitted)

4. DeBusk, M.M.; Allard, L.F.; Blom, D.A.; Narula, C.K.; The structure and stability of sub-nanometer platinum supported on alumina, Ind. Eng. Chem. Res. (to be submitted)

Figures

Figure 1: CO oxidation cycle on single Pt atoms adsorbed on (010) θ-alumina surface.

Figure 2: Two Pt atoms (left) and two atom clusters (middle & right) on 010 surface of θ-Al_2O_3.

Figure 3: Three Pt atoms (left) and three atom clusters (middle & right) on 010 surface of θ-Al_2O_3.

Figure 4: Four Pt atoms and cluster on 010 surface of θ-Al_2O_3

Figure 5: Pt3Pd cluster supported on θ-alumina 110 surfaces [Pd atom is dark blue and Pt atoms are gray].

Figure 6: ACEM images of 0.18% Pt/θ-Al_2O_3 (left) and 1.0% Pt/θ-Al_2O_3 (right)

Figure 7: EXAF of 0.18% (top-left) and 1% Pt on theta-alumina; the figure on bottom left and right are from literature for comparison where sample A is 0.18% and sample B is 2% Pt on iron oxide from ref 10.

Figure 8: CO oxidation on 0.18% Pt/θ-Al_2O_3 (left) and 1.0% Pt/θ-Al_2O_3 (right).

Figure 9: IR of CO adsorption on 0.18% Pt/θ-Al_2O_3 and 1.0% Pt/θ-Al_2O_3 at RT (left) and on 0.18% Pt/θ-Al_2O_3 at RT and 170°C (right)

Figure 10: Coalescing Pt-Pd (1:1 ratio) particles (left) and Pt map (right) which shows that Pt is in the core.

Figure 11: NO_x conversion under fast-NH_3-SCR conditions over Cu-SSZ-13 (a commercial catalyst) and CuFe-SSZ-13 in 150-650C range. Our catalyst, CuFe-SSZ-13 exhibits higher NO_x conversion activity as compared with commercial catalyst.

Figure 12: Diffuse reflectance UV-Vis of Cu-SSZ-13 and CuFe-SSZ-13.

Figure 13: EXAFS of Cu-SSZ-13 and CuFe-SSZ-13.

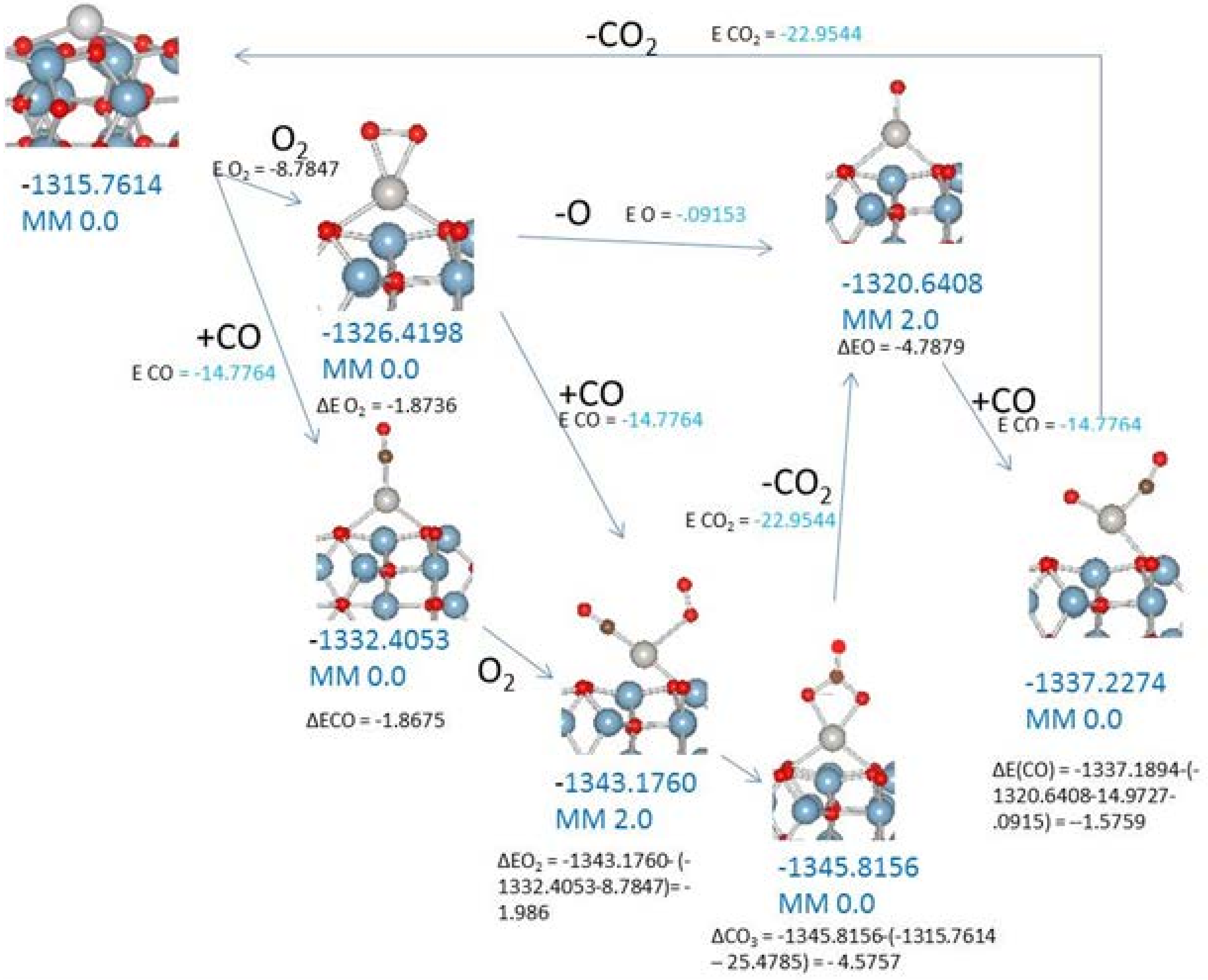

***Figure 1**: CO oxidation cycle on single Pt atoms adsorbed on (010) θ-alumina surface.*

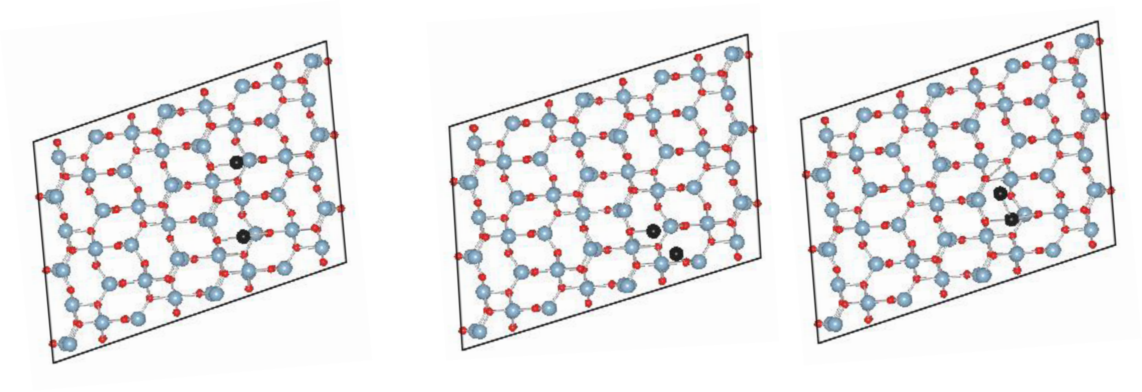

Figure 2: *Two Pt atoms (left) and two atom clusters (middle & right) on 010 surface of* θ-Al_2O_3

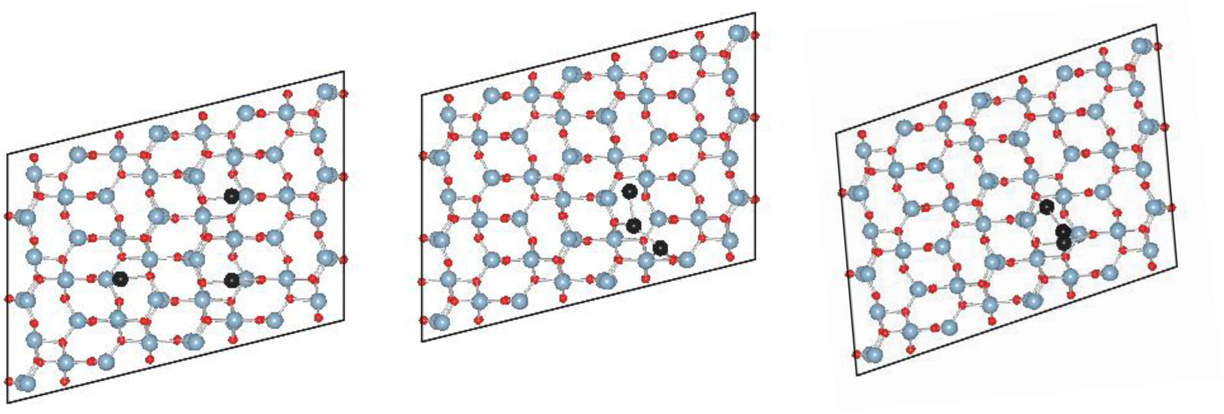

Figure 3: *Three Pt atoms (left) and three atom clusters (middle & right) on 010 surface of* θ-Al_2O_3

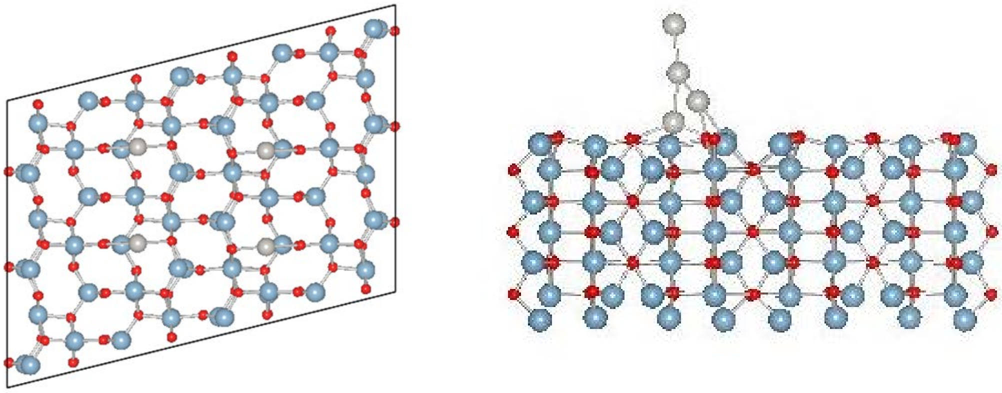

Figure 4: *Four Pt atom and cluster supported on* θ*-alumina 110 surfaces*

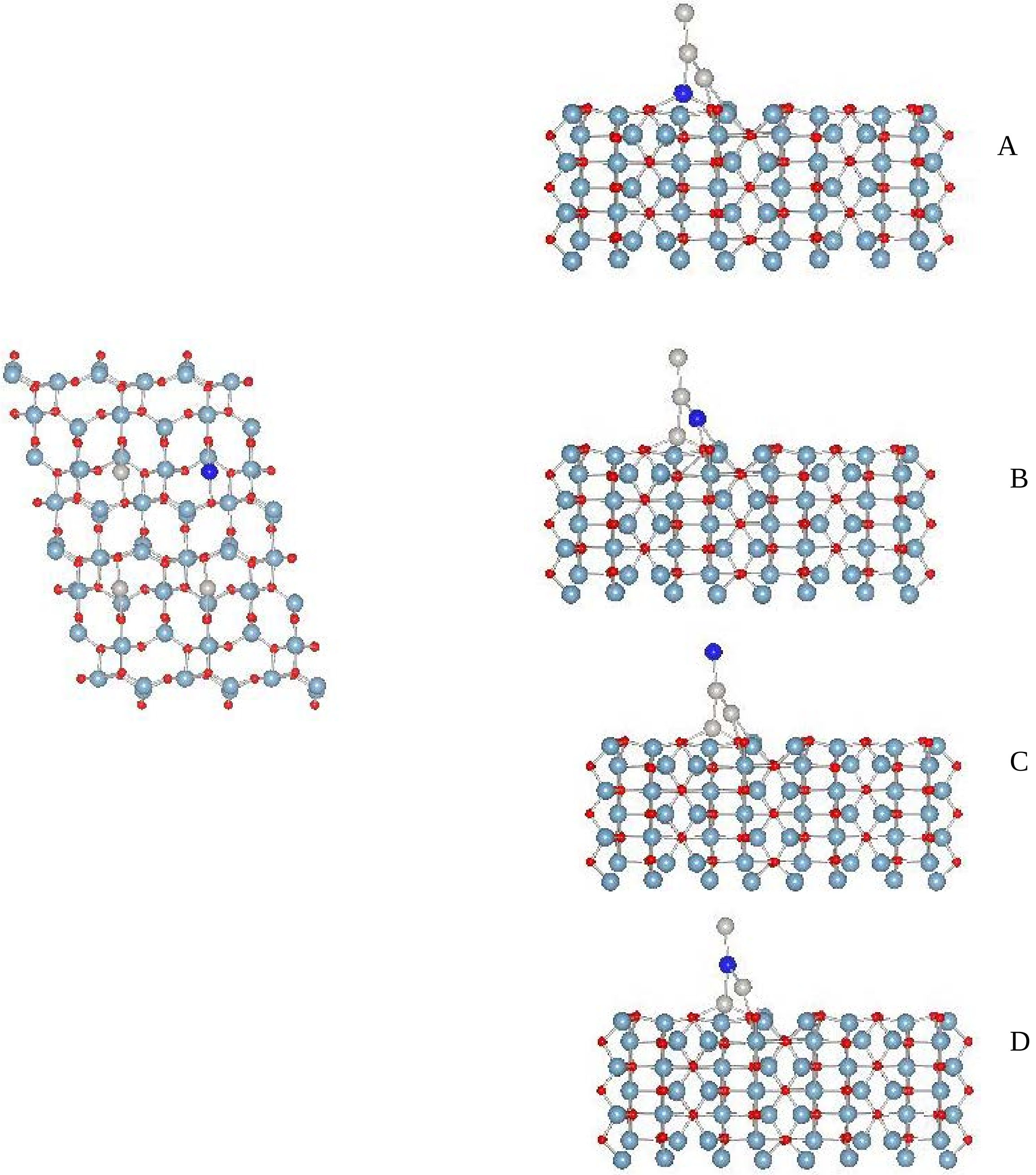

Figure 5*: Pt*$_3$*Pd cluster supported on* θ*-alumina 110 surfaces [Pd atom is dark blue and Pt atoms are gray]*

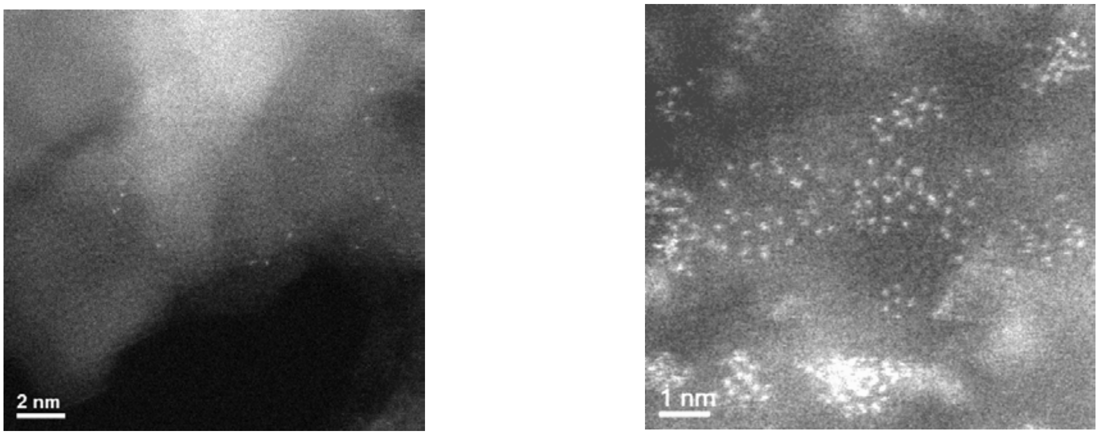

Figure 6: *ACEM images of 0.18% Pt/θ-Al_2O_3 (left) and 1.0% Pt/θ-Al_2O_3 (right)*

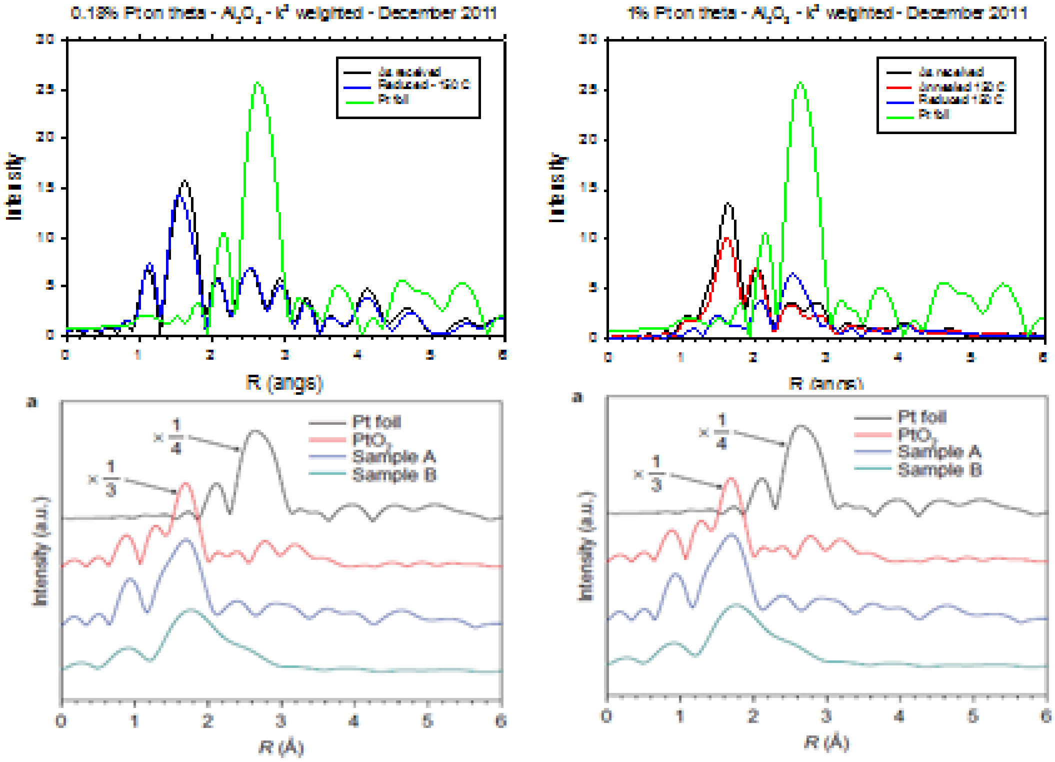

Figure 7: *EXAF of 0.18% (top-left) and 1% Pt on theta-alumina; the figure on bottom left and right are from literature for comparison where sample A is 0.18% and sample B is 2% Pt on iron oxide from ref 10.*

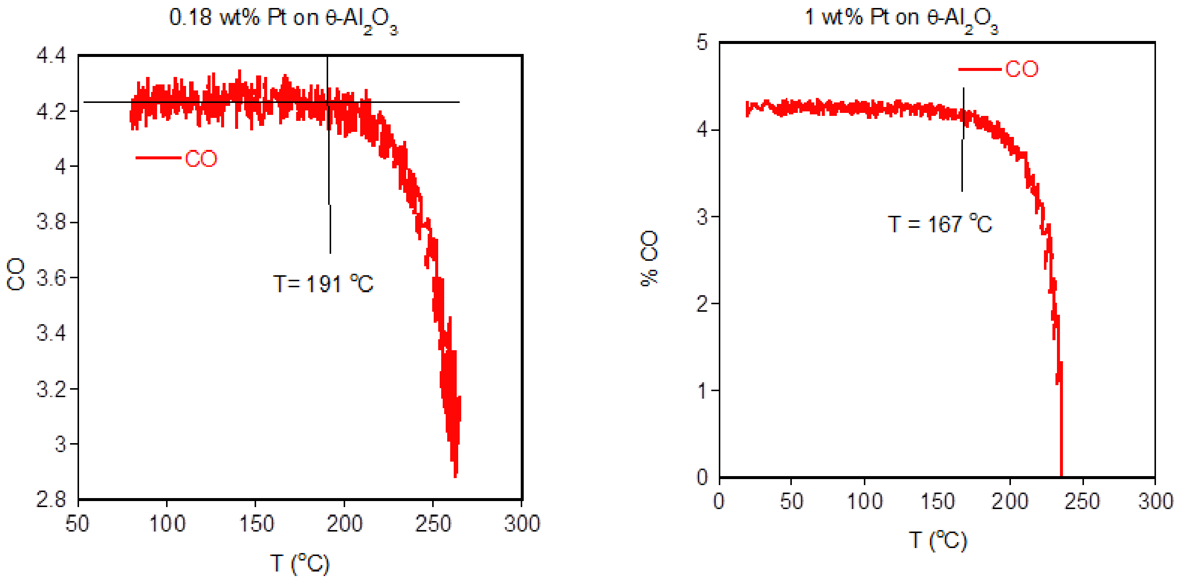

Figure 8*: CO oxidation on 0.18% Pt/θ-Al$_2$O$_3$ (left) and 1.0% Pt/θ-Al$_2$O$_3$ (right)*

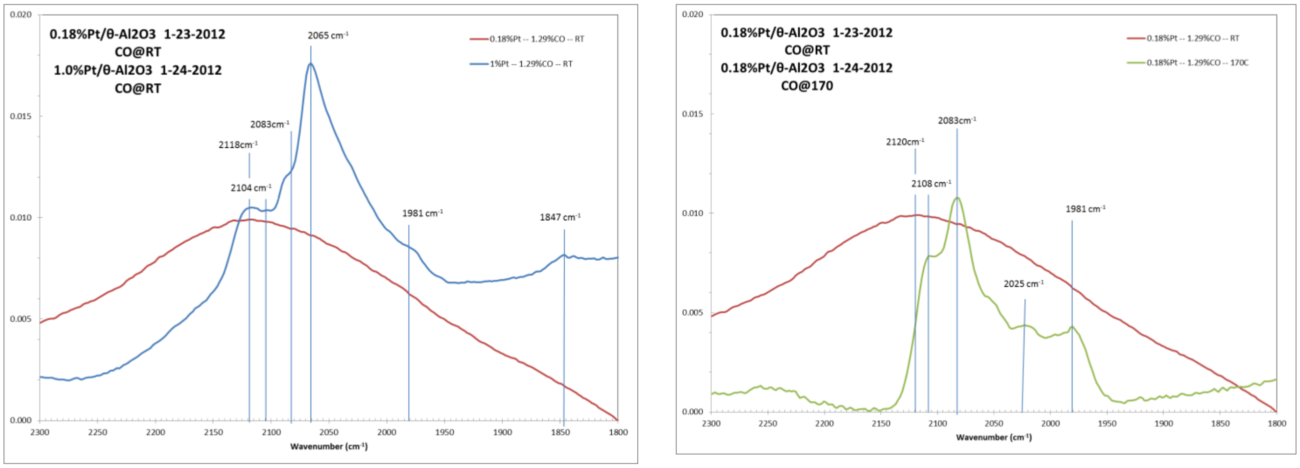

Figure 9*: IR of CO adsorption on 0.18% Pt/θ-Al$_2$O$_3$ and 1.0% Pt/θ-Al$_2$O$_3$ at RT (left) and on 0.18% Pt/θ-Al$_2$O$_3$ at RT and 170°C (right)*

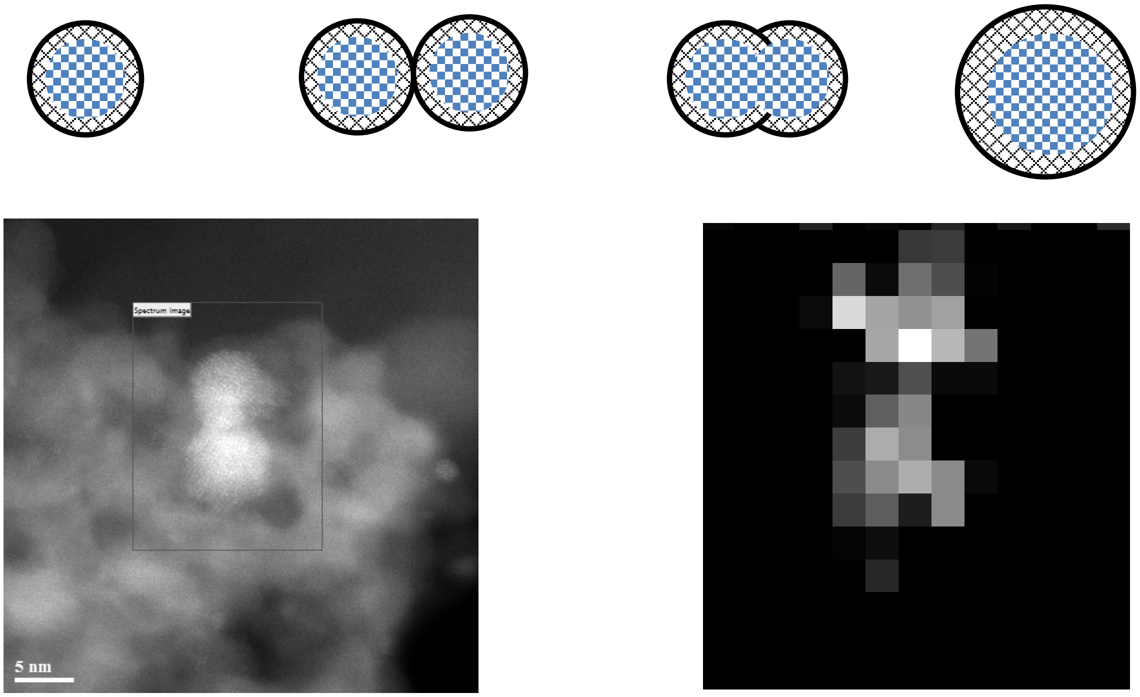

Figure 10: *Reverse mitosis type pathway to coarsening of Pt-Pd particle where both core and shell merge to create a larger Pt-Pd core-shell particle (top). Coalescing Pt-Pd (1:1 ratio) particles (left) and Pt map (right) which shows that Pt is in the core (bottom).*

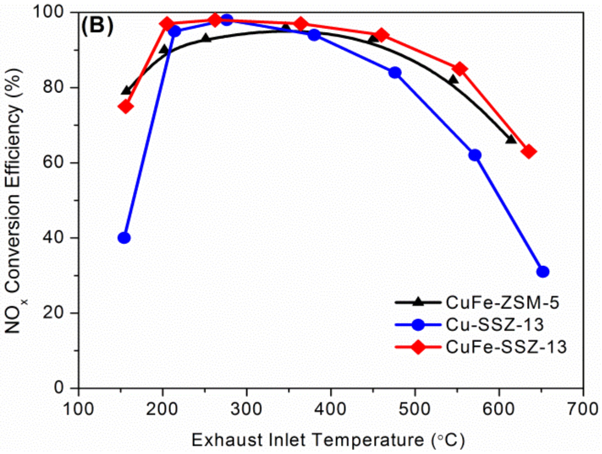

Figure 11: *NO$_x$ conversion under fast-NH$_3$-SCR conditions over Cu-SSZ-13 (a commercial catalyst) and CuFe-SSZ-13 in 150-650C range. Our catalyst, CuFe-SSZ-13 exhibits higher NO$_x$ conversion activity as compared with commercial catalyst [from Narula et al. J. Phys. Chem. C, 2012, 116, 23322.*

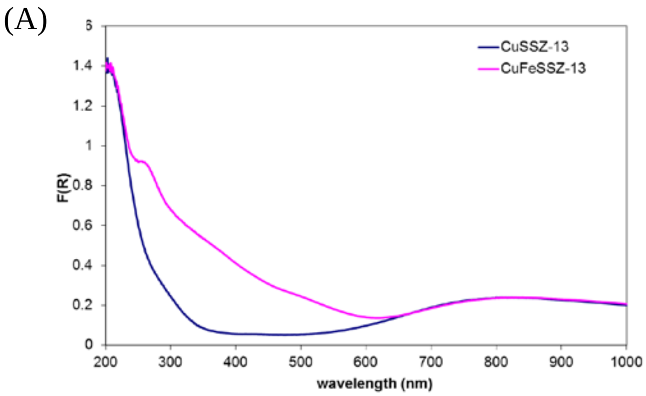

Figure 12. *Diffuse reflectance UV-Vis of Cu-SSZ-13 and CuFe-SSZ-13*

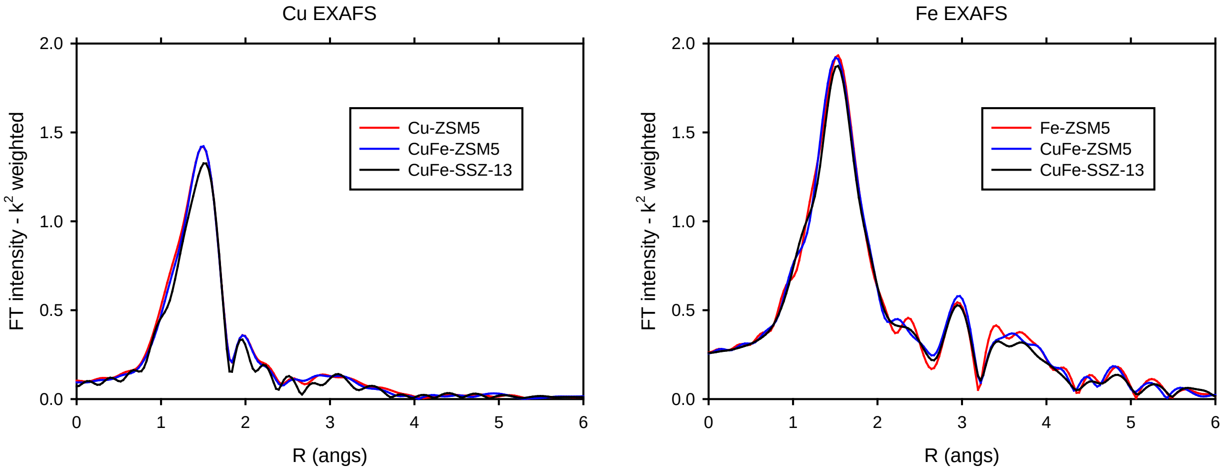

Figure 13*: EXAFS of Cu-SSZ-13 and CuFe-SSZ-1*

Agreement 19214 - Effects of Biodiesel Fuel on Diesel Particulate Filter Materials

M. J. Lance, A. A. Wereszczak, M. K. Ferber, T. J. Toops, E. J. Nafziger*, B. G. Bunting*, and E. E. Fox*
Ceramic Science and Technology Group
Oak Ridge National Laboratory
P.O. Box 2008, MS 6068, Bldg. 4515
Oak Ridge, TN 37831-6068
(865) 241-4536; fax: (865) 574-6098; e-mail: lancem@ornl.gov
** Fuels, Engines and Emissions Research Center, ORNL*

DOE Technology Manager: Jerry L. Gibbs
(202) 586-1182; fax: (202) 586-1600; e-mail: jerry.gibbs@ee.doe.gov
ORNL Technical Advisor: J. Allen Haynes
(865) 574-4556; fax: (865) 241-1034; e-mail: haynesa@ornl.gov

Contractor: Oak Ridge National Laboratory, Oak Ridge, Tennessee
Prime Contract No.: DE-AC05-00OR22725

Objectives

- To characterize changes in the microstructure and material properties of diesel particulate filters (DPFs) in exhaust gas produced by biodiesel blends.

Approach

- Use a stationary generator to produce diesel exhaust for long-term 24/7 aging of DPFs in diesel and biodiesel exhaust.
- Improve determination of elastic moduli and failure stresses of aged DPF samples by measuring them in pure tension through gripping the samples with epoxy.
- Characterize SiC DPFs aged in biodiesel exhaust provided by NREL/Ford/MECA collaboration.

Accomplishments

- Conducted a baseline test of the stationary generator using a cordierite DPF with ULSD fuel.
- Established a pure tension testing protocol and measured as-received and engine tested DPFs.
- Measured thermo-mechanical properties of DPF tiles tested during accelerated biodiesel aging.

Future Direction

- Using the stationary generator, accelerated aging with Na and K doping in order to simulate long-term biodiesel exposure will be conducted and DPF material degradation will be measured.
- Characterize a second round of aged DPF samples aged with both Na and K at the same time provided by NREL/Ford/MECA collaboration.

Introduction

In the spring of 2008, soot was collected on uncatalyzed cordierite diesel particulate filters (DPFs) from a 1.7L Mercedes-Benz engine fueled with biodiesel blends (4 volumetric blends 0 - 100%) for the study of soot oxidation kinetics. The soot was removed by backflushing the filters with pressurized air after which the filters were stored in ambient conditions on a shelf still within the can. Approximately 3 months later, the DPF bricks were removed from the can at which point significant degradation of the DPFs that had seen biodiesel exhaust was observed. No degradation of the DPF run with ultra-low sulfur diesel (ULSD) was found. In addition, after burning the collected soot, the biodiesel soot had cordierite and padding residue in amounts roughly proportional to the biodiesel volume percent in the fuel. This result suggests that biodiesel may cause degradation of DPF materials under some conditions. This project has the objective to investigate this possibility and potential degradation mechanisms resulting from biodiesel operation.

To investigate the effect of biodiesel fuel on DPF material degradation, two experimental efforts are being employed. First, a stationary generator has been purchased and set up to operate 24/7 using different fuels. The exhaust is sent through a DPF which can be aged in a controlled way in this manner. The mechanical properties of the DPF are then measured in order to determine if any material degradation has occurred. As part of this effort, a new methodology of testing DPFs in pure tension was devised.

The second approach is to obtain DPFs from a collaboration with the National Renewable Energy Laboratory (NREL), the National Biodiesel Board (NBB), the Manufacturers of Emission Controls Association (MECA), and Ford Motor Company that is focusing on light duty applications and is funded through the Office of Vehicle Technologies, Fuels Program.

These two approaches are complimentary to one another and allow us to compare results from two different engine-testing methods in order to better understand their different effect on DPF materials. Results show that the samples generated by the collaboration with NREL did not show any degradation of the SiC DPF at the temperatures investigated, however, an increase in stiffness of the cordierite DPFs was measured after 106 cycles at 700°C inlet temperature using ULSD fuel.

Results

Installation of Stationary Generator

Emission control devices are required to operate on-road for 435,000 miles without failure. In order to test DPFs for this duration an accelerated aging method needs to be employed or else the test will be too costly and time-consuming to be practical. Engine companies use multi-million dollar test cells to run engines for months at a time to test systems under real-world conditions. In order to be more economical, a single-cylinder stationary generator was chosen to produce diesel exhaust which is used to produce the temperature excursion expected during DPF regeneration. This approach allows us to generate diesel exhaust using different fuels that have been dosed with chemicals to increase the Na and K content so as to match long-term operation with biodiesel fuel. At the same time, the stationary generator can be operated unattended for 24/7 which just daily refueling. This approach generates many samples in a cost effective way while simulating conditions expected during on-road use in biodiesel and diesel exhaust.

The stationary diesel generator for thermal cycling has been purchased and installed and is shown in Figure 1. The generator is a Pramac P6000S silenced diesel gen-set and has been installed at the NTRC (National Transportation Research Center) building at ORNL. The engine is 10 hp and is rated for 4800 W and is connected to an Avtron K490 load bank. Shakedown testing indicated the need for a complete change of the exhaust system due to the use of a glass-pack muffler which shed fibers and face-plugged the DPF and due to excess cooling of exhaust, which was done by the manufacturer for safety reasons. These two problems have been corrected by a complete rebuild of the exhaust system (shown in Figure 2). Thermal cycling of the diesel particulate filter is done by a combination of generator load and exhaust fuel injection.

Figure 1. Picture of the stationary generator.

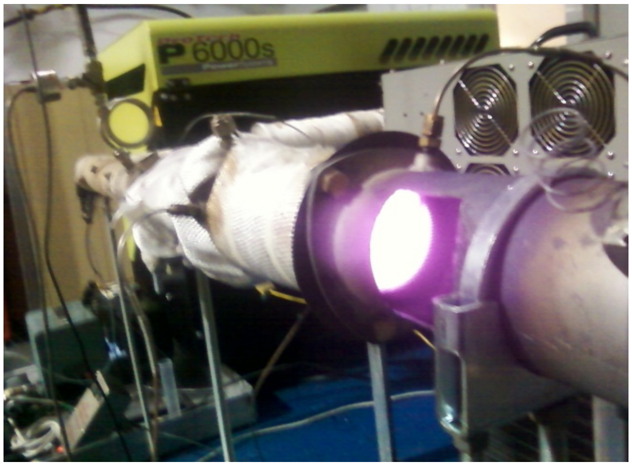

Figure 2. The outlet side of the DPF during active regeneration.

In order to more efficiently conduct engine experiments with a variety of fuel blends, an auxiliary fueling system was designed. This external fuel system combines four separate tanks in a manifold arrangement. With a multiport selector valve, any one of four fuels may be chosen. Thought was taken to ensure streamlined fuel changeovers with low downtime and no fuel cross-contamination, by means of staged drain paths with easy access, remote fill neck assemblies, and a self-priming lift pump. The fuel setup is shown in Figure 3. Electrical static discharge within the multiple fuel streams was eliminated with helical wrapping of the fuel pipes with a copper conductor, and tailoring the fluid flow velocities in the supply and return streams.

Figure 3. Auxilary fueling system and manifold panel.

A wideband lambda sensor, as shown in Figure 4, was added to monitor air/fuel ratio and oxygen content in the exhaust. A frequency signal conditioner was integrated into the data acquisition system to monitor generator performance, and help ensure repeatable operation.

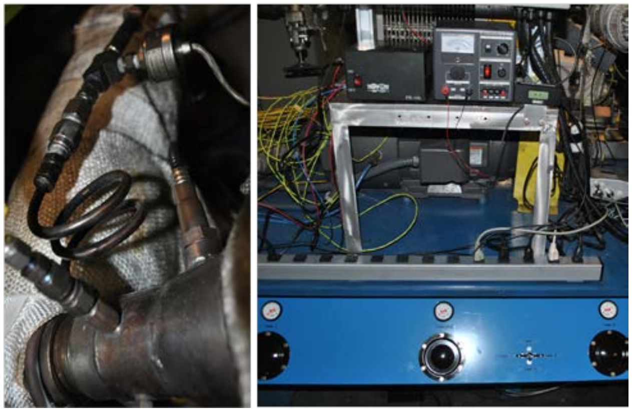

Figure 4. Wideband lambda sensor, pressure transducers and control hardware.

A LabView interface was written to control the engine-out temperature by turning the load bank on and off. When the load bank is on, the generator operates under full-load conditions and the outlet temperature increases. A second control is the fuel pump which injects fuel after the engine but before a diesel oxidation catalyst (DOC) which produces a large exotherm entering the DPF. The temperature within the DPF and at the engine-out, DPF-in and DPF-out locations are measured with thermocouples and recording using the LabView software as shown in Figure 5. Work is nearly complete on enabling the DPF-in temperature to be controlled using a closed loop with the fuel pump speed.

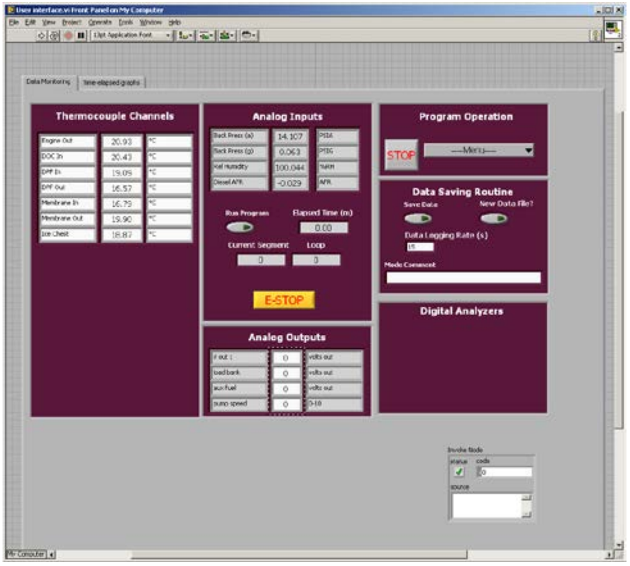

Engine Out	20.93	°C
DOC In	20.43	°C
DPF In	19.05	°C
DPF Out	16.57	°C
Membrane In	16.79	°C
Membrane Out	19.90	°C
Ice Chest	18.87	°C

Back Press (a)	14.107	PSIA
Back Press (g)	0.063	PSIG
Rel Humidity	100.044	%RH
Diesel AFR	-0.029	AFR

Elapsed Time (m) 0.00

Current Segment 0

Loop 0

Data Logging Rate (s) 15

Mode Comment

f out 1	0	volts out
load bank	0	volts out
aux fuel	0	volts out
pump speed	0	0-10

status ✓ code 0

source

Figure 5. Labview interface for controlling stationary generator and reading the system outputs.

A standard test was devised to simulate regeneration of a DPF in a short amount of time and is shown in Figure 6. Thermal cycling of the DPF is done by a combination of generator load and exhaust fuel injection and can reach temperatures up to 1200ºC in a 15 minute cycle. The maximum temperature gradient measured in the DPF approaches ~100°C/inch at the outlet of the DPF between the center and the circumference (see Figure 7). Since typical regeneration occurs every 1,000 miles, this test would simulate 100,000 miles of operation in just one day. Since the generator comes with many built-in safety features, this test can be performed without any personnel present, thereby greatly improving the flexibility of the testing while reducing the cost.

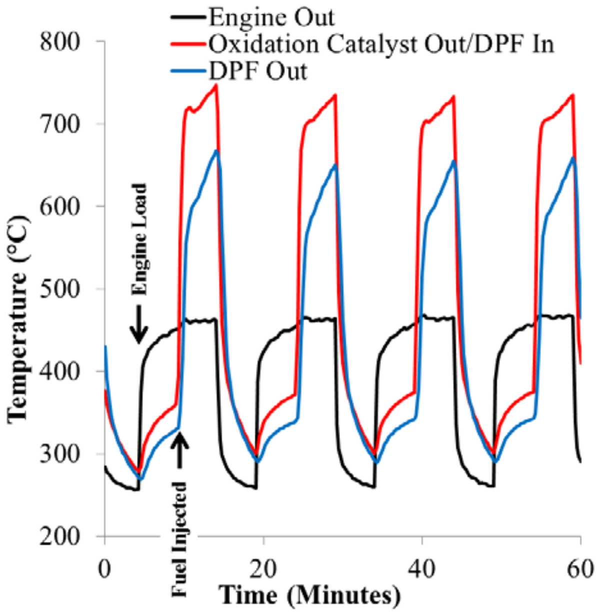

Figure 6. First DPF tested for 106 cycles using the generator and ULSD fuel.

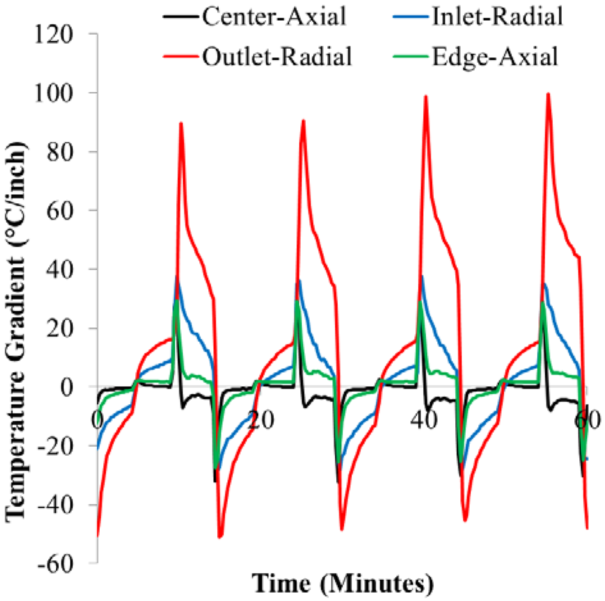

Figure 7. Temperature gradients present in the DPF during operation.

Seventeen 6X8.5 inch cordierite DPFs were donated by Corning for this testing. The as-received DPFs were far too large for the stationary generator to flow adequate exhaust through and so were reduced in size to 5 3X6 inch cylinders (see Figure 8). These DPFs were canned using padding and a clam-shell tube and the temperatures inside the DPF were measured by inserting a thermocouple wire into the outlet side of the DPF. After engine testing, each DPF was further reduced in size using a lathe to 14 1X3 inch specimens that can be used for mechanical properties testing as will be explained below. Therefore, each testing condition results in many specimens which will improve the statistical confidence of the measurements. Also, mechanical properties can be measured axially since seven specimens will come from the inlet half and seven from the outlet half of the DPF.

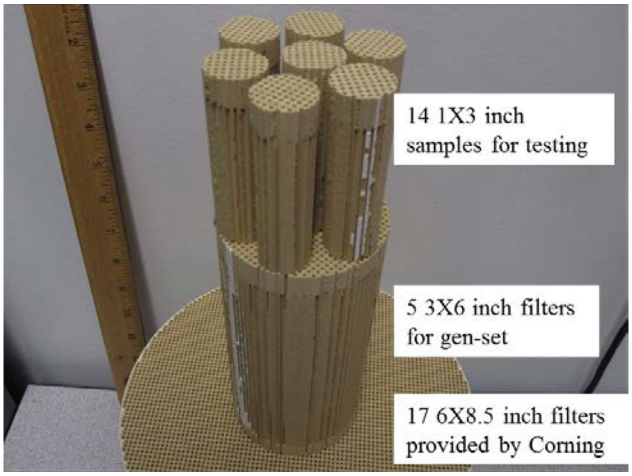

Figure 8. Samples that are used for generator testing and subsequent mechanical properties testing.

Tensile Testing of DPF Specimens

A tensile test method that utilizes the 1X3 inch DPFs from the stationary generator (see Figure 8) has been established. The method is based upon mounting the specimens in epoxy, as shown in Figure 9, allowing them to be readily gripped across the entire DPF surface area on the top and bottom thereby largely solving the gripping problem commonly encountered when testing very brittle materials like these. In addition, there are several advantages to tensile testing over other (bend or compression) test methods. Coupled with the measurement of tensile elongation using contact extensometers, the sought-after tensile testing will enable the measurement of a continuous tensile stress -

tensile strain curve. Such definitive data will allow for the interpretation of non-linear tensile response, and provide critical information on the (continuous or tangent) elastic modulus as a function of tensile strain. Also, the load is applied across a much larger volume of material compared to bending tests which will improve the statistics of the measurements. Finally, the fracture strength is less likely to be controlled by the surface flaws generated during sample machining since the load is applied uniformly through the thickness of the specimen and not with the maximum load just on the surface as with flexural testing.

Figure 9. Tested DPF specimen that has been gripped by embedding both ends in epoxy.

An example of a measured tensile response on an as-received DPF is shown in Figure 10. The non-linear response of the specimen under load compares well to previous measurements conducted using ring-on-ring testing [1]. This phenomenon is due to the microstructure of the DPF which is highly porous and micro-cracked. As load is applied, the micro-cracks will open up thereby reducing the elastic modulus of the DPF as shown in Figure 10.

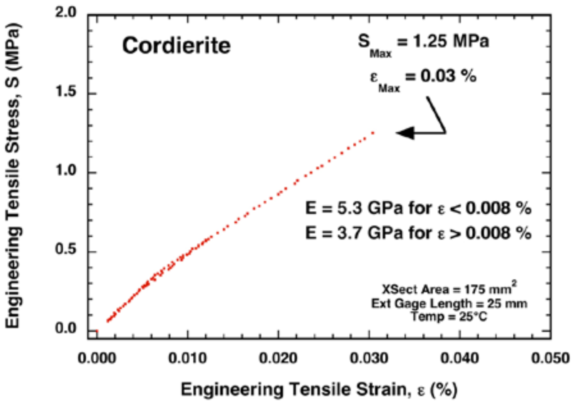

Figure 10. Representative tensile stress-strain curve measured with an as-received cordierite DPF tensile specimen.

The engine testing had the effect of increasing the DPF stiffness as shown in Figure 11. The stiffness increase may be due to sintering that occurs in the DPF while at 700°C however, this is the first measurement from the first engine test so this result in tentative. Testing is proceeding on DPFs run at temperatures approaching 1000°C where a more severe effect on the stiffness and fracture strength is expected.

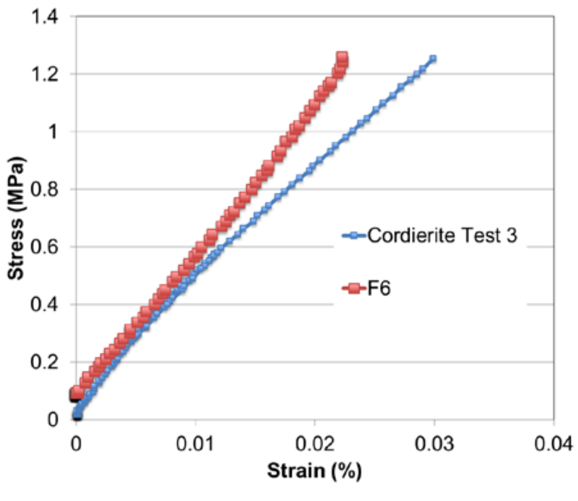

Figure 11. Comparison of the stress-strain curve for an as-received specimen (Cordierite Test 3) and one extracted from the DPF tested in Fig. 6 (F6).

NREL/NBB/MECA/Ford Consortium

SiC DPF samples were acquired from the National Renewable Energy Lab (NREL) which is a member of an industry-led team investigating the effects of biodiesel operation on emission control technologies. NREL is aging full production exhaust systems from a 2011 Ford F250 pickup using four separate fuels: ULSD, B20 + 14 ppm Na, B20 + 14 ppm K and B20 + 14 ppm Ca in order to simulate 150,000 miles of operation using a 100-hr test. The test protocol consisted of a three-mode, one-hour test cycle that was developed for catalyst aging: 15 minutes at 200°C, 15 minutes at 340°C, and 30 minutes at 700°C. Cores were extracted from each DPF and mounted in epoxy in order to analyze the location and composition of the ash produced in this run. SEM images (see Figure 12) and x-ray spectrometry using energy dispersive spectroscopy (EDS) did not reveal penetration of the ash elements into the SiC substrate; however, extraneous material from upstream found its way into the DPF channels including alumino-silicate fibers from the padding and ZrO_2 particles from the diesel oxidation catalyst.

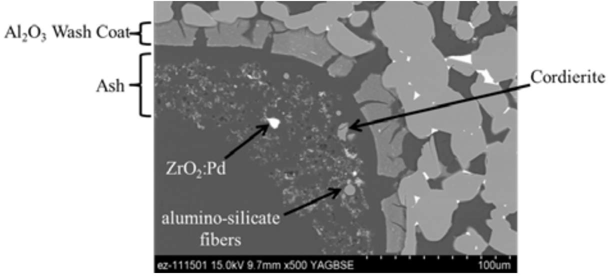

Figure 12. SEM image showing the cross-section of B20 + Na additive sample after simulated 150,000 miles (1 cm from outlet).

For mechanical properties measurements, two parallelepipeds were cut out of each of the four test conditions and a fresh DPF and these were then sliced into tiles for testing. The location of the squares is shown in Figure 13 and an example of a tile before and after testing under biaxial flexure is shown in Figure 14.

Figure 13. Tested SiC DPFs with two parallelepipeds and one core cut out.

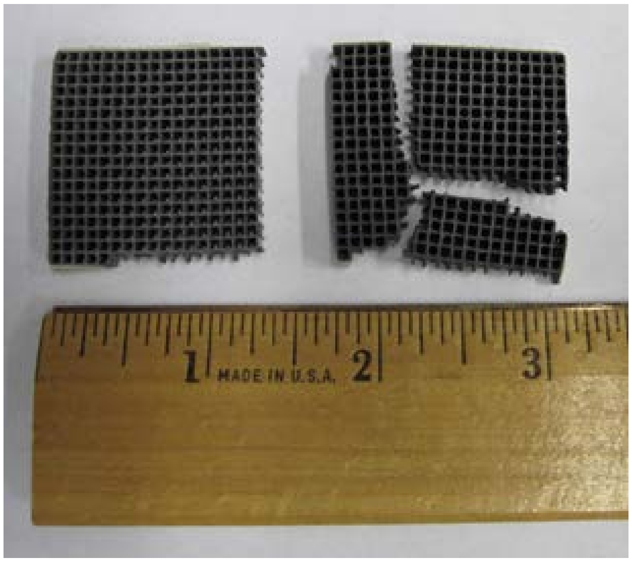

Figure 14. SiC tiles used for testing before (left) and after (right) fracture.

Mechanical testing of DPF specimens was initiated for the estimation of the materials (tensile) failure stress as a function of location in the tested brick. This was done in order to have a measurement of the onset of material degradation in these porous DPF materials which would be difficult to discern using microscopy or other techniques. Elastic modulus estimation of the tested SiC DPF materials are also pursued because knowledge of its accurate value is needed for estimating measured tensile failure stresses. Also, the pure tension testing described above was not employed here because it was still under development when these samples arrived from NREL.

Biaxial flexure testing of the tiles subjects the tensile side of the specimen to an equibiaxial radial tensile stress using a ring-on-ring test fixture (i.e., axisymmetric 4-point-bending). These specimens should always fail from the weakest strut orientation. Such testing is featured in ASTM C1499 [2]. An illustration of how the tiles are mechanically loaded is shown in Figure 15.

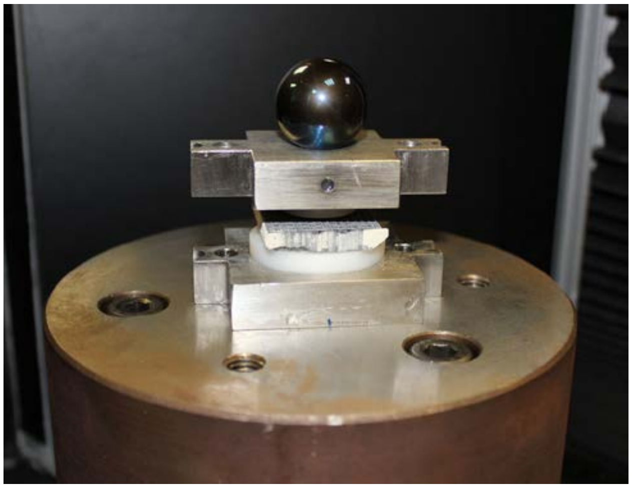

Figure 15. Biaxial flexure test setup for square SiC DPF test coupons.

The estimation of specimen failure stress occurs via the flowchart shown in Fig. 16. Mechanical testing and finite element analysis are combined to achieve this. As with any mechanical-based method of estimating elastic modulus of a test coupon, appropriate reference testing was completed in order to subtract out the effect of machine compliance.

The loading of the tile specimen produces a definitive relationship between compressive force and load-point-displacement. The same loading scenario is then modeled with FEA (enabled thru ORNL's micro-FEA software and the actual capturing of the DPF strut structure) by adjusting the DPF material's elastic modulus until the experimentally measured load-point-displacement matches the measured maximum compressive force. The arrived-at elastic modulus value is what is reported as the material elastic modulus, and is needed for the estimation of failure stress.

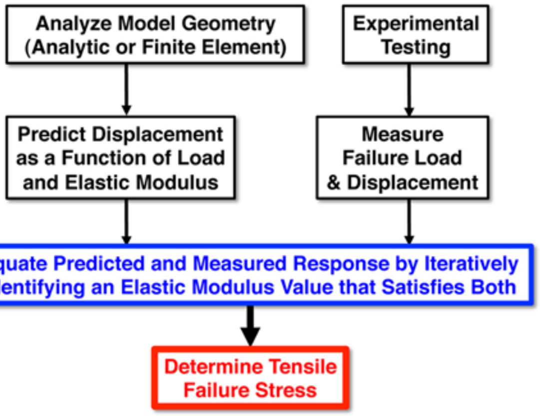

Figure 16. Modeling and experimentation pathway to determine maximum failure stress.

For measurement of material strength, approximately 60 tiles (shown in Figure 14) were extracted down the length of the DPF. These tiles were approximately 30mm square by 3mm thick. 30 of the tiles were taken from the radial center of the DPF while the other 30 were taken closer to the radial edge. The biaxial maximum stress for each of the aged samples is shown in Figure 17. This plot shows the failure stress measured at both the inner and outer radial position on the DPF. The error bars represent one standard deviation based on the 30 individual tiles measured down the length of the DPF. Results indicate that there is no statistically significant difference in the failure stress between any of the aged parts and a fresh sample.

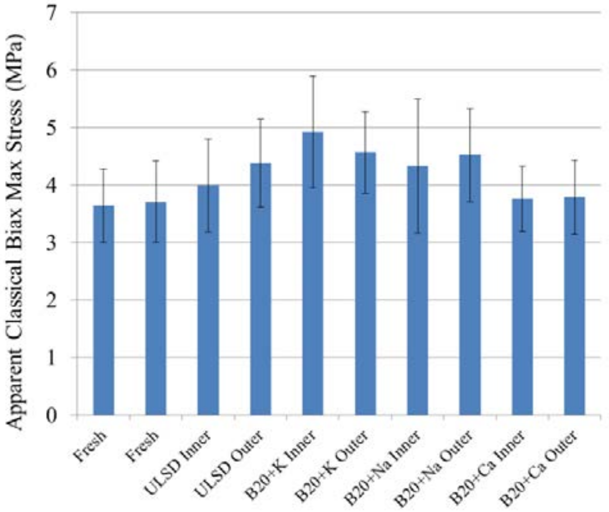

Figure 17. Biaxial maximum stress for aged SiC DPF samples.

Measurement of the coefficient of thermal expansion (CTE) was conducted using a high-temperature dilatometer on one-inch long 3 by 3 channel specimens. A small spring load was applied along the axial direction of the sample and the expansion of the sample was measured. Figure 18 shows the CTE for each of the aged samples as well as a fresh DPF. The CTE for all samples is approximately 4 ppm/°C at 200°C and rises to approximately 5.5 ppm/°C at 800°C. There is no apparent difference in the CTE between any of the aged parts and a fresh sample. These results show that this test did not generate any measurable change in the mechanical properties of the SiC DPF material. A more aggressive test is being conducted now that combines both Na and K impurities in the fuel that is expected to have a greater chance of producing DPF degradation.

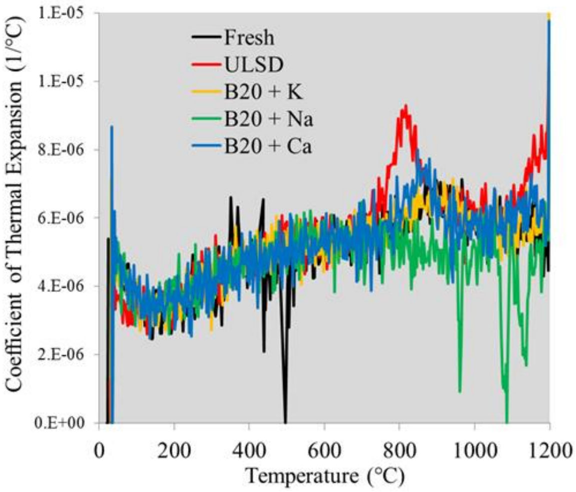

Figure 18. CTE of aged DPF samples

Conclusions

- A stationary generator was installed and modified for DPF material testing using different fuels with 24/7 unattended operation.
- A new mechanical test method based on applying pure tensile load to DPF cylinders through the use of epoxy to grip the DPF was established.
- SiC DPF samples that had been exposed to accelerated testing with biodiesel fuel were tested. No material degradation of the DPF was measured.

References

1. Wereszczak, A., Fox, E., Lance, M., Ferber, M., *Failure Stress and Apparent Elastic Modulus of Diesel Particulate Filter Ceramics.* SAE Technical Paper 2012-01-1252, 2012.
2. *Standard Test Method for Monotonic Equibiaxial Flexural Strength of Advanced Ceramics at Ambient Temperature*, in *ASTM C1499* 2009, ASTM International: West Conshohocken, PA.

Publications and Presentations

- E. E. Fox, A. A. Wereszczak, M. J. Lance, and M. K. Ferber, "Failure Stress and Stiffness Analysis of Ceramic From a 25-mm Diameter Diesel Particulate Filter," proceedings paper submitted to, and presented at, the 36th International Conference and Exposition on Advanced Ceramics and Composites, Daytona Beach, FL, January 23-26, 2012.
- Wereszczak, A., Fox, E., Lance, M., Ferber, M., Failure Stress and Apparent Elastic Modulus of Diesel Particulate Filter Ceramics. SAE Technical Paper 2012-01-1252, 2012.
- A. A. Wereszczak gave a presentation to the C28 Advanced Ceramics Committee on the DPF mechanical test coupons developed in this project, Daytona Beach, FL, January 22, 2012.

Agreement 20091 – Electrically Assisted Diesel Particulate Filter Regeneration

M. J. Lance, J. E. Parks, A. A. Wereszczak, W. P. Partridge,* R. M. Connatser,* V. Y. Prikhodko,**
E. E. Fox, and M. K. Ferber
Ceramic Science and Technology Group
Oak Ridge National Laboratory
P.O. Box 2008, MS 6068, Bldg. 4515
Oak Ridge, TN 37831-6068
(865) 241-4536; fax: (865) 574-6098; e-mail: lancem@ornl.gov
**Fuels, Engines and Emissions Research Center (FEERC), ORNL*

DOE Technology Manager: Jerry L. Gibbs
(202) 586-1182; fax: (202) 586-1600; e-mail: jerry.gibbs@ee.doe.gov
ORNL Technical Advisor: J. Allen Haynes
(865) 576-2894; fax: (865) 574-4913; e-mail: haynesa@ornl.gov

---

Contractor: Oak Ridge National Laboratory, Oak Ridge, Tennessee
Prime Contract No.: DE-AC05-00OR22725

Objectives

Study efficiency benefits and materials issues associated with the electrically-assisted diesel particulate filter (EADPF) device developed by General Motors (GM). This project is divided into three tasks:

Task 1: Fuels, Engines and Emissions Research Center (FEERC)

- Characterize potential fuel savings of the approach and related benefits to other emission control devices.
- Measure gas and substrate temperatures to obtain accurate picture of conditions experienced during regeneration.

Task 2: Ceramic Science and Technology Group (CerSAT)

- Resolve current disconnect between cordierite substrate model predictions and actual substrate durability.
- Use data and results to develop general design rules on heater geometries to optimize substrate durability.

TASK 1

Objectives

- Characterize the potential fuel savings of the electrically-assisted diesel particulate filter (DPF) approach.
- Measure gas and substrate temperatures during DPF regeneration with non-thermally conductive fiber optic based techniques.

Approach

- Measure fuel savings as compared with conventional DPF regeneration techniques with a full-size DPF system on a 1.9-liter GM 4-cylinder diesel engine on an engine dynamometer.
- Measure substrate temperatures with fiber optics via black-body radiation during DPF regeneration.
- Compare temperature measurement history of substrates with materials characterization of substrates (Task 2) to determine failure mechanisms.

Accomplishments

- Demonstrated EADPF reduction of fuel penalty for DPF regeneration of 50% as compared with traditional fuel-only regeneration technique (completed in FY11).
- Measured EADPF substrate temperatures during regeneration with blackbody radiation fiber optic probe technique as a function of particulate loading.

Introduction

Diesel engines operating at lean air-to-fuel ratios are more efficient than gasoline engines which commonly operate at stoichiometric air-to-fuel ratios. While the diesel engine dominates the heavy-duty truck market, the expansion of diesel engines in light-duty truck and passenger car markets has been limited by various factors. One traditional limitation has been emissions or, specifically as addressed here, particulate matter (PM) emissions which are commonly referred to as “soot”.

In order to reduce PM emissions to meet customer expectations and U.S. EPA emissions regulations, diesel engines use an exhaust emission control technology known as the diesel particulate filter (DPF). The DPF is a ceramic (commonly cordierite or SiC) monolithic filter in the exhaust system that filters PM from the entire exhaust stream during normal operation (Figure 1). Periodically, the DPF is cleaned or “regenerated” to oxidize or “burn” the accumulated PM in the filter. The regeneration procedure occurs by raising the temperature of the DPF to approximately 600ºC or higher where the carbon-rich PM readily oxidizes.

Virtually all modern diesel engine vehicles are sold with the DPF technology which is performing well in the field and reducing PM emissions by >95%. However, the current technique for DPF regeneration consumes extra fuel which is oxidized over a diesel oxidation catalyst in the diesel exhaust to heat the DPF to regeneration temperatures. This extra fuel or “fuel penalty” reduces the fuel economy advantage of the diesel engine.

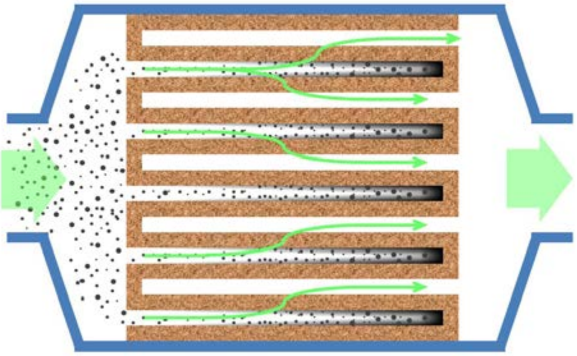

Figure 1. Cross-section schematic of a diesel particulate filter.

General Motors (GM), the CRADA partner for this project, has developed a DPF technology that utilizes electrical power to heat the DPF for regeneration. This technology called Electrically-Assisted Diesel Particulate Filter (EADPF) may greatly reduce the fuel penalty associated with DPF regeneration. In this project Oak Ridge National Laboratory (ORNL) is collaborating with GM to better understand material limitations of the EADPF approach so that the technology can be commercialized and realize fuel savings for diesel engine vehicles. Task 1 of the project focuses on measuring the DPF exposure temperatures in exhaust on a full size engine platform. Task 2 focuses on the material failure mechanisms and accuracy of predictive models to develop temperature-specific design rules.

Results

During FY11 studies, the EADPF system was operated on a GM 1.9-liter 4-cylinder diesel engine, and the EADPF technology demonstrated a 50% reduction in the fuel penalty associated with regeneration in comparison to the traditional fuel-based DPF regeneration technique. The EADPF approach also demonstrated a 60% reduction in the time required for regeneration.

In FY12, the focus of the engine-based studies changed to measurement of the DPF cordierite substrate temperature during the regeneration process. A technique for measuring the substrate temperature was developed based on blackbody radiation emitted from the hot walls of the cordierite. Specially designed angle-tipped fiber optic probes inserted into the downstream flow channels of the DPF substrate enabled collection of blackbody radiation from the substrate walls (Figure 2). The collected light spectra were analyzed to determine the temperature of the substrate at various probe locations in the DPF. In adjacent flow channels, type K thermocouples measured gas temperatures at similar positions along the flow axis.

In comparing the substrate temperatures measured with the blackbody radiation technique to the gas temperatures measured with the thermocouples, a small (10-30°C) temperature difference was observed with the substrate temperatures being slightly higher. A more dominant effect occurred due to the amount of PM loaded on the DPF at the start of regeneration. Exothermic heating of the substrate from PM oxidation along the flow axis of the DPF substrate caused a thermal wave to traverse the substrate during regeneration. The measured peak temperatures increased with increasing PM load (Figure 3). The peak temperatures also grew along the flow axis with the downstream end of the DPF experiencing the highest peak temperatures.

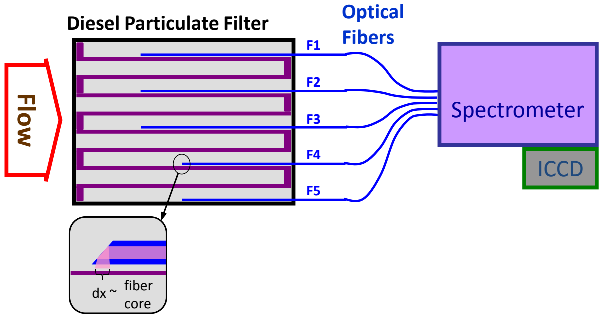

Figure 2. Schematic of the fiber optic probes applied to the DPF substrate to measure temperature via collection and analysis of blackbody radiation spectra.

Relative to the durability and risk of fracture of the cordierite substrate, the parameter with the strongest effect on durability is the PM loading at the beginning of regeneration. While PM on the DPF benefits the process by providing a heat source during oxidation, excess PM can lead to excessively high substrate temperatures especially at the downstream portion of the substrate. Thus, control and accurate prediction or measure of the PM loading during EADPF operation is a critical need for successful operation.

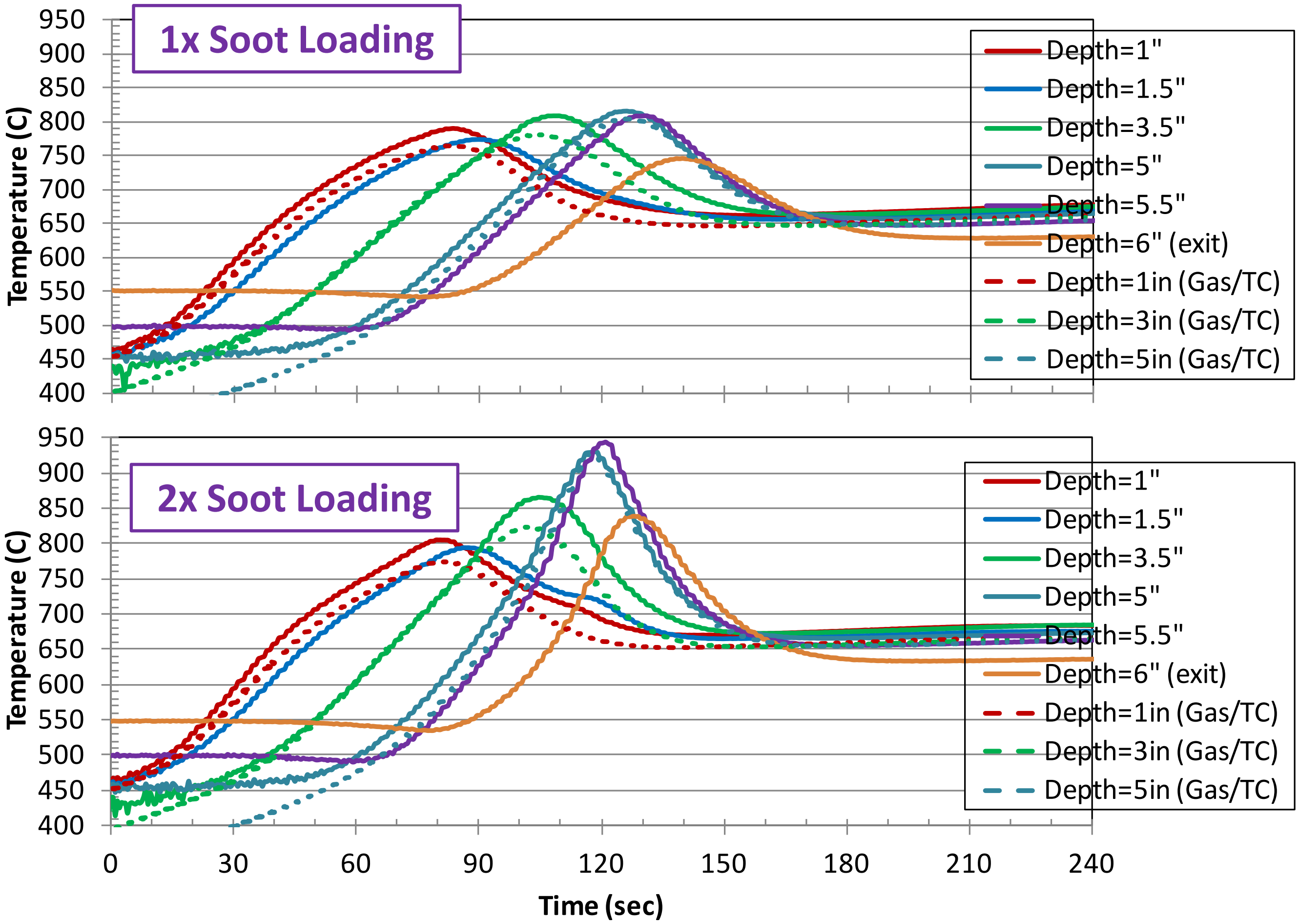

Figure 3. Substrate (solid lines) and gas (dashed lines) temperatures measured at different depths along the flow axis of the DPF substrate during regeneration. Results are shown with two different soot loadings with the bottom plot data representing twice the loading of the top plot. The highest temperatures occur at the downstream portion of the DPF due to exothermic release of heat from the soot oxidation process along the DPF.

Conclusions

The EADPF technology offers a 50% reduction in the fuel required to regenerate a DPF based on engine studies. Measurements of substrate temperatures during regeneration were successful and showed a 10-30ºC higher temperature than gas temperatures measured with thermocouples. However, the dominant parameter affecting DPF substrate temperature is the amount of PM loaded on the DPF at the regeneration start. Excessive PM leads to exothermic energy release during oxidation that can result in exceeding substrate temperature limits in the downstream portion of the DPF.

TASK 2

Objectives

- Separately measure the elastic properties of the skin and interior cordierite materials in DPFs.
- Develop empirical equations that facilitate the acceptance of using the herein described mechanical test methods within the DPF manufacturing and end-user communities.
- Develop general rules of DPF design. Heater designs are corporate sensitive to General Motors and are protected under the CRADA, so

specifics about their designs and resulting stresses cannot be divulged in this publicly-available final report.

Approach

- Use previously measured elastic properties and failure stress results from the use of alternative test coupons as input in finite element analysis (FEA) of a DPF subjected to an arbitrary regeneration cycle.
- Compare different zone heating arrangements in FEA and determine maximum (First Principal) tensile stress.
- Make recommendations of which zone heating arrangements produce the minimum tensile stresses.

Accomplishments

- Made recommendations to General Motors about suggested zone heating arrangements for DPF regeneration.
- Completed Final CRADA report.

Future Direction

None. Project ceased at end of FY12.

Introduction

Diesel particulate filter (DPF) technology enables the fuel efficient diesel engine to meet emission regulations for particulate matter. The DPF collects particulate from the exhaust stream during operation. It then is periodically regenerated by increasing its temperature to between 600 and 1000ºC (see Figure 3). This causes the carbon-containing trapped particulate to oxidize and form gaseous CO_2 enabling continued filtration at a lower backpressure. But the regeneration causes thermal gradients in the brittle ceramic which can be problematic.

Two lifetime-limiting consequences of overly severe thermal gradients are crack initiation and propagation. The formation and existence of such cracks can compromise the intended filtering function of the DPF and ultimately result in their need for replacement. Therefore, the end-user has interest in managing the operating conditions so the DPF successfully fulfills its purpose without initiating those cracks.

Two criteria must be satisfied in tandem to promote and achieve maximum service lifetimes in DPFs under severe operating conditions. The ceramic comprising the DPF must have sufficiently high tensile strength and the tensile stresses (such as those caused by operating thermal conditions) must be sufficiently low. Obviously, if the anticipated operating conditions produce high tensile stresses, then a stronger DPF should be considered for use. Otherwise, if the only available candidate DPF ceramics have a limited tensile strength, then the operating conditions need to be restrained so that overly-high tensile stresses do not arise. In either circumstance, the understandings of both the DPF ceramic strength and the DPF service conditions are needed to successfully employ a DPF.

Results

In an attempt to confirm this project's earlier reporting of the DPF cordierite having an elastic modulus of approximately 1-2 GPa (measured with biaxial flexure, sectored flexure, and o-ring compression testing), thin test coupons of isolated cordierite were carefully harvested out of DPFs and then loaded in three point bending. These specimens were very fragile so care was taken to cause sufficient bending prior to their fracture. The three-point-loading enabled the use of classical beam bending analysis with measurement of the applied compressive force and corresponding load-point-deflection. An elastic modulus of approximately 1 GPa was representative of that force-deflection bending response, and that is consistent with the authors' earlier reported values. This provided additional confirmation that this elastic modulus of about 1 GPa is an accurate portrayal of DPF cordierite stiffness, and that resonance-based values of elastic modulus (about an order of magnitude larger) are misleadingly high.

Much of this project's technical work from FY11 was disseminated at several conferences during FY12. Their content generated a lot of discussion with the attendees. A poster was presented at the 17th Directions in Engine-Efficiency and Emissions Research (DEER) Conference in October 2011. A presentation and companion conference paper were given at the 2012 International Conference on Advanced Ceramics and Composites in January 2012. Lastly, a presentation and companion paper were given at the 2012 SAE Conference in April 2012.

A substantial amount of FEA was executed in FY12 on candidate regeneration heater designs. It incorporated lower valued elastic modulus data measured in this project, and described in the FY11 Annual Report, with several different regeneration heater designs. The potential heater designs are corporate sensitive to General Motors and are protected under the CRADA, so specifics about their designs and resulting stresses cannot be divulged here.

Conclusions

The use of a lower valued elastic modulus, consistently and repeatedly measured in this project, ultimately affects the potential regeneration heater design of a DPF.

Publications and Presentations

- E. E. Fox, A. A. Wereszczak, M. J. Lance, and M. K. Ferber, “Failure Stress and Stiffness Analysis of Ceramic From a 25-mm Diameter Diesel Particulate Filter,” proceedings paper submitted to, and presented at, the 36th International Conference and Exposition on Advanced Ceramics and Composites, Daytona Beach, FL, January 23-26, 2012.
- Wereszczak, A., Fox, E., Lance, M., Ferber, M., Failure Stress and Apparent Elastic Modulus of Diesel Particulate Filter Ceramics. SAE Technical Paper 2012-01-1252, 2012.

Project 18865 – Application Specific Materials Simulation, Characterization and Synthesis

Agreement 9105 - Ultra-High Resolution Electron Microscopy for Characterization of Catalyst Microstructures and Reaction Mechanisms

L. F. Allard, W. C. Bigelow, M. B. Katz,* X-Q. Pan,* G. Graham,*** A. Drews,** D. P. Nackashi,*** J. Damiano****
Oak Ridge National Laboratory
P.O. Box 2008, MS-6064
Oak Ridge, TN 37831-6064
** Materials Science & Technology, University of Michigan, Ann Arbor, MI*
*** Ford Research Laboratory, Dearborn, MI*
**** Protochips Inc., Raleigh, NC*

DOE Technology Manager: Jerry L. Gibbs
(202) 586-1182; fax: (202) 586-1600; e-mail: jerry.gibbs@ee.doe.gov
ORNL Technical Advisor: J. Allen Haynes
(865) 576-2894; fax: (865) 574-4913; e-mail: haynesa@ornl.gov

---

Contractor: Oak Ridge National Laboratory, Oak Ridge, Tennessee
Contract No.: DE-AC05-00OR22725

Objectives

- Develop and utilize new *in situ* techniques for ultra-high resolution imaging of catalytic materials in gaseous environments to study reduction of NOx emissions in diesel and automotive exhaust systems.

Approach

- Partner with Protochips Co. to expand capabilities for *in situ* reaction studies with unique gas-cell reactor system for the aberration-corrected electron microscope.
- Utilize Gen 3 gas-cell holder for atomic imaging of catalysts at elevated temperatures and gas pressures up to a full atmosphere, particularly in studies of “self-regenerating” catalysts for emissions reduction in partnership with Ford Research Laboratory and the University of Michigan.

Accomplishments

- Capabilities with the “Gen 3” gas-cell reactor were expanded by modifications to the gas control manifold to permit gas flow through the cell, and gas flow experiments showed that flow in the cell could be characterized accurately to be within the “viscous, laminar flow” regime. Capillaries on the Return side of the cell can be used to control flow conditions to replicate “real world” reactions.
- *In situ* reaction studies of Pt and Rh-doped perovskite self-regenerating catalysts added to the understanding of the behavior of the catalytic species during sequential redox reactions, and correlated well to prior bench-top reaction studies.
- Our past work on the notion of “single-atom catalysis” on which we have collaborated with several groups both nationally and internationally has been further highlighted by several presentations and publications during this FY. Insufficient funding precluded continuation of these studies to a large extent.

Future Directions

- Complete the studies of perovskite-based NOx reduction “self-regenerating” catalysts, including Pd in $LaFeO_3$ and $BaCeO_3$, and Rh/Pt in $CaTiO_3$.
- Introduce a new “Gen 4” gas-cell reactor specimen holder comprising a number of advanced design improvements over the Gen 3 gas-cell, including MEMS-fabricated heater devices with an improved design and better control of artifact structures than were present on the Gen 3 heaters.

Introduction

Our research this year concentrated on utilization of the *in situ* gas cell holder for the JEOL 2200FS aberration-corrected electron microscope for concentrated studies of perovskite-based "self-regenerating" catalysts (formerly called "intelligent catalysts") aimed at reduction of NO_x emissions in automotive engine systems. We also expanded the capabilities of the gas-cell holder to allow flowing gas under controlled conditions that replicate "real world" tests using bench-top reactor systems with bulk volumes of catalytic material. Details of both these thrust directions are described in the following.

In Situ Microscopy Development:

Our gas manifold control system was modified as shown in the schematic of **Fig. 1**. A stainless steel "Return" cylinder was added to the system, with appropriate valving to allow the cylinder to be evacuated by the scroll pump, and then to permit gas flow through a return line from the capillary that exits the Return side of the holder into the new cylinder. In order to control the gas Supply to the holder at higher pressures (up to at least a full atmosphere), a new Baratron capacitance manometer was added to the Supply cylinder, as shown in the schematic. Front views of the gas manifold "before and after" the modifications are shown in **Fig. 2**; the second Baratron gauge controller is shown on the top of the manifold. Details of the capillary arrangement inside the "clamshell" cover for the specimen holder, mounted on the side of the microscope column, are shown in **Fig. 3**. The primary consideration is the use of capillary tubing on the Return side of the holder that is smaller than that on the Supply side. The reason for this is that we calculated that the gas flow behavior should follow that as described by the Poiseuille equation for viscous, laminar flow [1], which shows that flow rates are controlled by the fourth power of the relative diameters of the Supply and Return capillaries. In the example of Fig. 3, with equal lengths of capillaries, the gas flow through a 50-micron Return capillary supplied by a 175-micron Supply capillary will be lower by a factor of $(50/175)^4$, or a factor of 0.0067. The additional advantage of this geometry is that the pressure inside the cell with the 50-micron Return capillary is calculated to be 99.7% of the pressure in the Supply cylinder, whereas if a 175-micron Return capillary were used, in addition to a very much greater flow rate (given in units of Torr-liters per second), the pressure in the cell would be only 0.707 of the pressure in the Supply cylinder. Many experiments with flow at different Supply pressures into the Return tank through 3 different capillary sizes were conducted, using the set-up shown in **Fig. 4**. An example result of the tests, with a 50 micron Return capillary (PEEK tubing) and an initial Supply pressure of 300 Torr flowing into a nominal zero Torr Return cylinder is shown in **Fig. 5**. The match between computed and measured flow rates is evident (see **Table 1**), confirming the utility of the Poiseuille equation for the viscous, laminar flow that prevails in our experiment.

Based on all our experiments, we are now confident that we can set up virtually any experimental condition (pressure, flow rate and temperature) inside the gas cell that can be reasonably related to real world experimental conditions. For example, by controlling the pressure in the Return cylinder relative to the pressure in the Supply cylinder, the flow rate can be varied over a full order of magnitude. At a Supply pressure of 600 Torr, with zero Torr in the Return cylinder the flow through a 50-micron capillary is 4.64×10^{-4} T-L/sec, whereas setting the Return pressure at 570 Torr reduces the flow to 0.45×10^{-4} T-L/sec. Similar conditions prevail when the Supply pressures are above 100 Torr, but to date we have not looked carefully at the low-pressure regime since we are primarily interested in catalyst reactions at higher pressures that mimic conditions of use of typical automotive catalysts.

This is a powerful advantage of our *in situ* gas reaction system, relative to the systems used with "environmental" TEMs; the E-TEM is

limited to pressures during gas reactions of 10 Torr or below, since the sample is not contained in an enclosed gas cell. Pressures in the region of the specimen have to be limited in order not to compromise the operating pressure of the electron optical column. So we are confident that our present gas-cell holder technology offers a significant and unique advantage over other competing characterization technologies to support catalyst materials research programs.

In Situ Reaction Studies of Self-Regenerating Catalysts:

Our collaboration with the University of Michigan and Ford Scientific Laboratory colleagues on studies of perovskite-based self-regenerating catalysts progressed significantly this year. Materials studied included Pt on barium cerate (Pt-BCO), and both Pt and Rh on calcium titanate (Pt-CTO and Rh-CTO). The catalytic species were all substituted for either Ce or Ti in the perovskite lattices at the 0.05 atom% level in the samples (e.g. $CaTi_{0.95}$ $Pt_{0.05}O_3$). These materials are prospective self-regenerative automotive catalysts aimed at retaining precious metal dispersion more robustly than current automotive catalyst formulations.

A number of examples of the results of reactions conducted with the Gen 3 gas cell have been reported in earlier quarters. A caveat on that early work is that we had not been able to fully characterize the temperature behavior of the heater devices when assembled into a full gas cell geometry. Devices are calibrated by Protochips Co. using a small vacuum chamber and a set of infra-red cameras (one for the low-temperature regime, and one for temperatures of 600°C to 1200°C). So calibrations can be conducted either in a vacuum, or with the chamber filled with a given gas at different pressures. Heater devices used in our present work were typically calibrated in vacuum and at pressures of 50, 100, and 500 Torr, and it was shown that the current required for heating to a given temperature increased markedly in the first 100 Torr of gas pressure, then leveled off so that at 500 Torr, the current required was only a few percent (see details e.g. Publications #1). Since in the gas cell the outside of the heater device is in a vacuum environment, while the interior of the cell sees gas at a given pressure, we presumed that the heater behavior would be somewhere in the range between the vacuum calibration and the “at-pressure” calibration (half-way between the two curves seemed a reasonable assumption). However, our experience with the behavior of the catalyst in vacuum at a “known” temperature, and then with the behavior in the gas cell at a “presumed known” temperature suggested that we were actually likely to be at a significantly higher temperature for our high-pressure, high-temperature trials than desired. Accordingly, we undertook to further understand the temperature behavior by measuring the voltage and the resistance of the heater device, as the current through the heater membrane was varied over a range of mA that from RT to 500°C (relative to the vacuum calibration). We found that there was a small offset in resistance and voltage for pressures in the cell of 300 Torr and above, but not to the extent experienced with the heater membrane calibrated fully in a gas environment in the test chamber. Furthermore, there was essentially zero change in the voltage-resistance measurements with the gas allowed to flow through the cell, a totally unexpected result.

Our conclusion was that in future experiments we would use the vacuum calibration for current vs temperature, with only a small percentage offset for the presence of the gas in the cell. A final determination of the temperature behavior of devices in the gas cell will be made by direct calibration in the Protochips facility using their calibration station. Results of those calibration experiments will be reported in the next quarterly.

Results from the latest *in situ* reaction experiments are shown in the following figures. **Figure 6** is a High-Angle Annular Dark-Field (HAADF) and bright-field (BF) image pair at low magnification, showing the dispersion of Pt-CTO catalyst aggregates on a SiN film supported over a 6-micron hole in a heater membrane. The higher average atomic number of the catalyst support relative to the SiN film causes the catalyst material to appear in bright contrast in the HAADF image. The uniform distribution of fine features in the SiN film is simply an artifact structure in which the SiN material is slightly thicker than the base film. Shown in **Figs. 7 and 8** are low magnification and high magnification image sets of the same particles at various stages of *in situ* processing over a full redox cycle. The metal comes out of solution upon reduction, and strongly interacts with the perovskite support upon re-oxidation, partially re-dissolving into the support. *In situ* testing is crucial to understanding the dynamics of this reaction because gas flow and temperature conditions can be altered in real time based on morphological observations, whereas *ex situ* post-mortem observations miss important but transitory effects.

Coming developments:

While not yet ready for commercialization, our continued development of the “closed-cell” reactor technology for *in situ* electron microscopy of catalytic materials offers promising capabilities for understanding the behavior of catalysts during “real-world” reaction experiments. The expectation of the “Gen 4” reactor holder soon to be available from Protochips Co., and an improved design of heater devices will give further advantage to our experimental capabilities. The new holder and new devices are scheduled for fabrication so that delivery is expected before the end of the year. Changes in the heater device geometry, for example, are shown in **Fig. 9**; the original devices typically were fabricated with a 7 x 7 or 5 x 5 array of 6-micron holes in the ceramic heater membrane, with a nominal 30 micron thick amorphous SiN film over the holes to support the catalyst material and to seal the gas inside the cell. **Figure 9a** shows the CAD drawing of the new device, with comparison enlargements of the membrane hole pattern in the Gen 3 vs Gen 4 devices shown in **Fig. 9b,c**. The holes in the Gen 4 device are slightly larger at 8 microns diameter (center hole of 10 microns), which we believe will expedite the pre-calibration inspection in the SEM that we typically have to do to qualify a device for further use. In addition, the new devices will be prepared with thinner SiN films (~20 nm) to allow even better imaging capabilities.

Comment on “single-atom catalysis” studies:

Over the past 3 years, we have developed collaborations with several groups that have pursued the notion of the ability of single atoms to catalyze certain reactions, such as the water-gas-shift reaction for hydrogen production, and the CO oxidation reaction. In a recent paper [Ref. 1], Sir John M. Thomas, one of the most renowned catalytic chemists in the world highlighted our work on Pt/alumina, conducted with PNNL colleagues, originally published in Science (Ref. 2), and we have subsequently shown additional examples with other groups, such as the unambiguous demonstration that single atoms of Pt on Fe_2O_3 supports are better for CO oxidation reactions than any current commercial catalyst, published in Nature Chemistry [Ref.3]. Publications/ Presentations numbers 4-10 below were generated during FY12, based on work over the past 2 years. Funding has limited the scope of further pursuit of this exciting new area of catalytic chemistry, with the exception of our continuing activities with C. Narula and colleagues at ORNL.

Concluding Remarks:

We have continued to make significant progress in our capabilities for studies of catalyst reaction mechanisms at elevated temperatures under selected gaseous environments, utilizing the unique MEMS-based heating technology offered by our collaborator, Protochips Inc. Adding the capability to flow gases through the gas-cell specimen holder for the JEOL 2200FS ACEM, and the demonstration of the ability to image at the atomic level even at pressures of a full atmosphere in the cell, allows electron microscopy studies to accurately mimic the conditions achieved in bench-top reactor. We emphasize that *this is the only technology in the field that combines these features*; competitive instrumentation involving the use of dedicated environmental electron microscopes cannot achieve comparable experimental conditions (e.g. pressures no higher than about 10 Torr under heating conditions are achievable in such microscopes).

References:

1. John Meurig Thomas, Zineb Saghi, Pratibha L. Gai; "Can a Single Atom Serve as the Active Site in Some Heterogeneous Catalysts?", Topics in Catal (2011) **54**:588–594.

2. Ja Hun Kwak, Jianzhi Hu, Donghai Mei, Cheol-Woo Yi, Do Heui Kim, Charles H.F. Peden, **Lawrence F. Allard** and Janos Szanyi; "Co-ordinatively Unsaturated Al^{3+} Centers as Binding Sites for Active Catalyst Phases of Platinum on γ-Al_2O_3," *Science*, 25 September 2009, **Vol 325**, Issue 5948, 1670-73.

3. B. Qiao, A. Wang, X. Yang, **L.F. Allard**, Z. Jiang, Y. Cui, J. Liu, J. Li and T. Zhang, "Single-atom catalysis of CO oxidation using Pt1/FeOx," *Nature Chemistry*, **Vol. 3**, August 2011, pp. 634-641.

Publications and Presentations FY2011:

1. "Novel MEMS-based Gas-Cell/Heating Specimen Holder Provides Advanced Imaging Capabilities for *In Situ* Reaction Studies," **L. F. Allard**, S. H. Overbury, W. C. Bigelow, M. B. Katz, D. P. Nackashi and J. Damiano; Microsc. Microanal. **18**, 656–666, 2012

2. "Innovative Closed-Cell Reactor Permits *In Situ* Heating and Gas Reactions with Atomic Resolution at Atmospheric Pressure," L.F. Allard, S.H. Overbury, M.B. Katz, W.C. Bigelow, D.P Nackashi and J. Damiano; Microsc. Microanal. 18 (Suppl 2), 2012, 1118-19.

3. "*In Situ* Observation of the Evolution of Pt Particles in a Perovskite-Based Catalyst During Redox Cycling at High Temperature and Atmospheric Pressure with Atomic Resolution," M.B. Katz, **L.F. Allard**, Y.W. Duan, G.W. Graham and X.Q. Pan; *Microsc. Microanal.* **18** (Suppl 2), 2012, 112-13.

4. "Behavior of Pt Atoms on Oxide Supports During Reduction Treatments at Elevated Temperatures, Characterized by Aberration-Corrected Stem Imaging," Steven A. Bradley, Wharton Sinkler, Douglas A. Blom, Wilbur Bigelow, Paul M. Voyles and **Lawrence F. Allard**; *Catalysis Letters* , 142 (2012), 176-182, doi: 10.1007/s10562-011-0756-2

5. "Behavior of Pt clusters during reduction treatments at elevated temperatures, characterized by aberration-corrected STEM imaging and EXAFS;" S.A. Bradley, S.R. Bare, S.D. Kelly, S.I. Sanchez, W. Sinkler and **L.F. Allard**, 15th International Conference on Catalysis, *Munich, Germany, July 2012.*

6. "Design of a Highly Active Ir/Fe(OH)*x* Catalyst: Versatile Application of Pt-Group Metals for the Preferential Oxidation of Carbon Monoxide;" Jian Lin, Botao Qiao, Jingyue Liu, Yanqiang Huang, Aiqin Wang, Lin Li, Wansheng Zhang, **Lawrence F. Allard**, Xiaodong Wang, Tao Zhang, *Angewandte Chemie*, **124**(12), 2974–2978, March 19, 2012

7. "Single-Atom Catalysis: Pt1/FeOx for CO Oxidation and Preferential Oxidation of CO in H_2;" B. Qiao, A. Wang, X. Yang, **L. F. Allard**, Z. Jiang, Y. Cui, J. Li, T. Zhang and J. Liu, *Microsc. Microanal.* **18** (Suppl 2), 2012, 35 doi:10.1017/S1431927612003601

8. "Single-atom catalysis: CO oxidation on single Pt atoms supported on θ-alumina;" Chaitanya K. Narula;" **Lawrence F. Allard**, Melanie M. DeBusk, David R. Mullins, G. Malcolm Stocks, Xiaofan Yang, Mina Yoon, and Zili Wu, *ACS 2012*, Philadelphia, PA, August 2012.

9. "Catalysis by Isolated Single Atoms of Palladium;" Eric Peterson, Andrew DeLaRiva, Abhaya Datye, Ja Hun Kwak, Charles H F Peden, Jeffrey Miller and **Lawrence F. Allard***;15th International Conference on Catalysis,* Munich, Germany, July 2012.

10. “Single-atom-catalysis: the concept, catalyst design and applications;” A. Wang, B. Qiao,; **L.F. Allard**, J. Li, J. Liu, T. Zhang, *15th International Conference on Catalysis*, Munich, Germany, July 2012.

Communications and Visits:

Larry Allard has developed a new association with BASF Co. (Islip, NJ) and, through an initial Work-for-Others (WFO) project funded by BASF has successfully completed analysis of an experimental catalyst material. BASF contact person was Dr. George Munzing. New work is presently being planned with other researchers at BASF.

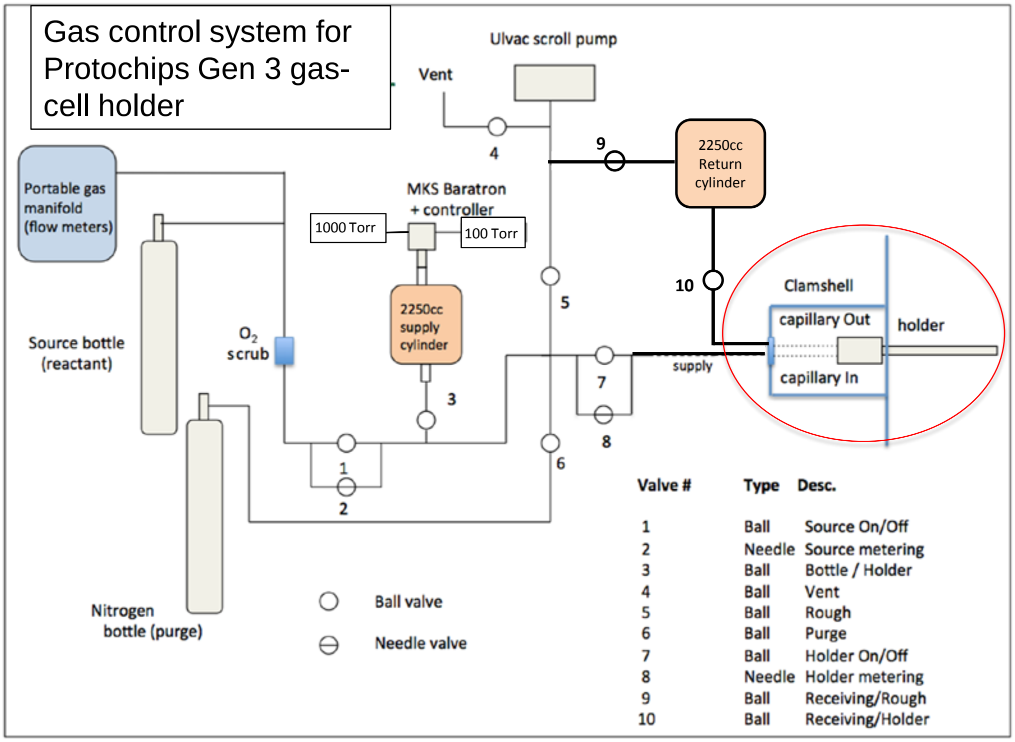

Valve #	Type	Desc.
1	Ball	Source On/Off
2	Needle	Source metering
3	Ball	Bottle / Holder
4	Ball	Vent
5	Ball	Rough
6	Ball	Purge
7	Ball	Holder On/Off
8	Needle	Holder metering
9	Ball	Receiving/Rough
10	Ball	Receiving/Holder

Fig. 1. Schematic showing new features of gas-handing manifold for in situ gas-cell holder; system modified to allow gas flow through holder. Details of clamshell gas lines shown in Fig. 3.

Fig. 2. Before (a) and after (b) views of gas manifold, showing Baratron gauge added on Supply tank to permit precise control of higher pressures, and added Receiving tank (circled) to permit gas flow through Return capillaries, per Fig. 3.

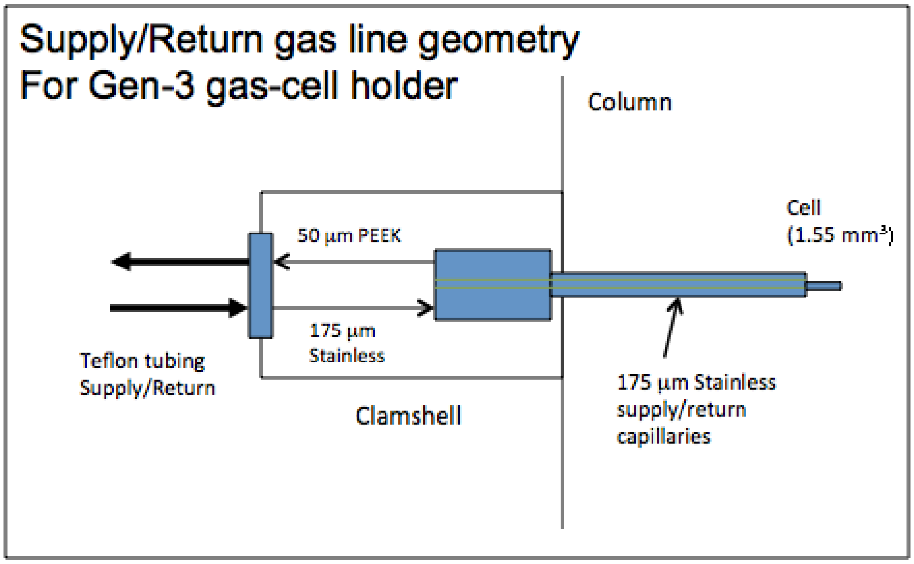

Fig. 3. Details of the gas capillary supply and return lines inside clamshell, and inside reactor holder are shown. See text for details.

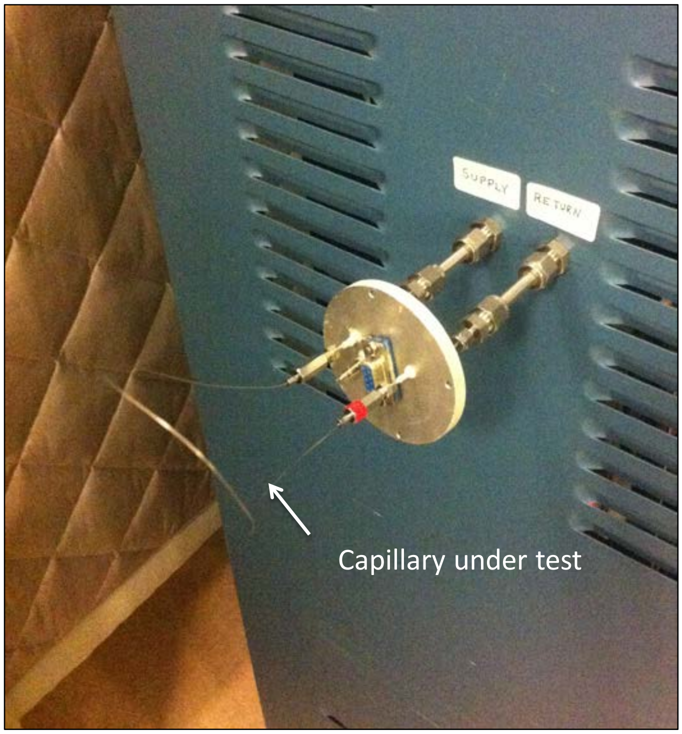

Fig. 4. Gas flow through capillary tubing was tested by direct loop to supply and return ports on gas-handling manifold.

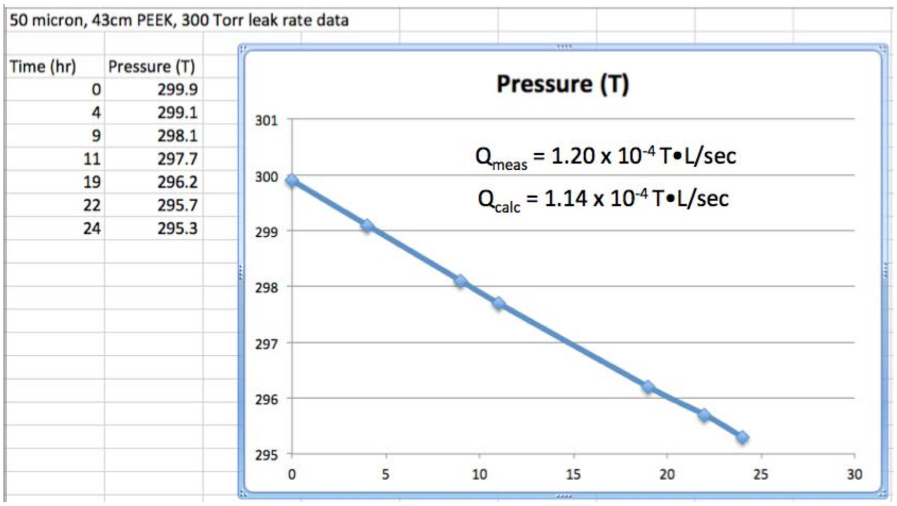

50 micron, 43cm PEEK, 300 Torr leak rate data

Time (hr)	Pressure (T)
0	299.9
4	299.1
9	298.1
11	297.7
19	296.2
22	295.7
24	295.3

$$Q_{(T \bullet L/sec)} = 88.9\, d^4 \bullet (p_{av})^2 \bullet \frac{\Delta p_{S\text{-}R}}{L}$$

Fig. 5. Example of flow measurement through 50-micron capillary at a supply pressure of 300 Torr, showing good agreement between experimental and calculated flow rates for viscous, laminar flow conditions.

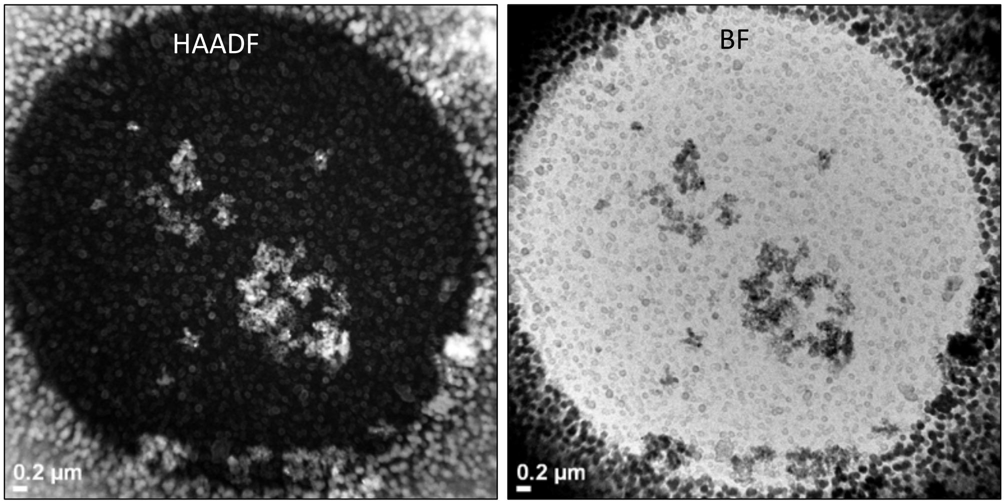

Fig. 6. HAADF and BF images of a typical area of SiN film over hole in heater membrane with Pt-CTO catalyst aggregates deposited. CTO particles show in bright contrast in the HAADF image. Some artifact structures are visible as fine details in the BF image; these features are also SiN and do not affect results.

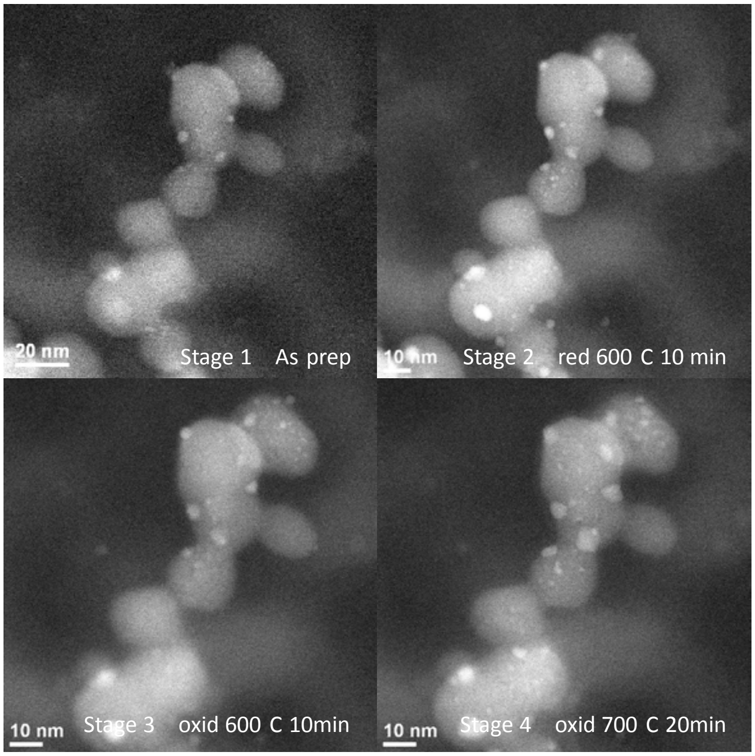

Fig. 7. Low-magnification HAADF images of redox sequence at 600 Torr, showing development of Pt nanoparticles during reduction, and some growth during oxidation cycle. See text for details.

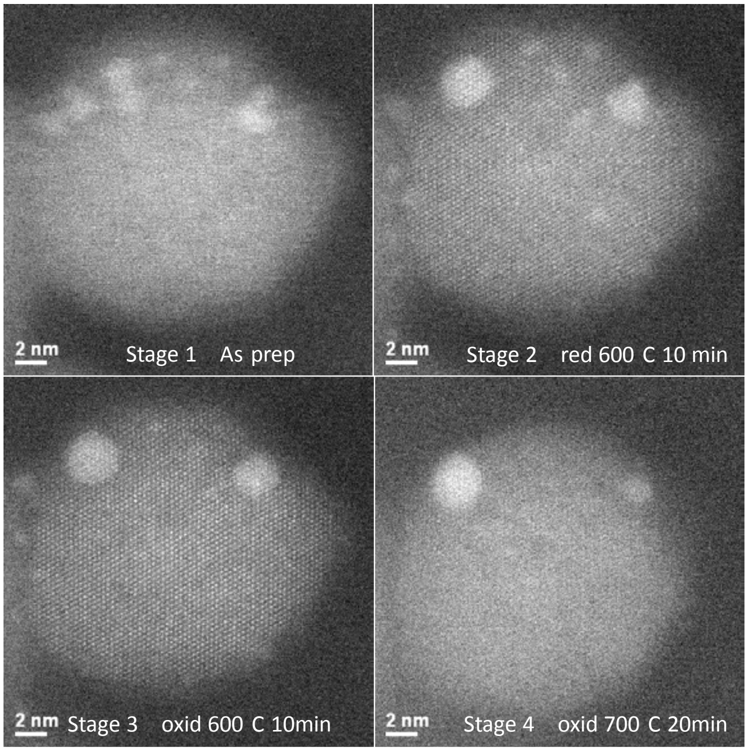

Fig. 8. High-magnification HAADF images of redox sequence at 600 Torr, showing development of nanoparticles during reduction, and limited dissolution during oxidation cycle. Note atomic lattice in Stage 2 and 3 images. See text for details.

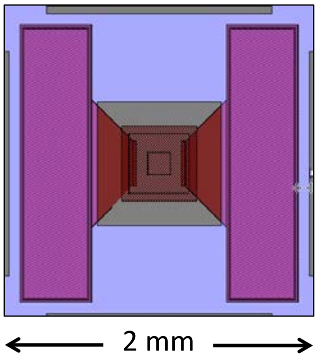

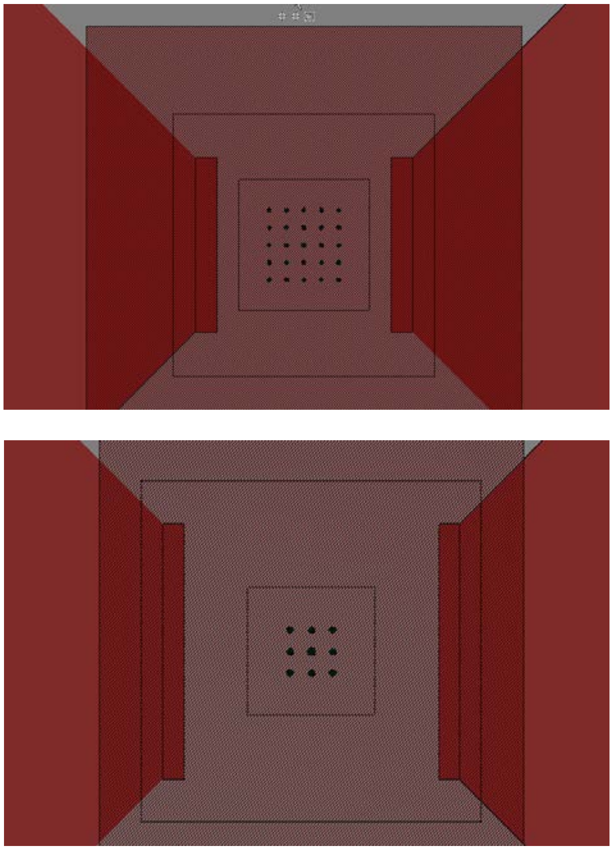

Fig. 9. CAD schematic of Gen 4 device; Gen 3 devices were typically fabricated with a 5 x 5 array of 6-micron holes; center region will contain a 3 x 3 array of 8-micron holes in heater membrane, covered by a 30 nm SiN film to support catalyst particles.

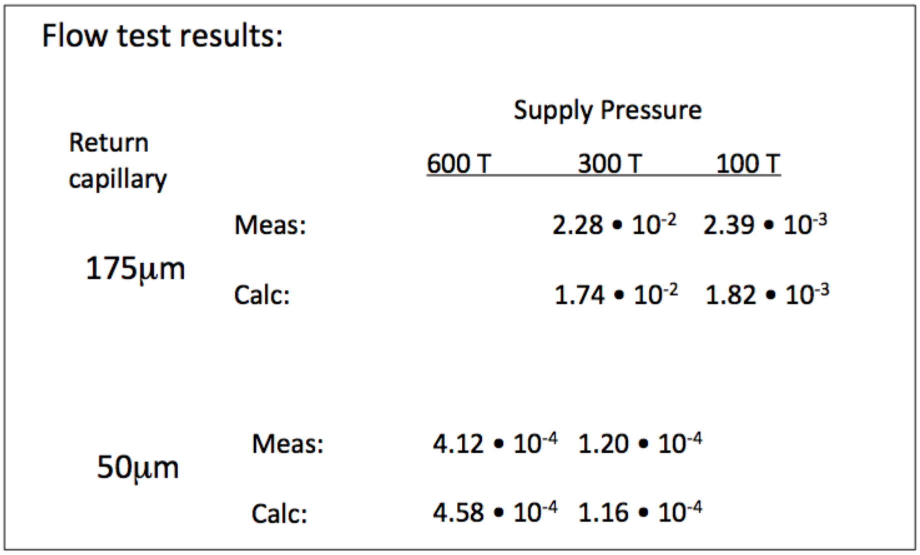

Flow test results:

Return capillary		Supply Pressure		
		600 T	300 T	100 T
175µm	Meas:		$2.28 \bullet 10^{-2}$	$2.39 \bullet 10^{-3}$
	Calc:		$1.74 \bullet 10^{-2}$	$1.82 \bullet 10^{-3}$
50µm	Meas:	$4.12 \bullet 10^{-4}$	$1.20 \bullet 10^{-4}$	
	Calc:	$4.58 \bullet 10^{-4}$	$1.16 \bullet 10^{-4}$	

Table 1. Measured vs calculated flow rates show good agreement, for viscous, laminar flow conditions. These tests allow us to reliably select the gas cell conditions required for a given experiment.

Agreement 14957 - Modeling of Thermoelectrics

A. A. Wereszczak and H. Wang*[†]
* *Ceramic Science and Technology Group*
[†] *Diffraction and Thermophysical Properties Group*
Oak Ridge National Laboratory
P.O. Box 2008, MS 6068, Bldg. 4515
Oak Ridge, TN 37831-6068
(865) 576-1169; fax: (865) 574-6098; e-mail: wereszczakaa@ornl.gov

J. Sharp, R. McCarty, and A. Thompson
Marlow Industries, Inc.
10451 Vista Park Road
Dallas, TX 75238-1645
(214) 342-4287; e-mail: rmccarty@marlow.com

DOE Technology Manager: Jerry L. Gibbs
(202) 586-1182; fax: (202) 586-1600; e-mail: jerry.gibbs@ee.doe.gov
ORNL Technical Advisor: J. Allen Haynes
(865) 576-2894; fax: (865) 574-4913; e-mail: haynesa@ornl.gov

Contractor: Oak Ridge National Laboratory, Oak Ridge, Tennessee
Prime Contract No.: DE-AC05-00OR22725

Objectives

- Non-CRADA sub-project: Measure thermomechanical and thermophysical properties of candidate thermoelectric (TE) materials (TEMats) for waste heat recovery to advance TEMats and devices (TEDs).
- CRADA sub-project: Support Marlow with their development of high temperature TEMats and TEDs.

Approach

- Non-CRADA sub-project: Develop characterization test methods that will benefit the TEs and TEDs manufacturing and end-user communities.
- CRADA sub-project: Measure properties of proprietary Marlow materials and provide development support.

Accomplishments

- Non-CRADA sub-project: Seebeck coefficients and electrical resistivities were measured by numerous laboratories as part of a round-robin study and interlaboratory variability assessed. The labs measured equivalent Seebeck coefficients; however, there was variability in the measured electrical resistivities.
- CRADA sub-project: Performed testing of Marlow TEMats and supportive evaluation of their TEDs and the constituents used in them.

Future Direction

- Non-CRADA sub-project: Measure properties of additional high-temperature capable TEMats and provide supportive characterization R&D to support the improvement of TEMats and TED modeling.
- CRADA sub-project: Perform thermomechanical and thermophysical property measurements of proprietary Marlow TEMats and assist in development of Marlow TEDs.

Introduction

Potential next generation thermoelectric devices (TEDs) comprised of p- and n-type materials enjoy strong interest for implementation in high temperature and oxidizing environments in which waste heat could be used to generate electricity. However, the intended thermoelectric function of these devices will only be enabled if the TED is designed to overcome the thermomechanical limitations (e.g., brittleness) that are usually inherent to these materials. A thermoelectric material (TEMat) with a combination of poor strength and low thermal conductivity can readily fail in the presence of a thermal gradient, thereby preventing the exploitation of the desired thermoelectrical function.

This challenging problem can be overcome with the combined use of established probabilistic design methods developed for brittle structural components, good thermoelastic and thermomechanical databases of the candidate TEMat comprising the TED, and iteratively applied design sensitivity analysis. This project executes this process to involve TEDs.

This project has two parts. The first sub-project focuses on the thermomechanical and thermophysical evaluation of candidate TEMats that are of interest to the entire TE community for high temperature (e.g., 550°C) waste heat recovery. The development of appropriate strength test fixturing and methods are required as there are no widely accepted strength test practices (e.g., ASTM) for thermoelectric materials. The second sub-project involves a CRADA with Marlow Industries and the thermomechanical and thermophysical characterization of their proprietary TEMats and supportive evaluations of their TEDs and the constituents used in them.

There will be several outcomes from this work. Mechanical reliability of prototypical TEDs will be evaluated from a structural brittle-material perspective, and suggested redesigns will be identified. Thermomechanical reliability of developmental TEMats will be assessed, and minimum required thermomechanical properties of hypothetical TEMats would be identified that produce desired reliability in a TED.

Results

The results from FY12 work are broken up into two sections: the non-CRADA and CRADA sub-projects.

<u>*Non-CRADA sub-project (Non-sensitive)*</u>

The non-CRADA section is comprised of three different subsections; mechanical and dilatometry evaluations, transport property and residual stress evaluations, and International Energy Agency (IEA) activities.

Mechanical and Dilatometry Evaluations:

While mechanical evaluation of TEMats has been the primary focus, additional attention is being devoted now to the mechanical evaluation of TEDs and the (non TEMat) constituents used in them. In preparation for that, ultrasonic (scanning acoustic microscope) and shear testing capabilities were established this year. The testers are shown in Figs. 1-2, and are now being used to evaluate the metallization quality.

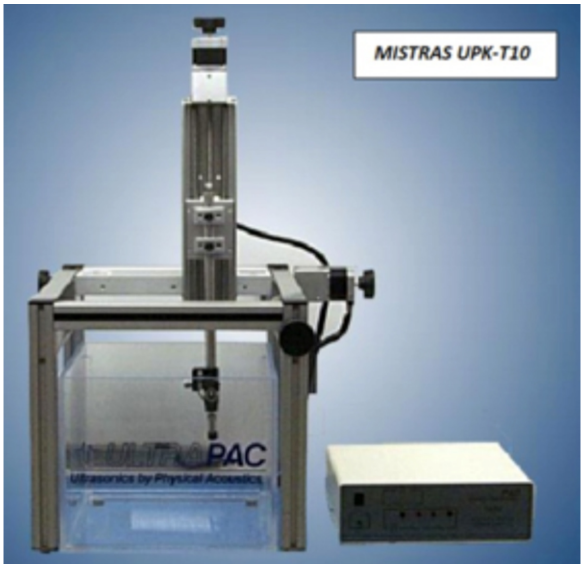

Figure 1. Scanning acoustic microscope used for the non-destructive evaluation of the interface between adjoined layers in TEDs.

Advanced software features include an operator configuration with selection for:

- Operator name.
- Right-hand or left-hand joystick, or both.
- Joystick button preferences.
- Reference table of microscope position settings.

All of which can be stored and transferred with the operator to another machine for quick setup.

Figure 2. A Nordson-Dage 4000 shear tester is used to measure shear strength of adjoined layers in TEDs.

Coefficient of thermal expansion testing of a candidate metallization material for use in Marlow TEDs was completed using (thin) stand-alone test coupons with high-temperature x-ray diffraction. Conventional dilatometry could not be used because the available material was too thin and had insufficient mechanical stiffness for use in the dilatometer's sample holder.

An idle and non-operable low-temperature capable dual-rod dilatometer was resurrected back into operation. Components of it are shown in Fig. 3. Interest exists to be able measure the coefficient of thermal expansion (CTE) of thermoelectric device constituents down to at least -40°C, and this dilatometer was designed for that capability. It uses liquid helium as its coolant, and is able to also heat up to approximately 200°C. Various parts of its hardware were repaired and its stable operation was confirmed using a sapphire test coupon. An example of its results are shown in Fig. 4 for a copper alloy, and it is being used in our CRADA with Marlow to measure low-temperature CTE of candidate metallization materials for use in their TEMats.

Mechanical test methods are under development that will impose a graded strain on a thermoelectric device using biaxial flexure. This will allow the mimicking of thermal-gradient-induced strain on devices, and enable simplistic failure analysis study of the constituents in these devices.

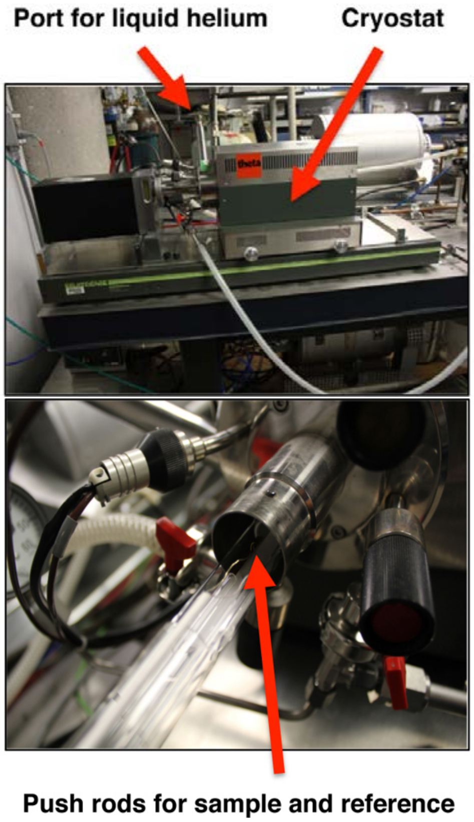

Figure 3. A cryogenic dual-rod dilatometer is being used to measure coefficient of thermal expansion of TED constituent materials.

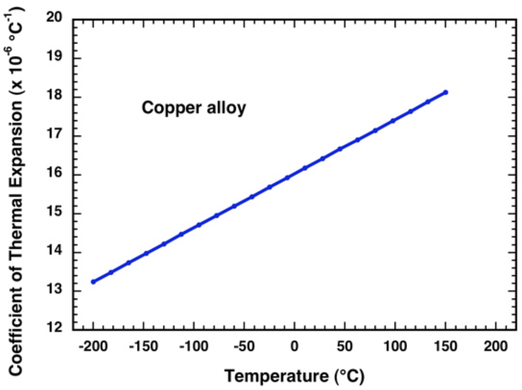

Figure 4. Example of resulting coefficient of thermal expansion measurement as a function of temperature down to -200°C.

Transport Property & Residual Stress Evaluations:

Neutron residual stress measurements were conducted at the High Flux Isotope Reactor (HFIR) at ORNL. The highly penetrating feature of neutrons allowed each leg in a TE module to be examined non-destructively. Figure 5 is a schematic view of neutron beam paths. To demonstrate the technique we used a "couple cut" from a 8x8 skutterudite module and two free standing n-type and p-type legs as reference, as shown in Fig. 6.

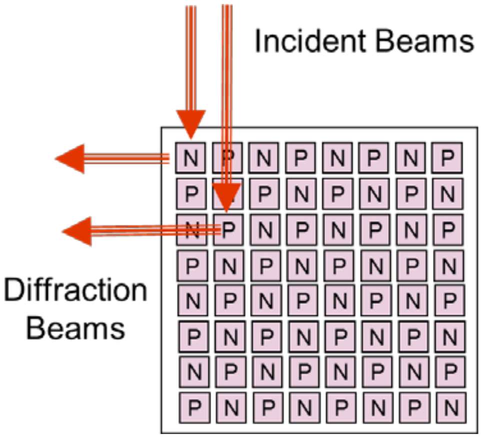

Figure 5. Neutron beam paths in an 8x8 skutterudite module.

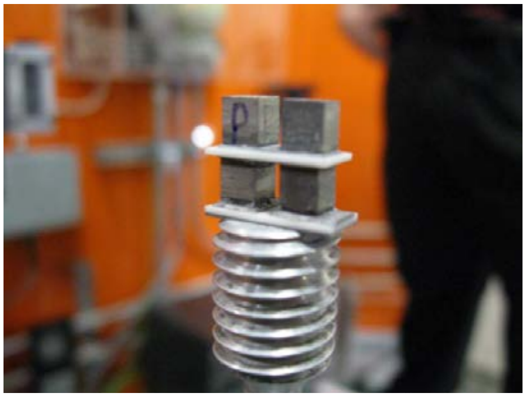

Figure 6. A skutterudite couple cut from the 8x8 module (bottom) with two stress-free legs mounted on the top as references.

The neutron signal for skutterudite was not as strong as metal with simple crystal structures. The large unit cell gives multiple diffraction peaks. The strongest peaks from 2θ=73-80 degrees selected from Si (220) crystal were used. As shown in Fig. 7, the n-type and p-type legs both showed four peaks in the region after 30 minutes of data collection. The gauge volume used was 3 x 3 x 0.5 mm and about 10 measurements in the Z-direction (heat and electric current flow direction) were carried out on each leg.

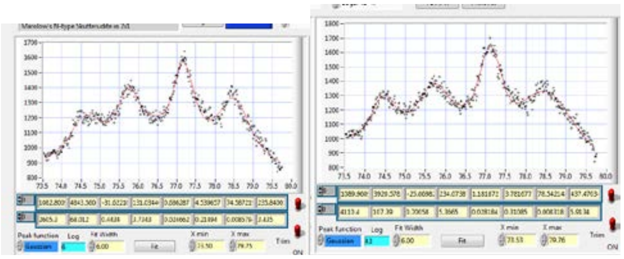

Figure 7. Neutron diffraction peaks for n-type(left) and p-type(right) legs. The red lines are curve fitting results.

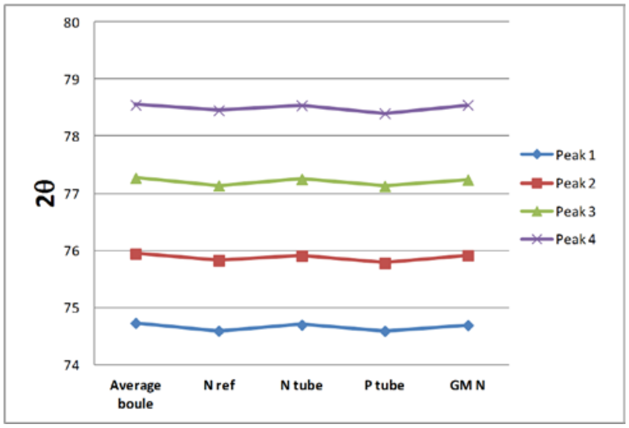

Figure 8. Peak positions determined by curve fitting on reference materials and powders.

N-type and p-type curve fitting with four peaks observed in the region, Fig. 7, were carried out for the legs, reference legs, and reference powders. The results are shown in Fig. 8. It was found that the "stress-free" (free-standing) reference legs had pre-existing residual stresses due to the thermally sprayed diffusion barriers. On the other hand, the powders used for hot-press were true stress-free references and could be used to calculate residual stresses in the TE legs of functioning modules. The neutron method has been demonstrated to be feasible to measure residual stress in TE modules. Detailed measurement on skutterudite modules will be conducted in FY13.

IEA Progress:

ORNL leads the International Energy Agency (IEA) annex VIII on Thermoelectrics under the Implementing Agreement of Advanced Transportation Materials (AMT). In FY12, the TE annex participants conducted the 2nd international round-robin on Marlow bismuth telluride. Two sets of materials were sent to 7 laboratories around the world. The results on electrical properties were significantly more consistent compared to the 1st round-robin conducted in FY11, as shown in Fig. 9.

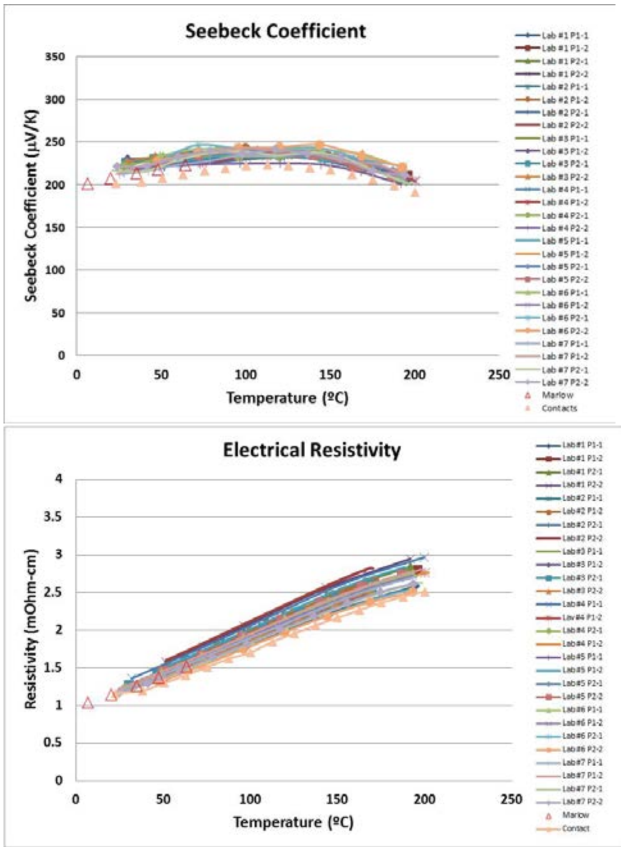

Figure 9. Seebeck coefficient and electrical resistivity of round-robin No. 2 on Marlow bismuth telluride.

In Fig. 10, thermal diffusivity and specific heat data from the 2nd round-robin showed more scatter indicating a difficulty of getting consistent results for thermal conductivity from the various labs. The sources of error were analyzed and the estimated error in the figure of merit, ZT, calculation can range from 12-20%. The IEA-AMT TE annex has developed a test procedure for TE materials. The 3rd international round-robin on half-heusler material started in May 2012. The temperature is from 300 to 800K covering the entire automobile exhaust gas temperature range.

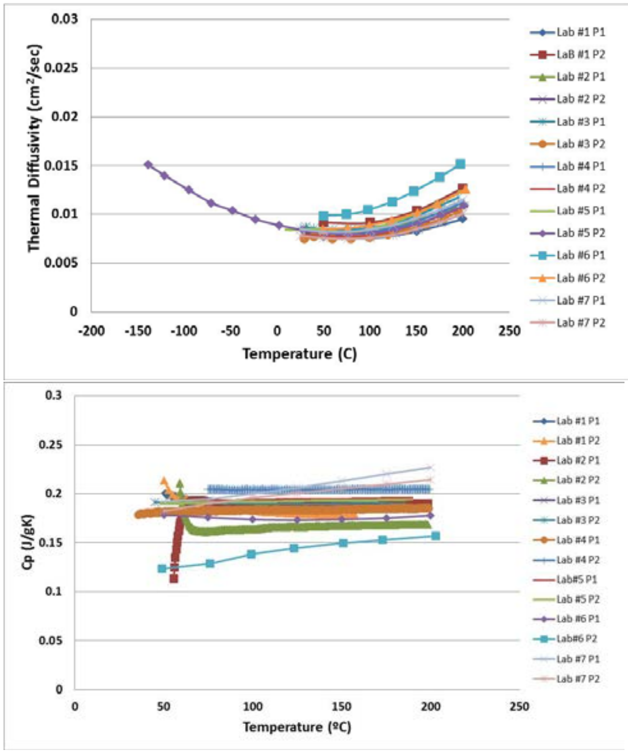

Figure 10. Thermal diffusivity and specific heat results of round-robin #2.

<u>*CRADA sub-project (Sensitive)*</u>

A CRADA with Marlow Industries continued in FY12. It is presently scheduled to end in FY13 (31 March 2013). The primary intents are to measure the transport properties, thermomechanically and thermophysically characterize their proprietary TEMats, and provide supportive mechanical evaluation of their TEDs and the constituents used in them. Testing of their materials continued throughout FY12. Transport properties of Marlow production and research thermoelectric materials were evaluated. Hundreds of specimens were tested but their results are not divulged here owing to the sensitivity of the CRADA.

ORNL continues to provide support to Marlow on high temperature transport properties measurements. Transport properties on melt-spun skutterudites and other Marlow materials were performed. The results are being used at Marlow as a basis for materials selection and device design.

Summary

For the non-CRADA portion of this project, new mechanical test facilities and transport property measurements were generated in FY12 including a 2nd IEA round robin measurement effort. For the CRADA portion, numerous tests were completed to assess mechanical and transport properties of Marlow TEMats and Marlow TEDs.

Publications

1. J. Y. Cho, X. Shi, J. R. Salvador, G. P. Meisner, J. Yang, H. Wang, A. A. Wereszczak, X. Zhou, and C. Uher, "Thermoelectric Properties and Investigations of Low Thermal Conductivity in Ga-Doped Cu_2GeS_3," *Physical Review B*, 84:085207 (2011).
2. J. R. Salvador, J. Y. Cho, Z. Ye, J. E. Moczygemba, A. J. Thompson, J. W. Sharp, J. D. König, R. Maloney, T. Thompson, J. Sakamoto, H. Wang, A. A. Wereszczak, and G. P. Meisner, "Thermal to Electrical Conversion of Skutterudite-Based Thermoelectric Modules," *Journal of Electronic Materials*, 10.1007/s11664-012-2261-9 (2012).
3. H. Wang, W. Porter, H. Böttner, J. König, L. Chen, S. Bai, T. Tritt, A. Mayolett, J. Senawiratne, C. Smith, F. Harris, P. Gilbert, J. Sharp, J. Lo, H. Kleinke, L. Kiss, "Transport Properties of Bulk Thermoelectrics – An International Round-Robin Study, Part I: Seebeck Coefficient and Electrical Resistivity," accepted for publication, *Journal of Electronic Materials*, September 2012
4. H. Wang, et al., "International Energy Agency Topical Report: Transport Properties of Bulk Thermoelectrics," ORNL Report #32716, September 20, 2011.

Agreement 16308 – Thermoelectrics Theory and Structure

D. J. Singh
Materials Science and Technology Division
Oak Ridge National Laboratory
P.O. Box 2008, MS 6056, Bldg. 4100
Oak Ridge, TN 37831-6056
(865) 241-1944; fax: (865) 574-7659; e-mail: singhdj@ornl.gov

DOE Technology Manager: Jerry L. Gibbs
(202) 586-1182; fax: (202) 586-1600; e-mail: jerry.gibbs@ee.doe.gov
ORNL Technical Advisor: J. Allen Haynes
(865) 576-2894; fax: (865) 574-4913; e-mail: haynesa@ornl.gov

---

Contractor: Oak Ridge National Laboratory, Oak Ridge, Tennessee
Prime Contract No.: DE-AC05-00OR22725

Objectives

- Find ways to optimize existing thermoelectric materials and discover new families of high performance thermoelectrics for waste heat recovery applications using modern, science-based materials design strategies.
- Find low cost materials that have high thermoelectric figures of merit and are suitable for vehicular applications.

Approach

- First principles calculations based on quantum mechanics are used to calculate electronic structure and thermoelectric properties of materials.
- Boltzmann transport equations are solved to obtain electrical transport properties.
- Vibrational properties are investigated and mechanisms for thermal conductivity reduction are assessed.

Accomplishments

- Performed first principles calculations of transport and other properties of potential thermoelectric materials.
- Discovered that heavily doped n-type $CrSi_2$ will be a high performance thermoelectric material at elevated temperatures suitable for exhaust waste heat recovery.
- Found that the chalcogenide Bi_2Se_3 may be a high performance thermoelectric material in the 300 – 600 K range if appropriately doped and nanostructured.
- Determined that CoSbS is a potential high performance thermoelectric with ZT values at high temperature potentially exceeding unity.
- Found that the chalcopyrite $AgGaTe_2$ could exhibit ZT values as high as 1.8 if doped and optimized, and that a large number of compounds share the physical and electronic structure of this compound.

Future Directions

- Identify new high performance low cost thermoelectric compositions suitable for vehicular applications.
- Calculate doping level dependence of thermoelectric properties to guide optimization of existing materials.

Introduction

The use of thermoelectric devices to convert waste heat in vehicle exhaust to electricity offers potentially significant energy savings. Among the requirements for the effective use of such devices is the availability of high performance thermoelectric materials, with low cost and other properties needed for application in vehicles. The dual requirement for both high performance and low cost has constrained thermoelectric applications in the automotive industry, although thermoelectrics have been effectively inserted in the context of seat cooling. In this regard, there is interest in improved thermoelectric materials, not only for waste heat recovery, but also for zonal heating and cooling in automobiles. High performance thermoelectric materials have the potential for improving fuel efficiency and at the same time improving occupant comfort by directing cooling where needed in the cabin.

We are developing improved materials using a science-based approach with a primary focus on materials for waste heat recovery. In particular, we are using materials design strategies based on first principles calculations of electronic, vibrational and transport properties to identify potentially low cost, high performance thermoelectric materials suitable for application in vehicles. We are also calculating properties of existing materials as a function of doping and other parameters to obtain information needed for optimization of these materials. The emphasis is on the thermoelectric figure of merit, *ZT*, at temperatures relevant to waste heat recovery, as well as materials properties of importance in engineering thermoelectric modules, for example anisotropy and mechanical properties. High $ZT=\sigma S^2T/\kappa$ requires a combination of high thermopower (S), good electrical conductivity (σ), and low thermal conductivity (κ). Finding materials with the needed combination of properties is challenging because, for example, high thermopower and high conductivity most commonly occur in different doping regimes. [1] We use state-of-the-art computational tools such as the linearized augmented planewave method [2] and the BoltzTraP code [3].

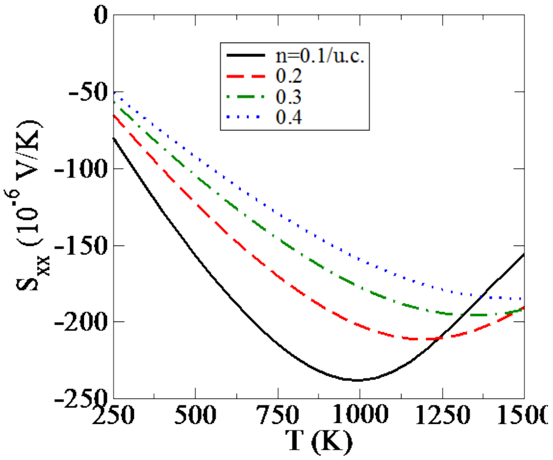

Figure 1: Calculated thermopower of n-type $CrSi_2$. Values at or exceeding 200 μV/K in a wide temperature and doping range above 750 K. Doping of 0.1/unit cell is equivalent to 9.25 x 10^{20} cm^{-3}.

Results

(1) Chromium silicide ($CrSi_2$):

Vehicular waste heat recovery requires both high performance and low cost. One material apparently overlooked by the scientific community in this regard is Chromium silicide ($CrSi_2$). Until quite recently, it was widely believed [4] not to have favorable high-temperature thermoelectric properties due to a comparatively small band gap of 0.35 eV [5]. However, we found [6] that this material may indeed show highly favorable n-type thermoelectric properties in the range from 900 – 1250 K, at very heavy dopings of 1-4 x 10^{21} cm^{-3}, and in addition good p-type performance in this temperature range as well (see Figs. 1 and 2 below). These results are due to the remarkably heavy valence and conduction bands present in this material, a useful design criterion for high performance thermoelectrics.

Vehicle exhaust temperatures are at the lower end of the above range during extended highway driving, for example, and therefore this material may be of substantial value as a high performance thermoelectric for

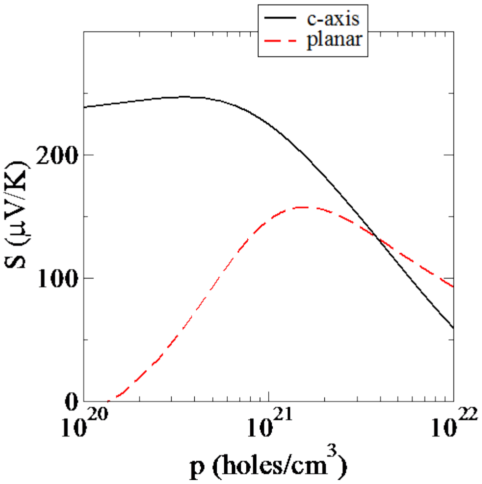

Figure 2: Calculated p-type thermopower at 1250 K for $CrSi_2$.

waste heat recovery. This material is composed of abundant, inexpensive and non-toxic elements. In view of its melting point of 1711 K, it is quite likely to be stable at temperatures and operating conditions of interest in an exhaust waste heat recovery system. It can also be doped both p-type and n-type, a substantial advantage for applications where issues of thermal expansion give a substantial advantage to materials that can be used for both p-type and n-type legs in a thermoelectric generator. A detailed technical report describing these results was published with open access.

(2) Chalcogenide Thermoelectrics:

A. Nanostructured hole-doped Bi_2Se_3

The thermoelectric material most commonly used in room temperature heating and cooling applications, as may see application to hybrid electric vehicles, is the chalcogenide Bi_2Te_3. However, this material suffers from several disadvantageous properties for practical applications, including the scarcity of Te and a band gap too small to permit effective use at temperatures much exceeding room temperature. With these concerns in mind, we performed first principles calculations of the sister chalcogenide material, Bi_2Se_3, which has been far less studied as a potential thermoelectric.

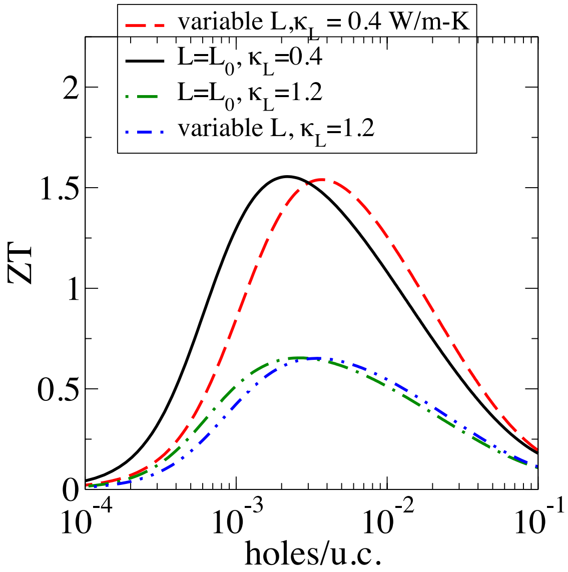

Figure 3: Figure-of-merit ZT at 500 K for hole-doped Bi_2Se_3, with nanostructuring included (black, red) and without (blue,green).

We found [7], as depicted in Figure 3, that if the lattice thermal conductivity is reduced by appropriate nanostructuring techniques, as have already been applied to Bi_2Te_3,[8,9] this material may show ZT's exceeding unity in a wide temperature range between 300 and 600 K.

This is an important result because it suggests that nanostructured Bi_2Se_3 may be a useful thermoelectric material both at room temperature (for heating/cooling applications) and at elevated temperature (for exhaust waste heat recovery applications). This is of great interest because Se, unlike Te, is available in quantities sufficient for widespread applications, and at \$65 per pound [10] is significantly less expensive than Te (\$160 per pound).

B. Marcasite structure CoSbS

Continuing our investigation of chalcogenide thermoelectrics comprised of inexpensive and abundant elements, we conducted first principles calculations of the band structure and transport of CoSbS (a material which had previously undergone scant investigation). The promising results found stimulated experimental investigations at Oak Ridge National Laboratory. Our theoretical calculations found favorable thermopower for both p-type and n-type doping, depicted in Figs. 4 and 5, particularly at high temperatures.

The experimental work on several n-type Nickel-doped samples found substantial thermopowers, and a significant ZT of 0.35 at 773 K, as depicted in Figure 6 below. We expect that significantly higher ZTs of unity or greater may be attainable on this material as the transport, including electrical resistivity and thermal conductivity, has not yet been optimized.

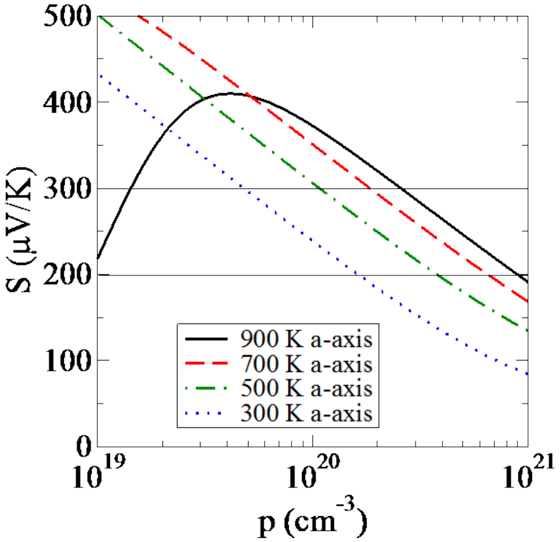

Figure 4: Calculated thermopower of p-type CoSbS. The lines at 200 and 300 μV/K delineate the range where optimal performance (i.e. ZT) is most likely to be found.

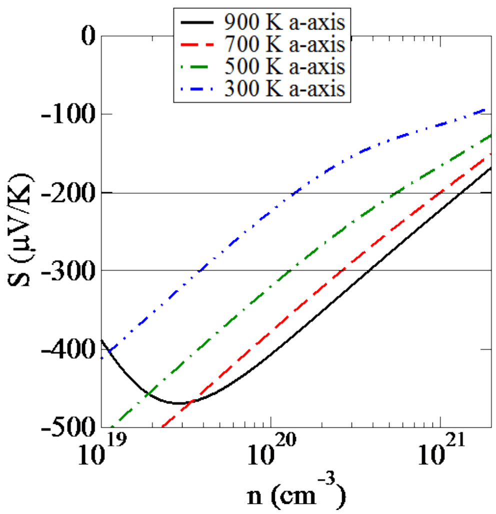

Figure 5:Calculated thermopower for n-type CoSbS.

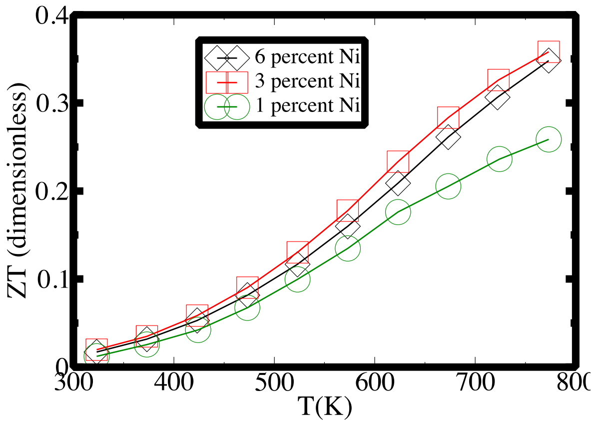

Figure 6:Experimental results for ZT on several samples of Nickel-doped CoSbS.

C. Chalcopyrite structure $AgGaTe_2$

We performed first principles calculations [11] on this material, which has already shown a ZT of 0.9 at high temperature with minimal optimization, finding that ZT values of as much as double this value are feasible with full optimization. Recent work on a closely related (isostructural and isoelectronic) material $CuGaTe_2$ shows [12] a ZT of 1.4, again with only partial optimization. Although $AgGaTe_2$ is composed of scarce and costly elements, as stated in our publication there is a large number of materials that share the same physical and electronic structure as this material, and it is likely that a material with more common constituents and good performance can be found and optimized.

D. N-type PbSe

We also found that p-type PbSe could be a high performance thermoelectric. [13] We have recently revisited n-type PbSe [14] with a revised electronic structure approximation which improves band gap accuracy and now find, in accord with recent experimental observations, that n-type PbSe can also be a high performance thermoelectric, with ZT values exceeding unity at high temperature.

Conclusions

We are obtaining new insights into thermoelectric materials performance using Boltzmann transport theory based on first principles electronic structures. We found that n-type $CrSi_2$ can be an excellent n-type high temperature thermoelectric if appropriately doped and optimized. We also found that nanostructured, optimized Bi_2Se_3 may show good performance between 300 and 600 K, and (in joint work with Brian Sales' group) found that a sulfide comprised of abundant, inexpensive elements – CoSbS – may show good thermoelectric performance if fully optimized. We also discovered that the chalcopyrite $AgGaTe_2$ may have ZT values of 1.8 or higher if fully optimized. Finally, our recent predictions [13,15] concerning the potential thermoelectric performance of optimized PbTe and PbSe have been confirmed [16,17,18,19] by the groups of G.J. Snyder, M.G Kanatzidis and Z.F. Ren. Present maximum observed ZT values in these materials are 2.2 (PbTe) [18] and 1.7 (PbSe) [19]. This compares with the ZT value of approximately 1.0 in materials currently used in applications.

References

[1] D.J. Singh and I. Terasaki, "Nanostructuring and more," Nature Materials **7**, 616 (2008).
[2] D.J. Singh, "Planewaves, Pseudopotentials and the LAPW Method, 2nd Edition," Springer, Berlin (2006).
[3] G.K.H. Madsen and D.J. Singh, "BoltzTraP: A code for calculating band-structure dependent quantities," Computer Physics Communications **175**, 67 (2006).
[4] C.B. Vining, "Thermoelectric Properties of Silicides," in *CRC Handbook of Thermoelectrics*, (D.M. Rowe, ed.) CRC Press: Boca Raton, 1995.
[5] L.F. Mattheis, "Electronic structure of CrSi2 and related refractory disilicides," Phys. Rev. B **43**, 12549 (1993) and references therein.

[6] D. Parker and D.J. Singh, "Very heavily electron-doped CrSi2 as a high-performance high-temperature thermoelectric material," New J. Phys. **14**, 033405 (2012).
[7] D. Parker and D.J. Singh, "Potential thermoelectric performance from optimization of hole-doped Bi2Se3," Phys. Rev. X **1**, 021005 (2011).
[8] W. Xie, X. Tang, Y. Yan, Q. Zhang and T.M. Tritt, "Unique nanostructures and enhanced thermoelectric performance of melt-spun BiSbTe alloys," Appl. Phys. L Rseett. **94**, 102111 (2009).
[9] B. Poudel *et al*, "High-Thermoelectric Performance of Nanostructured Bismuth Antimony Telluride Bulk Alloys," Science **320**, 634 (2008).
[10] United States Geological Survey report available at http://minerals.usgs.gov/minerals/pubs/commodity/selenium/mcs-2012-selen.pdf
[11] D. Parker and D.J. Singh, "Thermoelectric properties of AgGaTe2 and related chalcopyrite structure materials," Phys. Rev. B 85, 125209 (2012).
[12] T. Plirdpring et al, "Chalcopyrite CuGaTe2: A High-Efficiency Bulk Thermoelectric Material," Adv. Mat. **24**, 3622 (2012).
[13] D. Parker and D. J. Singh, "High-temperature thermoelectric performance of heavily doped PbSe," Phys. Rev. B **81**, 035204 (2010).
[14] D. Parker, D.J. Singh, Q. Zhang and Z. Ren, "Thermoelectric properties of n-type PbSe revisited," J. Appl. Phys. **111**, 123701 (2012).
[13] D.J. Singh, "Doping-dependent thermopower of PbTe from Boltzmann transport calculations," Phys. Rev. B **81**, 195217 (2010).
[16] Y. Pei, X. Shi, A. LaLonde, H. Wang, L. Chen and G. J. Snyder, "Convergence of electronic bands for high performance bulk thermoelectrics," Nature **473**, 66, (2011).
[17] H. Wang, Y. Pei, A.D. LaLonde and G.J. Snyder, "Heavily doped p-Type PbSe with high thermoelectric performance: an alternative for PbTe," Adv. Mat. **23**, 1366 (2011).
[18] K. Biswas, J. He, I.D. Blum, C-I Wu, T.P. Hogan, D.N Seidman, V.P. Dravid and M.G. Kanatzidis, "High-performance bulk thermoelectrics with all-scale hierarchical architectures," Nature **489**, 414 (2012).
[19] Q. Zhang, F. Cao, W. Liu, K. Lukas, B. Yu, S. Chen, C. Opeil, D. Broido, G. Chen and Z. Ren, "Heavy Doping and Band Engineering by Potassium to Improve the Thermoelectric Figure of Merit in p-Type PbTe, PbSe, and $PbTe_{1-y}Se_{y}$," J. Am. Chem. Soc. **134**, 10031 (2012).

Agreement 20370 – Life Cycle Modeling of Propulsion Materials

Sujit Das
Energy and Transportation Science Division
Oak Ridge National Laboratory
National Transportation Research Center
Knoxville, TN 37932-6472
(865) 946-1222; fax: (865)946-1314; e-mail: dass@ornl.gov

DOE Technology Manager: Jerry L. Gibbs
(202) 586-1182; fax: (202) 586-1600; e-mail: Jerry.gibbs@ee.doe.gov
ORNL Technical Advisor: Allen Haynes
(865) 576-2894; fax: (865) 574-4913; e-mail: haynesa@ornl.gov

Contractor: Oak Ridge National Laboratory, Oak Ridge, Tennessee
Prime Contract No.: DE-AC05-00OR22725

Objectives

- Develop life cycle technical models that address the viability of existing and new lightweight propulsion materials from economic, energy, and environmental perspectives.
- Use technical modeling to estimate specific technology improvements and major drivers that are detrimental to the viability of advanced propulsion materials technologies.

Approach

- Examine the viability of advanced propulsion materials technologies on a life cycle basis, since the life cycle stages beyond the manufacturing stage form a major share of total life cycle impacts.
- Develop technical models to estimate the impacts of major input parameters at specific processing steps on the overall viability of a propulsion materials part manufacturing technology.

Accomplishments

- Completed the cost-effectiveness analysis of a 25% vehicle mass reduction goal in light-duty vehicles

Future Direction

- Life cycle cost analysis of advanced powertrain technologies using automotive system cost model.

Cost Effectiveness of a 25% Vehicle Mass Reduction Goal in Light-Duty Vehicles

The pressure to lightweight vehicles is stronger than ever due to high gasoline prices and new fuel economy and emissions regulations for model years 2017-2025 that require car and light truck performance equivalent to 54.5 mpg and reductions in greenhouse gas emissions to 163 grams per mile in 2025. Vehicle lightweighting represents one of several design approaches auotmakers are currently evaluating to improve fuel economy. There has also been a recent trend of lighitweighting expensive alternative powertrains for better economics from downsized powertrain cost. The Lightweight Materials' (LMs') component of the U.S. Department of Energy's Vehicle Technologies Program has a 50% weight-reduction goal comparable to 2002 vehicles for passenger vehicle body and chassis systems, with safety, performance, and recyclability. In order to achieve this long-term weight reduction goal, LM has set a few annual intermediate weight reduction goals, 25% being the goal for which the cost-effectiveness has been examined here using the baseline 2002 midsize automobile cost model developed during FY2011.

The cost-effectiveness of the proposed weight reduction goal is determined based on the vehicle retail and life cycle cost analysis of three potential lightweight material types of substitution scenarios in various body and chassis components to achieve the desired weight reduction goal. Besides baseline conventional internal combustion engine powertrain, two other advanced powertrain types (i.e., downsized, boosted and the hybrid electric) in combination with three potential lightweight material types of substitution in body and chassis components are also being considered in order to determine how the cost-effectiveness of the desired 25% vehicle weight reduction goal can be achieved with these two alternative powertrain technologies being seriously considered in the industry today. The eleven vehicle scenarios include the two baseline vehicles based on conventional internal combustion engine (ICE) and electric hybrid and the remaining nine are the three alternative lightweighting material pathways for body and chassis combined with two baselines and downsized and boosted ICE powertrain alternative. Lightweighting material pathways include lightweight metals (primarily aluminum and magnesium), carbon fiber reinforced polymer composites (CFRP), and multimaterial.

Using the DOE-developed Autonomie vehicle performance software by Argonne National Laboratory, the fuel economy improvements for a 25% lower vehicle curb weight relative to a 2002 baseline mid-size vehicle was estimated. Vehicle retail price and life cycle/ownership estimates were made for the four scenarios considered using the 35+ major component-level ORNL Automotive System Cost Model (ASCM) developed for a mid-size passenger car. Using the component data and specific alternative component technology data available from the industry representing a specific scenario, lightweighting cost effectiveness is estimated. The 2002 baseline mid-size vehicle considered is a 1477 kg curb weight; 185 HP, port fuel injected, V6 aluminum, four valves per cylinder, naturally aspirated engine; and adjusted city, highway, and combined fuel economy estimated to be 18.8 mpg, 26.5 mpg, and 23.3 mpg, respectively. It is estimated that the fuel economy of 25% lightweight conventional ICE powertrain vehicles will improve by 21%, while the engine power will reduce from 136 kW to 108 kW compared to the baseline vehicle. The fuel economy of the downsized and boosted ICE engine is estimated to be 32.5 mpg or 28.3% higher than the ICE baseline engine; compared to a near doubling in the fuel economy for the hybrid configuration with the 25% lighter vehicle mass.

Total per-vehicle target mass savings of 369 kg (with the exception of 494 kg in the case of heavier electric hybrid powertrain) are disaggregated between two savings components: (1) powertrain (i.e., primarily engine mass impacts) and secondary mass savings due to mass decompounding (in the range of 149 – 215 kg) and (2) lightweight material substitution savings. The estimated total material substitution savings for various scenarios were disaggregated at the level of 35+ major vehicle components considered by the ORNL ASCM. Depending on the scenario under consideration, a combination of various lightweight material components has then been selected in order to meet the desired lightweight material substitution mass savings target. Due to the limited scope of this study, component-level lightweight mass savings potential estimates were based entirely on the review of literature about demonstrations and validations of such applications. Table 1 indicates the necessary lightweight material substitutions at the major component level (level in terms of kg indicated within the parenthesis of each major vehicle component) for three lightweight pathways to achieve the desired mass savings target for the baseline conventional ICE powertrain.

Lightweight material component cost data are being estimated using two approaches (limited technical cost modeling and published available supplier cost assessments). The former approach was used in those cases where the lightweight technology is relatively more mature and has already been commercialized to a certain extent. Some of the lightweight metal component cost estimates are already available in the ASCM used for the vehicle life cycle cost estimation here, where functional cost relationships have been developed based on the numerous technical cost assessments. Supplier cost assessments were used in cases where the detailed technology data necessary for the cost estimation were unavailable as the technology is yet-to-be commercialized.

Figure 1 shows the relative cost effectiveness of eleven scenarios in terms of vehicle life cycle cost as a percent of the 2002 baseline conventional ICE engine vehicle's life cycle cost. Seven components of vehicle retail price, i.e., powertrain, body, chassis, interior, electrical, assembly, and overhead, are shown along with operation cost which is the difference between the net present value of vehicle ownership cost and the vehicle retail price. The powertrain, body, and overhead are the three leading contributors to the vehicle retail price. The vehicle operation cost is about 40-50% of the total vehicle ownership cost. Between the two baselines considered, the hybrid powertrain has a 15% higher retail price, but a 3% reduction in vehicle ownership cost relative to the baseline ICE. The higher powertrain cost is the contributor to the higher hybrid vehicle retail price, as one would expect.

A 25% vehicle lightweighting in the nine scenarios will lead to a vehicle retail price premium in the range of 5% to 49% compared to the baseline conventional ICE powertrain and produces at most a 6% reduction in vehicle ownership cost. The lightweighted vehicle's increased retail price is mainly due to body costs that nearly doubled to achieve the 25% lightweighting. Among the three alternative powertrain lightweighting options considered in terms of vehicle retail price, the downsized and boosted powertrain option is the most cost-effective option, whereas the hybrid is the least favorable option compared to the conventional ICE powertrain. This difference is due to the fact that the downsized and boosted option contributes about 18 kg mass savings, so it requires less body and chassis lightweighting and results in an 5-11% retail price increase, compared to 8-6% increase for the lightweighted conventional ICE powertrain. The retail price premium due to additional lightweighting necessary for the hybrid powertrain vehicle—with its heavier powertrain—is estimated to be 31-49%. However, this vehicle's cost-effectiveness is significantly improved at the vehicle ownership cost level, and the cost premium is estimated to be +1 to +8%, compared to the cost advantage of -1 to -6% earned by the downsized and boosted powertrain. The retail price premium (+8-16%) for the lightweighted conventional powertrain vehicle falls within these two advanced powertrains, whereas its life cycle costs carry a maximum 1% premium in the case of carbon fiber-reinforced polymer composites and multi-material lightweighting material pathways.

Since lightweighting of hybrid vehicles is based on maintaining the electric powertrain from the baseline hybrid, a relatively small decrease in powertrain cost with reduced engine size from 136 kW to 108 kW did not have any significant impact on its overall cost-effectiveness. Compared to the baseline hybrid vehicle, the lightweight hybrid vehicle's retail price increased by 14-30%, while the vehicle ownership cost increased more moderately, in the range of 4-11%.

Among the ten scenarios considered, with vehicle retail price increases ranging from 5-49% above the 2002 baseline ICE powertrain, only five scenarios are anticipated to have vehicle operation costs (based on the fuel price assumption of $3/gal) sufficiently low enough to produce vehicle ownership costs equal to or less than the baseline vehicle. These five vehicle scenarios—Hybrid, conventional ICE lightweight metals, and downsized and boosted lightweight metals, lightweight CFRP and lightweight mixed-materials —have vehicle ownership costs 1% to 6% less than the baseline, thereby resulting in a payback period within the assumed vehicle lifetime of 12 years as shown in Table 2. The downsized and boosted (D&B) powertrain requires the least lightweighting to meet the 25% weight reduction target, thereby allowing recovery of the increased cost within three years of vehicle life in most cases even at a conservative fuel price of $3/gal. Hybrid vehicles are anticipated to have a discounted payback period of 6-7 years, slightly higher than reported in the literature which is generally based on the simple payback period. Among the lightweighted vehicle scenarios with traditional ICE powertrains, only light metals provides a payback period within the vehicle's life. For a relatively shorter payback period (in the range of 4-6 years) necessary for the consumer acceptance of advanced technology vehicles, only five scenarios achieve a discounted payback period of four years at a fuel price range of less than $7.00/gal as shown in Table 2. With the recent fuel price trend, hybrid vehicles seem to be competitive, as do the CFRP and mixed-material scenarios with the downsized & boosted powertrain. The light metals pathway with the conventional ICE powertrain has a four year payback period with gasoline at $3.50-$4.00/gal.

Conclusions

Demonstration and validation of a cost-effective, multiyear vehicle weight-reduction strategy requires a system-level automotive life cycle cost model that considers not only the interdependency of various components within a vehicle, but also vehicle ownership cost, including vehicle operation cost and vehicle retail price. A significant fuel economy gain of 28.3% and 100% can be obtained in the case of a 25% lightweighted mid-size downsized and boosted and hybrid electric powertrains, respectively, compared to conventional ICE powertrain vehicle. Achieving the 25% vehicle mass reduction target in a 2002 mid-size vehicle will require a vehicle retail price premium in the range of 5 – 49%, the low- and high-end range values associated with the downsized and boosted powertrain and the hybrid powertrain, respectively. The downsized and boosted powertrain requires a smaller lightweighting price premium since a small part of overall lightweighting is being provided by the downsized and boosted engine and in this case the vehicle ownership cost is estimated to decrease in the range of 1-6%. The evaluation of three alternative lightweighting material pathways indicates a light-weight metals pathway to be the cost effective one irrespective of the powertrain type. Using a fuel cost of \$3/gal, the payback period of the 25% lightweight downsized and boosted vehicle is estimated to be less than 6 years. At a fuel price of about \$4.00/gal, a payback period of four years as preferred by consumers willing to buy advanced technology vehicles can be obtained in all cases of downsized and boosted powertrain. It is anticipated that with further cost optimization of lightweight components substitution, the cost-effectiveness of 25% vehicle mass reduction goal can be further optimized. A combination of advanced powertrain such as downsized and boosted and body and chassis component lightweighting is essential to achieve the cost-effectiveness of vehicle mass reduction target from a vehicle ownership cost perspective.

Publications/Presentations

None

Special Recognitions and Awards/Patents Issued

None

Table 1. Lightweight material component substitution considered under three different lightweight material pathways combined with the *conventional ICE powertrain*

Parameters	**Lightweight Metals**	**CFRP**	**Multi-Material**
Components and mass savings (kg)	Al Cradle (12) Al BIW (116) Al Panels (26) Al Front/Rear Bumpers (4) Polycarbonate Glass (2) Al Suspension Control Arms (12) Al Braking System (7) Al wheels + Tire (8) Mg IP Beam (5) Mg Steering Wheel Column (2) Mg Seat Frames (18) Fuel (9)	Cradle (16) BIW (145) Closure Panels (29) Front/Rear Bumper Impact Module (3) Seat Structure (17) Fuel (9)	Mg Cradle (12) MMV BIW (105) Al Panels (26) MMV Front/Rear Bumpers (4) Polycarbonate Glass (11) Al Suspension Control Arms (12) Al Brake Actuators +Knuckles (5) Mg wheels + Tire MMV (9) MMV IP Beam (3) Mg Steering Wheel Column (2) MMV Seats (17) Exterior Lighting (4) Fuel (9)
Total Mass Substitution Savings (kg)	**220**	**220**	**220**

Table 2. Discounted Payback Period and Fuel Price Estimates for Cost-Effectiveness of 25% Lightweight Vehicles

Powertrain	**Hybrid**	**ICE Powertrain**			**D&B Powertrains**			**Hybrid Powertrains**		
Lightweighting Scenario	na	Metals	CFRP	MultiM	Metals	CFRP	MultiM	Metals	CFRP	MultiM
Discounted Payback (yrs) @3.00/gal	6-7	>12	>12	>12	1-2	5-6	2-3	>12	>12	>12
Gas price ($/gal) for a 4-yr pay-back	$4.00-$4.50	$3.50-$4.00	>$7.00	>$7.00	<$2.00	$3.50-$4.00	<$2.00	>$7.00	>$7.00	>$7.00

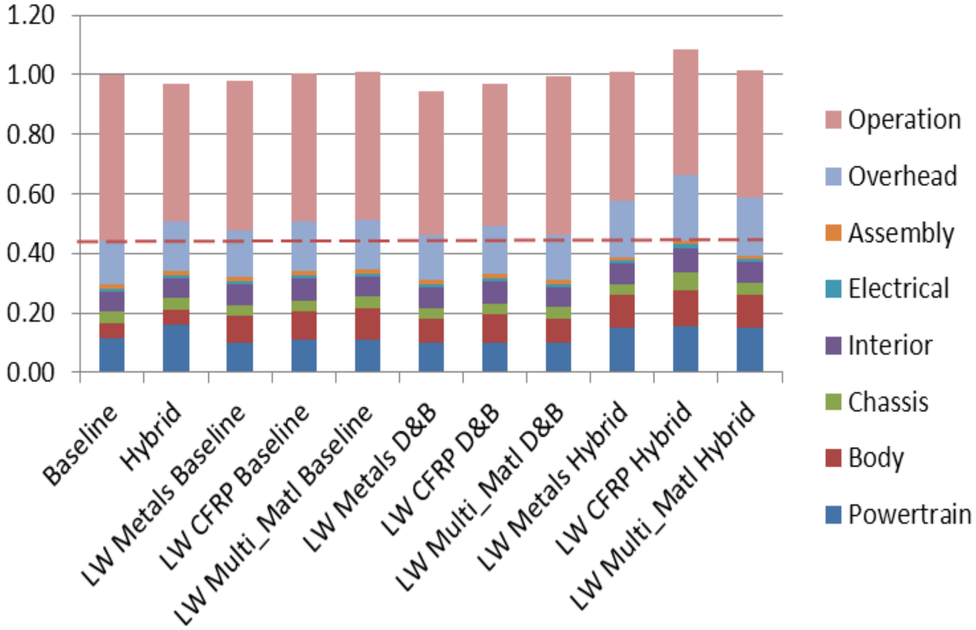

Figure 1. Cost effectiveness of alternative 25% lightweight vehicle scenarios

ORNL/TM-2012/571 January 2013
Printed with a renewable-source ink on paper containing
at least 50% wastepaper, including 10% post consumer waste.

U.S. DEPARTMENT OF
ENERGY | Energy Efficiency &
Renewable Energy

For more information
eere.energy.gov